

TECHNICAL UNIVERSITY OF LIBEREC
FACULTY OF TEXTILE ENGINEERING

Study program: P3106 Textile Engineering
Study branch: 3106V007 Textile and Material Engineering

**DYNAMICS OF LIQUID PENETRATION INTO
FIBROUS MATERIALS**

**DYNAMIKA PRŮNIKU KAPALIN DO
VLÁKENNÝCH MATERIÁLŮ**

DISSERTATION THESIS

Author: Ing. Bc. Eva Košťáková
Supervisor: Prof. RNDr. David Lukáš, CSc.

V Liberci 30.9.2011

Prohlášení

Byla jsem seznámena s tím, že na mou disertační práci se plně vztahuje zákon č. 121/2000 o právu autorském, zejména § 60 (školní dílo).

Beru na vědomí, že Technická univerzita v Liberci (TUL) nezasahuje do mých autorských práv užitím mé disertační práce pro vnitřní potřebu TUL. Užiji-li disertační práci nebo poskytnu-li licenci k jejímu využití, jsem si vědoma povinnosti informovat o této skutečnosti TUL; v tomto případě má TUL právo ode mne požadovat úhradu nákladů, které vynaložila na vytvoření díla, až do jejich skutečné výše.

Disertační práci jsem vypracovala samostatně s použitím uvedené literatury a na základě konzultací se školitelem.

V Liberci 30. 9. 2011

.....

Podpis

ANNOTATION

The thesis have brought a way to the recognition or clarification of some legalities from the branch of dynamics of liquid penetration into porous materials, its simulation by means of Auto models and its application on a “journey” to the solution of the factual problem with the production of composite materials reinforced with electrospun nanofibre layers. Thus the complete text is divided into three parts.

The first part is focused on introduction of dynamics of liquid penetration into porous materials. Theoretical part dealt with basic terms and legalities of wetting. There are described model of cylindrical capillary and model of radial capillary as model systems for better understanding of drops penetration into complex porous or even textile structures. There is also part devoted to the enhancement of liquid penetration into porous materials with the intention of ultrasound usage. Experimental part should bring a design of a simple and an effective method for studying the dynamics of liquid penetration into fibre materials and its testing for a scale of nonwovens with different geometrical parameters (change of fibre volume fraction, change of orientation of fibres, change of fibre diameter...).

The second part of the thesis shortly describes basic terms and legalities of automodels and Monte Carlo methods, examples of automodels usage for simulation of wetting phenomenon. Testing and evaluation of a possibility to use the simulation models for the observation of wetting dynamics follows the theoretical part as an introduction of thesis author the simulation study.

The last part is devoted to nanofiber-reinforced composites. There are described composite nanofibers and nanocomposites reinforced by carbon nanotubes and electrospun nanofibers. Experimental part involves the description of a concrete solution for composite materials reinforced with electrospun nanofibre webs. The manufacturing process requires special approach because the electrospun nanofibre web brings several untraditional complications, which are necessary to solve. The entrance to the world of “nano” dimensions brings great challenges (problems), but evidently also several advantages in results. The thesis does not focus on testing and applied research in the branch of electrospun nanofibre reinforced composites. The work wants to show that it is possible to apply all theoretical knowledge, experimental and simulation skills for concrete examples.

Keywords: *wetting dynamic, dewetting, nonwovens, Ising model, method Monte Carlo, nanocomposites, electrospinning.*

ANOTACE

Tato disertační práce se zabývá problematikou dynamiky průniku kapalin do vláknenných materiálů a to v rovině experimentální, pomocí počítačových simulací, ale i v konkrétní praktické aplikaci při výrobě kompozitních materiálů. Práce je rozdělena do tří hlavních částí.

První část je zaměřena na dynamiku průniku kapalin do porézních materiálů obecně. Teoretická část obsahuje základní termíny a zákonitosti smáčení. Jsou zde popsány modely válcovité a radiální kapiláry jako dva základní modelové systémy pro lepší porozumění komplexnímu procesu pronikání kapek do porézních vláknenných i nevláknenných struktur. Je zde také část věnovaná možnostem podpory pronikání kapalin do porézních materiálů a to účinkem ultrazvuku. Experimentální část představuje nejprve navrženou jednoduchou a efektivní metodu pro studium dynamiky průniku kapek zejména do vláknenných materiálů s relativně velmi hrubým povrchem. Tato metoda je pak využívána k testování dynamiky průniku kapek do různých druhů netkaných textilií s ohledem na: (i) změny jejich geometrických parametrů (zaplnění, orientace vláken, průměr vláken); (ii) změny viskozity kapalin použitých ke smáčení a (iii) změny dynamiky průniku kapek do netkaných textilií při použití ultrazvuku.

V druhé části je stručně představen Isingův model, metoda Monte Carlo, Kawasakiho kinetika a další termíny a zákonitosti nutné k uvedení do problematiky počítačových simulací procesů smáčení. Vlastní počítačové simulace a jejich vyhodnocení jsou součástí experimentů v této části práce. Tyto počítačové simulace jsou zaměřeny jak na procesy vedoucí k rovnováze (k čemuž jsou prioritně tyto simulace určeny) tak zejména na odhalení možnosti jejich využití v simulacích dynamických jevů – sledování dynamiky průniku kapalin do porézních materiálů. Tyto simulace jsou samozřejmě porovnávány zejména s teoretickými poznatky z první části této práce.

Výroba a testování kompozitních materiálů s nanovláknennou výztuží je tématem poslední, třetí části předkládané disertační práce. V teoretické části jsou představena kompozitní nanovláknna, kompozity vyztužené uhlíkovými nanovláknny či nanotubicemi a kompozity vyztužené elektrostaticky zvlákněnými nanovláknny. Právě elektrostaticky zvlákněná nanovláknna jsou pak použita jako jediná či sekundární výztuž kompozitních materiálů v experimentech, kde výrobní proces vyžadoval netradiční přístup a řešení několika nezvyklých problémů spojených se vstupem do „nano“ oblasti vláknenných materiálů. Výsledný kompozitní materiál byl vyroben zejména jako konkrétní příklad využití teoretických znalostí, znalostí a zkušeností získaných z experimentů a simulací procesu smáčení uvedených v této disertační práci.

Klíčová slova: dynamika smáčení, netkané textílie, Isingův model, metoda Monte Carlo, nanokompozity, elektrostatické zvláknění.

ACKNOWLEDGMENTS

I would like to thank to my supervisor Prof. RNDr. David Lukáš, CSc. for guidance, interest, advice, valuable comments and patience. I thank also to Ing. Jan Grégr from Department of Chemistry, Faculty of Sciences, Humanities and Education, Technical University of Liberec for a nice and very stimulating discussions and to Ing. Richard Charvát Ph.D. from Department of Fine Arts, Faculty of Art and Architecture, Technical university of Liberec for the processing of 3D illustrations of the simulations. Many thanks belong to my colleagues from the Department of Nonwovens and mainly to my family and friends for their supporting during this thesis writing.

PODĚKOVÁNÍ

Na tomto místě děkuji školiteli a vedoucímu Katedry netkaných textilií Prof. RNDr. Davidu Lukášovi, CSc. za odborné vedení, zájem, rady, cenné připomínky a trpělivost, se kterou se mi věnoval. Také děkuji Ing. Janu Grégrovi z Katedry chemie, Fakulty přírodovědně-humanitní a pedagogické, Technické univerzity v Liberci za milé a velmi podnětné diskuse a Ing. Richardovi Charvátovi Ph.D. z Katedry výtvarných umění, Fakulty umění a architektury, Technické univerzity v Liberci za zpracování 3D ilustrací ze simulací. Dále bych chtěla poděkovat svým kolegům z Katedry netkaných textilií. V neposlední řadě chci poděkovat mé rodině a přátelům za podporu během zpracovávání této disertační práce.

CONTENT

1. Introduction.....	3
2. Wetting Processes.....	4
2.1. <i>Basic Terms and Legalities of Wetting</i>	4
2.2. <i>Wetting Models</i>	6
2.2.1. Model of Cylindrical Capillary.....	6
2.2.2. Model of Radial Capillary.....	13
2.2.3. The Shape of Drops.....	16
2.2.4. Drop Penetration into Porous Materials.....	20
2.2.5. Usage of Ultrasound for Enhancement of Liquid Penetration.....	22
2.3. <i>Wetting Experiments</i>	24
2.3.1. Description of Experiment Procedure.....	
2.3.2. Radial Capillary.....	28
2.3.3. Drop Penetration into Nonwovens.....	30
2.3.4. Recapitulation of Experimental Results.....	44
2.4. <i>Reference</i>	46
3. Simulation.....	48
3.1. <i>Basic Term and Legalities of Simulation Model</i>	48
3.2. <i>Auto Model Used Computer Simulation of Wetting</i>	53
3.3. <i>Computer Simulation Outputs</i>	54
3.3.1. Equilibrium States Computer Simulation.....	56
3.3.2. Wetting Dynamic Computer Simulation.....	68
3.4. <i>Recapitulation of Simulation Results</i>	75
3.5. <i>References</i>	76
4. Fiber Reinforced Composites.....	77
4.1. <i>Fiber Reinforced Composite Materials</i>	77
4.2. <i>Review on Nanofiber Composites</i>	78
4.2.1. Composite Nanofibers.....	79
4.2.2. Composites Reinforced by Nanofibers.....	80
4.3. <i>Composites Reinforced by Electrospun Nanofibrous Layers</i>	83
4.4. <i>Conclusions</i>	93
4.5. <i>References</i>	94
5. General Conclusions.....	96
6. Appendixes.....	97

Notation

A	area
C, k	constant
C_g	simulation gravitational energy
C_{ij}	exchange energy between cell i and cell j in the neighborhood of i -cell
d	distance between plates of radial capillary
D	diameter
E	energy
e	thickness
F	force
g	gravitational acceleration
H	Hamiltonian / total energy
h	height
J	suction velocity
L	length
m	mass
N	number of cells
P	pressure
p_1	capillary pressure
p_2	hydrostatic pressure
Q	flow rate
$r; R$	radius
$R_1; R_2$	radii of curvature
S	contact area
S	Hankinson's spreading coefficient
t	time
V	volume
V_{av}	volume penetrated into material
V_{SC}	sphere cap volume
W	transition probability
w	width
$\bar{x}; \bar{y}$	configurations of the system
Z	partition function of the system
α	exponent of allometric functions
β	angle of cylindrical capillary plunging
ρ	density
τ	statistical temperature
τ_p	dimensionless time
γ	surface tension
μ	viscosity
θ	contact angle

θ_a	advancing contact angle
θ_r	receding contact angle
κ^{-1}	capillary constant / capillary length
σ_{LSS}	interlaminar shear stress
σ_{max}	flexural stress
τ_p	dimensionless time

A photograph of a red door with a silver handle and keyhole, set in a white frame. The door has two arched panels at the top and two rectangular panels at the bottom. The background is a plain white wall.

There are things known
and there are things unknown,
and in between are the DOORS...
J. Morrison

Content:

1. Introduction	3
2. Wetting Processes	4
2.1. Basic Terms and Legalities of Wetting	4
2.2. Wetting models	6
2.2.1. Model of cylindrical capillary	6
2.2.2. Model of radial capillary	13
2.2.3. The Shape of Drops.....	16
2.2.4. Drop penetration into porous materials	20
2.2.5 Usage of ultrasound for enhancement of liquid penetration.....	22
2.3. Wetting experiments	24
2.3.1. Description of experiment procedure	24
2.3.2. Radial Capillary	28
2.3.3. Drop penetration into nonwovens	30
4. Simulation Issue – Auto models	
5. Conclusions	
6. Appendixes	

1. Introduction

A reader of following pages could ask a question, if the interest about a special physical phenomena related to wetting is not inappropriate for a thesis of a student dealing with textile engineering? Accordingly, an important question will be put and answered here in the introduction of the thesis; What is a continuity between studying the wetting dynamics of droplet or liquid reservoir into solid porous surface and textile engineering?

Continuity is very easy and the answer can be found in the course of each activity, when liquid comes into contact with a fiber thus textile material. And there are really a lot of branches of these activities. Some examples are: testing of baby diapers and hygienic materials for incontinent patients, binding of nonwovens by means of basic fibre material's impregnation by liquid binder, production of wet wipes for both babies and grown-ups and production of composite materials reinforced by textile materials especially in the course of their manufacturing by so called "wet way". In every case, it is necessary for the liquid to penetrate into fibre material within a certain time and create required liquid body shape. It is possible to explain this through the example of wet wipes production. A spun-laced nonwoven material is carried at a definite speed over a punched cylinder, where a special body lotion is placed (sprayed) on the nonwoven material. The lotion has to penetrate into the textile material within a definite time and impregnation has to be completed.

However the thesis attends, rather than production of wet wipes, to the last example mentioned above, thus a production of fibre reinforced composite materials by so-called "wet way", when dry fibre reinforcement is impregnated with a liquid matrix.

The complete text is divided into three parts.

The first part is focused on introduction of dynamics of liquid penetration into porous materials. Theoretical part dealt with basic terms and legalities of wetting. There are described model of cylindrical capillary and model of radial capillary as a model systems for better understanding of drops penetration into complex porous or even textile structures. There is also part devoted to the enhancement of liquid penetration into porous materials with the intention of ultrasound usage. Experimental part should bring a design of a simple and an effective method for studying the dynamics of liquid penetration into fibre materials and its testing for a scale of nonwovens with different geometrical parameters (change of fibre volume fraction, change of orientation of fibres, change of fibre diameter...).

The second part of the thesis shortly describes basic terms and legalities of automodels and Monte Carlo methods, examples of automodels usage for simulation of wetting phenomenon. Testing and evaluation of a possibility to use the simulation models for the observation of wetting dynamics follows the theoretical part as an introduction of thesis author the simulation study.

The last part is devoted to nanofiber-reinforced composites. There are described composite nanofibers and nanocomposites reinforced by carbon nanotubes and electrospun nanofibers. Experimental part involves the description of a concrete solution for composite materials reinforced with electrospun nanofibre webs. The manufacturing process requires special approach because the electrospun nanofibre web brings several untraditional complications into the process, which are necessary to solve. The entrance to the world of "nano" dimensions brings great challenges (problems), but evidently also several advantages in results. The thesis does not focus on testing and applied research in the branch of electrospun nanofibre reinforced composites. The work wants to show that it is possible to apply all theoretical knowledge, experimental and simulation skills for concrete examples.

The work have brought a way to the recognition or clarification of some legalities from the branch of dynamics of liquid penetration into porous materials, its simulation by means of Auto models and its application on a "journey" to the solution of the factual problem with the production of composite materials reinforced with electrospun nanofibre layers.

2. Wetting Processes

Wetting of fibrous materials is a very interesting and complex problem. Therefore, firstly basic models are theoretically presented as wetting of cylindrical capillary and model of radial capillary. Then droplet penetration into porous materials is described in detail. Furthermore, own method for measuring the volume of droplets on a porous substrate is introduced. Particular experimental studies devoted to drops penetration into nonwovens using the unique method and their main results are described in the final chapters.

2.1. Basic Terms and Legalities of Wetting

The first short part of the thesis deals with basic theoretical knowledge. Presentation of basic pivotal treatises is exactly the subject of this chapter. One of the mostly cited publications in up-to-date professional articles is the treatise of Adamson & Gast [1]. The work aims at wetting and phenomena connected with behaviour of three-phase systems thus systems involving liquid, solid and gas or only of two-phase systems thus liquid and its vapour or gas in general terms. The eminent publication deals not only with basic terms, as capillarity and connected surface tension or surface energy, Young-Laplace equation, capillary wicking or capillary constant, methods for measurement of surface tension at liquid-gas interface, i.e. static methods (the drop weight method, the ring method, Wilhelmy slide method, sessile drop or bubble method, pendant drop method) but also with dynamic methods (flow methods, capillary waves method, maximum bubble pressure method). However, the book also deals with more particular themes as for example contact angle hysteresis, influence of solid surface roughness on the contact angle of sessile drop, dynamic change of contact angle during spreading of a drop on the solid surface. Then it is possible to find there information about adhesion, namely assumption for ideal adhesion, polymer adhesion, about wetting, water repellence of solid surface and vice versa, detergency and last but not least gas adsorption dependence on an interface with solid material, chemisorptions and catalysis etc.

The next very important publication, which together with the book mentioned above can be regarded as the best “textbooks” for the basics of studying wetting issues, is the book of de Gennes and his co-workers, authors of many professional articles related to the wetting phenomena: Brochard-Wyart & Quéré [2]. What is offered here is not a comprehensive review of the latest research but rather a compendium of principles. The beginning of the publication contains of course explanations of basic wetting and capillarity phenomena, another part includes more specialized conceptions as hysteresis and elasticity and dynamics of triple line, hydrodynamics of interfaces, usage of surfactants. There are also two really important and unusual chapters. Their objectives are to explain and describe wetting phenomenon related to so called dewetting and transport phenomena. Dewetting is a relatively uncanny notion. The authors of the above mentioned book are pioneers of utilization of this term. Hence dewetting is a really uncommon but very important phenomenon.

Another crucial treatise aimed at interface and wetting phenomena is a book, which was written by Myers in 1999 [3]. The treatise contains a historical aspect of the wetting issue and brings industrial and natural examples, where the above given mainly wetting phenomena occur. The book offers a current state of knowledge in chapters on absorption and biological systems in addition to the important areas of colloid stability, emulsions and foams, monolayer films, surfactants, and wetting. Naturally the book contains basic general terms as surface tension, contact angle, its hysteresis, rough surface effect, wetting of heterogeneous surfaces, thermodynamics of wetting, Young-Laplace equation, Harkinson spreading coefficient, a description of an influence of surfactants on wetting. Everything is described with reference to the expository part. This publication can be considered to be a useful introduction available to the complex area of surface and colloids science. Other worthy of attention publications can be recommended to persons interested in the given field. These following monographs are more particular thus one-track.

The first of them deals with droplet dynamics as the title of the book prompts. The book begins with the theoretical background important for droplet dynamics, it continues with the presentation of the various methods for generating single droplets and regular droplet systems. A detailed description of the experimental methods employed in droplet research is also included. Dynamics of droplets is described with respect to droplets impinging on a wall and the wall impact of droplets regarding their elasticity, change of shape, evaporation, spraying and so on. The publication written by Frohn & Roth [4] focuses on several examples of droplet dynamics and their numerical simulations.

A group of authors lead by Shchukin wrote another remarkable monograph [5]. The book covers major areas of modern Colloid and Surface Science (sometimes also referred to as Colloid Chemistry) which is a broad area at the intersection of Chemistry, Physics, Biology and Materials Science investigating the disperse state of matter and surface phenomena in disperse systems. There are clarified issues such as Dupre's attempt, Helmholtz's energy* density change at the interface of phases area, thermal influence of thermodynamic parameters' (free energy, internal energy, entropy) excesses at surface layer, Hamaker's constant, Laplace's law, Tompson-Kelvin's law, Langmuir's scale and so on. Information about measuring possibilities of surface energies (not only for liquid-gas interface) for low molecular materials is also available in the book.

Connection between wetting phenomena and production of composite materials in the so called "wet" way is a part of the book written by Stokes & Evans [6], namely in its seventh chapter entitled "Polymer composites". Darcy's law and Kozeny-Carman equation are explained for example and also a passage devoted to capillary phenomenon assisted during fiber reinforcement impregnation by liquid matrixes can be found there. So generally the work describes the properties, processing, and behavior of fluid interfacial systems and treats solid surfaces and interfaces with respect to composite production.

An older publication written by Kutilek [7] may not be left out. The monograph focuses on the field of liquid flow (water mainly) in porous media. The book presents not only equilibrium behavior of three-phase systems, but also surveys basic equations of motion and flowing phenomena.

* Helmholtz's energy is common physical quantity called Free Energy.

2.2. Wetting Models

Pivotal work, which has motivated the author of the thesis, is an article [8] from an outstanding French “workshop” that deals with drop suction into porous membranes. The group of researchers, lead by Brochard-Wyart, is the leader in Europe in the field of wetting physics. It is necessary to describe the model situations as the model of cylindrical capillary and the model of radial capillary and their theoretical background at first.

2.2.1. Model of Cylindrical Capillary

If the dynamics of wetting porous materials, as textiles are, is taken into consideration, the first well known, frequently used model is the one of a cylindrical capillary. The basic mechanism of liquid penetration into porous materials can be demonstrated by studying penetration into a simple cylindrical capillary. There are two important aspects in the usage of a capillary model, as Marmur has already written in his publication [12]. The first is the quantitative understanding of how liquids penetrate into a porous material of a known structure and the second is the characterization of porous materials by measuring liquid penetration in them.

The number of articles dealing with this topic is really huge. But the author of this work is convinced it is necessary to deduce all three possible solutions of the Lucas-Washburn equation. The main reasons are: i) better comparison of results from experimental part with theoretical assumptions and ii) better understanding of the results. So here is the Lucas-Washburn equation and its promising solutions.

Firstly there should be written that invasion of the capillary by a liquid can proceed only if the surface energy of the wall decreases with wetting, thus if the following condition $\gamma_{sl} < \gamma_{sg}$ (γ_{sl} is a solid-liquid surface tension and γ_{sg} is a solid-gas surface tension) is valid.

The model of liquid penetration into the cylindrical capillary is based on the Hagen-Poiseuille law [17]. The Hagen-Poiseuille law describes the effect of pressure on the velocity of liquid which fills the cylindrical capillary. The law says that the mean velocity dh/dt of a Newton viscous liquid of viscosity μ , in the tube of radius r and length h , between the ends of which the pressure difference is $\Delta P_e = (p_1 - p_2)$, is given by the following equation:

$$\frac{dh}{dt} = \frac{r^2 \Delta P_e}{8\mu h}. \quad (2.1)$$

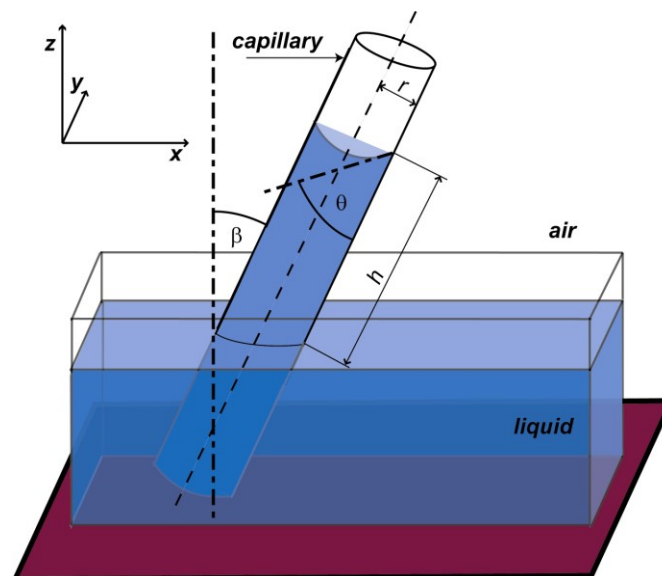


Fig.2.1: The cylindrical capillary with random orientation sunk to a liquid reservoir. A liquid meniscus in the capillary is not affected by gravity because of the very small capillary diameter, $2r$.

The law (2.1) was the initial point for two important pieces of work, which arose independently from each other. They dealt with the theoretical analysis of wetting processes of fiber formations and were written by Lucas [9] and Washburn [10] in the twenties of the last century. The Hagen-Poiseuille's law was modified for a capillary of diameter D (radius r), plunged in liquid angle-wise β , see Fig.2.1. Angle β is measured from a vertical line (orthogonal to the free level of liquid) clockwise up to the axis of capillary. Pressure p_1 rises in the capillary due to surface tension γ of a liquid. If a meniscus of the liquid forms an angle θ (include an angle θ) with the wall of the capillary, pressure p_1 can be expressed in the following way:

$$p_1 = \frac{2\pi\gamma \cos \theta}{\pi r^2} = \frac{2\gamma \cos \theta}{r}. \quad (2.2)$$

The meniscus is a shape of a liquid, which has a density ρ , in the immediate vicinity of the capillary wall (wetted subject). Pressure p_2 is a hydrostatic pressure at high h described with the following expression:

$$p_2 = h\rho g \cos \beta. \quad (2.3)$$

The next relation results from the equations (2.1), (2.2) and (2.3):

$$\frac{dh}{dt} = \frac{r\gamma \cos \theta}{4\mu h} - \frac{r^2 \rho g \cos \beta}{8\mu}. \quad (2.4)$$

Solutions of Lucas-Washburn's equation depend mainly on the orientation of the capillary and the direction of liquid flow. Solutions are written below, but firstly it is useful to rewrite formula (2.4) to a simpler form using parameters a and b :

$$a = \frac{r\gamma \cos \theta}{4\mu}; \quad b = \frac{r^2 \rho g \cos \beta}{8\mu}. \quad (2.5)$$

Then the Lucas-Washburn equation can be written as

$$\frac{dh}{dt} = \frac{a}{h} - b. \quad (2.6)$$

Equation (2.6) will be solved for three different cases depending on the angle β .

The first solution of Lucas-Washburn's equation for horizontal capillary

The solution aims to describe a horizontal liquid capillary connected with a liquid reservoir (Fig.2.2). Angle β equals to 90° . Accordingly, $\cos\beta=0$ and thus parameter b from formula (2.5) is also zero and equation (6) can be written now as

$$\frac{dh}{dt} = \frac{a}{h}. \quad (2.7)$$

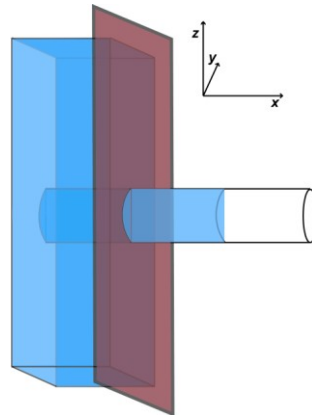


Fig.2.2: The cylindrical capillary with horizontal orientation sunk to a liquid reservoir.

Equation (7) can be solved by the variable separation method and integration

$$hdh = a dt,$$

$$\int hdh = a \int dt.$$

Integration of both sides of equation (2.7) gives

$$\frac{1}{2} h^2 = at + C, \quad (2.8)$$

where C is an integration constant. If initial conditions are $(t=0; h=0)$ substituted in equation (2.8), the constant C obviously equals to zero ($C=0$). So resulting formula is

$$h = \sqrt{2at} = \sqrt{\frac{r\gamma \cos \theta}{2\mu}} t. \quad (2.9)$$

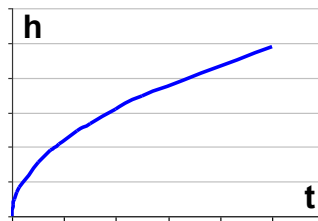


Fig.2.3: Function $h=h(t)$ derived above.

Then equation (2.9) is the solution of the first scenario of a capillary sinking into the liquid reservoir, where the capillary is horizontal. Equation (2.9) is valid not only for the process if the tube is horizontal, but also for cases in the early stages of capillary rise [13], when gravity effects are negligible.

The second solution of Lucas-Washburn's equation for vertical capillary

The solution refers to a liquid's upward wicking (Fig.2.4). A value of angle β falls between 0° and 90° ($\beta=90^\circ$ is not included in this interval, the solution for this case is described above), so an expression $\beta \in (0^\circ, 90^\circ)$ can be written. Thus parameter b in formula (2.5) is surely a positive number.

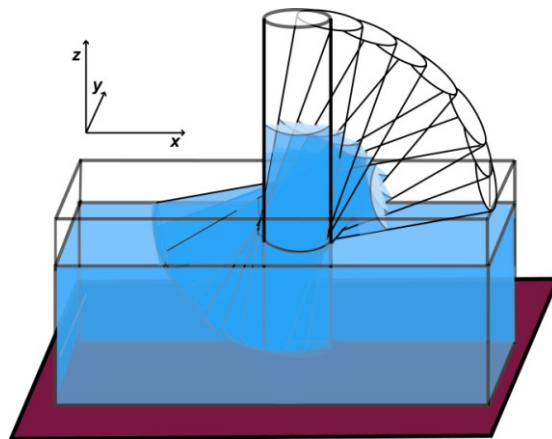


Fig.2.4: The cylindrical capillary sunk to a liquid reservoir.

The nonlinear differential equation (2.6) with constant coefficients can be solved by variable separation method and consequent integration in the following way

$$\frac{hdh}{a-bh} = dt;$$

$$\int \frac{hdh}{a-bh} = \int dt = t + C \quad (2.10)$$

where C is a constant. The integral in the left part of the above written term can be transformed like this

$$\int \frac{hdh}{a-bh} = -\frac{1}{b} \int dh - \frac{a}{b^2} \int \frac{dy}{y}, \quad (2.11)$$

where $y = a - bh$. The term $\frac{h}{a-bh}$ from equation (2.10) was rewritten as follows

$$\frac{h}{a-bh} \left(\frac{b}{b} \right) = \frac{bh}{b(a-bh)} + a - a = -\frac{1}{b} + \frac{a}{b(a-bh)}.$$

The following solution of equation (2.6) is obtained by the application of the formula

$\int \frac{1}{x} dx = \ln|x| + C$, where C is a constant, with initial conditions: $t=0$; $h=0$,

$$t = -\frac{h}{b} - \frac{a}{b^2} \ln(a-bh). \quad (2.12)$$

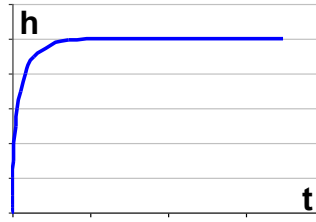


Fig.2.5: Function $h=h(t)$ obtained as the inversion of the equation (2.12).

The resultant expression represents an monotonously increasing function (see Fig.2.5). The limit $t \rightarrow \infty$ is found from equation (2.12). Then $\ln(a-bh) \rightarrow \infty$ and thus $a-bh=0$. Finally the limit, i.e. the maximal h value is $h_{\max} = \frac{a}{b}$.

Relation (2.4) can be solved in different ways under the assumption that the second term on the right side can be neglected. That can be done in the following cases: (i) gravitation is neglected, $g=0$; or (ii) a height in a capillary is small, so a notation ($h \rightarrow 0$) can be accepted. If one or both of these above mentioned conditions are true and the term on the right side of equation (2.12) is neglected then the following relation is valid

$$\frac{dh}{dt} = \frac{r\gamma \cos \theta}{4\mu h}. \quad (2.13)$$

Equation (2.13) can be solved by the variable separation method

$$\int h dh = \int \frac{r\gamma \cos \theta}{4\mu} dt. \quad (2.14)$$

Hence it comes to solution (2.9), which was found for horizontally oriented capillary, under a condition $h=0$ for $t=0$.

The third solution of Lucas-Washburn's equation for downward liquid flow

The solution is devoted to a downward liquid flow inside a capillary from a reservoir placed above (Fig.2.6). Angle β is between 90° and 180° , so i.e. $\beta \in (90^\circ, 180^\circ)$. Thus parameter b from (5) is surely a negative number. This third solution of equation (4) is similar to the second one, but the parameter b is negative. So $b = -B$ is installed in formula (2.12).

$$t = -\frac{h}{(-B)} - \frac{a}{(-B)^2} \ln\left(1 - \frac{(-B)}{a}h\right) = \frac{h}{B} - \frac{a}{B^2} \ln\left(1 + \frac{B}{a}h\right). \quad (2.16)$$

Solution $t(h)$ of relation (2.16) describes h as decreasing function of time t .

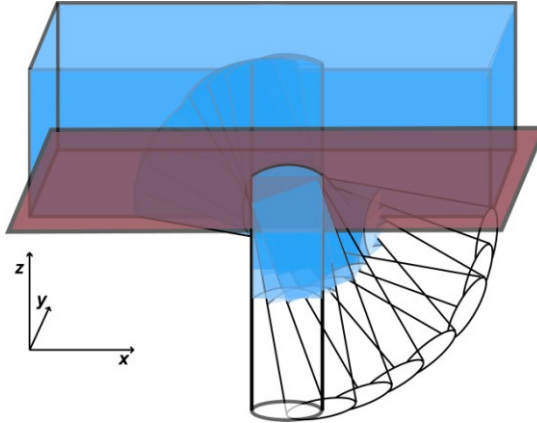


Fig.2.6: The cylindrical capillary sunk to a liquid reservoir. The capillary directions appointed by angle β orient a liquid flow downwards.

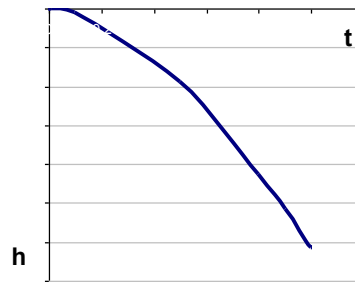


Fig.2.7: Function $h=h(t)$ obtained as the inversion of the equation (2.16).

How does a graph of function $h=h(t)$, which is an inverse function to $t=t(h)$ look like? The graph of function $h=h(t)$ follows a straight line from a certain limit of time, $t(h) \cong \frac{h}{B}$, and height (see Fig.2.7).

The following simplification of equation (2.16) can be carried out. If $\frac{B}{a}$ is almost $n \left(\frac{B}{a} \approx 1 \right)$, then the

following term can be written $\left(h \gg \ln\left(1 + \frac{B}{a}h\right) \right)$ for larger values of h . So then the second term on the right side of equation (2.16) can be left out and the solution is

$$t = \frac{h}{B} \quad (2.17)$$

$$\text{or } h = -\frac{r^2 \rho g \cos \beta}{8\mu} t$$

Is it a good approximation of the third solution of equation (2.4)? This simplification can be explained physically this way: the gravitational term has an increasing influence in the course of downward liquid flow with increasing time t and decreasing height h . This increase growth is linear what immediately results from the Lucas-Washburn equation after the omission of the capillary part.

Back to the horizontal liquid penetration into an empty cylindrical capillary, the equation (2.9) can be rewritten in a dimensionless form in the following way

$$X^2 = 2\tau_p. \quad (2.18)$$

In this equation X is the dimensionless penetration distance ($X \equiv \frac{h}{r}$), where h is the penetration distance into the capillary – term ‘height’ was used above. Time τ_p is dimensionless

$$\tau_p = \frac{\sigma \cos \theta}{4\mu r} t. \quad (2.19)$$

The same situation is valid for liquid penetration states when the effect of gravity may be neglected, as for example in case of the initial stages of vertical penetration.

The Lucas-Washburn equation has been verified, studied and used in a lot of cases, for example [21-29], and is still the frequently used, when the behavior of liquid in contact with capillary-porous systems is approximated and researched. Allowedly, the fact that the Lucas-Washburn equation is valid only for systems of limited liquid size must not be omitted. The truth is that for several years wetting of porous media was dealt only with infinite liquid reservoirs. The aims of researchers have been focused on resolving the hydrodynamic problems arising from the bulk flow of liquid [11-16], the contact angle and the motion of the solid-liquid-fluid contact line and the third group has dealt with the theory of capillary penetration, which has been extended to non-uniform capillaries and porous systems [17,19, 20].

The first revolutionary articles appeared at the end of the eighties in the last century. One of the most important should be an article written by Marmur [14] in 1988. Marmur had an interest to study the effect of the size of the liquid reservoir on the process of capillary liquid penetration. He has discussed the thermodynamics and the kinetics of a small drop that is brought in contact with a cylindrical capillary. The studied situation can be described in the following manner: A drop in the form of a spherical segment of a liquid is attached to a cylindrical capillary. It is assumed that the liquid does not meet the outside of the capillary (see Fig.2.8). Marmur has gone behind the basic differential equation proposed by Lucas and Washburn. But he has extended the theory of capillary penetration including the case of liquid reservoir of a finite size.

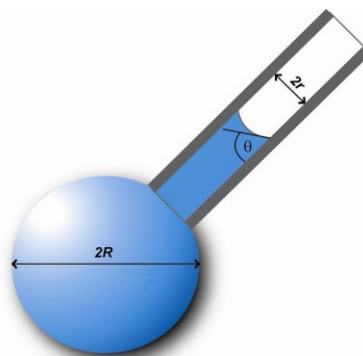


Fig.2.8: Scheme of the penetration of a small spherical drop into a cylindrical capillary, where R is the spherical drop radius, r is the radius of a cylindrical capillary and θ is contact angle.

The effect of the drop size stems from the increased pressure inside the drop due to increasing curvature (decrease of the curvature radius R of the drop) during the liquid penetration process. Marmur's very interesting and of course also very important results relating to a drop

penetration into a cylindrical capillary, which are adopted from his above-mentioned article [14] follows:

- (i) The thermodynamic distinction between penetration of a liquid and no penetration into a capillary depends on the size of penetrating drops – the diameter $2R$ of the penetrating drop must be higher than the diameter of the penetrating drop in equilibrium, the condition is valid only for cases when contact angle is smaller than 90° , then the diameter of penetrating drop in equilibrium is negative;
- (ii) The height of capillary rise in a gravitational field, for a drop of finite size, is higher than that for an infinite liquid reservoir as long as the liquid volume is sufficient to accommodate the rise;
- (iii) The rate of penetration into a capillary in case of a drop is higher than that for an infinite liquid reservoir;
- (iv) The difference between the behavior of a drop and an infinite liquid reservoir becomes more pronounced as the contact angle is higher.

All of these claims are theoretically established (deduced) in the above mentioned Marmur article. So it is really amazing that merely a curvature of the drop is the reason for a higher velocity of liquid penetration into a cylindrical capillary and even to the greater distance in comparison with a liquid penetration into the cylindrical capillary from an infinite reservoir.

Penetration of liquids into capillaries as models of porous materials has been studied from various points of view for several years, for example [1, 6, 9, 10, 13]. However, due to the complexity of porous materials, particularly textiles, the phenomena involved in their penetration are not yet completely understood. Modeling of the penetration process has been usually done in terms of an equivalent set of capillaries, which in some cases were assumed to be of varying cross sections. But there have been still another inherent aspect of penetration of drops into thin porous media, which has not been studied. It is the effect of the radial motion of the liquid on the dynamics of penetration. The effect was firstly described by Marmur [11] in 1988. The model was named “The Radial Capillary”.

2.2.2. Model of Radial Capillary

What are new ideas in the radial capillary model? When a drop of liquid penetrates into a thin porous material (as for example an ink drop into a paper), the liquid-vapor interfacial area at the liquid front is continually increasing. So this is the main difference between the radial and the cylindrical capillary model, where the liquid-vapor interfacial area at the front is either constant or oscillating due to variations in the cross sections of capillaries. The radial capillary model, which describes the radial penetration of a liquid between two flat plates, can serve as a limiting model for penetration into thin porous materials, similarly to the usage of the cylindrical capillaries as a model for porous media in general. The radial capillary consists of two parallel, rigid and nonporous plates, the distance between which is d (see Fig.2.9). There is a small hole in the upper plate. Gravity is neglected, thus it does not matter which plate, upper or lower, is perforated. The drop of the liquid may penetrate through this hole into the radial capillary. The liquid reservoir is a drop in the form of a spherical segment. It is generally known that small drops are almost spherical even in a gravity field. The drop is placed above the hole and after a certain time period the liquid enters the area between the plates. The shape of a liquid body inside the radial capillary during and after the penetration is assumed axis-symmetric. The shape of liquid body meniscus inside the radial capillary has to have a constant curvature (R_2). Since the analysis neglects gravity, so the vertical cross-section of the meniscus will be approximated by a circle arc.

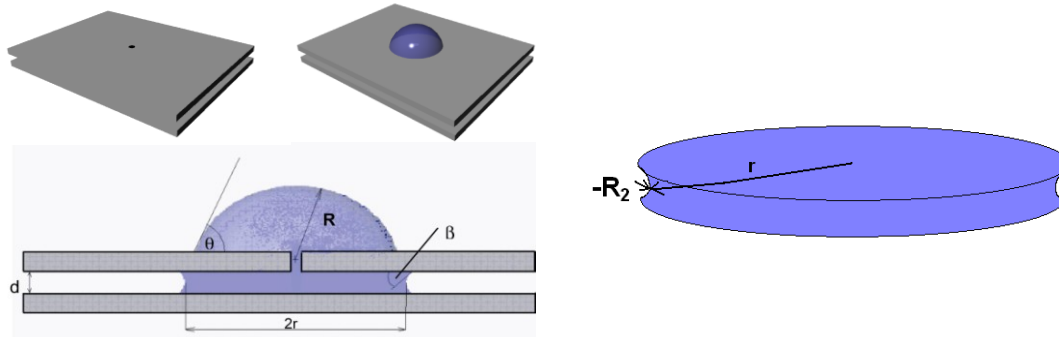


Fig.2.9: The radial capillary model is presented on the left side, where θ is an outside contact angle; R is a radius of the outside drop part; β is a contact angle inside the radial capillary and r is the radius of liquid shape inside the radial capillary. The liquid body with the first r and the second $-R_2 = d/(2 \cos \theta)$ radii of curvature inside the radial capillary is on the right side.

The difference between inside and outside contact angles stems from the contact angle hysteresis. It can be supposed that inside the radial capillary the contact angle is an advancing, while outside the radial capillary it is a receding angle. Therefore, two limiting models exist: The first ignores the possibility of hysteresis (see Fig.2.10a) – the outside contact angle θ is constant and the radius of drop curvature decreases during penetration. However the second limiting model does not ignore the possibility of hysteresis (see Fig.2.10b), thus θ decreases and the radius of curvature increases during drop penetration. Marmur in [11] expected that the real situation would be between these two limiting cases.



Fig.2.10: Two limiting cases of droplet penetration into a radial capillary: a) the unlocked regime, b) the locked regime.

If the process of penetration into the radial capillary is between initial (no liquid inside) and final state (no liquid outside), the shape of the liquid body between the plates is characterized with two radii of curvature: r and $-R_2$, which is the radius of curvature in the plane perpendicular to plates.

If we take into consideration Laplace pressure in the droplet outside the capillary, Laplace pressure in the liquid body inside the capillary and the ambient pressure (see Fig.2.11), we find* the condition of spontaneous liquid penetration into the radial capillary (2.20).

* The relation (2.20) is obtained from this consideration $p_1 = \frac{2\gamma}{R}$; $p_2 = \gamma \left(\frac{1}{r} - \frac{2 \cos \theta}{d} \right)$; and $p_1 - p_2 > 0$.

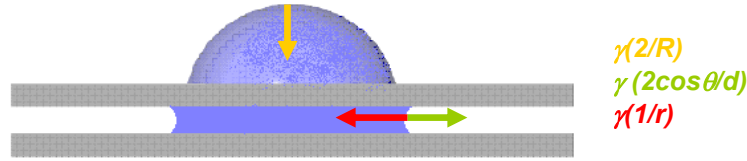


Fig.2.11: Scheme of Laplace pressure's actions inside a liquid body penetrating into the radial capillary leading to a condition of spontaneous penetration of liquid drop into the radial capillary.

The penetration condition is:

$$r > \frac{Rd}{2R \cos \theta + 2d} \quad \text{or} \quad r_p = \frac{Rd}{2R \cos \theta + 2d}, \quad (2.20)$$

where r_p is the lowest r which allows spontaneous penetration. Radius r_p is the so-called "priming radius".

The kinetic model, laminar fully developed quazi-steady-state flow, with a constant contact angle taken again from [11] is used for the kinetic description of liquid penetration between the plates of radial capillary. Considerations start from the Navier-Stokes equation for a cylindrical symmetrical convection, neglecting acceleration of a liquid. The solution of Navier-Stokes equation has radial component only and only incompressible liquids can be taken into consideration. It is possible to find a general differential equation for the velocity of penetration into a radial capillary (2.6), after the implementation of other, above-mentioned assumptions:

$$y \ln y \left(\frac{y}{y_0} \right) dy = \left(U - \frac{1}{2y|\cos \theta|} + \frac{1}{\rho|\cos \theta|} \right) d\tau_p \quad (2.21)$$

where the dimensionless quantities used are

$$y \equiv \frac{r}{d}; \quad y_0 \equiv \frac{r_p}{d}; \quad U \equiv \frac{\cos \theta}{|\cos \theta|}; \quad \rho \equiv \frac{R}{d}; \quad \tau_p \equiv \frac{\gamma|\cos \theta|}{6\mu d} t,$$

τ_p is dimensionless time, γ is surface tension, μ is a dynamic viscosity of a liquid [11]. The three terms inside parentheses on the right side of the relation (2.21) represent d , r and R respectively.

If an infinite liquid reservoir is taken into consideration, analysis independent from the effect on the droplet size is performed. After integration of equation (2.21) the following equation is obtained

$$y^2 \left(\frac{\ln y}{y_0} - \frac{1}{2} \right) + \frac{y_0^2}{2} = 2\tau_p. \quad (2.22)$$

It is noticeable from the graph in Fig.2.12 that function $y(\tau_p)$ has a parabolic shape, so the function will have almost a linear character for sufficiently high values of dimensionless time. It is also obvious from the figure that in this example the velocity of infinite liquid reservoir penetration should be constant during the whole process of liquid penetration into the radial capillary. But during the drop's penetration process into the radial capillary the velocity of penetration is modified because of the changes of drop outside radius R .



Fig.2.12: Graphical expression of equation (2.22) for liquid penetration from infinite reservoir into the radial capillary. The graph shows a dependence of $y=r/d$ as a function of τ_p .

When a finite drop penetrates into a capillary (either cylindrical or radial) the process is self-accelerated [12]. The radius of the drop (outside capillary) decreases during penetration, hence the pressure inside the drop increases and that accelerates penetration.

Article [11], which firstly described the model of radial capillary in 1988, has brought the following specific conclusions: i) The radial capillary needs to be initialized for spontaneous penetration, ii) The penetration into a radial capillary from an infinite reservoir is slower than the penetration into either a cylindrical capillary or a unidirectional flat plate capillary; iii) The penetration of a drop of finite size is faster than that of a liquid from an infinite reservoir. The difference in rates becomes more pronounced as the contact angle is increased; iv) Hysteresis of the contact angle of the drop on the outside surface of the plate may partially counteract the increase in the rate of penetration, caused by the finite size of the drop; v) Capillary penetration is theoretically possible for inside contact angles higher than 90° when the drop is sufficiently small and when hysteresis is not dominant.

It is obvious that Marmur has developed the concept of radial capillary and the thermodynamics and kinetics of penetration into it and that the system may be useful not only for understanding the geometrical effect related to radially expanding liquid front during the process of capillary penetration into porous materials which surely involve textile materials, too.

There is an example of radial penetration of a drop placed on a paper [16]. Paper has a similar fibrous structure to textile materials, for example wet laid nonwovens. The example is important for the printing industry. The process of penetration of dye drops into a piece of paper consists of the penetration of the liquid into the paper and consecutively of a radial growth of the wet stain in the paper [12]. In connection with the above-mentioned example, the following power law was found by Kissa [17].

$$A=kt^n, \quad (2.23)$$

Where A is the area of the wet stain, t is time and k and n are empirical constants. The value of n was found experimentally to be between 0.30 and 0.35 . These low values of n could not be accounted for the existing theory. Using the theoretical model of radial capillary, the kinetics of radial penetration is calculated as $A \approx kt^{0.9}$ [16]. Thus the slow kinetics characterized by $n=0.3-0.35$ could not be explained simply on the basis of the radial geometry of liquid penetration into porous systems. To check the possibility that a different mechanism of penetration is involved a simple experiment was carried out and described in [16]. This was achieved by using a vertical short glass cylindrical capillary to drive the liquid from a Petri dish ("infinite" reservoir) into the paper, as it is shown in Fig.2.13.

The kinetics of wet area growth fitted very well to that predicted by the radial capillary model: $A \approx kt^{0.9}$. Then the glass capillary was disconnected from the paper. At this point there was a finite amount of liquid in the paper, which continued to spread according to equation (2.23), with n being around 0.35 . Thus, it was demonstrated that this value of n was due to the finite amount of liquid in the wet stain. The simple explanation of the mechanism of continued penetration in this case is capillary suction of the liquid by small pores from the large pores, whereas the latter become unsaturated – filled again by air [16]. This mechanism was termed "the re-distribution effect" and it presents another important impact of structural character of porous materials on the liquid kinetic behaviour.

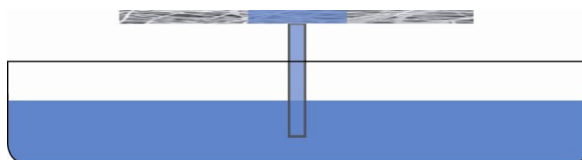


Fig.2.13: Scheme of liquid penetration from a Petri dish into paper (or generally a porous material) through a short cylindrical capillary.

Other very interesting information relating to the radial capillary penetration containing particular experimental data can be found for example in these selected publications [30-32].

2.2.3. The Shape of Drops

The knowledge of a drop shape is critical for a description of a drop's behavior during its penetration into porous materials. There is a huge difference between the so called spherical drops and cake drops or puddles. Now, it is necessary to mention where the difference lies.

It is generally known that when the spreading coefficient S ($S = \gamma_{sg} - \gamma_{sl} - \gamma$, where the three γ 's are surface tensions at the solid-gas, solid-liquid and liquid-gas interfaces, respectively) is negative (partial wetting regime), a drop of liquid deposited on a horizontal flat solid surface exhibits a contact angle θ determined by Young's law, which projects the equilibrium forces onto the solid plane ($\gamma \cos \theta = \gamma_{sg} - \gamma_{sl}$). The shape of the observed drop changes from perfectly spherical to almost completely flat depending on whether its radius R is small or large compared to the capillary length κ^{-1} introduced by relation (2.25).

So there is a particular length, beyond which gravity becomes important. Definition of the *capillary constant* / the *capillary length* is provided by Adamson [1]: Consider a small circular diameter capillary placed perpendicularly to the surface of liquid level in a reservoir. Let's suppose that the liquid meniscus in capillary is half-spherical, as it is shown in Fig.2.14. Thus the meniscus has two identical principal radii of curvature. They are equal to capillary radius r . Then, it is possible to write Laplace relation as $\Delta P = 2\gamma/r$, where γ is a surface tension. If h is a height of meniscus above liquid level (where $\Delta P = 0$ is exactly valid), then it is obvious that Laplace relation must be equal to the hydrostatic pressure acting inside the liquid cylinder. Then equation $\Delta P = \Delta \rho g h$ can be written, where $\Delta \rho$ is the density difference between liquid and gas phase (but usually the normal conditions are considered and this is why the density of gas is neglected and thus $\Delta \rho = \rho_{liquid}$). Hence

$$\rho g h = \frac{2\gamma}{r}. \quad (2.24)$$

The capillary constant κ can be written according to [1] as

$$\kappa^{-2} = \frac{2\gamma}{\rho g} = r h. \quad (2.25)$$

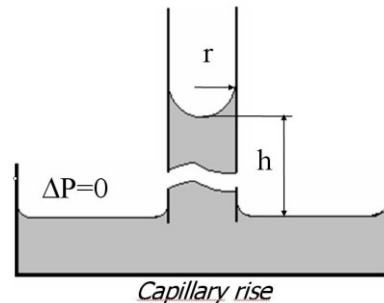


Fig.2.14: Scheme of liquid wicking into a cylindrical capillary from a reservoir, where h is height of meniscus above liquid reservoir level and r is capillary radius.

Factor "2" in equation (2.25) arises from this particular boundary value problem: for several other situations the capillary length is defined by $a^2 = \gamma / \Delta \rho g$ as for example for cake drops explained below. Some authors, for example Adamson in [1], denote capillary length as $\kappa^{-1} = a = \sqrt{\gamma / \rho g}$. This definition differs from (2.25) in factor "2". The capillary constant or capillary length κ^{-1} is valid only if half-spherical shapes of surface of liquid are considered. Distance κ^{-1} is generally of few millimeters. Thus as it is written in [2], gravity is negligible for sizes $2r < \kappa^{-1}$ (or $r < \kappa^{-1}$), where $2r$ is the width* of the drop. When this condition is met, capillary effects dominate. The opposite case $2r > \kappa^{-1}$ (or $r > \kappa^{-1}$) refers to dominant gravity effects in a drop or in a capillary.

* Width is the maximum Ferret diameter, i.e. the largest characteristic dimension.

For spherical drops, it means, capillary constant κ^{-1} is larger than width $2R$ ($\kappa^{-1} \gg R$) of a droplet, see Fig.2.15, thus capillary forces are the only ones that play a role. That is why the curvature of such drops must be constant according to Laplace's equation on their whole surface.

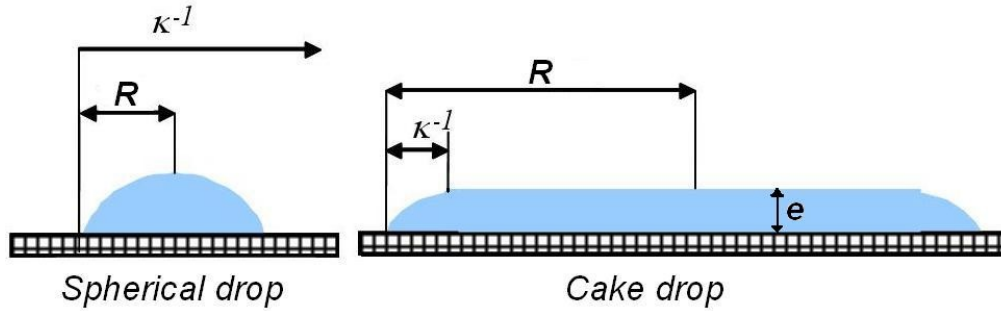


Fig.2.15: Schemes expressing a difference between "spherical" and "cake" drops according to capillary constant knowledge.

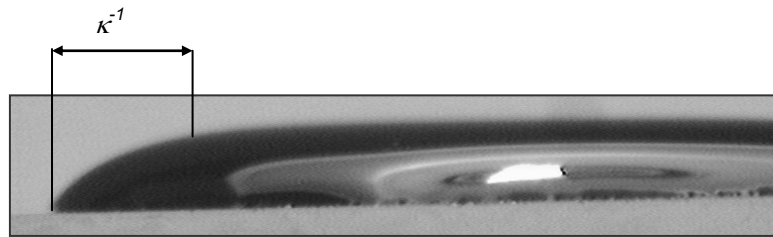


Fig.2.16: Real photo of a cake drop with denotation of a capillary length.

Liquid layers, i.e. big drops, of cake shape are called *cake drops*, *puddles* or *heavy drops*, as referred to in [2] and [8]. The drops are flattened by gravity and they take on the shape of cake or pancake of a thickness e . A drop will be called cake drop if the following condition is fulfilled:

$$R \gg \kappa^{-1}, \quad (2.26)$$

where R is radius of the drop's base, if it is circular. If a cake drop placed on a solid substrate is observed, it is possible to consider a horizontal distance from a drop's border to a place, where the flat surface of drop starts, as a capillary length, see the left part of Figs.2.15 and 16. Therefore the capillary length can be also described as the distance on which capillary forces express themselves to a large extent, meaning that a strong curvature of the drop surface can be observed (as it is visible in Fig.2.16).

When a cake drop is considered, relation (2.25) is changed by the following way:

$$\kappa^{-1} = \sqrt{\frac{\gamma}{\rho g}} \quad (2.27)$$

The change is realized because one radius of curvature goes to infinity. Then, as obvious from general equation for Laplace's pressure*, one term of the principal radii is equal to zero.

If a cake drop is in equilibrium state, the drop has a thickness e_0 . The value of e_0 can be calculated by expressing the equilibrium of horizontal forces acting on a portion of the liquid. Free energy F of the drop of constant volume V can be written as a function of its thickness e in the following way:

$$F = \frac{1}{2} \rho g e^2 \frac{V}{e} + \frac{V}{e} \left(\gamma + \gamma_{SL} - \gamma_{SG} \right). \quad (2.28)$$

Here V is the volume of liquid, e is the thickness of cake drop, V/e denotes the wetted area and γ_{SG} , γ_{SL} and γ are surface tensions at the solid-gas, solid-liquid and liquid-solid interfaces, respectively. It is

* General Laplace's equation is $\Delta P = \gamma \left(\frac{1}{R_1} + \frac{1}{R_2} \right)$, where R_1 and R_2 are radii of curvature of curved surface.

possible to derive the gravitational part (the first term) of equation (2.28) from the gravitational energy of a liquid cylinder, see Fig.2.17. When a small part of a liquid cylinder about height dh is taken into consideration, its volume is equal to $V=Ah$ and mass is $m=\rho Ah$, where A is the area of the base of cylinder and ρ is the density of liquid. Then gravitational energy's addition is $dE=h\rho g A dh$. Total energy E of a cylinder with thickness e is expressed using the following relation:

$$\int_0^e h\rho g A dh = \rho g A \int_0^e h dh = \frac{1}{2} h^2 \rho g A. \quad (2.29)$$

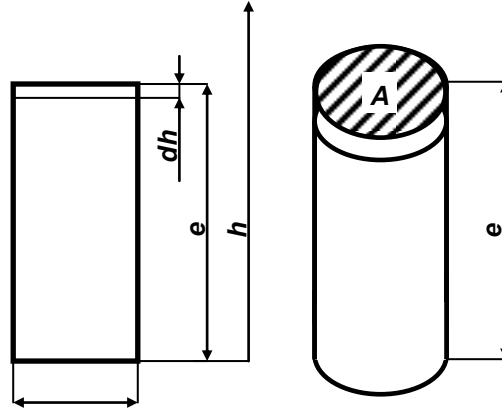


Fig.2.17: Scheme of liquid cylinder demonstrates the derivation of its gravitational energy.

The procedure of minimizing energy F while keeping volume Ae constant provides us with equation (2.30). Equation (2.28) can be minimized from $dF/de = 1/2\rho gV - V(-\gamma_{SG} + \gamma_{SL} + \gamma)(e^{-2}) = 0$. Equality $(-\gamma_{SG} + \gamma_{SL} + \gamma)(-e^{-2}) = 1/2\rho g$ comes consequently from the previous relation.

$$e_0 = \sqrt{2 \frac{-S}{\gamma g}} \quad (2.30)$$

where S is Harkinson's spreading coefficient defined above.

Spreading coefficient can be also written as a function of contact angle θ_0 of a drop on a solid substrate (through Young's equation):

$$e_0 = 2\kappa^{-1} \sin\left(\frac{\theta_0}{2}\right) \quad (2.31)$$

Relation (2.31) comes from Young's equation, $\gamma_{SL} = \gamma_{SG} + \gamma \cos \theta$ by means of subtracting γ from both sides of the equation. The following equation is obtained $\gamma_{SL} - \gamma_{SG} - \gamma = \gamma \cos \theta - \gamma$, from which results the relation $S = \gamma(\cos \theta - 1)$.

Then it is possible to get the following relation through the combination of equations (2.28) and (30): $e_0 = \sqrt{\frac{2S}{g\rho}} = \sqrt{\frac{2\gamma(1 - \cos \theta)}{g\rho}} = 2\kappa^{-1} \sqrt{\frac{1 - \cos \theta}{2}} = 2\kappa^{-1} \sin \frac{\theta}{2}$, which is identical to relation (2.31).

The following part is devoted to hysteresis during wetting. The hysteresis is very important mainly if porous materials are used, as for example fibrous materials. Hysteresis can be seen as unexpected shape of a monitored drop when observing the drop penetration into a fibrous material. Thus short introducing phenomena relating to hysteresis during wetting of such porous materials is necessary.

For an ideal surface wetted by a pure liquid, the contact angle theory predicts only one thermodynamically stable contact angle [52]. For real solid-liquid interactions, there is no unique contact angle rather than an interval of contact angles is observed. The largest contact angle is called "advancing" and the smallest contact angle is called "receding" contact angle. Since textile materials have complicated surface roughness and they are usually heterogeneous, the advancing contact angle is usually employed in discussions of wicking. Liquid droplets placed on a surface may produce an advancing angle if the drop is placed gently enough on the surface, or a receding angle if the deposition energy forces the drop to spread further than it would in the advancing case. The surface

morphology of solid materials or substrates (mainly the surface, of course) is very important here and of course influences shapes of drops. A change of surface roughness changes the surface wetting. For example if the roughness increases a hydrophilic substance becomes even more hydrophilic and a hydrophobic surface becomes literally super-hydrophobic [2]. In the text written above, an ideal surface was implicitly assumed. When a liquid drop is placed on a clean, planar, solid surface, an equilibrium contact angle θ can be observed. Contact angle θ is precisely the angle from the Young's formula. On real surfaces the contact angles of drops are often slightly dependent on the preparation conditions. The surface is usually not ideal (planar and clean) but it is marred by defects that are (i) either chemical (stains or blotches) or (ii) physical (surface irregularities). It is generally known that the hysteresis of prewetted materials is lower. When the porous material is "philic" to the liquid used it is usually not possible to measure receding contact angle. Detail information about hysteresis is described for example in publications [5, 33, 34].

On a non-ideal surface, the static contact angle turns out not to be unique. If, for instance, a drop is inflated, contact angle θ can exceed without the line of contact moving at all. Eventually, θ reaches a threshold value θ_A beyond which the line of contact finally does move. θ_A is referred to as the advancing angle. Likewise, when deflating a drop, θ can decrease down to limiting value θ_R known as the receding angle. Generally speaking, it can be said that observed angle θ depends on the ways the system was "prepared". And thus *contact angle hysteresis* is defined as the difference between limiting angles θ_A and θ_R . The difference between θ_A and θ_R is a measure of the state of cleanliness and roughness of a surface. The difference must be sufficiently small for good adhesion. Advancing and receding contact angle when deflating a drop is depicted in Fig.2.18.

The reason for contact angle hysteresis is heterogeneity (roughness, contamination, chemical uniformity and so on) of solid surfaces. Thus, places that create barriers for the natural movement of the contact line, exist on the solid surface. These barriers cause different contact angles than the contact angle that would be created on an ideal planar surface.

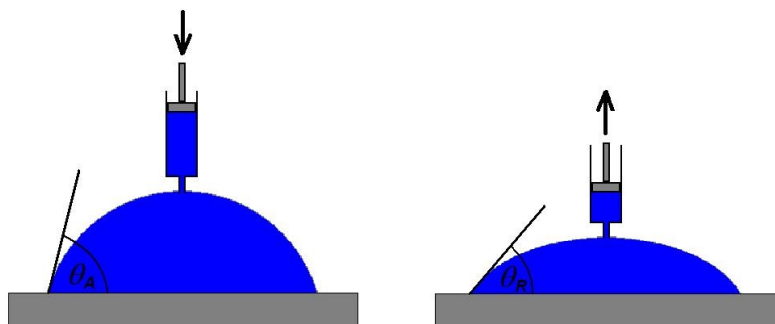


Fig.2.18: Advancing angle θ_A (on the left) when the drop is inflated and receding contact angle θ_R (on the right) when the drop is deflated.

The wetting relationship between a liquid and a porous material is difficult to characterize. Nonporous materials can be characterized very easily by means of contact angle. However, there is a simple question set and answered in de Gennes's publication, as well [2]. The question is: Is there a macroscopic contact angle between a liquid and a porous substrate? The answer is not simple. It is necessary to consider that an average contact angle can be defined only in an equilibrium situation. In case of a dry porous substrate under the condition of spontaneous liquid penetration inside ($\gamma_{SL} < \gamma_{SG}$) there is no sense to consider contact angle, as the liquid would instantly and irreversibly penetrate the porous medium. But the usage of a saturated porous substrate allows holding a drop resting on the substrate. The main problem is the correct saturation of the porous substrate. Thus the best variant is probably a way of capillary rise, by dipping substrate upside down into a liquid pool. Nevertheless, it is necessary to write cautionary remarks here: The contact angle measured this way is still just an approximation, because hysteresis can occur locally within the pores of the substrate and air bubbles can be trapped and change the drop's shape. Of course, an unavoidable complication is the fact that porous materials always have a somewhat random surface and internal structure, as well. Hysteresis effects often show up in the results. For example, a receding contact angle that is equal to zero is quite common. It means that the complete periphery of the drop placed on the porous substrate is "pinned" on the surface of substrate. The phenomena are far more complicated for textile materials, namely for nonwovens.

2.2.4. Drop Penetration into Porous Materials

In this chapter the approach is shifted from pure theoretical descriptions and models to a more practical one. Wetting of porous media describes the properties of another category of very rough surfaces. The three-dimensional nature of roughness raises the phenomena of liquid penetration and impregnation by liquid [2]. The dewetting processes on flat, smooth surfaces are relatively clear (see for example article [35]), although inertial regimes still raise some questions. But if the surface is porous, the situation is very different.

A drop placed on a porous medium does not merely spread on the surface but also penetrates into the depth of the material, thereby modifying its wetting properties. A liquid film deposited on a porous substrate recedes via two separate mechanisms: suction and dewetting. Suction through the pores is opposite to spreading.

The previously mentioned two models (model of cylindrical capillaries and model of radial capillary) are the most often used ones for dynamics of liquid penetration into porous materials. The following part is not devoted to models but to particular applications. Attention is focused mainly on the applicability of the radial model, because the cylindrical capillary model is very wide spread and there are an inexhaustible amount of articles related to the wetting of porous materials and their description by means of cylindrical capillaries model in the technical literature available. The greatest attention was devoted to the wicking phenomenon.

Liquid penetration into capillaries or porous media has been studied from various points of view for several years as shown in chapter 2.2. The first idea came from Lucas and Washburn [9, 10] at the beginning of the twentieth century. Several models were made for the better understanding of the basic phenomenon and problem of liquid penetration into porous systems. Majority of these models were set up from cylindrical capillaries, as for example [6, 14, 20]. The model of radial capillary is another type presenting the penetration of liquids [11]. This model was successfully applied for the description of liquid penetration into thin porous materials as a filter paper [19], thin nonwovens (droplet penetration into thin nonwovens - spun-laced materials and pressed air-laid materials is the subject of the upcoming article of this article's authors) and membranes [8]. These papers usually involve the spontaneous penetration of a drop into a porous medium. Article mentioned considers the forced penetration of a liquid droplet into a porous body of solid substrate. The paper [8] written by Bacri & Brochard-Wyart is introduced below.

The article is devoted to a forced droplet's penetration into porous membranes. Both spherical and cake drops were studied. The porosity of the membranes was extremely low (pore diameter deduced from Atom Force Microscope images was about $0.2 \mu\text{m}$) so it was necessary to use forced penetration, thus the liquid droplets were sucked in through the membranes. Removal of liquid (*spherical* and *cake drops*) deposited on a porous membrane by pumping with a prescribed pressure drop ΔP was studied. Two types of membranes were used: one with cylindrical non-connected pores and one with interconnected pores in order to know the influence of the internal structure of the porous substrate. Viscosity of liquids and the suction velocity were also varied. They choose two concentrations of glycerol (0 vol% and 80 vol%) in distilled water. They measured the permeability of both membranes by means of Darcy's law, the advancing and receding angles on dry and on prewetted membranes (where it was possible) for the characterization of membranes, and of course suction of spherical drops and cake drops into membranes. The main interest was in the behavior of radius R and thickness e of the sessile droplets as a function of time.

The measurements revealed very interesting results. Two suction regimes were found for small spherical droplets during the drops' suction into the porous substrate:

a) The Locked Regime – droplet radius R is constant and its thickness e decreases linearly with time and contact angle θ is still constant (see Fig.2.10b and Fig.2.19). If suction flow rate Q was varied as a function of time, it was possible to plot dh/dt (where h is the height of droplet) as a function of suction

velocity $J = \frac{Q}{A} = \frac{Q}{\pi R^2}$ (where A is the contact area between the droplet and the porous material). The

finally obtained curve was a line (in this case with a slope of about ≈ -2) for all measured systems (membranes – pore size $0.2 \mu\text{m}$; sintered glass discs – pore size $10-16 \mu\text{m}$);

b) The Unlocked Regime – contact angle θ remains steady and radius R decreases (see Fig.2.10a and Fig.2.19). They also checked that while the droplet was shrinking, its contact angle was about equal to the receding angle. The radius of droplet decreases linearly with time. When the suction velocity was plotted as a function of velocity dR/dt , the curve could be fitted with a line.

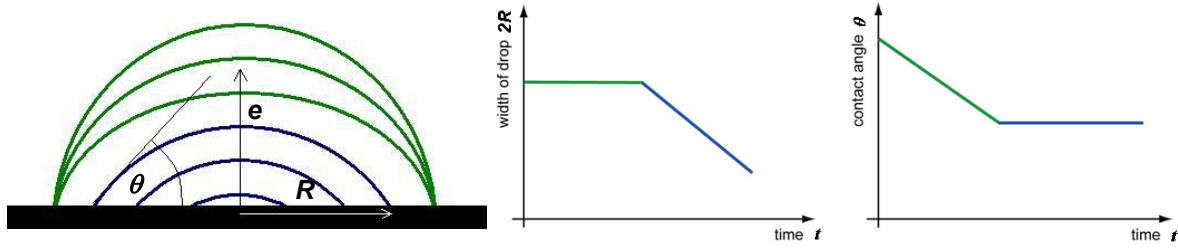


Fig.2.19: Scheme and orientation graphs for the better illustration of two different suction regimes found during a droplet’s penetration into porous membranes. Green lines represent the Locked regime and blue lines represent the Unlocked regime.

Suction of puddles – cake droplets – was another part of the droplet suction into porous membranes tests. A large amount of water (about 1.5 cm^3) was put on an isopore membrane and radius R of the cake droplet versus time was measured at varied applied pressure made by pump. Three suction regimes were found for cake droplets (see Fig.2.20):

a) The Gravitational Locked Regime – radius R remains constant and the thickness decreases linearly with time; at the beginning of the suction process the radius of the cake droplet is constant. The thickness decreases linearly with time. The rate of decrease of thickness $-de/dt$ is a linear function of applied pressure ΔP .

b) The Gravitational Unlocked Regime – radius R follows an exponential law as a function of time; Later during cake droplet penetration, the radius is not constant and decreases exponentially with time according to the following equation: $R = R_0 \exp\left\{-\frac{t-t_0}{\tau_p}\right\}$, where R_0 is the initial radius of the droplet.

The gravitational Unlocked regime starts and thus radius R begins to decrease, when the contact angle is close to the receding angle.

c) The Capillary Unlocked Regime (when radius R is smaller than capillary length κ^{-1} , the process returns to the regime of the small spherical drops where the capillary forces are dominant) – the radius of the droplet decreases linearly with time.

All these results can be interpreted assuming a quasi-equilibrium shape for the droplets and Darcy’s law for suction. The transient regimes (marked by dots in the graph in Fig.2.20) are unfortunately too short to be observed by classical cameras. They are studied in [36].

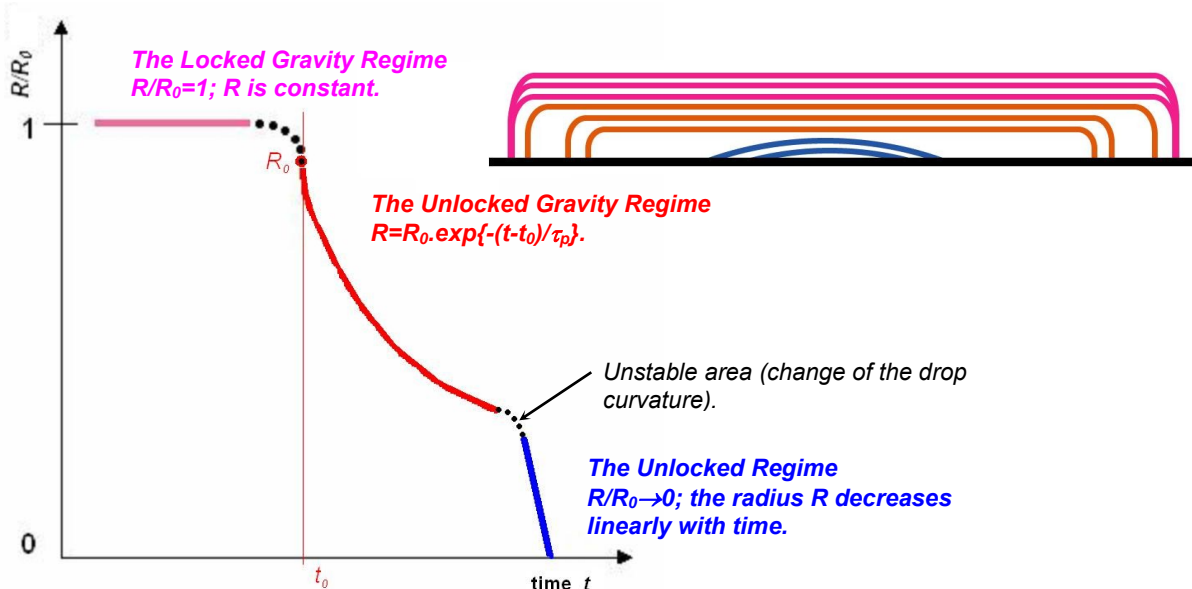


Fig. 2.20: Scheme and orientation graphs for the better illustration of three different suction regimes found during a cake droplet’s penetration into porous membranes. Pink lines represent the Locked Gravity Regime, red lines represent the Unlocked Gravity Regime and blue lines represent the Unlocked regime.

Finally it is necessary to mention at least the following several very interesting publications relating to drops penetration dynamics into porous materials [37-44].

2.2.5 Ultrasound Application for Enhancement of Liquid Penetration

Besides considerations about the process of liquid penetration into porous materials, it is also necessary to mention phenomena and mechanisms, which can influence the dynamics of liquid penetration into porous materials. This influence of the wetting process leads either to the acceleration or deceleration of wetting.

Principles for wetting, respectively liquid penetration, acceleration can have either physical or chemical character and it is possible to modify both the porous material (usually its surface) and the properties of the wetting liquid.

The best known adjustments for the improvement of the wetting of porous materials are:

- change of liquid surface tension
- pre-impregnation of porous material surface
- change of liquid viscosity, respectively decreasing viscosity (for example by a change of temperature)
- change of the roughness of a porous material surface
- change of the chemical composition of porous material surface (for example by plasma treatment)
- change of external surrounding pressure

Less known but apparently very effective method how to improve the dynamics of liquid penetration into porous materials is the usage of ultrasound treatment. Because the thesis also deals with the effect of ultrasound on the dynamics of liquid penetration into fibrous materials, it is necessary to introduce several publications which deal with ultrasound and its application for wetting porous materials. The topic is not known very well, thus there are only few publications about it.

One of these publications is an article [45] of Japanese researchers, who tried to find stronger bonds of interface between a matrix and its reinforcement in composite materials. They used carbon fibers from company Toray as a reinforcement and epoxy resin system as a matrix. Good wetting properties are fundamental for getting strong interfacial bonds. Huang et al. tested the improvement in the wetting of carbon fibers with epoxy resin by two ultrasound methods. One of them used an ultrasound transmitter directly inserted into a bath of resin. In case of the second method the ultrasound transmitter was directly placed onto a continuously moving carbon fiber bundle, which was pre-impregnated by resin. Authors of the article affirmed that resin was hold at temperature 20°C during the whole treatment. Viscosity, surface tension and strength of interphase bonds were tested. According to the authors, considerable decrease was experienced in the viscosity and surface tension of the resin system caused by the effect of ultrasound cavitations during the treatment. Viscosity decrease also enhanced the dynamics of resin penetration among carbon fibers. Interphase strength increased by about 15% after the usage of the treated resin matrix. Results of the second type of experiment showed an increase in the wetting properties between carbon fibers and epoxy resin, too. Higher percentage of oxygen was measured on the surface of treated fibers thanks to the ultrasound treatment. Interphase strength between treated fibers and untreated resin increased by about 35%. Both of these methods showed an ability to improve the wetting properties and final interphase strength in composite materials.

Torres from the Technical University of Liberec tried to repeat the first type of experiments introduced in [45]. Their results are described in conference contribution [46]. They used a highly viscous epoxy resin (1200/371 without hardener - Sindat Plzeň) and two ultrasound generators with different power. They changed the duration of the ultrasound treatment, as well. Samples of resin were of course kept at the temperature 20°C according to the above mentioned information. Viscosity and surface tension of the tested resin were measured after the treatments. Viscosity was supposed to decrease significantly, however these experiments had absolutely different results. Lower power of ultrasound treatment could not disperse cavitations through the complete volume of resin and higher power of ultrasound treatment lead to "cross linking-like" behavior in the resin and subsequently a significant increase in resin viscosity. These results showed that the decrease of viscosity by means of ultrasound treatment (as a method that enhances liquid penetration into porous materials) is not generally applicable. It is apparently necessary to keep to the certain terms or these results are true only for materials (liquids) of certain properties or a different physical characteristic supports liquid penetration into porous materials there. The last supposition is proven by the next publication.

Information about ultrasound utilization can be found in [47] which deals with so called wet textile processes, for instance dyeing, washing and textile finishing – post- treatments. These processes have two significant disadvantages: long process duration and low energy efficiency. As an agent for forcing wet textile processes, ultrasound treatment was tested. The usage of ultrasound

demonstrated encouraging results. Moholkar and Warmoeskerken showed in [48] that cavitations in a media (i.e. liquid, for example water) close to textile material surface are basic physical mechanisms for the enhancement of mass transfer in textiles. The authors of the article described methods for the quantitative estimation of ultrasound forcing mass transfers in textiles. They tested washing of dirtied (oil and carbon black) fabrics by means of ultrasound. This intensified experimental process of removing impurities was carried out in two different steps, because impurities penetrated between yarns and also between fibers (into yarns). The most important result from this study is that convection evoked by means of bubble movements (cavitations) helps to improve mass transfer in textile materials.

2.3. Wetting Experiments

An original own method for measuring the volume of sessile drops on a surface of porous materials is described in detail. The method, based on image analyses, was used for all evaluations of experiments devoted to drop penetration into radial capillary and various fibrous materials (nonwovens). Influences of liquid viscosity, fiber orientation and volume fraction on drop penetration into nonwovens were tested. Effect of ultrasound on the drop penetration into nonwovens was also studied and is described here.

2.3.1. Description of Experiment Procedure

The testing method used in the experimental part associated with wetting processes will be called *drop test* in the upcoming part. The method was designed exactly for studying the dynamics of drop penetration into porous materials, namely nonwovens.

The drop test is based on the recording of the penetration of a small drop, the weight or volume of which is known (measured as the difference in nonwoven weight after the drop penetration and before applying the drop) into a porous material. Drops were created spontaneously with a glass stick of adequate diameter (3 mm) for each liquid, and the stick was adequately dipped (approximately 10 mm) into the liquid for creating suitable drops. The test has following consecutive phases: preparation of nonwoven samples and liquid or solutions, preparation of a set up (a computer connected with a digital camera, as shown in Fig.2.21) for recording the drop's suction into the porous material, cutting of the recorded video with software to obtain a photo time sequence (VirtualDub, see Fig.2.22), usage of an image analysis software (LUCIA G, Matlab) for the determination of important data such as volumes of drops, shapes of drops and contact angles. Every video recording has had its own calibration by means of a scale. The scale is placed in the middle of the drop's mark exactly after the drop's penetration so it is also visible on the video recording, hence the whole system can be calibrated according to it. The behavior of a spherical drop during its penetration into porous materials is a sensitive test of porous materials wettability.

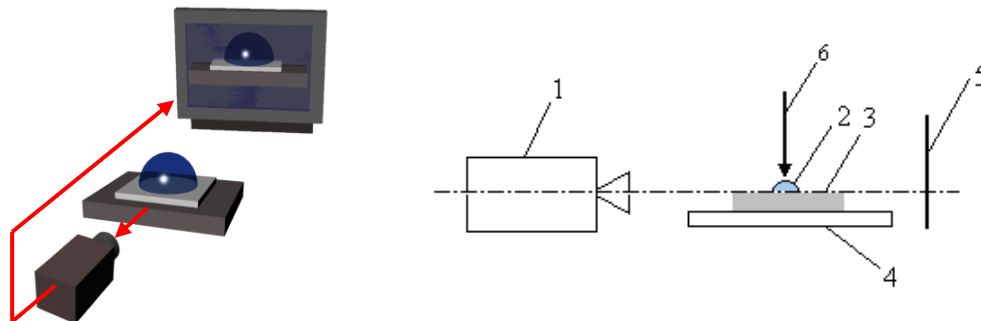


Fig.2.21: Scheme of an experiment configuration for spontaneous drop penetration: (1) a camera, (2) a drop on the surface of a porous sample (3) - mainly nonwoven material placed on a fixed underlay (4), dark background (5) can be used so that the drop edge can be differentiated better. A scale (6) for subsequent calibration of the system was inserted to each recording.



Fig.2.22: Example of drop penetration with time step 1 second (glycerin plus methyl violet, needle punched nonwoven).

Individual pictures were treated by image analysis. The drop volume is estimated as a volume of a sphere cap. Then *sphere cap volume* V_{sc} can be calculated from height h and width w of the cap, according to equation:

$$V_{sc} = \frac{\pi h}{6} (3R^2 + h^2) \quad (2.32)$$

Parameters R and h are shown in Fig.2.23. But for another understanding of a drop's behaviour during penetration, the area of droplet projection and contact angle of drops are also measured. Meaningful result for drop behaviour during penetration is graphical outputs from each experiment, where the changes in the drop's shape and contact angles are visible as a function of time, see Fig.2.24.

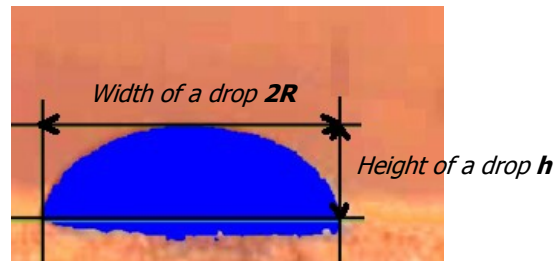


Fig.2.23: Example of the evaluation of a picture obtained from the recording.

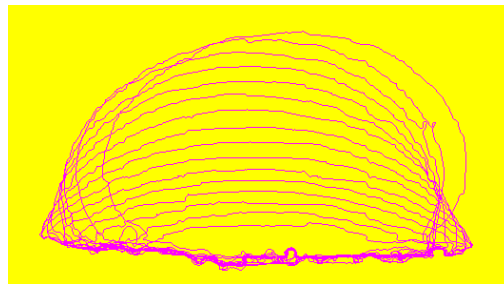


Fig.2.24: Example of a graphical output from image analysis of a drop's penetration into a nonwoven material. The change of drop's shape and contact angles is visible as a function of time.

However the above mentioned calculation of drop volume can be inaccurate, when the shape of the drop is not spherical. Due to these cases it was necessary to design and use a second method, referred to as "method of pixel calculation", which is also based on the usage of image analysis and software Matlab and is described below. The situation can arise when initial drop volumes – drops just after impact on a solid substrate – have to be measured. The condition for spherical drops is fulfilled, but inertial forces (gravity actions) from the drop's falling changed the spherical shape to an ellipsoidal – to be more precise, an oblate hemispheroid, for instance see Fig.2.25. The shape of the drop can be deformed during the drop's penetration progress due to hysteresis caused by the rough – fibrous surface.



Fig.2.25: Picture of a drop of non-spherical shape and the same drop with a plotted ellipse which characterizes its shape. An image of a spherical oblate is on the right side.

* A spheroid is a quadric surface in three dimensions obtained by rotating an ellipse around one of its principal axes. If the ellipse is rotated around its minor axis, the surface is an oblate spheroid. If all three radii are equal, the solid body is a sphere. If $a=b>c$, the solid body is an oblate spheroid.

The method of pixel calculation has a simple principle that can be divided into the following steps:

1) Firstly, individual color pictures have been separated from the video recording of a drop's penetration at a defined time interval (Fig.2.26.). The length scale calibration to a number of pixels has been noted.



Fig.2.26: Real picture of a drop on porous surface.

2) Every color picture was transferred to a binary form, as shown in Fig.2.27. The transformation was done by means of image analysis (software LUCIA G) using the *threshold* function. Thresholding of a picture is based on finding a threshold value. In case of a gray scaled picture, the value represents one number of two hundred and fifty-six numbers in the gray scale (from 0 to 255). For a fully-colored picture, the color threshold consists of three numbers that represents the so called RGB values – values of red, green and blue colors. After the selection of the threshold value, the pixels of the complete picture are checked. If the color parameters of a pixel (value of gray scale or RGB) are below the threshold mark, they will be substituted by zero – black color. If the color parameters of a pixel are above the threshold mark, they will be substituted by two hundred and fifty five – white color. The resultant picture has been saved as a bitmap (*.bmp).



Fig.2.27: Binary picture created from the picture above.

3) Fig.2.28 shows the binary picture, which was transported to software Matlab as a matrix of numbers 0 and 1. Then the software counted the pixels.

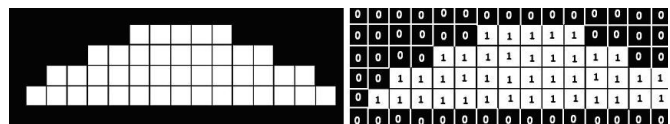


Fig.2.28: Scheme of a binary picture of a drop composed of pixels (white squares).

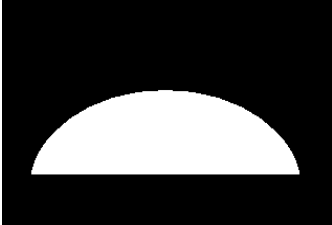
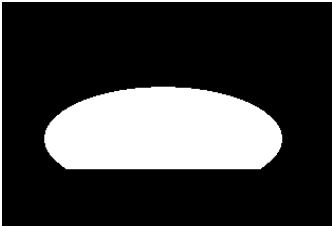
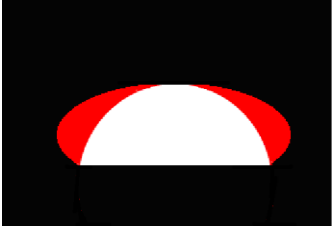
4) The total number of white pixels was calculated for every row of drop profile projection. The number presents the diameter of a cylinder of height $v=1$ pixel, assuming that drop is rotationally symmetric. All these discs (cylinders) were summed. After the calibration that defines how many length units are in one pixel in the real picture, the volume of drop was estimated.

The script used in software Matlab for drop volume calculation:

```
>>aa=imread(opening of picture file .bmp);
>>n=size(aa);
>>a=double(aa)
>>c=size(a)
>>v=sum(a,2)
>>calibration= number of pixels in the length unit.
>>heightofrow=(((calibration*v).^2)*pi/4)*1*calibration
>>result=sum(heightofrow,1)
```

In the following table, Tab.2.1, volumes of spherical and non-spherical droplet shapes are calculated according to both methods described above. The chapter should illustrate the differences between these methods.

Tab.2.1: Comparison of the methods used for calculation of droplet volumes.

	<p><u>Spherical droplet:</u></p> <p>Width = 255 pixels; Height = 78 pixels Volume of droplet calculated according to the calculation of sphere cap volume according to (2.32): 2 240 225 pixels³. Volume of droplet calculated according to the method of pixel calculation: 2 280 300 pixels³. Difference between results: 40 075 pixels³ (1,7%).</p>
	<p><u>Non-spherical droplet:</u></p> <p>Width = 186 pixels; Height = 78 pixels Volume of droplet calculated according to the calculation of sphere cap volume according to (2.32): 1 308 169 pixels³ Volume of droplet calculated according to the method of pixel calculation: 2 250 500 pixels³ Difference between results: 942 331 pixels³ (72%).</p>
	<p>In case of the non-spherical droplet, there is a big difference between the two methods, caused by the big mistake in the calculation according to the equation for sphere cap volume. The "mistake" is illustrated in the scheme with color red.</p>

The original method for evaluation of a drop penetration experiment was designed and tested specially for this type of studies. It was firstly introduced in [51]. The main advantage of the method is that all errors caused by drops of different shape from the spherical cap are eliminated. The method was used for all experiments listed in following subsections 2.3.2-4.

2.3.2. Radial Capillary

In this chapter the Marmur's [11] radial capillary model is studied and results of a practical experiment are presented. Radial capillary is of great practical importance – it describes the radial penetration of a liquid into thin porous media [17, 19] (e.g. penetration of ink into paper) whereas cylindrical capillary model represents penetration of liquids in porous media in general.

Experiments were carried out using two parallel glass plates with a small hole (of 1 mm diameter) in the upper one (Fig.2.29). The test liquid was 40vol% H_2O /60vol%glycerin. This concentration was chosen because a droplet of this solution has sufficient speed (according recording camera parameters) of penetration between the plates. A syringe was used to put the drop on the plate – the average drop volume was 150 μ l. The distance between glass plates was set with a foil put between the edges of the glass plates. Then the distance was measured using microscope: approximately 170 μ m. Recorded processes were then analyzed using software Lucia 4.61. The volume of the liquid that penetrated between the plates during a certain time period was calculated from the decrease in droplet volume, using the measured width and diameter of the droplet. The droplet was supposed to be spherical.

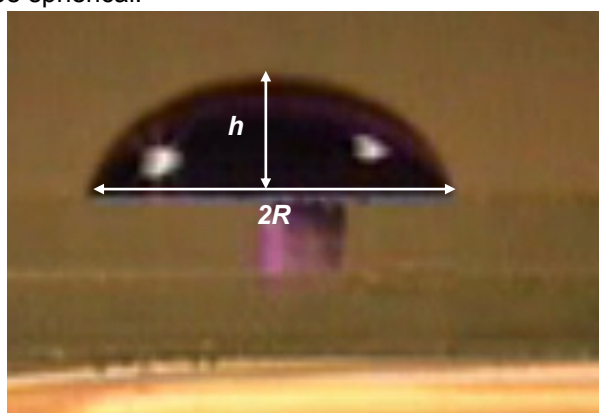


Fig.2.29: Example of drop penetration into a “radial capillary”; h – height of the droplet, R – radius of the base.

Experiments showed results introduced in Fig.2.30. Linear decreasing of outside drop volume is visible. The linear decreasing of outside drop volume means a constant velocity of drop penetration into radial capillary. It agrees with assumptions for infinite liquid reservoir, as it was described in the subsection 2.2.2. The linear characteristic is not valid for initial part of drop penetration, i.e. for the onset of penetration.

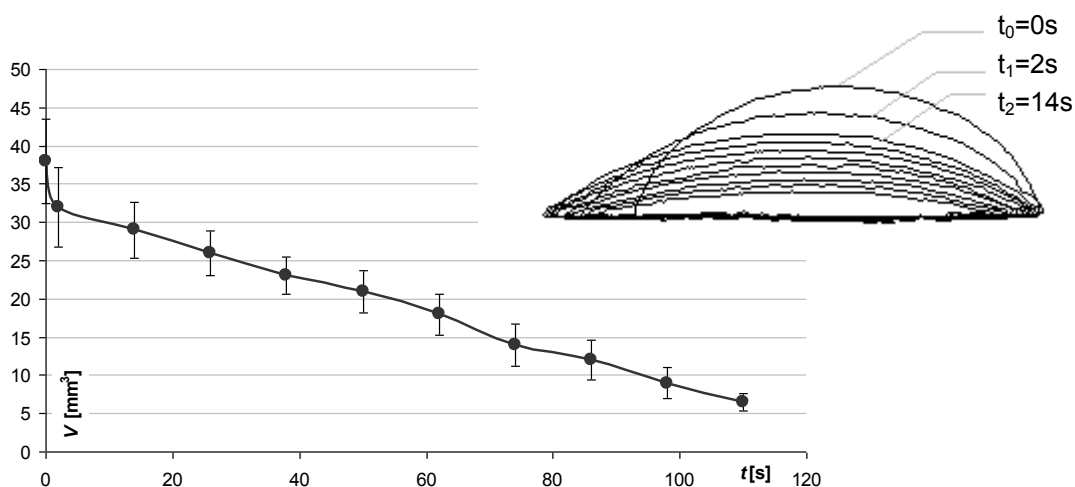


Fig.2.30: Example of a graphical output from image analysis (the first step = 2s, all other steps = 12s) on the right side and the graph for the average change of drop volume on the upper plate as a function of time (made from 15 different measurements).

The initial parts of drop penetrations were very interesting for all studied spherical drops. There was found different regime than these described by Marmur [11] and introduced in Fig.2.10. The different regime, which was observed at the beginning of drop penetration into radial capillary here, has expansive character. The contact angle decreases and radius of curvature increases as it is described in the subsection 2.2.2 for locked regime, but the contact area of outside drop volume and upper side of radial capillary increases in the initial part of drop penetration into radial capillary. The increasing of R – radius of drop base finished for all observed drops in time between 14 and 18s. Hereafter, from the graphic output of the image analysis, it has become visible that the real situation, except the initial part of penetration, is between two limiting cases described in Fig.2.10, as Marmur [11] supposed.

The model of radial capillary has some advantages and disadvantages, as well. The greatest concern is the correct set up of the experiment. The interface between the glass plate and the liquid was found to be significant.

2.3.3. Drop Penetration into Nonwovens

Influence of Liquid Viscosity

Nonwoven materials are used in several applications conjoined with transport of liquids (for example diapers, sanitary and hygienic materials, also production of composites reinforced with nonwovens, printing on thin nonwovens and so on). This part describes spontaneous droplet penetration into nonwoven materials. Three different liquids and three different nonwovens are used. The influence of liquid viscosity on penetration dynamics is studied.

The fibrous materials used in the experiment were:

- 1) Needle-punched nonwoven material with a surface density of $190 \pm 0.9 \text{ gm}^{-2}$ made from polyester fibers (the fineness of fibers was 6.7 dtex , fiber diameter $25 \text{ }\mu\text{m}$, fiber length 80 mm). The volume fraction calculated from densities (density of polyester fibers was 1360 kgm^{-3}) was 2.6%. The needle-punched material was hot pressed in order to obtain a thickness of 5 mm . When the needle punched nonwoven had already a thickness of 5 mm before pressing, only the surface was smoothed. Smoothing was necessary for the subsequent measurements. The fibrous materials were pressed at temperature 145°C for 2 minutes. Compression was done exactly before testing these materials, because the shape changes done this way are not stable and the material would relax after a longer time.
- 2) Needle-punched nonwoven with an area weight of $190 \pm 0.9 \text{ gm}^{-2}$ made from polyester fibers (the fineness of fibers was 6.7 dtex , fiber diameter $25 \text{ }\mu\text{m}$, fiber length 80 mm). The needle-punched material was hot pressed in order to obtain a thickness 1 mm (under the same conditions described above, the fibrous material was pressed at temperature 145°C for 4 minutes.). The volume fraction calculated from densities (density of polyester fibers was 1360 kgm^{-3}) was 16.9 %.
- 3) Perpendicularly laid thermal bonded nonwoven (so called struto [49]) with a surface density of $265 \pm 0.2 \text{ gm}^{-2}$ made from polyester fibers (the fineness of fibers was 6.7 dtex , fiber diameter $25 \text{ }\mu\text{m}$, fiber length 80 mm) and polyester/co-polyester bicomponent fibers (the fineness of fibers 2.2 dtex , fiber length 30 mm , melting temperature 135°C) in ratio 1:1. The resultant material had perpendicularly oriented fibers. The materials were finally slit with a vertical saw into two halves to obtain a material with really perpendicular orientation of fibers to the surface of the nonwoven. The final material thickness was 12.5 mm . The volume fraction calculated from densities was 1.6 %. Density of polyester fibers was 1360 kgm^{-3} , presence of bicomponent fibers was not taken into consideration, hence the value is a rough estimation only.

The liquids used in the experiment were:

- 1) Highly viscose epoxy resin 1200/371 without hardener (company Sindat Plzeň) with a viscosity of 195 Pas [46], surface tension $35,8 \text{ mNm}^{-1}$, and density $1,13 \text{ gcm}^{-3}$ (values provided by the producer).
- 2) Glycerin - viscosity $1,49 \text{ Pas}$ [50], surface tension $63,4 \text{ mNm}^{-1}$ [50] and density $1,26 \text{ gcm}^{-3}$ [50].
- 3) Mixture of glycerin and distilled water in volume ratio 7:3 with viscosity $22,5 \text{ mPas}$ [50], surface tension $64,8 \text{ mNm}^{-1}$ (the value was measured using microtensiometer Krüss K121 by the so called Wilhelmi's or plate method) and density $1,2 \text{ gcm}^{-3}$ [50].

All liquid properties were measured at temperature 20°C .

A scheme of experiments can be found in Tab.2.2. All experiments were accomplished according to the description in the subsection 2.3.1.

Tab.2.2: Scheme of materials used in the experiments– combinations of nonwovens and liquids.

Needle-punched material (5 mm)			Needle-punched material (1 mm)			Struto		
Glyc./water	Glycerin	Epoxy resin	Glyc./water	Glycerin	Epoxy resin	Glyc./water	Glycerin	Epoxy resin
15 samples	15 samples	15 samples	15 samples	15 samples	15 samples	15 samples	15 samples	15 samples

The volume of droplet on the surface of the porous material was consequently re-counted to the volume of droplet already penetrated into fibrous material, based on the knowledge of the initial droplet volume. According to these results graphs in appendix II were plotted. Each of these graphs presents fifteen different measurements with the same liquid and the same nonwoven material. There are also presented graphs of average values with marked standard deviations.

The supposed influence of viscosity of the used liquids on the rate of liquid penetration into porous materials is evident from Fig.2.31-33 made from all data for each experimental set up (same liquid and same nonwoven). These figures depict only cuts from the complete graphs for better visualization. Complete graphs can be found in appendix III.

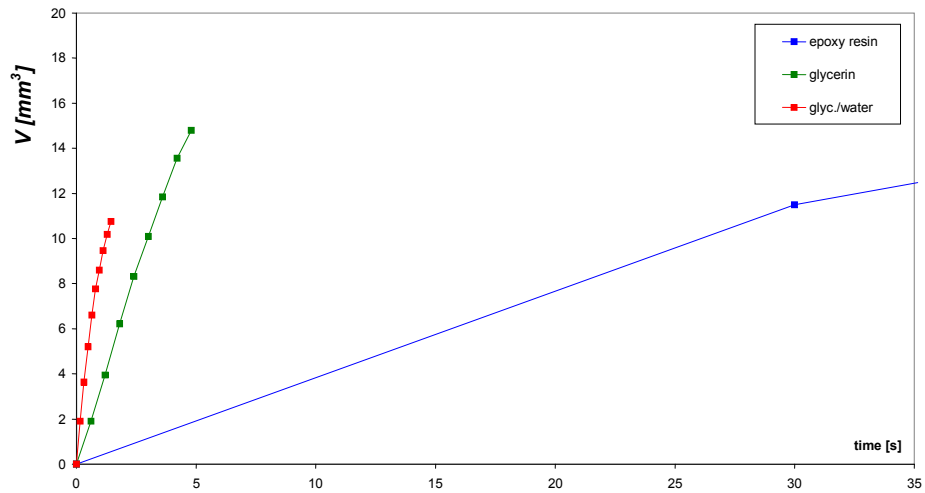


Fig.2.31: Dependence of the drop volume penetrated into a needle-punched material with thickness 1 mm on time for the three liquids with different viscosities.

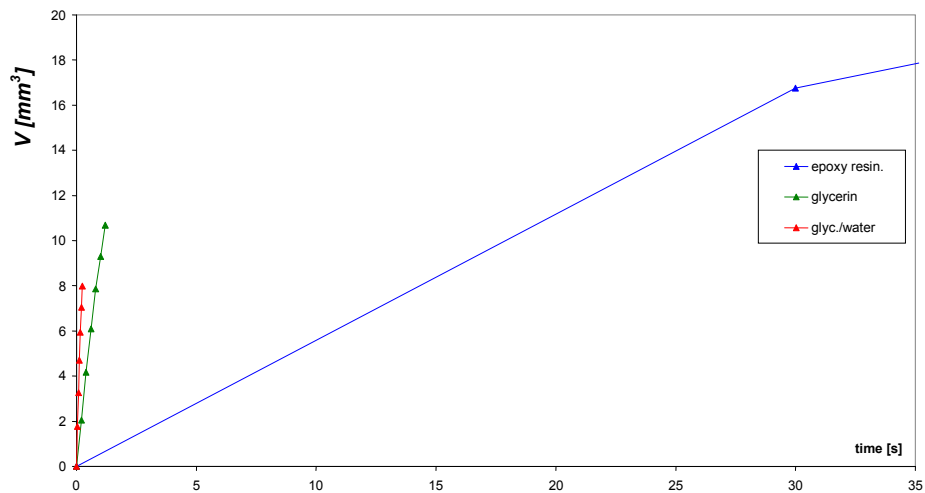


Fig.2.32: Dependence of the drop volume penetrated into a needle-punched material with thickness 5 mm on time for the three liquids with different viscosities.

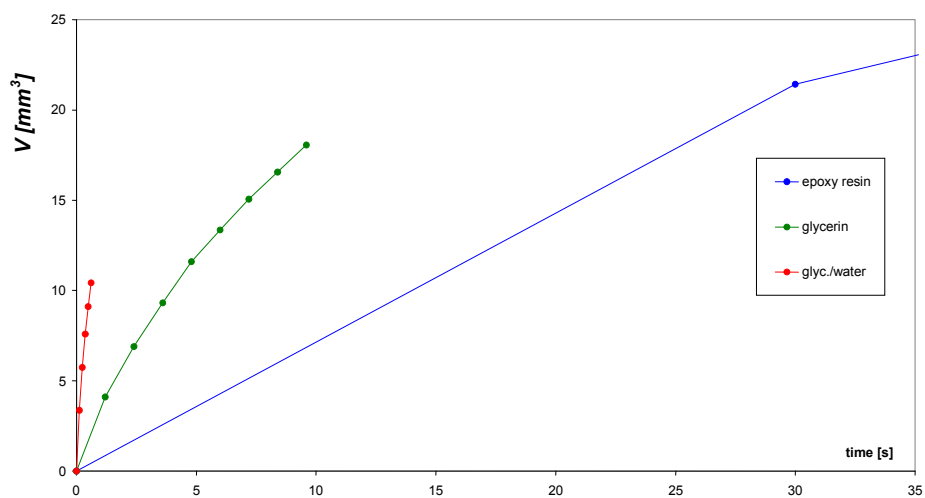


Fig.2.33: Dependence of the drop volume penetrated into struto on time for the three liquids with different viscosities.

Viscosity is one of the most important factors that influence a drop's penetration into porous materials. The results of experiments, which can be seen above, definitely agree with the theoretical assumption of Lucas and Washburn (section 2.2.1., equations (4) and (17) and appendix I). It is obvious from the equation and graphs that a decreasing viscosity leads to acceleration of the drop penetration rate into porous materials in case of all the three types of nonwoven materials.

But this theoretical and experimental agreement lies only in the tendency of relation between viscosity and velocity of drop penetration into nonwovens (decreasing viscosity results in increasing velocity of drops penetration). According to the theoretical assumption from equation (17), there should be an inverse proportionality between these two physical quantities. In experiments, there is a hyperbolic dependence ($y=ax^{-b}$), where y represents volume of liquid penetrated into nonwoven material and x represents time. But constant b varies between 0.42 and 0.53 (see appendix III). It is not 1 as it should be from theoretical models.

It is obvious that viscosity is not the only parameter which influences the dynamics of liquid or more precisely drop penetration into fibrous nonwoven materials. That is why nonwovens and fibrous assemblies are generally not ideal porous structures with perfectly aligned circular pores.

Influence of Nonwoven Structure

The other set of experiments is devoted to the behavior of droplet penetration into nonwovens with respect to their structural characteristics such as volume fraction and orientation of fibers creating the nonwoven material. The experiment in this chapter is divided into two parts. The first part is devoted to the study of drop penetration into nonwoven materials on production technology and associated orientation of fibers in these nonwovens relating to the direction of drop penetration. The second part of experiments deals with the effects of volume fraction changes in nonwovens on the studied dynamics of drop penetration.

Fiber orientation effects

The same fibrous materials and liquids already described above in the subsection 2.3.3 were used. These materials (referred to as *needle punched material (1 mm)*, *needle punched material (5 mm)* and *struto*) have three different fiber orientations. The majority of fibers and of course pores among fibers is supposed to be oriented horizontally for the first sample - needle punched material (1 mm). The second nonwoven sample, needle punched material (5 mm), is porous with multidirectional fiber orientation. Fibers were oriented horizontally by the carding machine at the beginning, but then the material was needle-punched. This operation reoriented a part of fibers to the vertical direction. The third sample, struto, represents a material with almost vertical fibers and pores among fibers, mainly when the material is slit and the drop is in contact with this side of the material.

It is necessary to note here that none of these samples has absolutely exactly the given orientation of fibers. The structure of nonwoven materials is more random than uniform, when only a small part of the material is taken into consideration. The surface of the spherical drop's bottom during penetration is usually about 15 mm^2 . All the fibers are also curled what changes the local orientation in the small sections of fibers. For struto, fibers are bonded with a thermoplastic material of low melting temperature, so there are non-fibrous particles in the material, too.

Average values of penetrated drop volume versus time for all three types of nonwovens were plotted in a graph to analyze the effect of fiber orientation in nonwoven materials on drop penetration. Three different graphs were created for each liquid – for glycerin/water see Fig.2.34, for glycerin vide Fig.2.35, for epoxy resin see Fig.2.37. All graphs are plotted after removing all extreme values of measurements and error bars represent standard deviations of the relevant measurements. Graphs for individual drop measurements of Fig. 2.34, 2.35 and 2.37 are introduced in appendix II.

Fig.2.35 shows behavior at the beginning of penetration into struto nonwoven and needle punched material with thickness 1mm. These phenomena can still be seen after removing all values of measurements. Complementary data were taken within a short time interval, $\langle 0.1 \rangle$ seconds, for the better visualization of the initial liquid penetration behavior and complementary Fig.2.36 was created accordingly.

The first visible results show change of curves order with change of liquid viscosity (see Fig.2.34 – 2.37). There is visible that drops penetration into three different nonwoven materials changes with change of viscosity of liquid.

In the set of experiments the orientation of fibers in the three used nonwovens was expected to have a characteristic influence on drop penetration. That assumption was based on the model of cylindrical capillary with different orientations. However, the assumption that nonwovens with fiber (and also pore) orientation in the direction of gravity should enhance drop penetration, did not prove to be valid generally in the above presented experiments. The obvious behavior according to the previous presumption was followed only in case of the highly viscous liquid – epoxy resin. The other two tested liquids exhibited another behavior. The explanation of that could be described by dividing drop penetration process into several consecutive steps.

- 1) The drop falls onto a nonwoven and is energetically supported by the inertial force from the fall. If the drop penetrates extremely quickly, it is possible to consider the dominant role of the forces in short times after fall-down.
- 2) The drop falls down on the surface of nonwoven and wetting process starts. In the beginning wetting is driven by capillary forces – and so called precursor films are created. The larger the number of fibers in contact with the drop is (higher volume fraction, larger surface area), the bigger amount of liquid is sucked into nonwovens.
- 3) Apparently, manifestation of gravitation forces arises as the third step after a relatively longer time as it was showed in the experiments with epoxy resin.

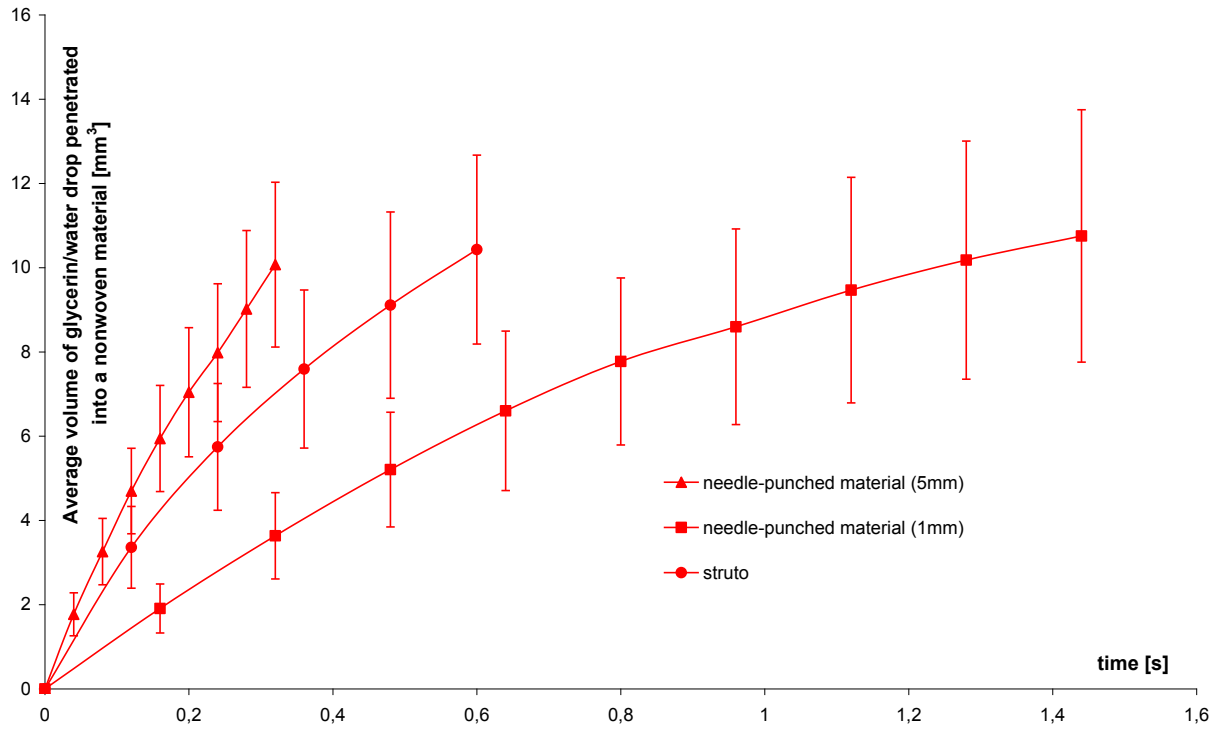


Fig.2.34: Average drop volume (glycerin/water) penetrated inside three various types of nonwoven materials as a function of penetration time.

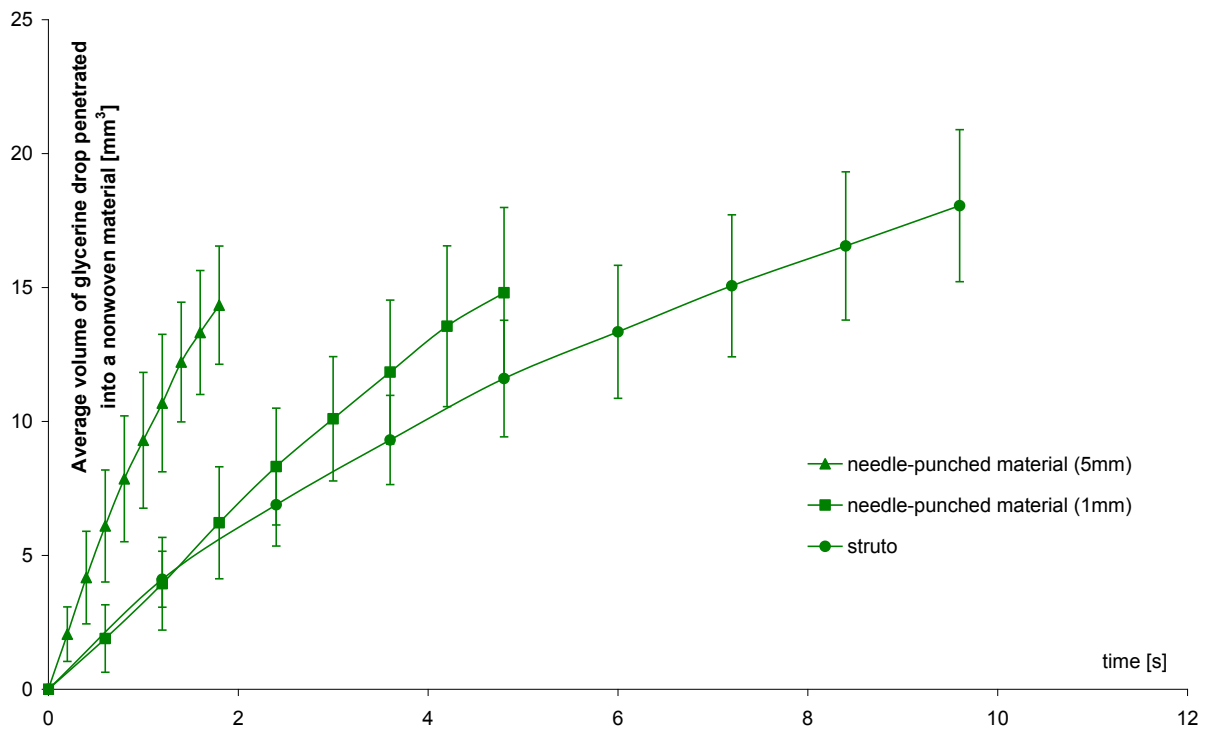


Fig.2.35: Average drop volume (glycerine) penetrated inside three various types of nonwoven materials as a function of penetration time.

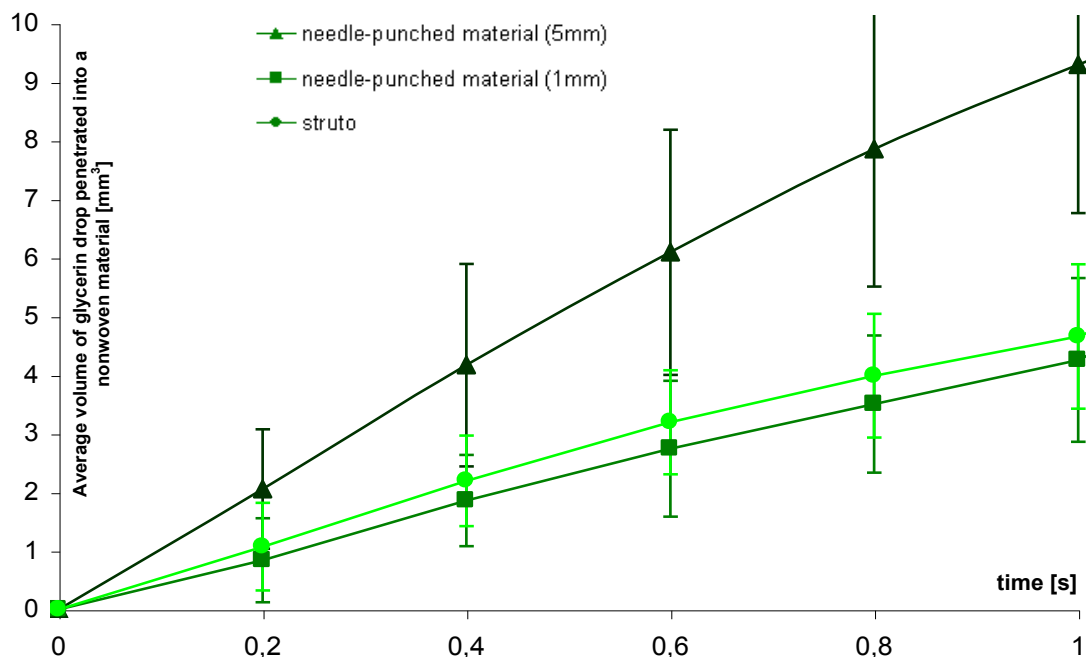


Fig. 2.36: Average drop volume (glycerin) penetrated inside three various types of nonwoven materials as a function of penetration time. Complementing data to Fig. 2.35 for time interval (0.1) seconds.

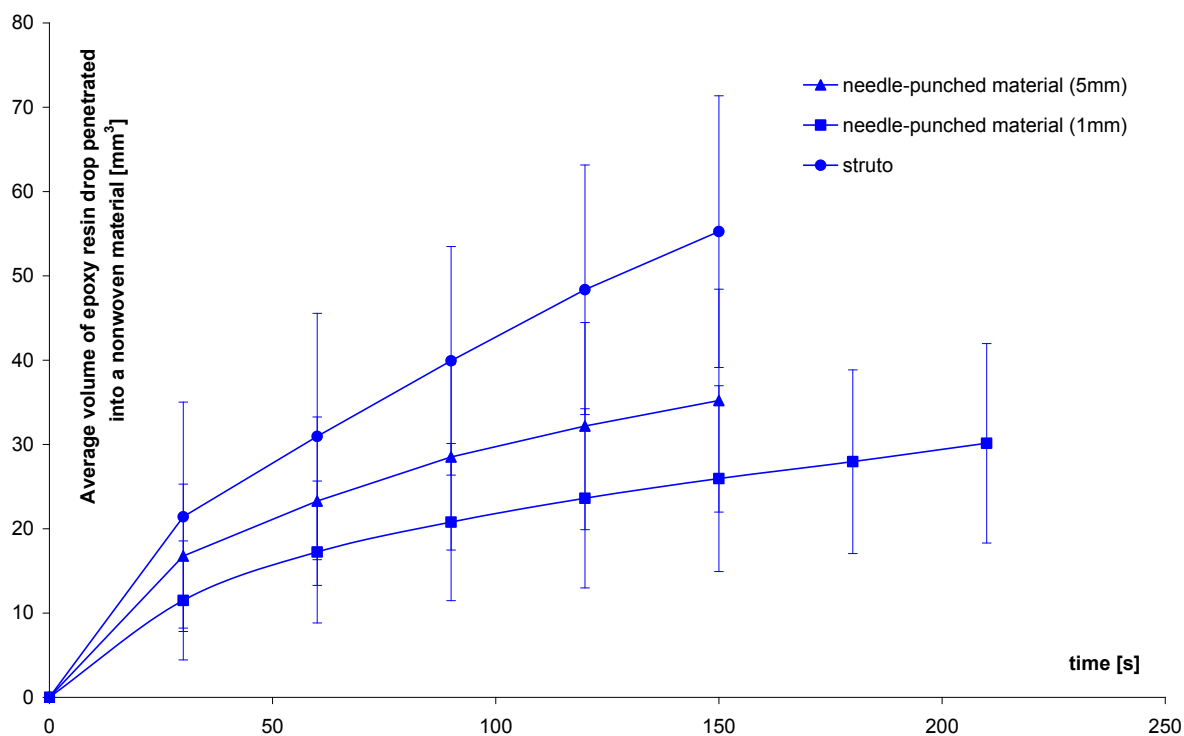


Fig. 2.37: Average drop volume (epoxy resin) penetrated inside three various types of nonwoven materials as a function of penetration time.

These three phases co-exist during the whole process, but the dominant effect in each phase differs, and that could be an explanation for the unexpected behavior of drops during their penetration. The unexpected behavior is also shown by the rearrangement of curves in Fig. 2.35 (respectively in Fig. 2.36).

However, during the drops penetration, various liquid composition can significantly react to the slight difference of fibrous material composition in used nonwovens. For instance a small difference in material composition of struto can be the reason of the unexpected behavior of drops during their penetration observed in the set of experiments.

Volume fraction effects

This subsection introduces two different sets of experiments. Both of them focus on volume fraction effects on drop penetration dynamics. The first of these experiments introduces drop behavior in contact with nonwoven material, where fineness of fibers and volume fraction is changed. The fibrous materials used in the experiment are needle-punched nonwoven materials with two different fiber finesses: 6,7 dtex (fiber diameter 25 μm , average fiber length 80 mm, surface density $194,45 \pm 0,07 \text{ gm}^{-2}$) and 17 dtex (fiber diameter 40 μm , average fiber length 80 mm, surface density $233,45 \pm 0,14 \text{ gm}^{-2}$). The needle-punched material is hot pressed in order to obtain the required thickness, together with which volume fraction is changed. The fibrous materials are pressed at temperature 145°C for 4 minutes. Pressing is carried out just before testing, because the shape changes done this way are not stable and the material would relax after a longer time. The volume fractions of measured materials are introduced in Tab.2.3.

Tab.2.3: Volume fractions of eight different types of tested nonwoven materials.

Volume fraction	Thickness of needle-punched material			
	1 mm	2 mm	3 mm	4 mm
Fineness of fibers				
6,7 dtex	0,140	0,070	0,047	0,035
17 dtex	0,168	0,084	0,056	0,042

In this set of experiments, only the mixture of glycerin and distilled water was used in volume ratio 7:3, the parameters of which are described above in the subsection 2.3.3. This mixture was chosen because of its suitability with regard to the total time of drop penetration into these types of nonwovens. All experiments were accomplished according to the description in the subsection 2.3.1.

The graphical results of the influence of nonwoven volume fraction on the dynamics of drop penetration are presented here in Fig.2.38. Needle-punched nonwoven materials made of polyester fibers were used. It is constructed from the average values of drop penetration rate. Linear regressions were used for finding the rate numbers for the nonwovens. Fifteen different drops of glycerin/water mixture (of weight between 0.02-0.03 g) were used to calculate each average value of the plot. The graph is composed of two lines, one for each fiber fineness.

Drop penetration rate increases obviously with increasing fineness and decreasing volume fraction of the studied nonwovens. The previous graph proves an increasing linear dependence between thickness of samples and velocity of drop penetration. Linear dependence is obvious from the regression coefficients R (in case of fineness 17 dtex $R=0,950$ and for fineness 6,7 dtex $R=0,997$).

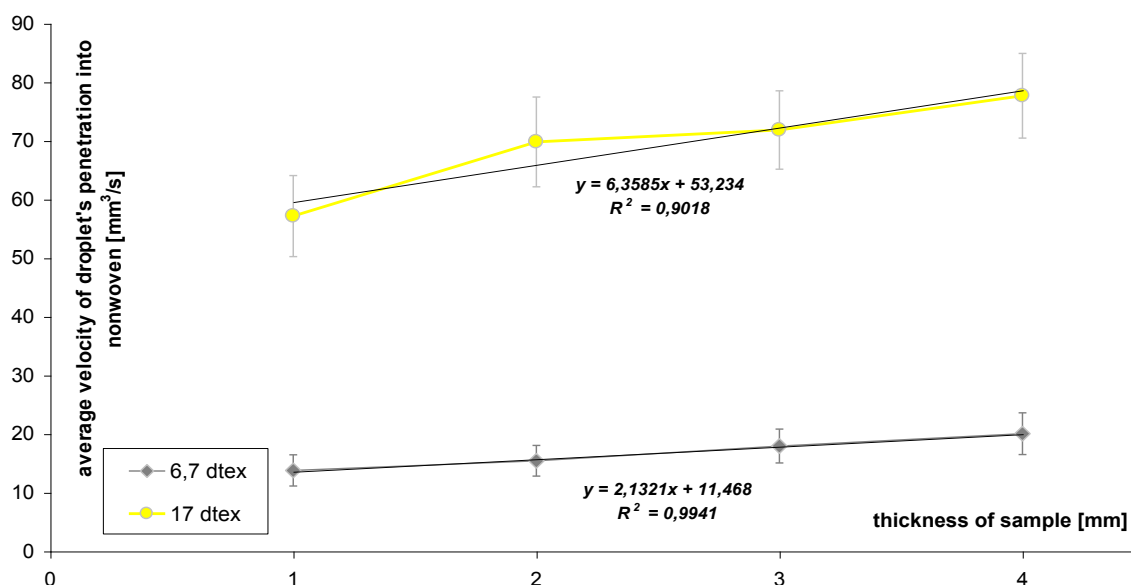


Fig.2.38: Average velocity of drop penetration into needle-punched nonwovens of different fiber fineness versus thickness of samples. Error bars represent standard deviations. See also the table of relevant volume fractions of nonwoven materials used.

The second set of experiments, published in [51], relating to the effect of the volume fraction of nonwoven materials on drop penetration focuses on a detailed study of drop penetration dynamic character using a wider range of drop sizes (weights). The material used in the experiment was a needle-punched nonwoven with the surface density of 225 gm^{-2} made from polyester fibers (fiber fineness $6,7 \text{ dtex}$, fiber diameter $25 \text{ }\mu\text{m}$). The needle-punched material was hot pressed in order to obtain a thickness of 1 mm and 3 mm . Glycerin, colored with intensive violet color, methyl violet, was used as the model liquid. Drops of different weight ($0,012 - 0,08 \text{ g}$) were dropped on the surface of the needle-punched nonwoven and their penetration was recorded using a camera as it is introduced in the subsection 2.3.1. More than forty measurements were analyzed this way. The volume of drop was calculated as a sphere cap. If the shape of drop was not spherical, the volume of drop was calculated with the special method using image analysis and software Matlab, as it is described in 2.3.1.

The two spherical drop suction regimes, described for the radial capillary model [11] and for porous membranes with random orientation of pores [8], were found in case of the spherical drop penetration into needle-punched nonwovens, as well (see Fig.2.39). The side-projections of drops in Fig.2.39 show three different regimes, which are described in subsection 2.3.4 and in Fig.2.55.

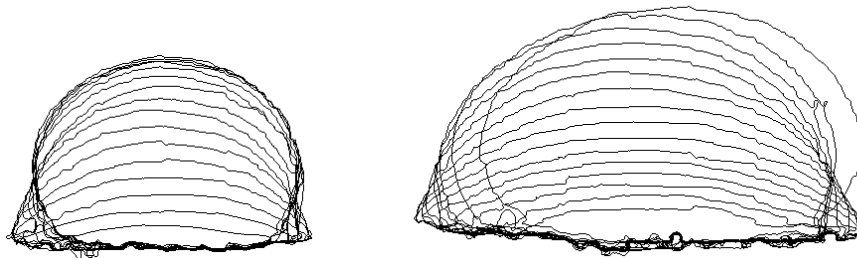


Fig.2.39: Examples of two drops (small one of $0,031 \text{ g}$ on the left and bigger one of $0,071 \text{ g}$). Graphic outputs from image analysis presenting shape change during penetration into a needle-punched nonwoven with thickness 3 mm .

The spherical drop penetration into the more bulky needle-punched nonwovens with thickness of 3 mm follows the model of dependence $V=At$ (see Fig.2.40), where V is the volume of liquid inside the nonwoven, A is a constant and t is time. But the drop penetration into the thin needle-punched nonwoven with thickness 1 mm follows the model dependence $V = \sqrt{At}$ (see Fig.2.41). Average regression coefficients are calculated from the particular regression coefficients determined from the linear regression of each data curve thus of each single drop penetration.

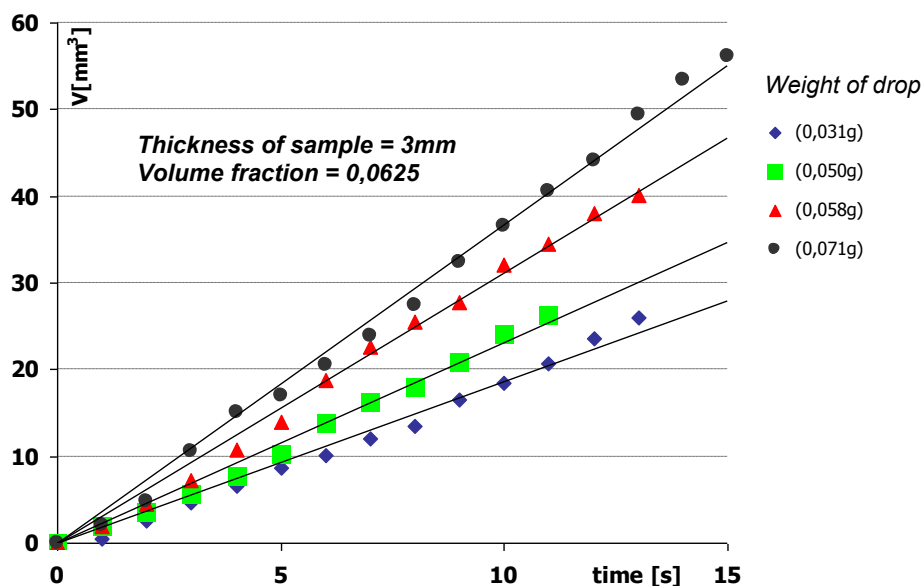


Fig.2.40: Linear dependence of penetrated drop volume on time for nonwovens with lower volume fraction. Average regression coefficient is $0,9952$.

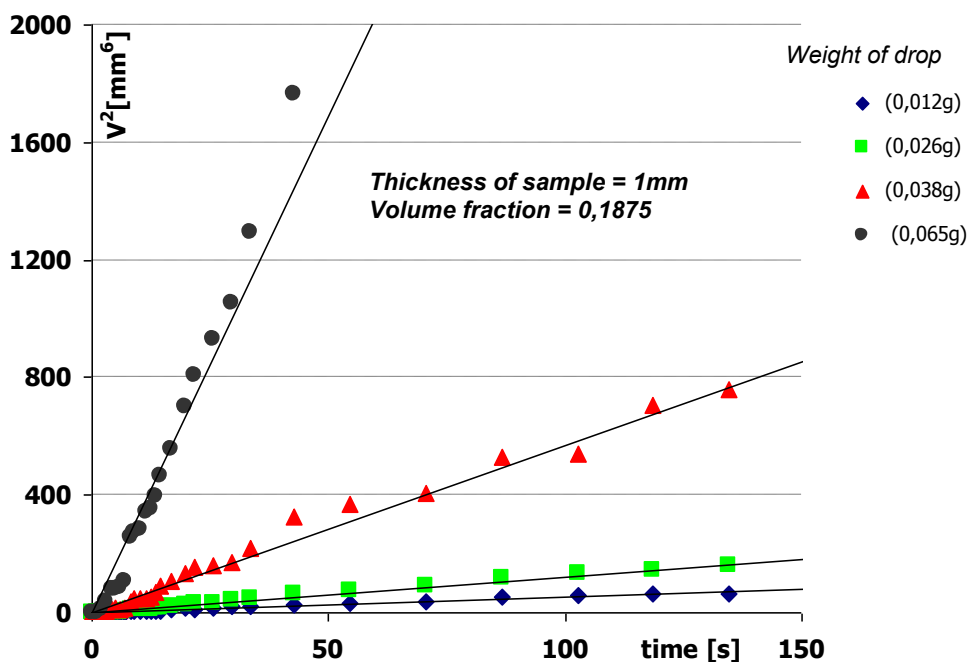


Fig.2.41: Linear dependence of the second power of penetrated drop volume V^2 on time for nonwovens with higher volume fraction. Average regression coefficient is 0,9928.

Influence of Ultrasound Treatment on Penetration Enhancement

This part is devoted to a better understanding of how ultrasound enhances drop penetration into nonwovens. It is generally known that highly viscous liquids penetrate fibrous structures with high volume fraction and with small pores very slowly. The extreme case is the penetration of a highly viscous resin into nanofibrous electrospun materials. It is well known that composite materials have to be impregnated fully by resin in the shortest possible time because of the solidification (curing) of resin. In that case, it is necessary to enhance the penetration of the fibrous material with some external energy, and not to use only spontaneous penetration. The experiments for the production of composite materials composed of electrospun nanofibrous layers and resins are described in Chapter 4 of the thesis. Here the same materials and the same resin were used as in the previous experiments. The main question was if it is possible to recognize or even record the changes of drop penetration enhanced by ultrasound compared to the spontaneous process.

The same nonwovens were used as in the previous part of the thesis (see chapter 2.3.3.). These materials are again indicated as needle punched material (*thickness = 1 mm*), needle punched material (*thickness = 5 mm*) and struto. Epoxy resin was used as the testing liquid because of its high viscosity. The properties of the resin can also be found above in chapter 2.3.3. The testing device structure for recording drop penetration into nonwoven materials is a little different from the previous one. The ultrasound created in the generator is transferred to the needle connected by a tin solder to the sonotrode (transmitter) as it is visible in Fig.2.43a. The needle goes through a small hole in the holder (bed) of the fibrous sample. Power requirement was $1.46 W$ and frequency $22 kHz$. The scheme of the complete set up of the experiment is illustrated in Fig.2.42. A sample of nonwoven material was laid down onto the bed so the needle was $2 mm$ above the upper surface of the nonwoven material (see Fig.2.43a). The needle diameter was $0.3 mm$ and total length of needle was $30 mm$. A drop of resin was laid on the end of the needle after activation of the ultrasound generator. The needle vibrates along the axis of the transmitter, thus ultrasound waves were spread from the top of the needle only. The process was of course recorded with a camera. The needle had to be cleaned after each experiment with a suitable solvent of the resin.

An example, one drop penetration set of photos is shown in Fig.2.44. Graphs in Figs.2.45-47 were constructed from the measured data for all three different fibrous materials in order to highlight the difference between penetration with and without ultrasound enhancement. The obvious result, that spontaneous penetration is slower than penetration enhanced by ultrasound, is revealed by the graphs.

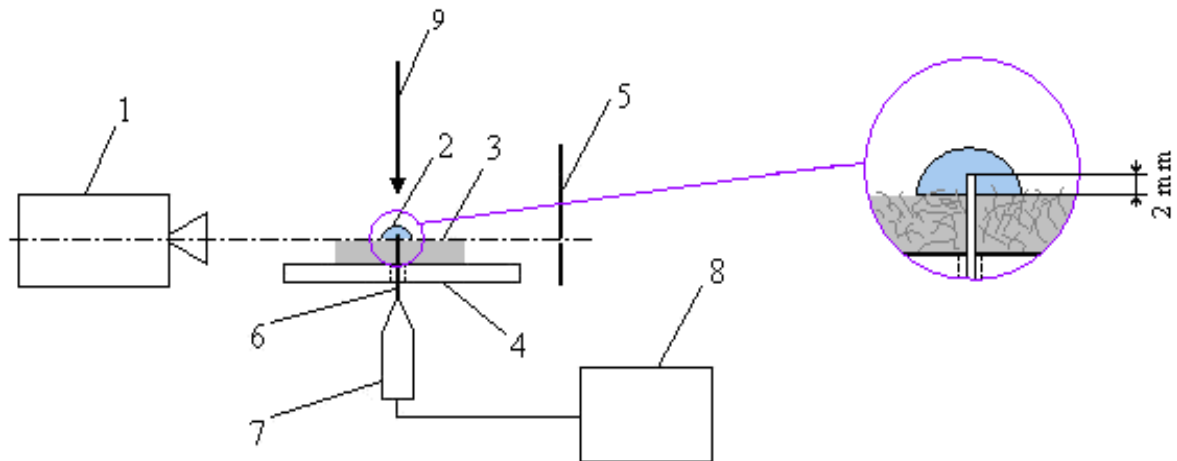


Fig.2.42: Scheme of an experiment configuration for drop penetration enhanced by ultrasound: (1) camera, (2) a drop on the surface of a porous sample (3) - mainly nonwoven material placed on a fixed underlay (4), dark background (5) can be used so that the drop edge can be differentiated better. Ultrasound energy is created in the ultrasound generator (8) and transmitted by a transmitter (7) and a metallic needle exactly into the penetrating drop. A scale (9) for subsequent calibration of the system has to be inserted to each recording.

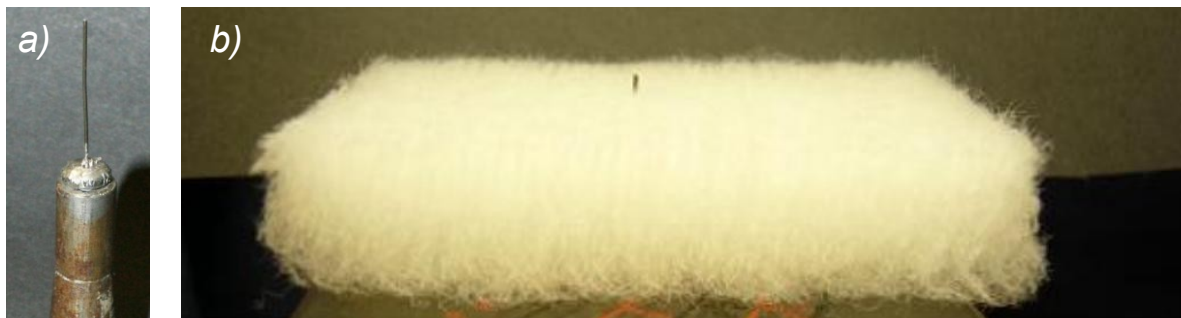


Fig.2.43: Photos of an experiment dealing with ultrasound influence to drop penetration preparation (a) the needle connected by means of tin solder to the sonotrode; (b) the needle tip, which extends 2 mm above the surface of the struto.

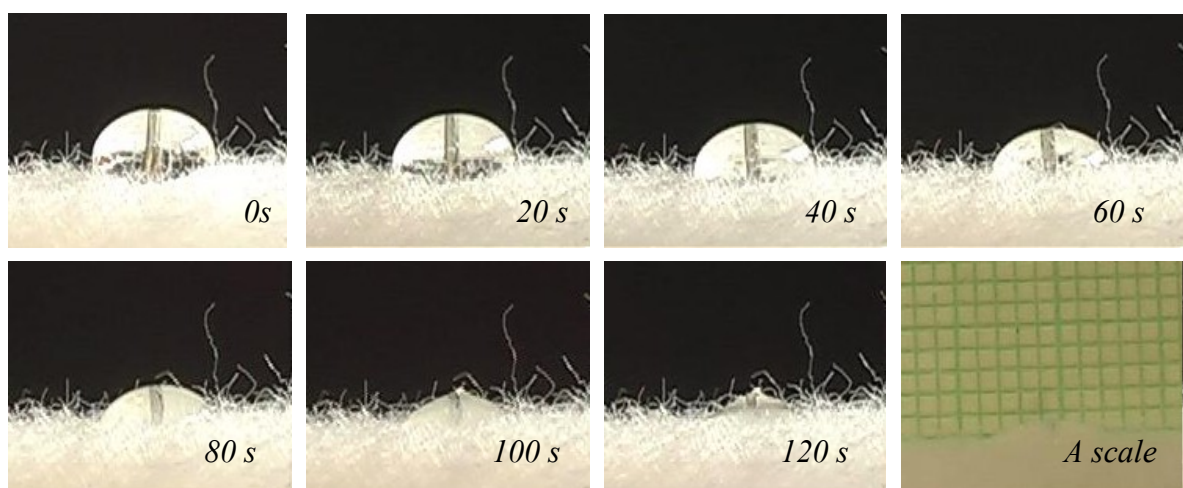


Fig.2.44: Photograph sequence showing the penetration of a drop into struto nonwoven enhanced by ultrasound (needle transmitting ultrasound to the drop is visible too).

The spontaneous penetration of resin drops into nonwovens had in all cases almost a linear character for the second power of average volume V^2 penetrated into the nonwoven versus time. It agrees with the Lucas- Washburn equation ($V = \sqrt{At}$) as shown in Fig.2.48.

However, penetration enhanced by ultrasound follows rather a linear curve, i.e. $V=A.t$, even when the penetrated volume is graphed versus time (see Fig.2.45-47). Fig.2.49 illustrates the effect of ultrasound on a drop better. Drops penetrating into the same struto nonwoven were there imaged at the same time, but only one of them was influenced by ultrasound. Both of them had the same weight (0.07g). The image was created by means of image analyzer LUCIA G. The changes of drop contact angles during penetration were also measured by the same software. The result graph of drops contact angle changes during developing time of spontaneous penetration and penetration enhanced by ultrasound is in Fig.2.50. The linear character of contact angle change and the different rate of contact angle decrease are obvious. The increasing rate of drop penetration into nonwovens enhanced by ultrasound could be explained with the formation of cavitations* and of course temperature increase. Cavitations influenced the shape of a drop during its penetration as shown in Figs.2.49 and 50. At the beginning of the process, visible cavitations can lift a drop and the contact angle increases as a consequence. An example of drop shape changes due to ultrasound is visible in Fig.2.51.

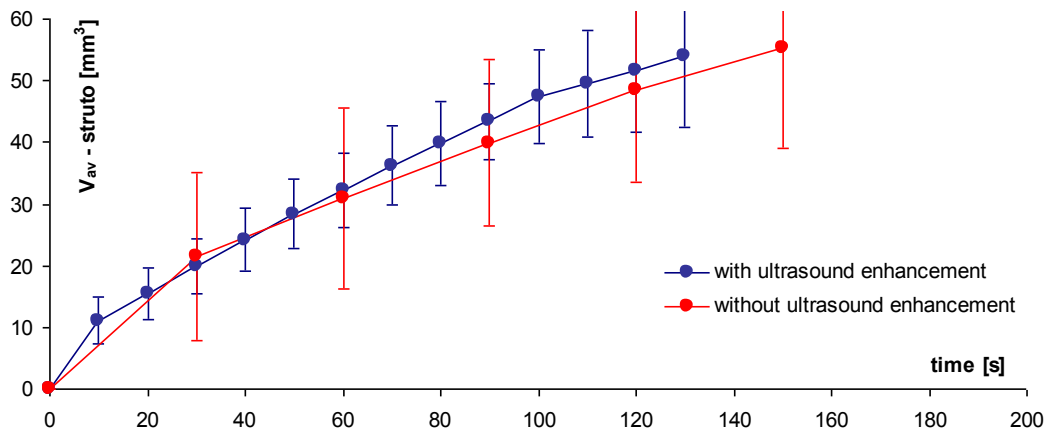


Fig.2.45: Average drop volume of epoxy resin (V_{av}) penetrating (spontaneously and enhanced by ultrasound) into the struto nonwoven structure as a function of time.

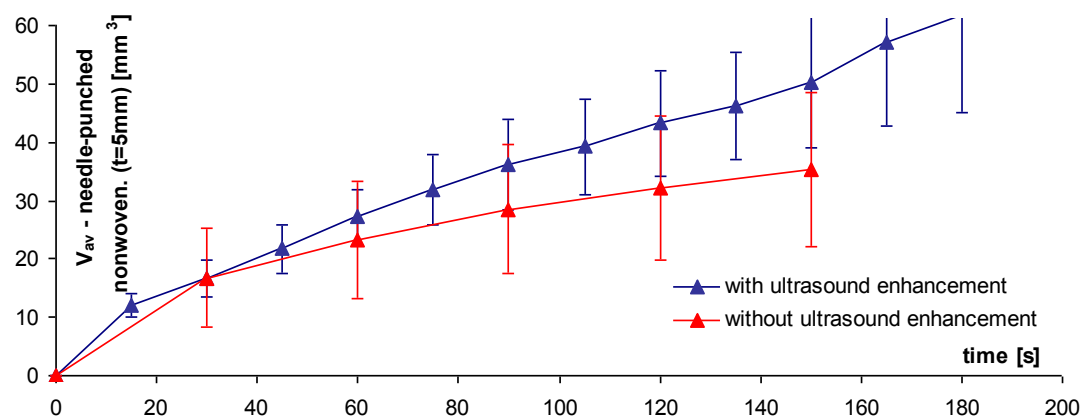


Fig.2.46: Average drop volume of epoxy resin (V_{av}) penetrating (spontaneously and enhanced by ultrasound) into the needle punched nonwoven ($t=5mm$) structure as a function of time.

* Cavitation is the rapid formation and collapse of vapor bubbles and voids in a liquid subjected to acoustic energy at high frequency and intensity ultrasound (analogous to thermal boiling but without the associated rise in temperature of the mass of liquid, although localized temperatures on the molecular level can be extremely high).

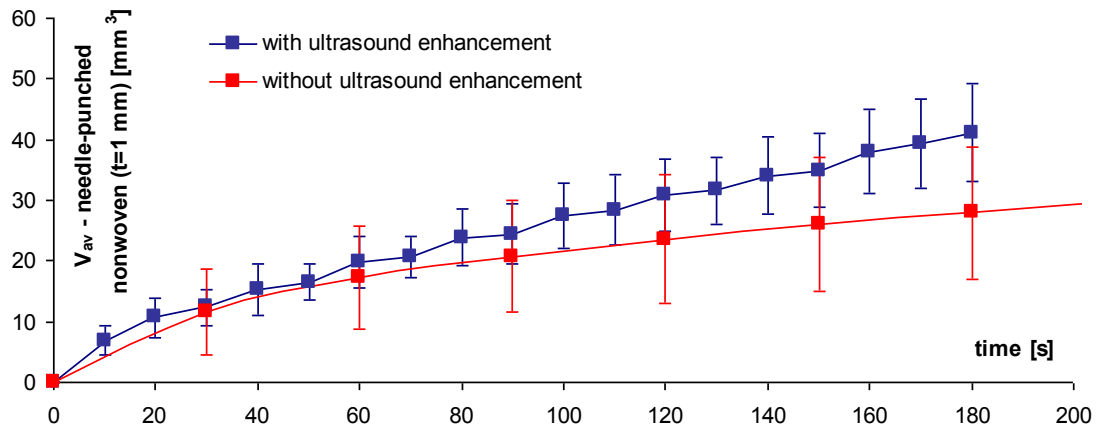


Fig.2.47: Average drop volume of epoxy resin (V_{av}) penetrating (spontaneously and enhanced by ultrasound) into the needle punched nonwoven ($t=1\text{mm}$) structure as a function of time.

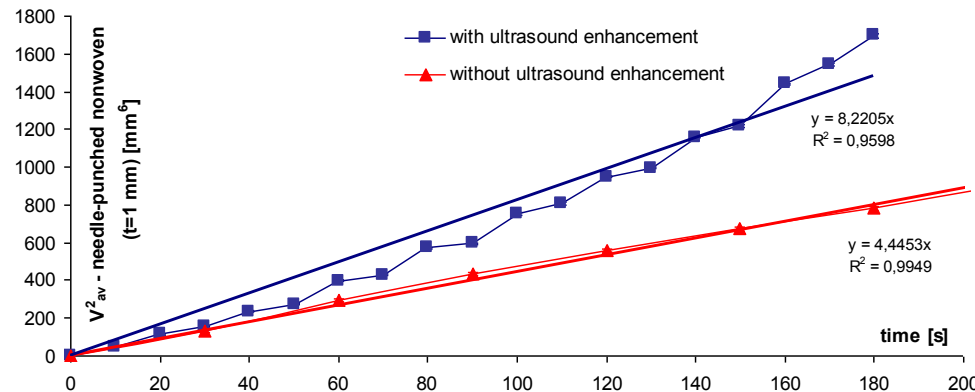
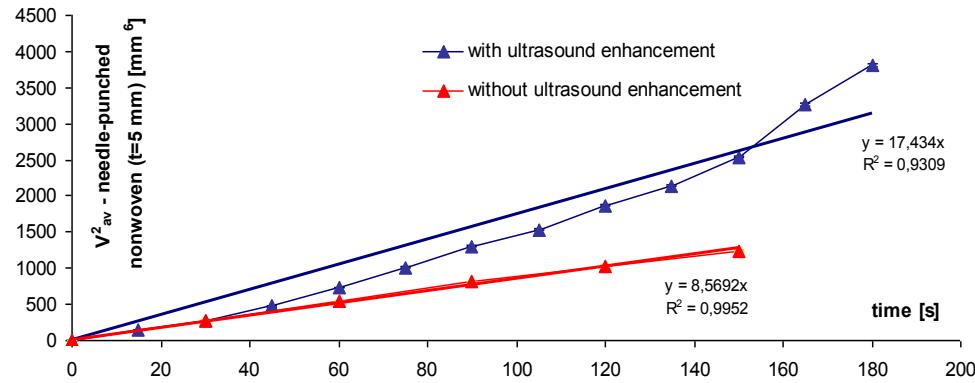
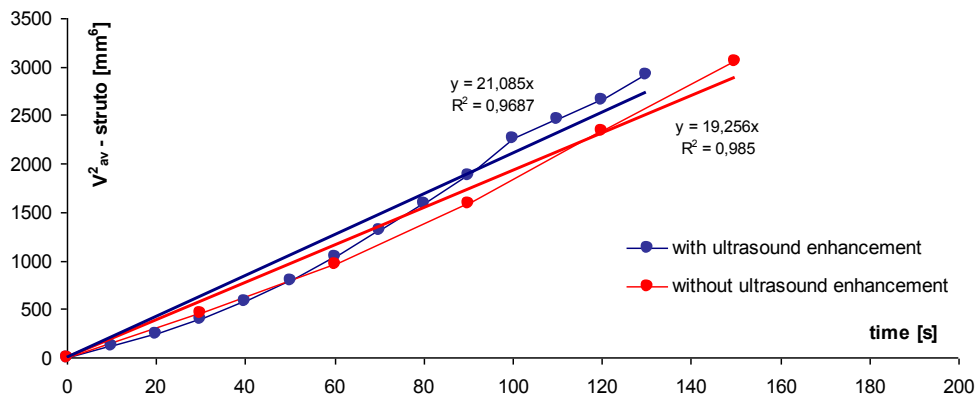


Fig.2.48: Second power of epoxy resin drop volume (V_{av}) penetrating into the nonwovens as a function of time. Regression curves, regression equations and second power of regression coefficients are plotted.

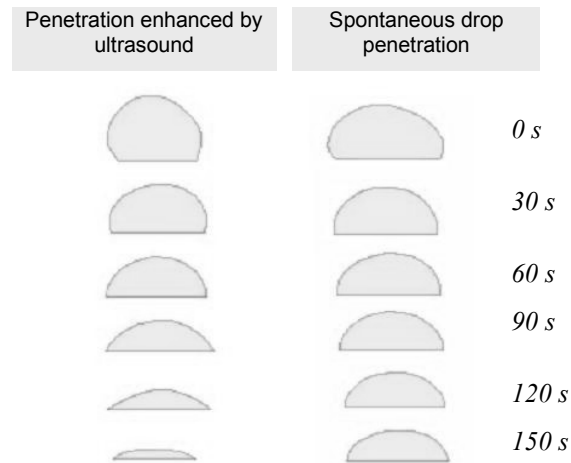


Fig.2.49: Penetration of epoxy resin drops enhanced by ultrasound (left side) and spontaneous penetration (right side) into *struto* nonwoven structure. The initial weight of drops is 0,07 g.

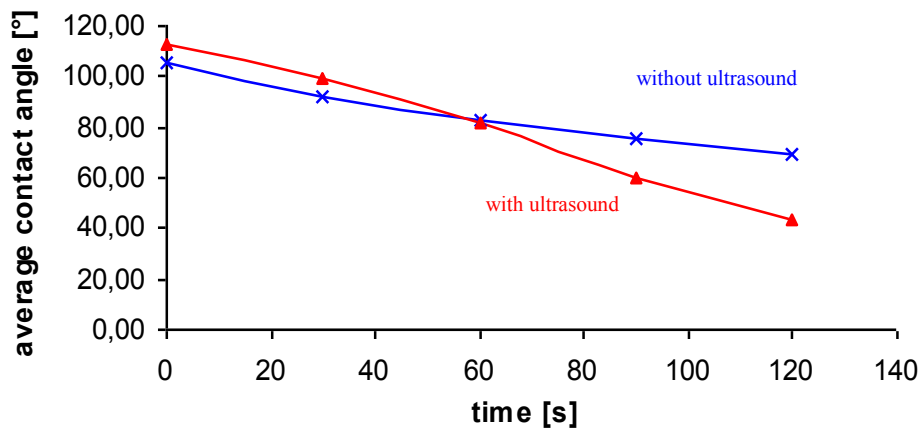


Fig.2.50: Changes of average contact angles during spontaneous drop penetration and penetration enhanced by ultrasound. The graph corresponds with images from Fig.2.49.

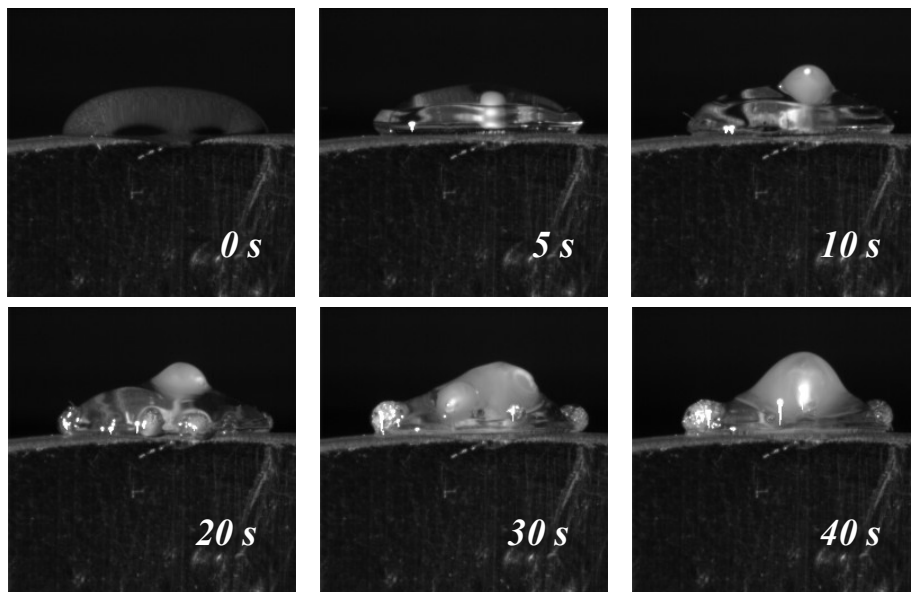


Fig.2.51: Example of a drop shape change due to ultrasound influence. An epoxy resin drop is placed directly onto the ultrasound transducer. The created cavitations process was recorded with a high speed camera.

Next Measured Characteristics of Drop Penetration into Nonwovens

Influence of spherical drop (used in all introduced experiments in the thesis) weight on liquid penetration velocity into nonwoven textiles was measured as a supplementary characteristic of the tested processes. It was necessary to find out if drop penetration velocity is affected by the weight of drop in Fig.2.52. The influence of drop penetration velocity on drop weight is introduced. Data from measurements using the nonwoven material with fiber fineness 17 dtex and thickness 1 mm were used. A mixture of glycerin/water ratio 7:3 was applied, as always in the thesis, as the liquid of drops. All other graphs (different nonwovens with different liquid drops) showed similar characteristics, thus only one graph is presented as a representative.

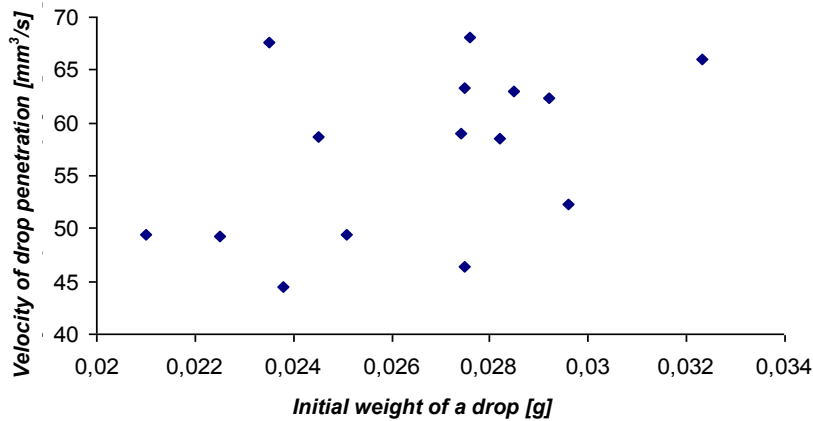


Fig.2.52: Velocity of drop penetration into nonwovens for the material with fiber fineness 17 dtex and thickness 1mm versus the initial weight of a drop.

No significant influence of drop weight on its penetration velocity can be seen in the graph. These results do not prove the supposed linear increasing dependence between drop weight and its penetration velocity. This phenomenon can be explained in the following way: only small spherical drops were used – intentionally – and their weight range is very small in all experiments (except in the second part of the subsection 2.3.3. devoted to studying of a dependence of nonwoven volume fraction effects to drops penetration) in the thesis. This is why it is possible to state that the influence of a spherical drop weight on its penetration velocity into a nonwoven material is not evident, if the drop weight range is sufficiently small.

However if the difference of used drop sizes (weights) is higher, the dependence between drop size (weight) and drop penetration velocity into a nonwoven material becomes evident. The velocity of drop penetration increases clearly with increasing drop size (weight) (see Fig.2.40 and Fig.2.53).

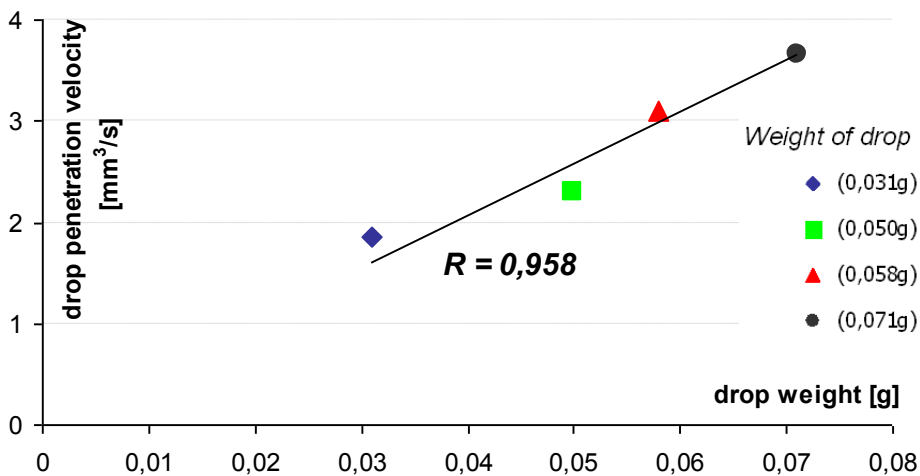


Fig.2.53: Influence of average drop penetration velocities on drop weight. Data taken from Fig.2.40, where linear dependences of penetrated drop volume on time for needle-punched material (thickness 3 mm) is presented.

2.3.4. Recapitulation of Experimental Results

This chapter summarizes results from the previous part of the thesis. It focuses on general results, advantages and disadvantages of the used experimental methods and also on the explanation of some discrepancies between theory and experimental data.

The found or verified general rules are the following:

- a) Decreasing viscosity increases the drop penetration velocity into nonwovens in all cases.
- b) The behavior of liquids of higher viscosities (as used resin is) corresponds with the orientation of fibers in the nonwoven. The more fibers are oriented in the direction of liquid penetration, the higher the velocity of drop penetration is. Liquids with lower viscosity are more influenced by capillary forces and hence their behavior does not follow the above mentioned rule.
- c) Decreasing value of volume fraction in nonwovens significantly increases the rate of drop penetration into nonwovens.
- d) The rate of penetration increases with the increasing fiber diameter in nonwovens.
- e) Usage of ultrasound for highly viscose liquids increases the rate of drop penetration into nonwovens. The enhancement increases with increasing volume fraction in nonwovens.
- f) The impact of drop size is not significant, if the drop weight range is sufficiently small. If the range of drop sizes is larger, the velocity of drop penetration increases with drop size increasing.

Almost all the above mentioned rules have exceptions. There are some conditions when these rules are not valid. The most decisive factor is which kind of forces (capillary or gravitational) play the dominant role during drop penetration or how these forces act together.

An example of such experiment can be introduced. As mentioned above, a decreasing value of volume fraction in nonwovens increases the rate of drop penetration into nonwovens. However, if a drop is appropriately small and the fibrous structure is very porous (see Fig.2.52), drop penetration can be very slow because of the dominant role of Laplace pressure, which does not allow a drop to change its shape and transport liquid into the fibrous structure.

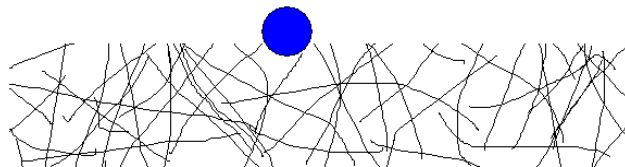


Fig.2.54: Illustration of a highly porous fibrous structure in contact with a small drop.

The process of liquid penetration into tested nonwovens can be generally divided into three regimes: i) The initial phase of penetration (blue color in Fig.2.55): the shape of droplet is not a spherical cap, the contact angles are higher than 90° and change, and the contact area between the droplet and the nonwoven material increases (width w increases); ii) The middle phase of penetration (red color in Fig.2.55): the shape of the droplet is a spherical cap, contact angle changes and the contact area between the droplet and the nonwoven material is constant (the width is almost constant); iii) The final phase of penetration (green color in Fig.2.55): the shape of the droplet is a spherical cap, the contact angle does not change and the contact area between the droplet and the nonwoven material decreases. Droplet height h almost linearly decreases during the whole time interval. It is one of drops from the experiment described in the second part of subsection 2.3.3 devoted to studying of nonwoven volume fraction to drops penetration (glycerin drop; the needle-punched material with thickness 3 mm) in Fig.2.55.

The initial phase of penetration, where contact angle is higher than 90° and width increases is not described in theoretical part. Publication [8] does not obtain such regime of drop penetration into porous materials. Thus the explanation of the regime presence can come from difference between nonwoven materials and porous materials used in that article. The reason for the difference is the different surface of these porous materials, as the rough surface of nonwovens with possible salient fibers can explain the different initial phase of penetration.

The data for width and contact angle in the middle and the final phase of penetration follow the theoretical predictions introduced in subsection 2.2.4 (see Fig.2.19) and publication [8].

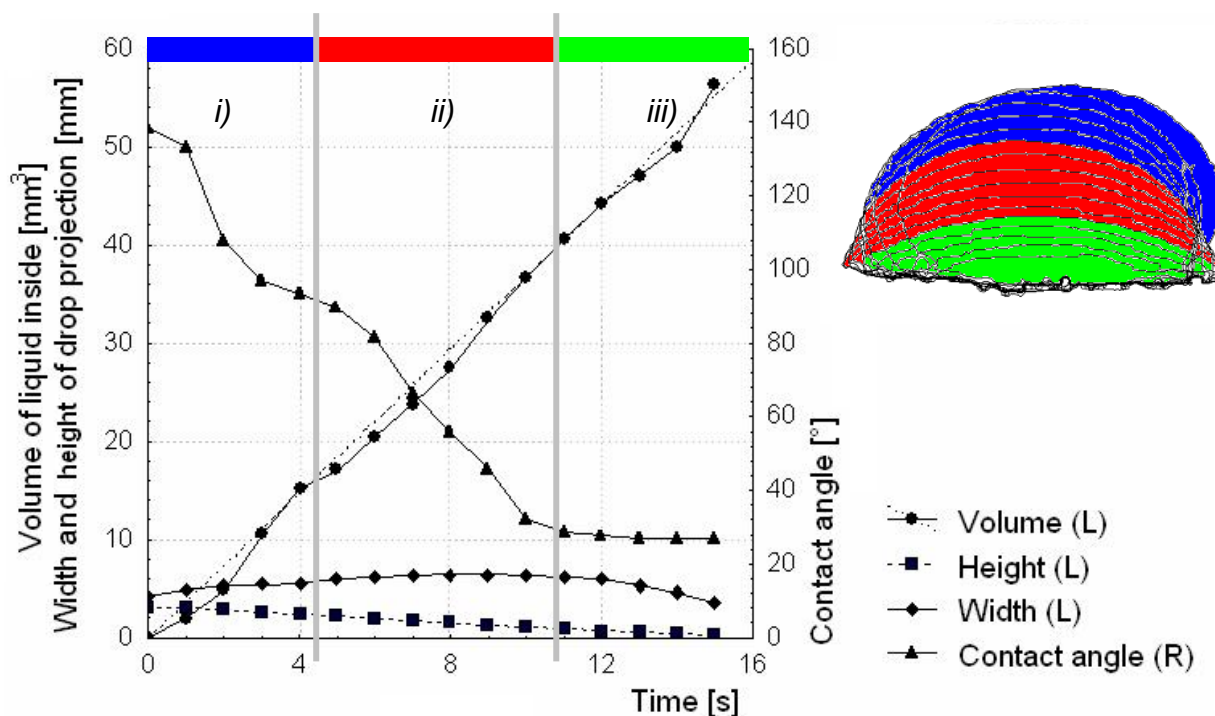


Fig.2.55: Example of the graphical recording of increasing the volume of liquid inside the nonwoven, the change of a height, a width and a contact angle of drop versus time and the image analysis for this drop. The weight of the drop was 0,07 g.

The following statements serve as an evaluation of the presented method of drop penetration measurements:

- The method significantly discloses the influence of liquid viscosity on different volume fractions and orientation of fibers in the nonwovens.
- The method is rather suitable for actions of longer duration (more than or about one minute). No accurate results can be measured during a very quick drop penetration.
- The method in modified set up can be also used for testing the effect of ultrasound on drop penetration into porous materials such as nonwovens.
- The method is very sensitive to the surface roughness of nonwovens (protruding fibers cause the problems). The surface of nonwovens plays a role when determining the base of a drop (a place of contact between the liquid and the porous material) for subsequent measurements of width and height of the drop.
- The method is not suitable for studying liquid movement in a porous material. For that purpose two cameras would be necessary to record the drop from the side and from the top. Then both recordings have to be evaluated together.
- The method is not only suitable for studying drop volume changes, but also for studying regimes of drop penetration (according to the section 2.2.4) and contact angle changes.
- A disadvantage of the method is the need for a long lasting human work. This problem can be solved by "automatization". Parts of decision-making and measurements can be transferred to the image analyzing software which can follow the input conditions. Then the method would be less time consuming
- It is necessary to admit the possibility of mistakes due to the fact that the initial volume of all drops used during the experiments may differ. A solution for this problem is difficult to find. A micro-syringe either makes several droplets or adds to drop energy, which could affect the whole measurement. On the other hand, according to the subsection 2.3.3 studying the influence of initial drop weight to the penetration velocity, the penetration rate is not influenced if the range of drop size is chosen appropriately.

2.4. References

- [1] Adamson, A., W., Gast, A., P.: Physical Chemistry of Surfaces, A Wiley-Interscience Publication, USA, 1997, ISBN 0-471-14873-3
- [2] De Gennes, P.-G., Brochard-Wyart, F., Quéré, D.: Capillarity and Wetting Phenomena, Drops, Bubbles, Pearls, Waves, Springer, ISBN 0-387-00592-7
- [3] Myers, D.: Surfaces, Interfaces and Colloids: Principles and Application, second edition, Wiley-VCH, USA, 1999, ISBN 0-471-23499-0(Electronic), ISBN 0-471-33060-4 (Hardback)
- [4] Frohn, A., Roth, N.: Dynamics of Droplets, Springer, Germany, 2000, ISBN 3-540-65887-4
- [5] Shchukin, E., D., Pertsov, A., V., Amelina, E., A., Zelenev, A.S.: Colloid and Surface Chemistry, Elsevier, 2001, ISBN 0444500456 (Ščukin, E., D., Percov, A., V., Amelinová, E., A.: Koloïdní chemie, Academia Praha, Czech Republic, 1990 (In Czech))
- [6] Stokes, R., J., Evans, D., F.: Fundamentals of Interfacial Engineering, Wiley-VCH, USA, 1997, ISBN 0-471-18647-3
- [7] Kutlík, M.: Vlhkost pórovitých materiálů (Moisture of porous materials), SNTL, Czech Republic, 1984 (in Czech)
- [8] Bacri, L., Brochard-Wyart, F.: Droplet suction on porous media, The European Physical J. E, Vol. 3 (2000)
- [9] Lucas, R.: Über (Ueber) das Zeitgesetz des Kapillaren Aufstiegs von Flüssigkeiten (Flussigkeiten), Kolloid Zeitschrift, Vol.23, pp.15-22 (1918)
- [10] Washburn, E., W.: The Dynamics of Capillary Flow, Physical Review, Vol. 17, p.273-283 (1921)
- [11] Marmur, A.: The Radial Capillary, Journal of Colloid and Interface Science, Vol. 124, No.1, pp.301-308 (1988)
- [12] Marmur, A.: Wetting in porous media: Some theoretical and practical aspects, Contact Angle, Wettability and Adhesion, Vol. 3, pp.373-383, 2003, ISBN: 90-6764-391-2
- [13] De Gennes, P.-G., Brochard-Wyart, F., Quéré, D.: Capillarity and Wetting Phenomena, Drops, Bubbles, Pearls, Waves, Springer, ISBN 0-387-00592-7
- [14] Marmur, A.: Penetration of a Small Drop into a Capillary, Journal of Colloid and Interface Science, Vol. 122, No.1, pp. 209-219 (1988)
- [15] Marmur, A.: Capillary rise in thin porous media, Journal of Physical Chemistry, Vol. 93, pp.4873 (1989)
- [16] Danino, D., Marmur, A.: Radial Capillary Penetration into Paper: Limited and unlimited Liquid Reservoir, Journal of Colloid Interface Science, Vol.166, Issue 1. pp.245 (1994)
- [17] Kissa, E.: Capillary sorption in fibrous assemblies, Journal of Colloid Interface Science, Vol. 83, Issue 1., p. 265 (1981)
- [18] Kvasnica, J.: Mechanika (Mechanics), Academia, Prague (1988)
- [19] Borhan, A., Rungta, K., K.: An experimental Study of the Radial Penetration of Liquids in Thin Porous Substrates, *J. Colloid Interface Sci.*, Vol. 158, pp.403-411 (1993)
- [20] Chwastiak, S., Journal of Colloid and Interface Science, Vol.42, 1973
- [21] Wong, P., Z., Schäffer, E.: Experimental study of contact line dynamics by capillary rise and fall, Contact Angle, Wettability and Adhesion, Vol.3, 9925-37, Editor: K.L. Mittal, VSP BV, ISBN 90-6764-391-2, 2003
- [22] Marmur, A., Cohen, D.: Characterization of Porous Media by the Kinetics of Liquid Penetration: The Vertical Capillaries Model, Journal of Colloid and Interface Science, Vol. 189, pp. 299-304, 1997
- [23] Young, W., B.: Analysis of capillary flows in non-uniform cross-sectional capillaries, Colloids and Surfaces A: Physicochemical Engineering Aspects, Vol.234, pp. 123-128, 2004
- [24] Blake, T., D., De Coninck, J.: The influence of pore wettability on the dynamics of imbibitions and drainage, Colloids and Surfaces A: Physicochemical Engineering Aspects, Vol. 250, pp. 395-402, 2004
- [25] Martić, G., Gentner, F., Seveno, D., De Coninck, J., Blake, T., D.: The possibility of different time scales in the dynamics of pore imbibition, Journal of Colloid and Interface Science, Vol.270, pp.171-179, 2004
- [26] Tavisto, M., Kuisma, R., Pasila, A., Hautala, M.: Wetting and wicking of fiber plant straw fractions, Industrial Crops and Products, Vol. 18, pp.25-35, 2003
- [27] Schoelkopf, J., Gane, P., A., C., Ridgway, J., C., Matthews, G., P.: Practical observation of deviation from Lucas-Washburn scaling in porous media, Colloids and Surfaces A: Physicochemical and Engineering Aspects, Vol.206, pp. 445-454, 2002
- [28] Ridgway, C., J., Gane, P., A., C.: Dynamic absorption into simulated porous structures, Colloids and Surfaces A: Physicochemical and Engineering Aspects, Vol. 206, pp.217-239, 2002
- [29] Zhmud, B., V., Tiberg, F., Hallstén, K.: Dynamics of Capillary Rise, Journal of Colloid and Interface Science, Vol. 228, pp. 263-269, 2000
- [30] Danino, D., Marmur, A.: Radial Capillary Penetration into Paper: Limited and Unlimited Liquid Reservoirs, Journal of Colloid and Interface Science, Vol. 166, pp.245-250, 1994
- [31] Hsu, N., Ashgriz, N.: Nonlinear penetration of liquid drops into radial capillaries, Journal of Colloid and Interface Science, Vol. 270, pp.146-162, 2004
- [32] Borhan, A., Rungta, K., K.: An Experimental Study of the Radial Penetration of Liquids in Thin Porous Substrates, Journal of Colloid and Interface Science, Vol. 158, pp. 403-411, 1993
- [33] Krüss GmbH, K121 Contact Angle and Adsorption Measuring System – User Manual, version 2.1, Hamburg 1996
- [34] Shaw, D. J.: Introduction to colloid and surface chemistry. Butterworths, London 1980, s. 241.
- [35] Brochard-Wyart, F., de Gennes, P., G.: Dynamics of Partial Wetting, Advances in Colloid and Interface Science; Vol. 39, pp. 1-11, 1992

- [36] Aradian, A., Raphaël, R., de Gennes, P., G.: Dewetting on porous media with aspiration, *The European Physical Journal E*, Vol. 2, pp. 367-376, 2000
- [37] Alleborn, N., Raszillier, H.: Spreading and sorption of a droplet on a porous substrate, *Chemical Engineering Science*, Vol. 59, pp. 2071-2088, 2004
- [38] Marmur, A., Cohen, R., D.: Characterization of Porous Media by the Kinetics of Liquid Penetration: The Vertical Capillaries Model, *Journal of Colloid and Interface Science*, Vol. 189, pp. 299-304, 1997
- [39] Hapgood, K., P., Litster, J., D., Biggs, S., R., Howes, T.: Drop Penetration into Porous Powder Beds, *Journal of Colloid and Interface Science*, Vol. 253, pp. 353-366, 2002
- [40] Bodurtha, P., A., Matthews, G., P., Kettle, J., P., Roy, I., M.: Influence of anisotropy on the dynamic wetting and permeation of paper coatings, *Journal of Colloid and Interface Science*, Vol. 283, pp. 171-189, 2005
- [41] Lewandowski, M., Perwuelz, A., Vroman, P.: Influence of porosity on capillary flow in textiles, 3rd Autex Conference, 2003
- [42] Bazilevsky, A., V., Kornev, K., G., Rozhkov, A., N., Neimark, A., V.: Spontaneous absorption of viscous and viscoelastic fluids by capillaries and porous substrates, *Journal of Colloid and Interface Science*, Vol. 262, pp. 16-24, 2003
- [43] Denesuk, M., Smith, G., L., Zelinski, B., J., J., Kreidl, N., J., Uhlmann, D., R.: Capillary Penetration of Liquid Droplets into Porous Materials, *Journal of Colloid and Interface Science*, Vol. 158, pp. 114-120, 1993
- [44] Starov, V., M., Zhdanov, S., A., Kosvintsev, S., R., Sobolev, V., D., Velarde, M., G.: Spreading of liquid drops over porous substrates, *Advances in Colloid and Interface Science*, Vol. 104, pp. 123-158
- [45] Huang, Y., Lieu, L., Qiu, J., Shao, L.: Influence of ultrasonic treatment on the characteristic of epoxy resin and their interfacial property of its carbon fibers composites, *Composites Science and Technology*, Vol. 62, Issue 16, pp. 2153-2159, 2002.
- [46] Torres, S., Novak, O., Lukas, D.: Effect of ultrasound on the viscosity and surface tension of PET and epoxy resins, 12th International Conference – STRUTEX 2005, TU in Liberec-Czech Republic, pp. 249-254.
- [47] Moholkar, V.S., Warmoeskerken, M.M.C.G.: Investigations in Mass transfer enhancement in textiles with ultrasound, *Chemical Engineering Science*, Vol. 59, Issue 2, pp. 299-311, January 2004.
- [48] Moholkar, V.S., Warmoeskerken, M.M.C.G.: Mechanical aspects and optimization of ultrasonic washing, *AATCC Review*, Vol. 2, Issue 2, 2002.
- [49] Jirsak, O., Wadsworth, L., C.: *Nonwoven textiles*, Carolina Academic Press (Durham, NC), 1999, ISBN 0890899878
- [50] Vohlídal, J., Julák, A., Štulík, K.: *Chemické a analytické tabulky (Chemical and analytical tables)*, Grada Publishing, ISBN 80-7169-855-5
- [51] Košťáková, E.: Spherical Drop's Penetration into Needle-Punched Nonwovens, 4th Autex World Textile Conference, Roubaix – France, 2004, ISBN 2-9522440-0-6
- [52] Pan, N., Gibson, P.: *Thermal and moisture transport in fibrous materials*, Woodhead Publishing Limited, Cambridge, pp. 469-541. ISBN-13: 978-1-84569-057-1.

3. Simulation

This part of the work is devoted to auto-model simulations. The models are based on so called modified Ising models and Monte Carlo method. Ising model is one of the auto-models for the modeling of real physical systems. These models are used mainly for simulation of wetting phenomena here. Ising model originally described a behavior of a group of elementary magnets with respect to external magnetic field value [2, 3]. Other applications of Ising model are in ecology, chemistry, cybernetics and modeling of images and textures. The models described and used in the thesis are strictly oriented towards computer simulations of selected transport wetting phenomena in connection with porous solid structure as model structure of radial capillary, cylindrical capillary and nonwoven-like structures.

Simulation's principles, potentialities and limits are described below. There are also notes about usage of this kind of simulations in relation to wetting dynamics. These computer models, their historical progress, basic principles, complete statistical-physical explanation and of course simulation examples are detailed in the monograph [1], written by Lukáš and Košťáková. Other particular information from detailed literature review and simulations outgoing from the same basics can found in thesis [4] and of course in several publications of the real "discoverer" of these computer simulations based on automodels (or modified Ising models) for the textiles and fibrous materials wetting description [5-9].

3.1. Basic Terms and Legalities of Simulation Model

The used computer simulations are based on *three-dimensional auto-models* (concretely *modified 3D Ising model*, as the model is called by some authors) with Kawasaki Monte Carlo kinetics. All these titles are briefly described bellow. More details are introduced in [1].

Automodels

The title „auto model“ represents the same theoretical background of many particular models. These particular models are usually used for real physical systems modeling. Apparently, the most used automodel in physics is the Ising model.

Ising model

The Ising model was introduced by Ising [2]. He used it for an explanation of fero-para magnetic transition, see [1]. A periodic lattice of cells with elementary magnets is the base of the model. These elementary magnets are represented by arrows with either up or down orientation, as it is visible in Fig.3.1. The model assumes that each magnet is sensitive only to the orientation of nearest neighboring magnets. So each lattice cell is defined by random variables (also known as the Ising variables) of values +1 and -1 corresponding to orientation of elementary magnets. Thermal fluctuations in the original Ising model are represented by random and subsequent flipping of magnets to new orientation in discrete steps. The new local configuration of an elementary magnet in a cell is then determined by comparison of the values of so called local conditional probabilities. The local conditional probability relates to a new orientation of the magnet in question. The local conditional probabilities depend on the sum of the interaction energies between the elementary magnet and its closest neighborhood and of course on the temperature. The lower the interaction energy of a configuration, the higher is the probability of its occurrence. Temperature also influences these transitional probabilities of magnet flipping. Increase of temperature means an increase of the occurrence of probability with higher interaction energy. The neighborhood can be changed according to the requests. The classical two-dimensional Ising model neighborhood, as it was introduced by Ising, consists of four cells (see Fig.3.1a) and is usually called as von Neumann neighborhood. Although later the Ising model was modified and interactions are assumed also among the nine elementary magnets, as it is illustrated in Fig.3.1b, and named Moore neighborhood.

The Ising model can be also used with various cell contents (liquid, fiber or gas for example). The particular simulation devoted to fiber wetting is described bellow in the chapter 3.2. There is consider also other modification of Ising model and it is a three-dimensional model, where the closest neighborhood consists of twenty-six cells.

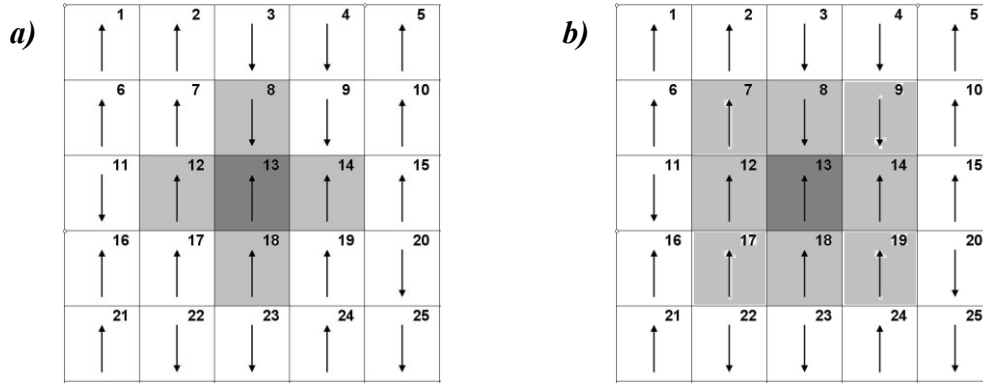


Fig.3.1: Two-dimensional Ising model lattice of cells. The lattice consists of 25 cells. Each of them contains an elementary magnet. The up magnet orientation \uparrow is assigned the value +1 of the random variable while the down orientation \downarrow is coded as -1. Each cell in the Ising model interacts only with its nearest neighbors. There can be used different types of neighborhoods: a) Classical Ising model, where the particular cell s_{13} neighborhood consists of four cells $\{s_8, s_{12}, s_{14}, s_{18}\}$; b) The modified Ising model where the neighborhood of the cell s_{13} consists of eight cells $\{s_7, s_8, s_9, s_{12}, s_{14}, s_{17}, s_{18}, s_{19}, \}$.

Kawasaki kinetics

Kawasaki kinetics relates to a cell selection for Ising variable exchange during a temporal development of a system. There are two types of Kawasaki kinetics. Kawasaki kinetics for short distances represents an exchange of cells, which are mutual neighbors. The first cell is chosen at random and the second one is chosen also randomly but only from the neighborhood of the first cell. Kawasaki kinetics for long distances allows exchange of cells which are not necessarily neighbors (see Fig.3.2).

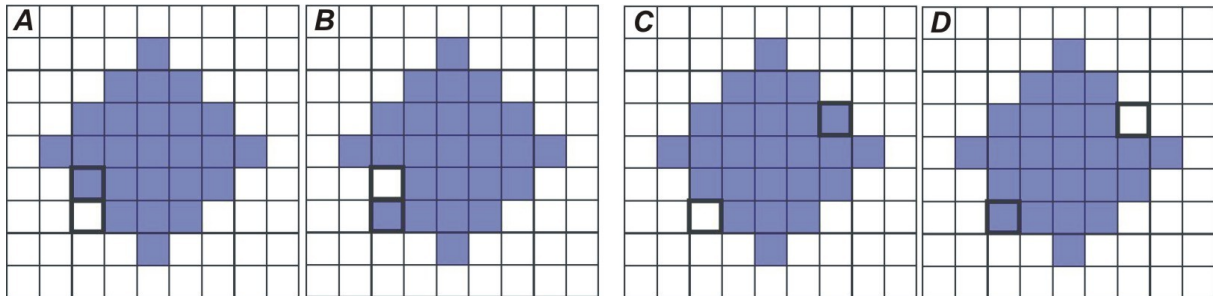


Fig.3.2: Two-dimensional lattice system with two different types of cell's selection from liquid-gas interface: A and B represent Kawasaki dynamics for short distances; C and D represents Kawasaki dynamics for long distance. Pictures A and C show the system before cell exchange and pictures B and D show the system after cell exchange.

Total energy of a system/Hamiltonian

The modeling system is characterized by its total energy/Hamiltonian H according to principles of statistical physics at every single state or time. The total energy is composed of energies from intermolecular interactions and interactions with external field, as the gravity one.

Energy E_i of every elementary cubic cell i is composed of two terms, as it is written in expression (3.1).

$$E_i = C_g z_i + \sum_{j=1}^{N_j} C_{ij} \quad (3.1)$$

Where C_g is gravitational constant ($m \cdot g$), z_i is a position of i cell at z axes, and C_{ij} represent exchange energies between cell i and cells j in the neighborhood of i -cell. In all presenting simulations, there is taken into consideration only the closest neighborhood. The closest neighborhood means the closest $N_j = 26$ cells in the three-dimensional simulation box as it is illustrated in Fig.3.3.

The expression of total energy/Hamiltonian H introduced as the equation (3.2) of the all system is the sum of all elementary energies E_i .

$$H = \sum_{i=1}^N E_i = C_g \sum_{i=1}^N z_i + \sum_{i=1}^N \sum_{j=1, i \neq j}^{N_j} C_{ij} \quad (3.2)$$

There is necessary to underline that the gravitational energy is calculated only for the liquid cells.

Total system energies difference of two configurations ΔH is calculated during the simulation. Thus, there is obvious that calculation of two chosen cells (one liquid and one gas cell) energies difference before and after their exchange is sufficient, because except these two cells the complete system is still in the same state.

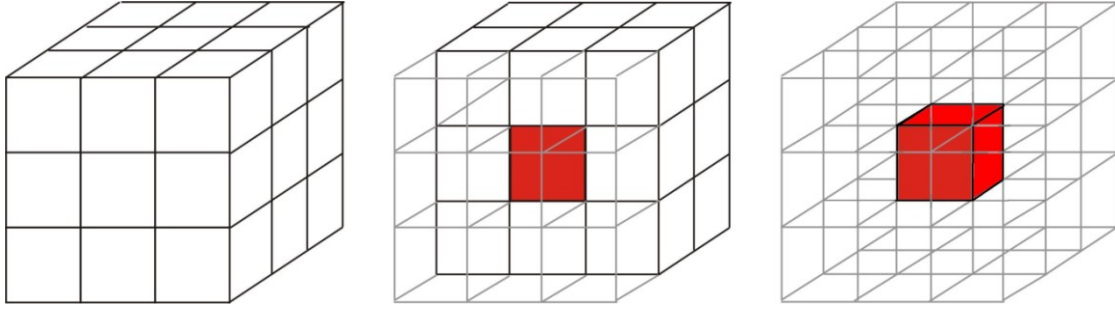


Fig.3.3: A red cell i in the center of its neighborhood consisting of 26 cubic cells.

Monte Carlo method

The Monte Carlo method is used in many applications. As it was described in the thesis [4], the method was applied for simulation of wetting, wicking and other liquid transport phenomena in fibrous assemblies due to its ability to simulate processes in statistical mechanics.

The Monte Carlo method is represented by a family of algorithms for systems simulations. It is based on using random numbers. The method Monte Carlo is based on carrying out random experiments with a model system and their evaluations. The method utilizes generators of pseudorandom numbers.

The Monte Carlo method is used for decision-making at changes of system configuration (corresponding with thermal fluctuation in the system) and random sampling according Kawasaki kinetics conditions in the presenting models in experimental part of the thesis.

Metropolis algorithm

Monte Carlo dynamics of special systems is described by Binder [12]. There is also mentioned a heuristic proof there, which shows that so called Metropolis algorithm, the simulation system described below, always reaches an area of its equilibrium probabilistic distribution. There are also described various kinds of dynamic utilized for simulations by Monte Carlo methods.

The Monte Carlo simulation of the Metropolis algorithm proceeds in following steps: i) setting of simulated system initial state; ii) change of initial system setting; iii) the energy difference ΔH of the initial and the changed system calculation; iv) if the difference ΔH is negative, the process continues with the new changed situation, otherwise adopt the changed state only with a certain probability described in Boltzman factor paragraph below.

Boltzman factor

A probability $P(\vec{x})$ of a certain system configuration \vec{x} is generally given by equation (4.3) known as the Boltzman Equation.

$$P(\vec{x}) = \frac{1}{Z} \exp\left(-\frac{H(\vec{x})}{\tau}\right), \quad (3.3)$$

* Pseudorandom numbers are numbers creating a succession, which appears to be random, but in reality these numbers are generated by deterministic algorithm. The prefix pseudo- is used for separation this type of random numbers from "real random" numbers, which rising as a random physical processes results. This thesis used the word "random" but with the "pseudorandom" meaning.

where Z is a partition function of the system, τ is statistical temperature and $H(\vec{x})$ is Hamiltonian of the certain system configuration \vec{x} . The Boltzman factor $\exp[-H(\vec{x})/\tau]$ can be derived on principles of statistical thermodynamics with contemplation on so called Canonic system (isolated system composed from two subsystems called system and reservoir, which interchange energy only). The detailed derivation of the Boltzman factor can be found in Binder's work [12]. The following text proves the Metropolis algorithm validity. It is based on expressions of basic statistical properties of the studied system. They are mainly occurrence probabilities of the system in configurations, which are proportional to a number of admissible configurations of reservoir (which has to be still in our consideration connected with the studied system). This calculation of the number of admissible configurations of reservoir is very complicated, thus there is better to work with comparison of two probabilities corresponding with the system occurrence in two configuration characterized by number of elements and total energy/Hamiltonian. If the number of elements does not change, then the system is characterized only by its total energy. Equation (3.4) describes a comparison of probabilities $P(x)$ and $P(y)$ of the system in configurations \vec{x} and \vec{y} . The following equation is a simple consequence of equation (3.3), because the partition function Z is constant for a given system and temperature.

$$\frac{P(\vec{x})}{P(\vec{y})} = \frac{\exp\left(-\frac{H(\vec{x})}{\tau}\right)}{\exp\left(-\frac{H(\vec{y})}{\tau}\right)} \quad (3.4)$$

Where the term $\exp(-H(\vec{x})/\tau)$ is known as Boltzman factor.

Now there is necessary to introduce transition probability $W(\vec{x} \rightarrow \vec{y})$ from the state configuration \vec{x} and state configuration \vec{y} , which is based on Boltzman factor and is used in the simulation models used in the present thesis. The simulation is based on Markov chains. Markov chains are based on fact that the simulations consist of consecutive steps / chains of configurations. These steps are represented by configurations of the system. It means that a configuration \vec{y} is reformed from a previous configuration \vec{x} with suitable transition probability $W(\vec{x} \rightarrow \vec{y})$. The process results to an equilibrium configuration distribution. When two successive configuration \vec{x} and \vec{y} are taken into consideration, a jump from \vec{x} to \vec{y} is characterized with a probability $P(\vec{x} \rightarrow \vec{y}) = P(\vec{x})W(\vec{x} \rightarrow \vec{y})$ and those in the reverse direction have a probability $P(\vec{y} \rightarrow \vec{x}) = P(\vec{y})W(\vec{y} \rightarrow \vec{x})$. The principal of so called detailed balance claims, that these transition probabilities are equal in equilibrium state.

$$P_{eq}(\vec{x})W(\vec{x} \rightarrow \vec{y}) = P_{eq}(\vec{y})W(\vec{y} \rightarrow \vec{x}) \quad (3.5)$$

Then there is obvious from equation (3.5) and equation (3.3) that the probability of transition P_{TR} depends only on the energy difference $\Delta H = H(\vec{y}) - H(\vec{x})$ of \vec{x} and \vec{y} states and can be written as

$$P_{TR} = \frac{P_{eq}(\vec{x})}{P_{eq}(\vec{y})} = \frac{W(\vec{y} \rightarrow \vec{x})}{W(\vec{x} \rightarrow \vec{y})} = \exp\left(-\frac{\Delta H}{\tau}\right). \quad (3.6)$$

In simulations which are used in this thesis, there are only two distinguished situations with regard to energy change ΔH , as it is shown in (3.7) and in Fig.3.4.

$$\begin{aligned} P_{TR} &= 1 & \text{if } \Delta H < 0 \\ P_{TR} &= \exp[-\Delta H/\tau] & \text{if } \Delta H \geq 0 \end{aligned} \quad (3.7)$$

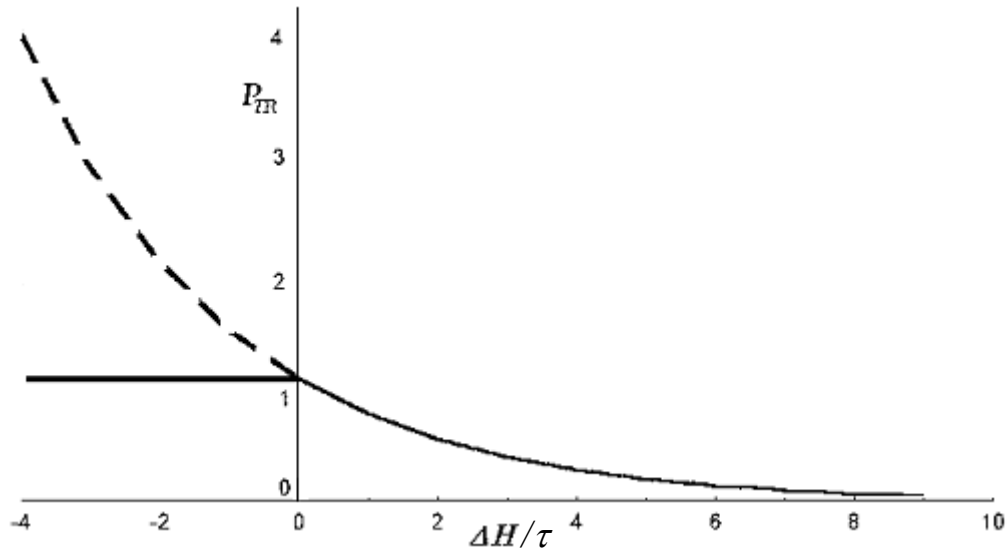


Fig.3.4: Transition probability P_{TR} dependence on energy change $\Delta H/\tau$ (dimensionless quantity).

The detailed principle of a decision making, in case of $\Delta H > 0$, in the simulation used in the thesis, is described in the next chapter. The situation, where $\Delta H > 0$, can in the simulation occur when the system works with certain temperature, thus $T \neq 0$. From physical point of view, the situation can be explained by thermal fluctuations existing. There is necessary to realized that the system is still in contact with the reservoir, even if the reservoir is not at these simulations perceptible. It is always necessary take into consideration its presence. The presence of reservoir is expressed by statistical temperature τ in presenting simulations. There is possible to explain the thermal fluctuations by means of a energy delivery from the reservoir to the system.

These simulations are obviously very suitable for the prediction of equilibrium states of systems, but the dynamic interpretation of the results raises the question. Attempting to describe the dynamics in simulations using the Monte Carlo method is except Binder monograph [12] also described in a publication written by team of Ivo Nezbeda at Charles University [14]. If taken into account only the simulation dedicated to the wetting of solids, where it is clear that the simulation of equilibrium states surely works well with this simulation procedure [5-8], but there is necessary to note that the similarity of the dynamics of wetting in the simulation and the reality has its restrictions. These restrictions are based on the nature of the algorithm used in the simulations, which is based only on the interaction energies and gravitational energy. From the study of the simulation models, it is possible to say that the dynamics will be similar to the more realistic model, the larger will have on her ability to influence forces resulting from surface tension thus capillary forces. The question remains for which models or the real situations in the wetting of fibrous materials are the dominant influence of capillary forces.

And just following part of the thesis is devoted not only to simulation of equilibrium states of systems (model systems and also systems similar to fibrous material wetted by liquid) but also to problems in the simulation of wetting dynamic using automodels and Monte Carlo methods for model systems (model of radial capillary, cylindrical capillary embedded in the liquid).

3.2. Auto Model Used Computer Simulation of Wetting

Simulation starts with a creating of three-dimensional simulation box, which is composed from finite number of elementary cubic cells. These cells are assigned with indexes according Cartesian system of coordinates. A lattice variable (so called Ising parameter), which represents different physical meaning of cell's content or more precisely different medium (liquid, gas, solid material), is assigned to each cell. A model of "liquid-fibrous material" is in initial configuration that mimics the real system at the beginning of liquid penetration into fibrous system. The system is in initial configuration energetically unstable. Thus over time a liquid transport into the fibrous system happened with the aim of finding an equilibrium state with the lowest total energy or more precisely with the aim of finding the most probable configuration (if the statistical temperature τ is not zero, then the equilibrium state is not the state with the lowest energy; concept of thermal contact between the system and reservoir). The system is heading towards equilibrium probability distribution of states/configurations. Configuration exchanges, therefore the transport of liquid, are achieved through changes of the positions of liquid cells with the gas containing cells. If evaporation is not considered, then the liquid retains its volume. It means there is constant number of cells liquid. Selecting and later moving are the cells from the liquid-gas interface only, what ensures that cells containing the liquid are not separated from each other.

Wetting process is modeled by Monte Carlo method, which is based on Kawasaki dynamics for long distances exchange as it was mention above. A liquid movement is caused by exchanges of cells, which contain liquid and gas, in the 3D lattice. The simulation runs in repeating steps and a structure of one step (which is called in this type of simulation Monte Carlo Step – MCS) consists of following operations:

- 1) A random chose of two different cells (one containing liquid and the last containing gas) from liquid-gas interface.
- 2) Total energy of the system is calculated according equation (3.2)
- 3) Positions of cells are exchanged
- 4) Total energy of the system is calculated again
- 5) Difference between total system energy before and after cells exchange is calculated
- 6) If the energy after the exchange is lower than the energy before exchange, cells will stay in their new positions and the next step starts. However, if the energy after the exchange is greater than the energy before the exchange, the decision-making process is more complicated. Firstly, there is necessary to decided about the size of temperature in the Ising model. If the temperature is zero, and if the energy after the exchange is higher than the energy before exchange, cells will return to their initial positions and the simulation continues from the first step. If the temperature is different from zero there is necessary to calculate so called transition probability (3.6) using Boltzman law described above. If the calculated probability is higher than randomly generating number from interval (0; 1), the exchange is accepted. However if the calculated probability is lower than the randomly generating number, the exchange is not accepted and cells are returned to their initial positions. The program goes again to the initial point of the simulation.

The next MCS starts the same process from another randomly chosen pair of cells. The simulation process is finished when the system achieves the equilibrium state. The energy of the system in equilibrium varies around a constant and minimal value. The simulation is also stopped when the number of MCS initially written to the particular simulation program is reacted.

3.3. Computer Simulation Outputs

Automodels (modified Ising model), Monte Carlo method and Kawasaki kinetics for long distance exchanges were used for simulations described in the following chapter. The simulation programs are written in program language C++ in software Borland C++ and Turbo C. There is possible to record data from the simulation at the end of it or after a selected MCS several times during simulation. There is possible to find also graphical outputs. The easiest and usually sufficient is two-dimensional representation of the three-dimensional simulation box by cross sections with different orientation and location. The illustration of the most used visualization of this type is introduced in Fig.3.5. Examples of these graphical outputs are in Fig.3.6. However, the simulation system is three-dimensional, but three-dimensional visualization of the system is very complicated. There is possible to use so-called orthographic camera projection. Then the final graphical result, created from data from the above described simulation by means of standard Python language used inside software Blender, can be as it is shown in Fig.3.7. The 3D visualization is very complicated process; this is why these examples were done in cooperation with R. Charvát from the Atelier of Virtual Reality Technical University of Liberec [15].

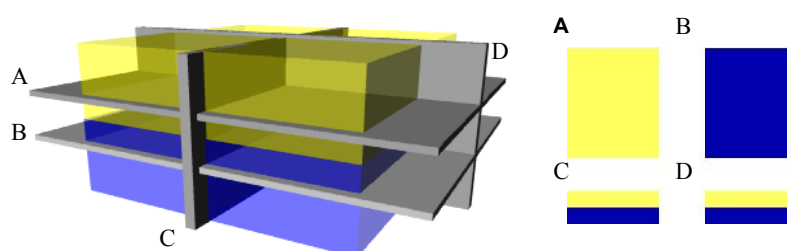


Fig.3.5: Four two-dimensional graphical outputs as cross-sections (A-D) on the right side from three-dimensional simulation model of gas (yellow) above a liquid reservoir (blue) on the left side.

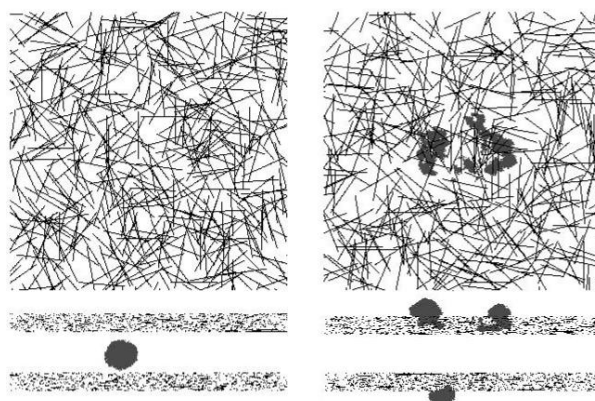


Fig.3.6: Graphical output from simulation of a liquid droplet in contact with nonwoven material with random orientation of fibers with two different liquid-fiber surface characteristics. Left side represents extremely high contact angle while right side represents process of droplet penetration into nonwoven material with lower contact angle.

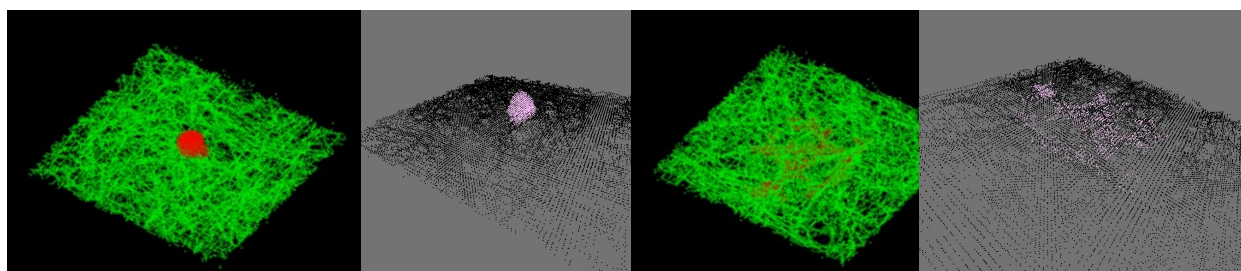


Fig.3.7: Three-dimensional graphical output from simulation representing droplet of liquid in contact with nonwoven material with random orientation of fibers at the beginning of penetration process and at the end of it. The graphical outputs were presented in [15].

The simulations were carried out with following variable values:

- a) *time* – Time is representing by Monte Carlo Steps. There is possible to set the number of MCS required for termination of the simulation process. The unit of time used in Monte Carlo dynamics is the Monte Carlo step per site (MCSPS), which corresponds approximately to one exchange trial for each cell in the simulation box.
- b) *temperature* – Temperature is representing by statistical temperature τ , which is known as arithmetic product of thermodynamic temperature and Boltzman constant. There is empirically known from the behavior of liquids in the simulation [4] that statistical temperature in these simulation should be about $\tau=30$. More about influence of various temperatures is written in the first part of chapter 3.3.1.
- c) *gravitation* - Gravitational constant C_g set up according to definition of potential energy of a body in gravitational field. The potential energy is arithmetic product of the body mass, gravitational acceleration and the high of the body location in the gravitational field. In the gravitational part of equation (3.1) is the high represented by the vertical z-coordinate of the cell, and the cell has unit volume and unit mass. Thus the constant C_g is equivalent to the value of gravitational acceleration $g=9,81 \text{ ms}^{-1}$. For the simulation, where the gravitation is required, the value of gravitational constant C_g is set to value 10.
- d) *contact angle* – Contact angles are important characteristics for liquid behavior in relation to solid surfaces. The contact angle setting in the simulation is based on calculation of values for surface tensions or surface energies (interaction energy) for all three couples of phases γ_{fl} , γ_{gl} and γ_{gf} , where *f* means fiber, *l* is liquid and *g* is gas, described in detail in [1]

$$\gamma_{fl} = \frac{2C_{fl} - C_{ll} - C_{ff}}{2} \quad \gamma_{gl} = \frac{2C_{gl} - C_{ll} - C_{gg}}{2} \quad \gamma_{gf} = \frac{2C_{fg} - C_{gg} - C_{ff}}{2} \quad (3.8)$$

and according to Young and Dupre equations [12] there is possible to find a value of contact

$$\cos \theta = \frac{\gamma_{gf} - \gamma_{fl}}{\gamma_{gl}}. \quad (3.9)$$

The equations above are valid for $\tau=0$.

The simulation system has the lattice unit (l.u.) as a natural length unit of a three-dimensional lattice, i.e. simulation box, which is equal to the distance between the neighboring cells. Other quantities (τ ; H ; C ; γ) are described and used in the chapter without units. Although there is necessary to supposed that their units are so called energy units (e.u.).

All simulations presented here are written in Borland C and Turbo C by simulation language C++. . An example of written simulation program, devoted to the liquid gas interface simulation in various temperature described in the subsection 3.3.1., is in Appendix VII. The used software and hardware give of course some limits (for example rate of the simulation and size of the simulation box). The most important limitation is the limitation of the simulation box size. The biggest box which can be simulated is $300 \times 300 \times 300$ l.u

3.3.1. Equilibrium States Computer Simulation

The chapter describes several computer simulations based on Auto model (Ising model) and Monte Carlo method important for better understanding of these models force and limit. All these simulations lead to equilibrium states. The simulation dynamics is not studied.

Liquid-gas interface at various temperatures

The first part of the simulation introduction is devoted to finding a certain statistical temperature τ and of course its thermodynamically equivalent temperature, by behavior observation during and at the end of simulation process. There is necessary to know a behavior of the real system in the particular thermodynamic temperature, which should be set up in the simulation system. In the particular case, there is presented finding of critical statistical temperature (thermodynamically temperature of liquid boiling). The simulation model finding the liquid density distribution $\rho(z)$ depending on the vertical coordinate z is used for this case.

Detailed information about the characteristics of interphase for better understanding can be found in [4, 16-18]. The simulation box had $100 \times 100 \times 30$ l.u.. The upper half of the box was fulfilled by gas and bottom half was filled by liquid. The gravitational constant was equal to zero. Interaction constants were set up as: $C_{ll} = -30$; $C_{gg} = -40$; $C_{gl} = -1$. The value of MCSPS was 100.

The problem with setting up of the particular temperature (temperature of boiling – critical temperature*) can be solved by a simulation series, where the density or better number of liquid cells changing along the z axis in horizontal level of simulating box is monitored. There was changed the statistical temperature τ of the system for each set of simulations. When the density of liquid along the z axis is constant at the end of the simulation process after the suitable long time (suitable number of MCSPS), there is possible to say, the temperature of evaporation of the simulating system was found. Thus liquid cells are homogeneously distributed in all simulating box at the end of simulation process with suitable number of MCSPS. There were evaluated numbers of liquid cells in each layer $N(z)$ depending on its height – its coordinate z . The resulting graph is introduced in Fig.3.8.

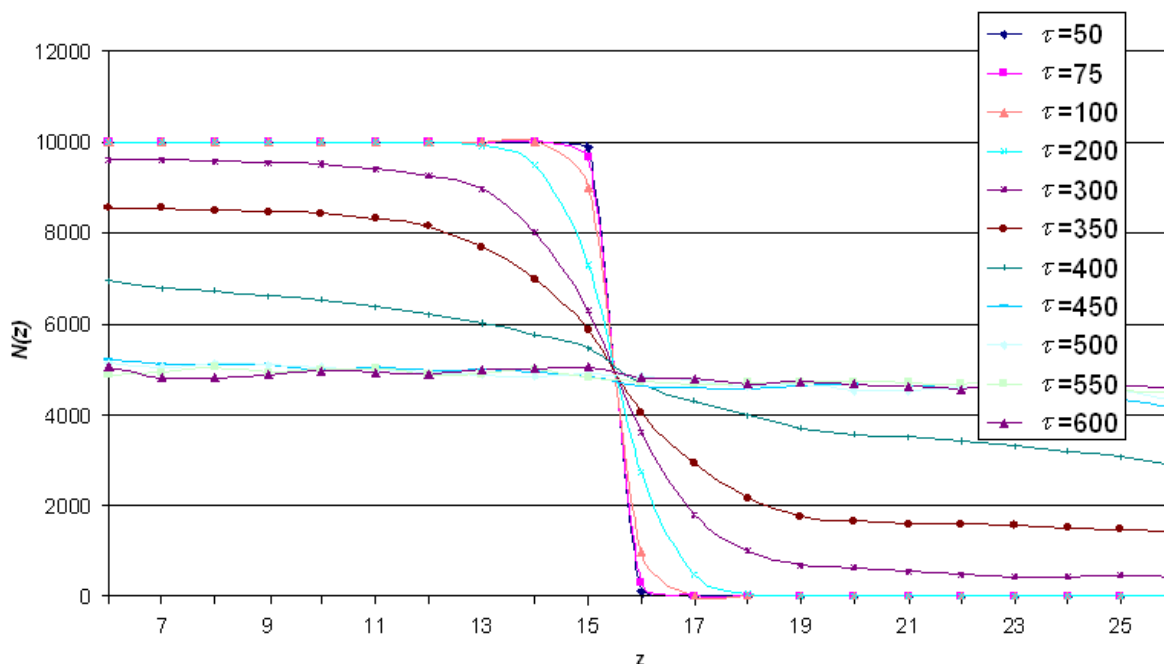


Fig.3.8: Numbers of liquid cells in each layer $N(z)$ depending on its height – its coordinate z .

The temperature is the critical temperature, when difference between liquid and gaseous phases disappears at suitable long time (suitable MCSPS). For these simulations was statistical temperature $\tau = 450$. The surface tension is given by an increase in free (Helmholz) energy [18] at the interface. The calculation procedure is drawn in Fig.3.9. However, positioning the dividing plane is not

* Surface tension decreases with the increase of temperature, reaching a value of 0 at the critical temperature. The critical temperature of a liquid is the temperature at which the liquid transforms completely to vapor/gas.

trivial. Thus the simpler method for the critical temperature finding was used as it is visible in Fig.3.10. The critical temperature is $\tau_c = 438$ e.u. for these types of simulation with variables described above.

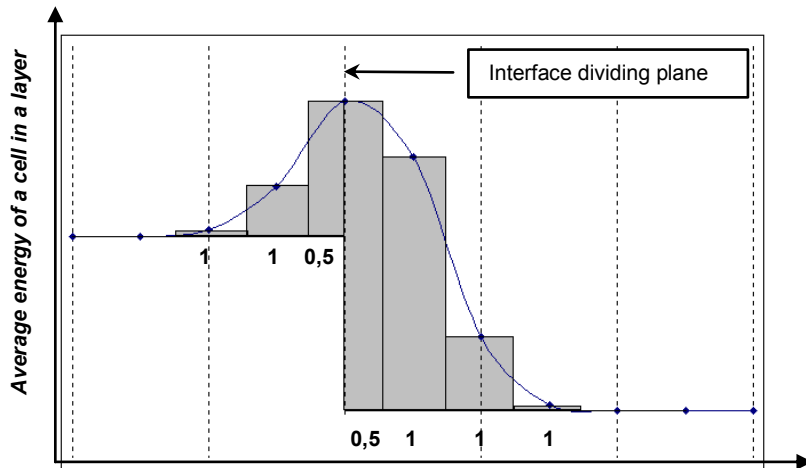


Fig. 3.9: Calculation of surface tension as a density excess of Helmholtz surface energy at liquid-gas interface. The sum of grey areas is the surface tension.

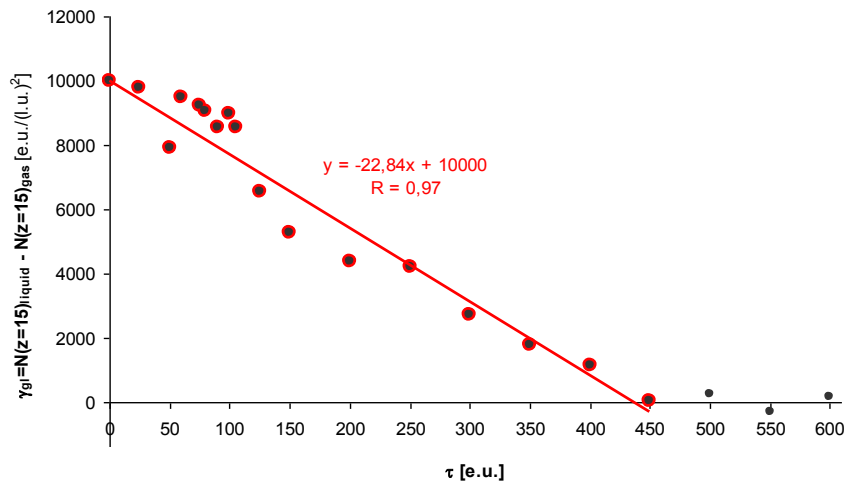


Fig.3.10: Graph of surface tension γ_{gl} calculated as the excess of Helmholtz energy at gas-liquid interface from simulations with different τ values. The liquid level was in $z=15$. The total number of cells in one layer in the simulating box is 10 000. The red line is regression function for red signed data (from $\tau=0$ to $\tau=450$).

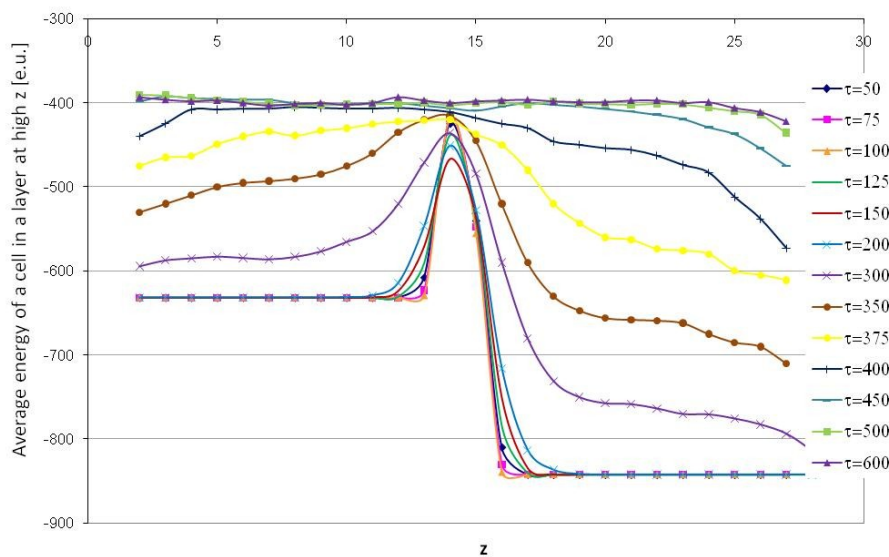


Fig.3.11: Graph of the average energy per one cell in a layer, depending on the coordinate z .

The total energy of system is increasing during the simulation because the system was at the lowest energy at the initial configuration (see Fig.3.12). Several graphical outputs from these series of experiments are presented in Fig.3.13. There is visualization of initial state, the same for all these simulations, and other simulation box cuts showing final equilibrium configurations at the end of simulation process.

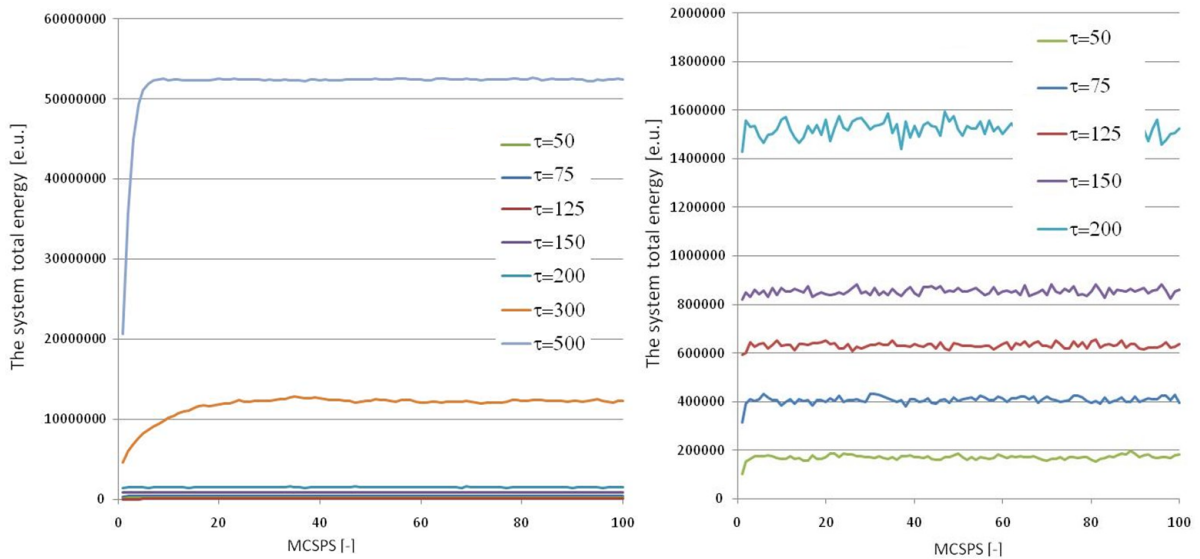


Fig.3.12: The total energy of system developing during simulation (increasing MCSPS). The detailed visualization for simulations to $\tau=200$ is on the right side.

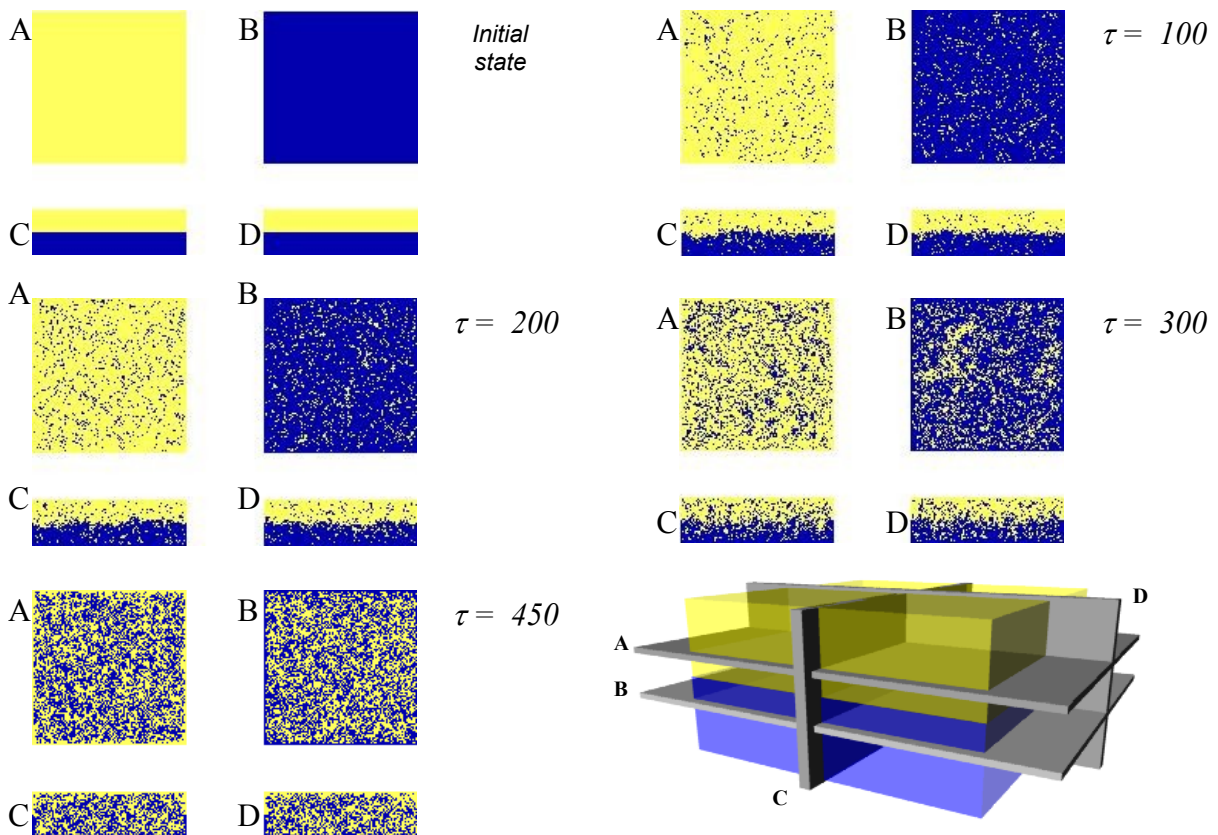


Fig.3.13: Graphical out puts from simulations introducing the system behavior at various statistical temperature after 100 MCSPS and illustration introducing these four different cuts of the simulating box.

By this approach there is possible to approximately find statistical temperature in the simulations corresponding with real thermodynamic temperature for simulation other phenomenon. For additional simulations introduced in this thesis the statistical temperature $\tau = 30$ is used as a thermodynamic temperature corresponding with temperature about $T=10^{\circ}\text{C}$ according Fig.3.10 in the subsection 3.3.1.

Drops on a flat substrate

Next simulation is devoted to spherical drop falling on a substrate at various surface tensions (interaction energies or contact angles). The main aim of the simulation was to show, that contact angles calculated from a set of interaction energies corresponds with contact angles measured at graphical outputs from simulations. There is necessary to note, that the large study comparing real data from measuring of contact angle of different types of drops liquid and results from such kind of simulations was detail described in [4].

The initial state of the simulation is shown at Fig.3.14. The simulation box had $90 \times 90 \times 70$ l.u.. The diameter of liquid sphere in initial configuration is $rk = 20$ l.u.. The liquid sphere is placed above the solid substrate at height $h = 56$ l.u.. MCSPS was 10. The gravitational constant was $C_g = 10$. Statistical temperature corresponds to normal laboratory conditions $\tau = 30$. The interaction constants for final various contact angles θ [°] in the simulations are introduced in Table 3.1. Each simulation was repeated ten times. The resulted values of total system energy are average values from these simulations.

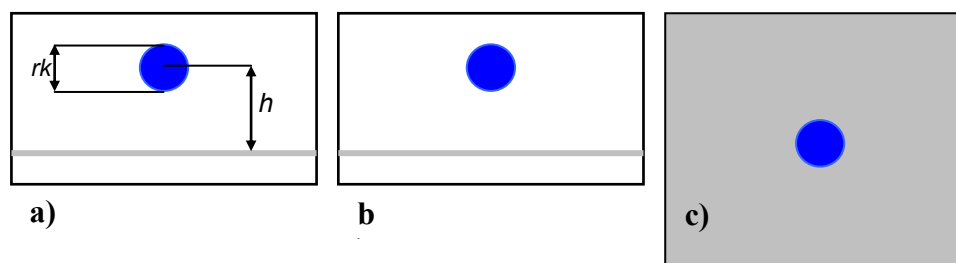


Fig.3.14: Initial state of the simulation box. Projection of the system a) parallel to the xz plane; b) parallel to the yz plane; c) parallel to the xy plane. White color represent gas, blue color represents liquid and gray color represents solid substrate.

Table 3.1: The interaction energies, calculated surface tensions and contact angles according (3.8) and (3.9).

simulation	C_{fl}	C_{ll}	C_{gf}	C_{gg}	C_{gl}	C_{ff}	$\cos\theta$	$\gamma(fl)$	$\gamma(fg)$	$\gamma(lg)$	θ [°]
A	3	-24	21	12	4	0	0	15	15	10	90
B	2	-24	21	12	4	0	0,1	14	15	10	84,3
C	1	-24	21	12	4	0	0,2	13	15	10	78,4
D	0	-24	21	12	4	0	0,3	12	15	10	72,5
E	-1	-24	21	12	4	0	0,4	11	15	10	66,4
F	-2	-24	21	12	4	0	0,5	10	15	10	60
G	-3	-24	21	12	4	0	0,6	9	15	10	53
H	-4	-24	21	12	4	0	0,7	8	15	10	45,6
I	-5	-24	21	12	4	0	0,8	7	15	10	36,9
J	-6	-24	21	12	4	0	0,9	6	15	10	25,8
K	-7	-24	21	12	4	0	1	5	15	10	0

The total energy of system was decreasing with time (MCSPS) for all simulations, as it is visible in Fig.3.15. There is interesting that each of these graphs is possible to divide into three parts. The first part, a slight decrease of total system energy, obviously corresponds to drop falling on the substrate. The second part, steep decrease of total system energy, belongs to the liquid body transformation into the most convenient arrangement. The third part, almost constant, presents a system balance achieve (slight variations are caused by fluctuations of the system).

There is possible to find in summary graph Fig.3.15, that equilibrium energy is higher for systems with higher contact angle. It seems that energy equilibrium achievement does not relate to contact angle of the system. Selected graphical outputs in Fig.3.16 show that the simulation works according requirements and presumptions, so linear decreasing of contact angle during simulations is visible. Contact angle, diameter and droplet in contact with solid substrate at the end of simulation measured by image analysis in dependence of contact angle calculating from interaction constant as it is shown in Tab. 3.1 are visible in Fig.3.17. As shown in [4] and also here, this kind simulation works without

problems. Equilibrium states correspond to real situations when appropriate values (C_{ij} , τ , C_g) are entered into the simulation. Linear droplet height decreasing and linear increasing of droplet base is evident from these measured data. However the measured values are smaller than calculating values from used interaction constants. Proper measurement of contact angles would require a much larger simulation box and a larger drop inside it, for decreasing influence of significant raster of output image to image analysis measurement.

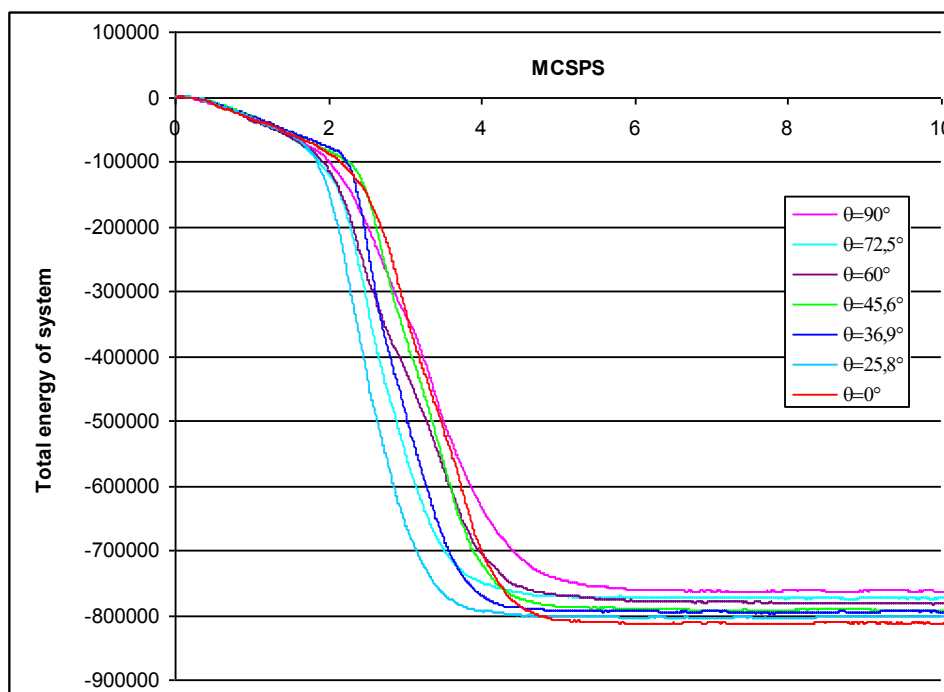


Fig.3.15: The total energy of simulating system versus time (MCSPS) for systems with various contact angles (interaction constants).

θ [°]	Final graphical output
90	
84,3	
78,4	
72,5	
60	
53	
45,6	
36,9	
25,8	
0	

Fig.3.16: Selected graphical outputs representing equilibrium state of the drop fallen on a solid substrate with measured contact angles (interaction constants).

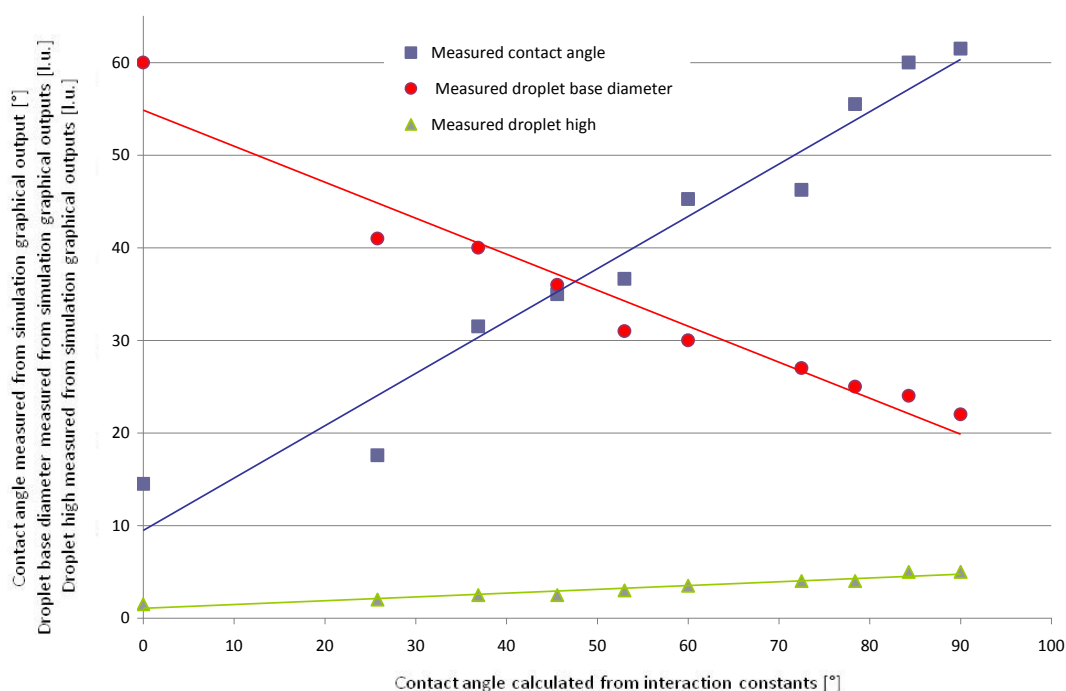


Fig.3.17: Contact angle, diameter and high of a droplet in contact with a solid substrate at the end of simulation measured by image analysis of resultant configurations in dependence of a contact angle calculating from interaction constant as it is shown in Tab.3.1.

But if the system is relatively small, liquid body is small and interaction constants are set up by differently some characteristic behavior of the system during simulation can change or the behavior need not to be recorded completely. Below is introduced simulation where the second part of dependence MCSPS versus total system energy was not found as a steep decrease. The liquid body transformation into equilibrium state is represented only by means of several fluctuations of total system energy. There is visible that the particular setting of the simulation is extremely important with regards to final results.

Initial state of the simulation system									
MCSPS		MCSPS		MCSPS		MCSPS		MCSPS	
1		7		13		19		25	
2		8		14		20		26	
3		9		15		21		27	
4		10		16		22		28	
5		11		17		23		29	
6		12		18		24		30	

Fig.3.18: The graphical outputs from the simulation showing development of the simulation in time steps (MCSPS). There is visible that the drop fell on substrate in MCSPS = 11, which corresponds with almost the lowest total energy of system in Fig.3.19.

The simulation box had $30 \times 30 \times 20$ l.u.. Interaction constants were set up like this: $C_{ff} = -40$; $C_{gg} = -30$; $C_{gl} = -5$; $C_{gf} = 20$; $C_{ll} = 10$; $C_{ff} = 0$. So the final contact angle was 90° . Diameter of the liquid sphere in initial state was $rk=8$. MCSPS was 40. Gravitational constant was used, thus $C_g=10$. Statistical temperate was $\tau = 30$. The graphical outputs from the simulation showing development of the simulation in time steps (MCSPS) and graph introducing the total energy of system versus time are further are presented below in Fig.3.18 and 3.19.

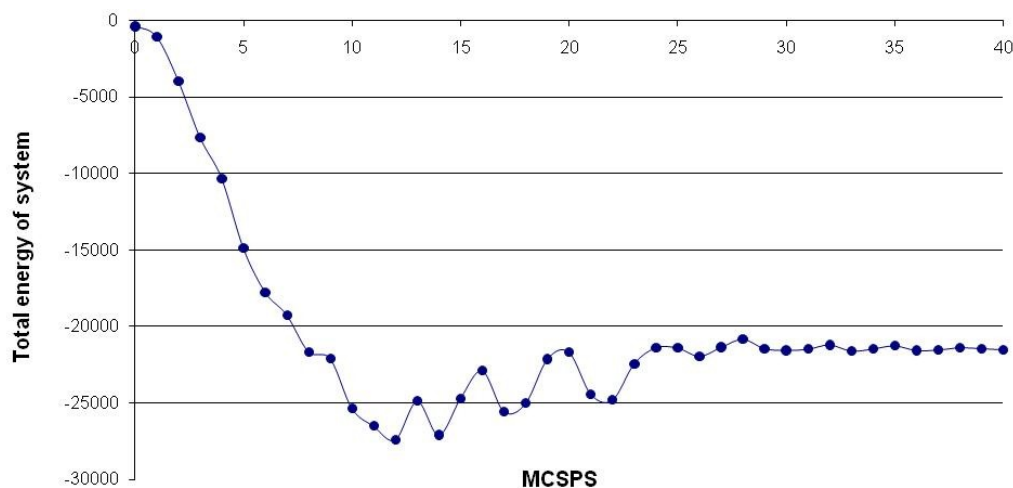


Fig.3.19: The total energy of simulating system versus time (MCSPS).

Drops inside fibrous material

The third part of the simulation is devoted to a real situation important for many applications in textile industry. The simulation represents drop's penetration into fibrous material with change of fiber orientation. There is also possible to change volume density of fibrous material, length of fibers, and thickness of fibrous material and so on [4-6, 9, 19, 22]. There is also possible to simulated liquid's or drop's penetration into fiber bundles, yarns or threads and so on [7, 8, 20, 21]. The fibrous system can be considered as a nonwoven material, if the fibrous structure in the simulation respects a structure of nonwovens.

The following part wants to demonstrate that there is also possible to study the results as it is not possible in reality. The simulation represents spherical drop's penetration into fibrous material. The changes of the liquid drop shape above a fibrous material caused by the liquid suction into substrate during time can be recorded by camera and then study by image analysis as shown in chapter 2.3.1. But what happens inside the fibrous system is not possible to record. There is a question now: How we can study the shapes of liquid bodies inside the fibrous systems? The answer is easier for thin fibrous materials than for bulky (thick) materials. There is possible to consider "spot" of liquid, which remains after the drop's penetration into fibrous material, for authoritative and decisive characteristic of liquid body inside the thin fibrous material. Since there can be supposed, that the height of equilibrium liquid body (arising after the sphere drop's penetration into thin nonwoven) is in all places identical. And also the spot of liquid is same from both a facial side and a reversal one. In this case, an area of spot of liquid can be measured by image analysis for acquirement of good information about the shape of liquid body inside the thin fibrous material after the drop's penetration (see Fig.3.20).

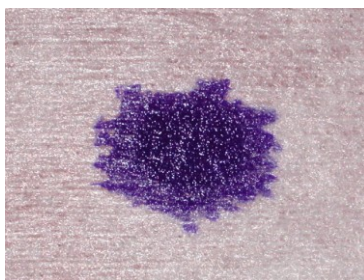


Fig.3.20: Photo of a spot of liquid body after the drop's of colored glycerin by methyl violet penetrated into the spun-laced nonwoven material from facial side.

If a study of equilibrium liquid bodies inside a bulky fibrous material is taken for consideration, the problem arises again. These liquid bodies are very complicated 3D systems. Detail study of these 3D liquid bodies in fibre materials is very difficult. The very good alternative is the studying of these phenomena by computer-aided simulations. The computer simulation, which uses a modified Ising model and Monte Carlo method, is suitable for investigation of the equilibrium liquid body inside the fibrous material.

The three-dimensional simulation box is fulfilled by fibrous material, spherical drop above the fibrous material and gas. Fibers were randomly generated into the define volume in simulating box. The volume fraction value was constant (0,22; 22% of define volume belonging to the fibrous system was fulfilled by fibers). The initial configuration of the simulating box is shown in Fig.3.21.

The orientation of fiber is given by two angles α and β . The angle α is defined as a deflection (\pm) from the coordinate x and the angle β determinates deflection (\pm) from coordinate z , both in Cartesian coordinate system. All fibers have the same angle $\beta = \pm 90^\circ$, they were horizontally oriented and they differ by limitation of angle α (see Fig.3.22). The angle α was changed to four times: random orientation $\alpha = \langle 0-180^\circ \rangle$; random orientation in interval $\alpha = \langle 60-120^\circ \rangle$; random orientation in interval $\alpha = \langle 67,5-112,5^\circ \rangle$ and aligned fibers $\alpha = 0^\circ$.

The three dimensional visualization of the fiber system is presented in Fig.3.23. The simulation box had $100 \times 100 \times 32$ l.u.. Length of each fiber was 50 l.u., thickness of fibers was 1 l.u. The diameter of the liquid sphere in initial configuration $rk = 6$ l.u.. The liquid sphere is placed above the solid substrate at height $h = 5$ l.u.. MCSPS was 150. The gravitational constant was $C_g = 10$ and statistical temperature was $\tau = 30$. Contact angle counted from interaction constants ($C_{ll} = -24$; $C_{gg} = 12$; $C_{gl} = 4$; $C_{gf} = 21$; $C_{fl} = -2$; $C_{ff} = 0$) was $\theta = 60^\circ$.

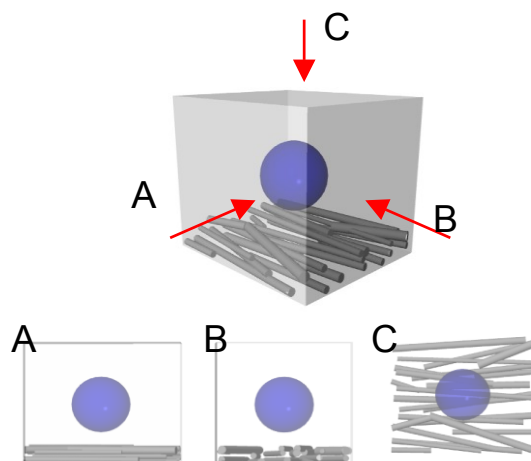


Fig.3.21: The initial configuration of the simulating system – a sphere of liquid above a fibrous system with specific orientation of fibers.

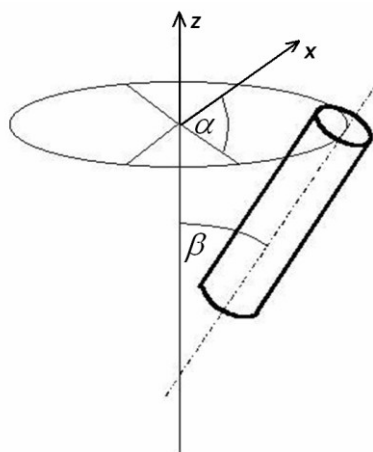


Fig.3.22: A fiber declined horizontally to α and vertically according to β with respect to axes x and z respectively.

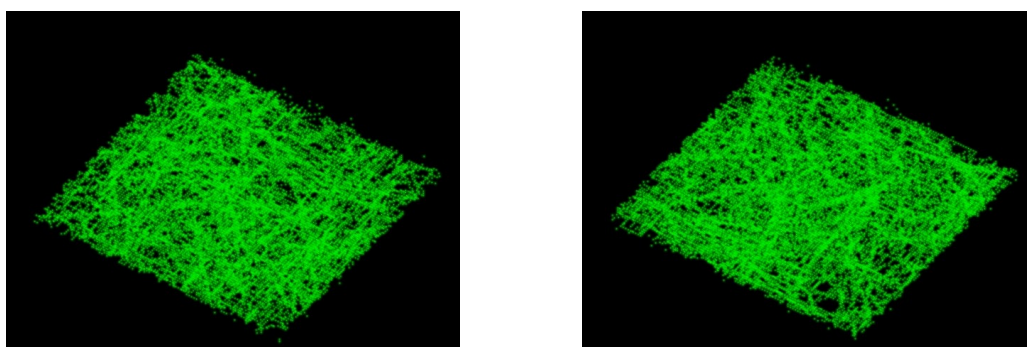


Fig.3.23: Two examples of threedimensional view of fibrous material used for simulations. Both examples are for a random orientation of fibers.

The outputs from the simulations are depicted in Fig.3.24. They present the fiber systems and inside of them the liquid bodies after the drop's penetration in equilibrium state after the simulation process were terminated. Also separated liquid bodies are shown in that figure. The ability to view itself liquid body is completely impossible in the real experiments.

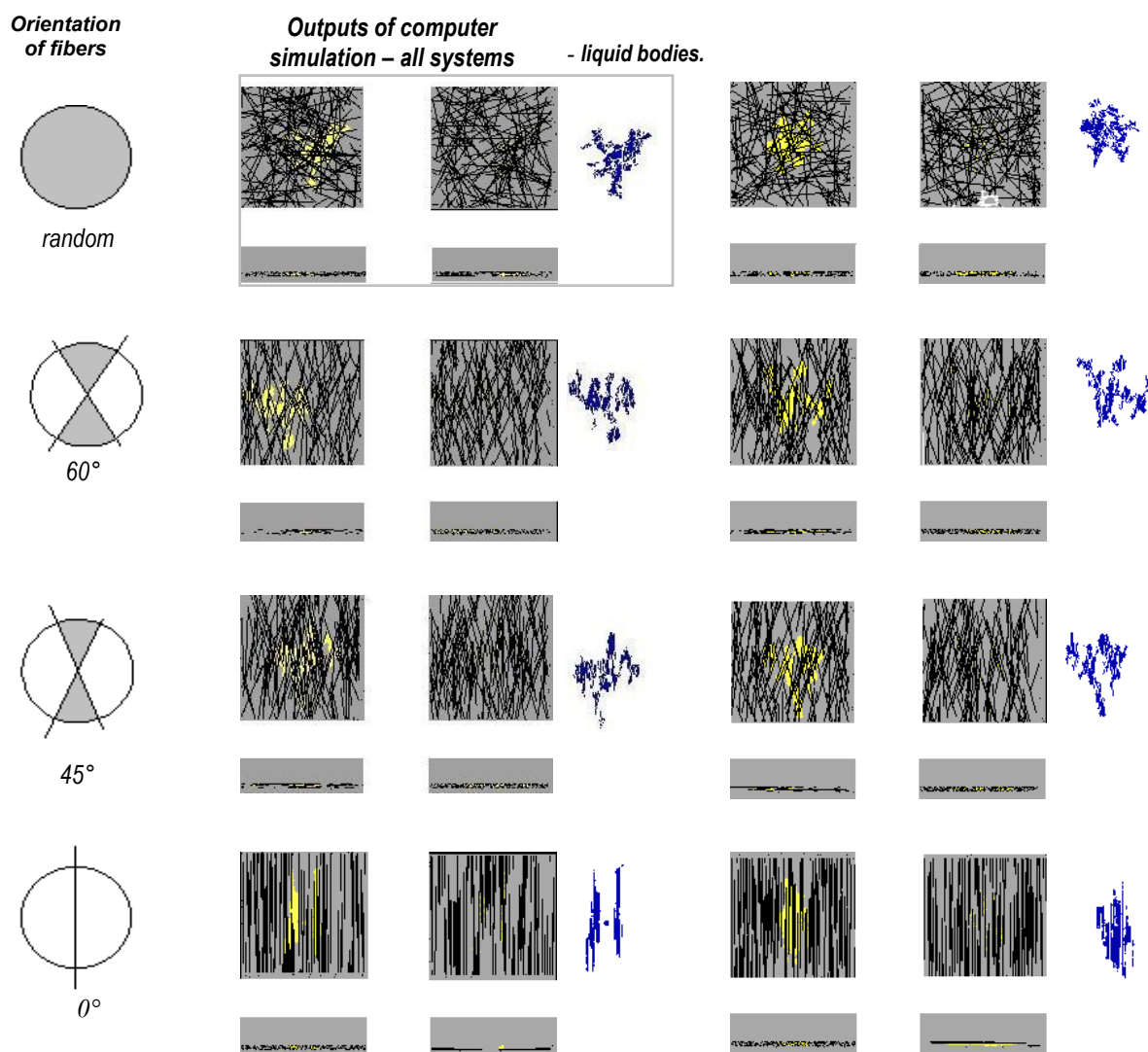


Fig.3.24: Two two-dimensional graphical outputs of the simulation for four various fiber orientations and contact angle $\theta=60^\circ$. Vertical and horizontal cross-sections of all systems and resultant liquid bodies are depicted.

Figures Fig.3.25 and Fig.3.26 show the three-dimensional visualization of the graphical simulation results. The contact angle was still $\theta=60^\circ$ in Fig.3.24 and Fig.3.25. But the change of contact angle is visible in Fig.3.26, where contact angle $\theta=90^\circ$ ($C_{ll} = -24$; $C_{gg} = 12$; $C_{gl} = 4$; $C_{gf} = 21$; $C_{fl} = 3$; $C_{ff} = 0$) was used. There is visible no complete penetration of droplet into the fibrous material in final equilibrium state of the system.

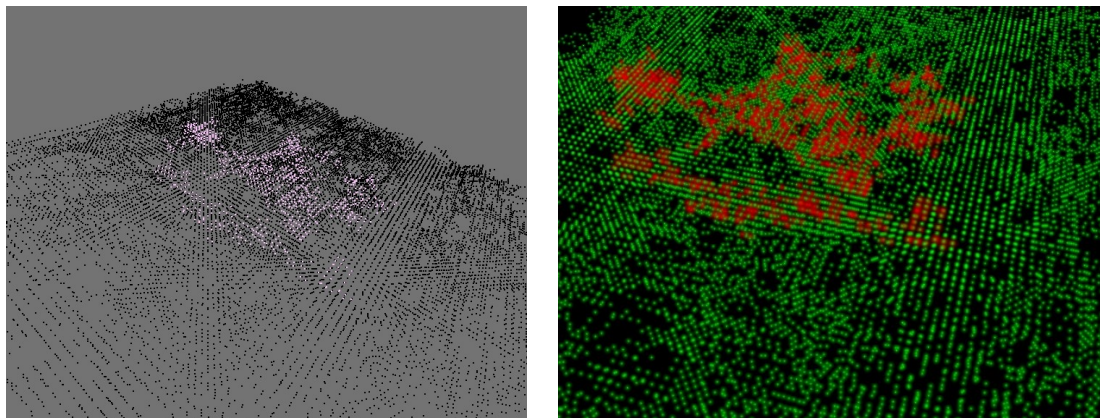


Fig.3.25: Three-dimensional graphical outputs from the simulation described above for the simulation in a gray frame in Fig.3.24. There is visible liquid body inside the fibrous system.

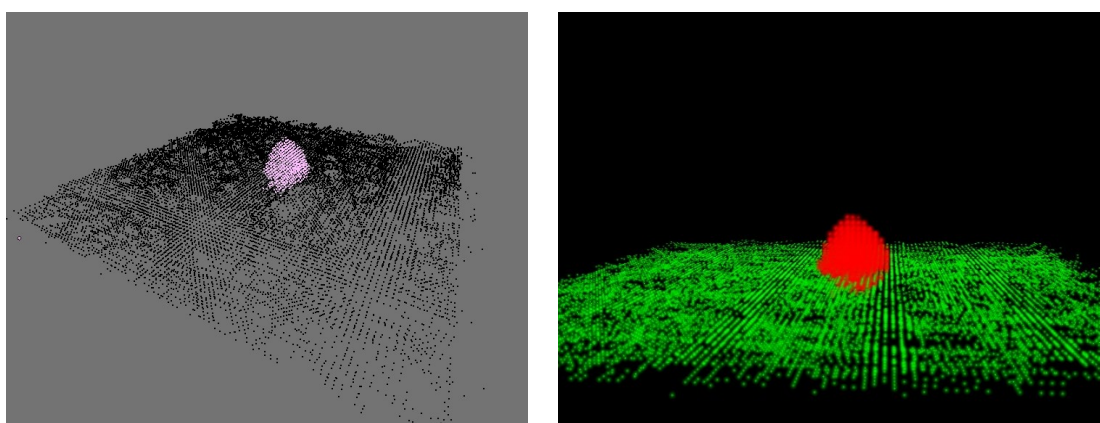


Fig.3.26: The graphical outputs for the system with random orientation of fibers described above with contact angle $\theta=90^\circ$.

From graphical results of this kind of simulation, there is obvious that liquid bodies shape copy structural characteristic of fibrous material as it is known from real experiments. Thus, the random orientation of fibers means liquid body spread almost uniformly in all directions. In contrast, the more uniform fiber orientation leads to more oriented liquid body transport during the drop penetration.

Mysteries in fiber mass wetting

This part of the thesis is focused on behaviour of liquids in contact with fibre materials having contact angle higher than $\theta=90^\circ$. Videlicet, if this situation would come in to being, it is not sure that wetting will not start. There exist several works showing the existence of equilibrium liquid columns imbedded into a fibre mass with a contact angle greater than $\theta=90^\circ$ [23, 24]. A transition to complete wetting is for a single fiber shifted with respect to a plain surface as has been shown in [25, 26]. The theoretical explanation of the particular problem was described by the author of this thesis and coauthors in [27].

The aim of the simulations in this chapter is to find examples of situations, when liquids with contact angle $\theta=180^\circ$ ($C_{ll} = -26$; $C_{gg} = -20$; $C_{gl} = -10$; $C_{gf} = -20$; $C_{fl} = -11$; $C_{ff} = 0$) stays inside the fiber material after a forced installation inside. A compact liquid body (cylinder of a small height) placed into a planar fiber materials with a) random horizontal fiber orientation or b) with parallel horizontal fiber orientation. Size of the simulating box was $300 \times 300 \times 100$ l.u.; size of fiber system was $300 \times 300 \times 20$ l.u.; liquid body in initial state had cylindrical shape with the diameter equal to 100 l.u.

and the height of the cylinder was $10 l.u.$; fiber volume fraction was $0,25$ and statistical temperature equals $\tau=50$. The orientation of fibers was solved as described above in chapter 3.3.1. Some examples of outputs are depicted in Fig.3.27.

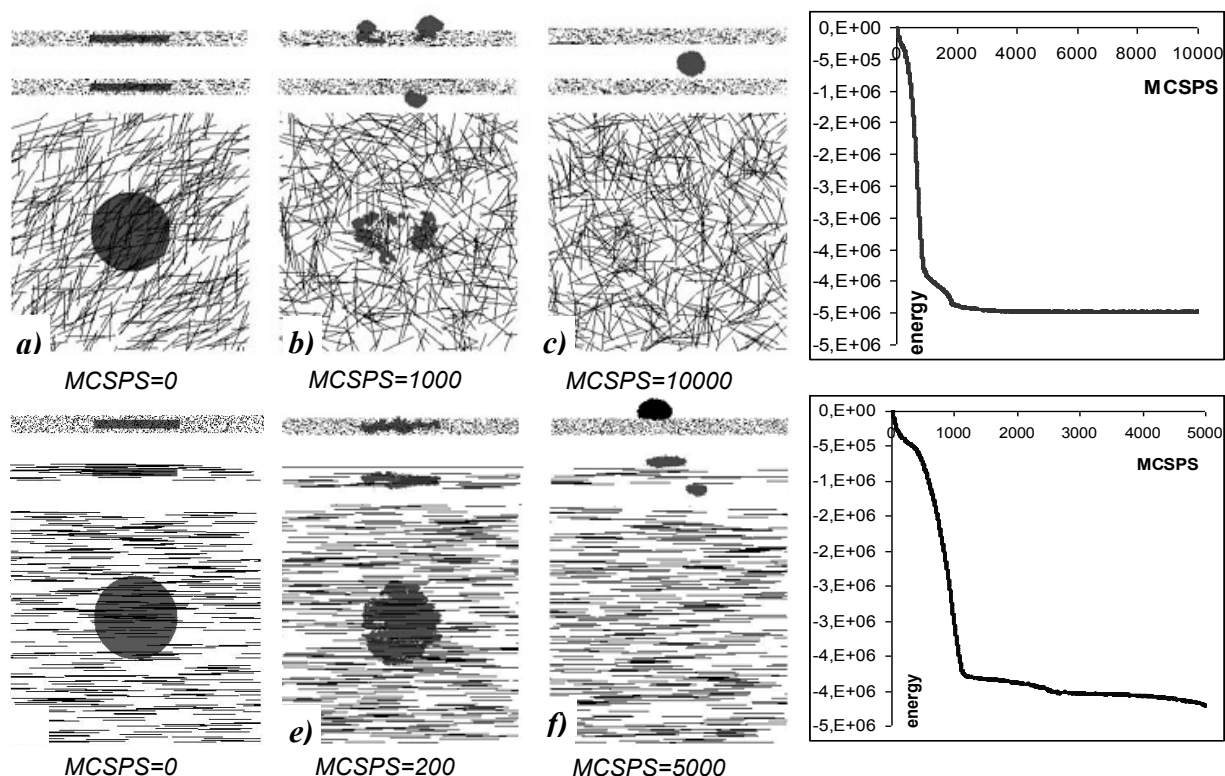


Fig.3.27: Initial and final states as graphical outputs of the simulations: a) Initial state of cylindrical liquid body installed into the material with random orientation of fibers; b) the graphical simulation result (MCSPS=1000); c) the final state of simulation (MCSPS = 10 000) with graph introducing energy versus MCSPS for this simulation process; d) Initial state of cylindrical liquid body installed into fibrous material with aligned fibers; e) the graphical simulation result (MCSPS=200); f) the final state after the simulation process (MCSPS = 5000) with graph introducing energy versus MCSPS for this simulation process.

Beside the planar fibrous material, also a cube filled by fibers was used for this type of simulations. Compact liquid body (a sphere) was placed into the bulky fibrous materials with a) random horizontal fiber orientation or b) with parallel horizontal fiber orientation. Size of the simulating box was $200 \times 200 \times 200 l.u.$; size of fiber system was $70 \times 70 \times 70 l.u.$; liquid body in initial state had a spherical shape with diameter $30 l.u.$; fiber volume fraction was $0,25$ and statistical temperature $\tau=50$. The contact angle was again $\theta=180^\circ$ ($C_{ll} = -26$; $C_{gg} = -20$; $C_{gl} = -10$; $C_{gf} = -20$; $C_{ff} = -11$; $C_{ff} = 0$). The orientation of fibers follows rules described above in chapter 3.3.1., thus all fibers have the same angle $\beta = 90^\circ$, they were horizontally oriented and they differ by angle α , which was randomly generated. So the final orientation of fibers was random from upper view. Some examples of outputs from our simulations you can see in Fig.3.28.

At the beginning of the simulation study, the general questions were: Does liquid get out of fiber material during a simulation? Under what conditions, it either gets out or does not get out? The simulation process showed different results for the planar fibrous material and for the cubic bulky fibrous material. There is visible from Fig.3.27 that liquid got out of fibrous material if the MCSPS was sufficiently high.

But it did not apply for the cubic bulky fibrous material. The liquid was not able to escape from fibrous material. The energy decreasing was done only by reorganization of liquid into bigger "holes" or rather pores inside the fibrous system. The graph presented in Fig.3.28 shows relatively high fluctuation, because a system effort to equilibrium state and escape from fibrous material is of course huge if the contact angle is 180° . Accordingly the simulations have shown, if there is surmounted the energetic barrier, than the liquid under special conditions cannot get out of fiber system. These simulations shows that if diameter of liquid body installed inside the fibrous material $2r \ll$ than

characteristic size of textile material and liquid droplet is completely closed inside, then the droplet is not able to escape from the fibrous material.

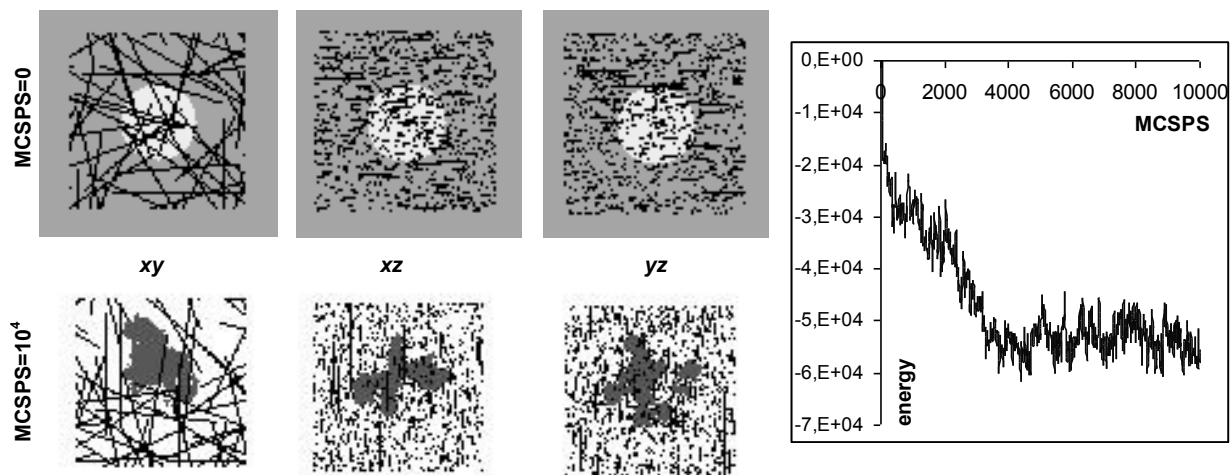


Fig.3.28: Initial and final state as graphical outputs of the simulation (MCSPS = 10 000) with graph introducing energy versus MCSPS for this simulation process.

This knowledge is important mainly for the usage as barriers (hydrophobic fibrous materials). Thin fibrous layer are able to evict also forcibly injected liquid, if the contact angle is sufficiently high. In contrast, bulky fibrous materials are not able to displace the liquid out. The phenomenon depends on the ratio between fibrous material thickness and droplet radius.

3.3.2. Wetting Dynamic Computer Simulation

Liquid wicking into cylindrical capillary

Simulations described below presents the efforts to confirm or disprove that this method is able to mimic the dynamic process of wetting. The model situation of liquid wicking into cylindrical capillary is very well theoretically described, as it is written in the chapter 2.2.1. This good theoretical description provides a relatively simple evaluation of the simulation results. The first experiment is used to show the dynamics behavior of systems during wetting.

The initial state of the simulation box includes a cylindrical capillary from a solid material partly embedded into a liquid reservoir, as it is shown in Fig.3.29. The simulation box had $20 \times 20 \times 100$ l.u.. The radius r_c of the cylindrical capillary was varied from 1 l.u. to 4 l.u.. Contact angles were between $\theta=5^\circ$ to $\theta=90^\circ$. MCSPS was 5000 for all simulations. Statistical temperature correspond with normal laboratory conditions $\tau = 30$. There were used simulation with gravitation, thus $C_g = 10$, and without gravitation $C_g = 0$. Infinite and finite liquid reservoirs were used in the simulation. The finite liquid reservoir means constant total number of liquid cells inside the simulating box. Conversely, in the infinite reservoir there is volume of liquid completely filled with the liquid in each step of the simulation, thus the liquid reservoir is infinite. Each simulation was repeated ten times. The result values of numbers of liquid cells inside the cylindrical capillary or total system energy of simulated systems are average values from these simulations. The number of liquid cells inside the cylindrical capillary was calculated in each step of the simulation. Then the number was recalculated (by dividing of capillary base area) to height of liquid cells inside the cylindrical capillary.

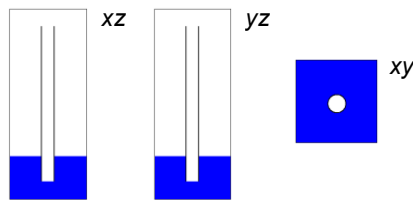


Fig.3.29: Initial state of the simulation presenting liquid wicking into a cylindrical capillary.

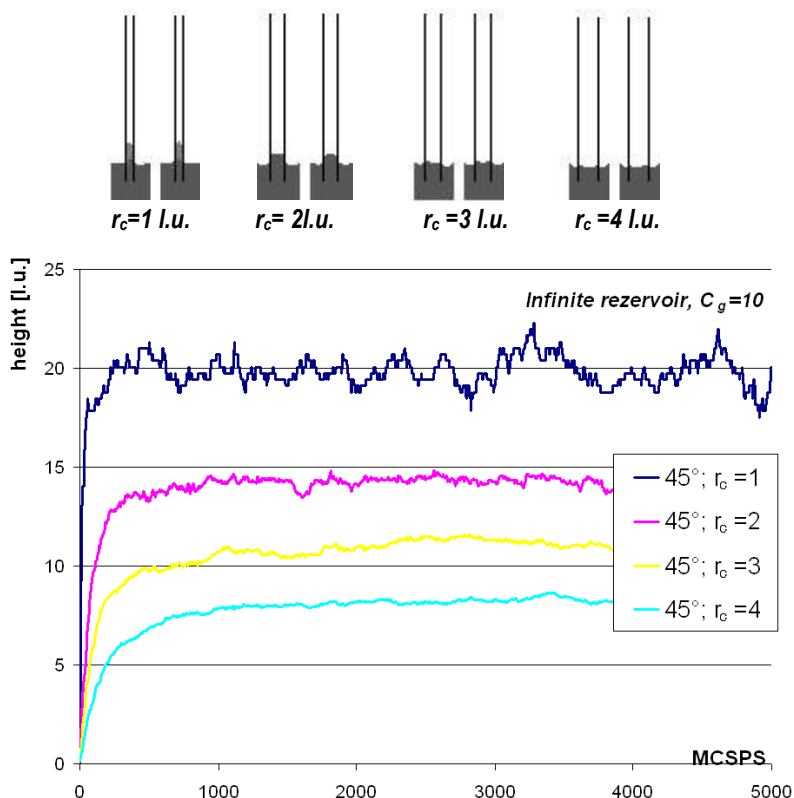


Fig.3.30: Example of the simulation graphical outputs and graph of height of liquid inside cylindrical capillary versus MCSPS. The simulation parameters were these: contact angle 45° ; finite liquid reservoir, gravitation $C_g = 10$; MCSPS 5000.

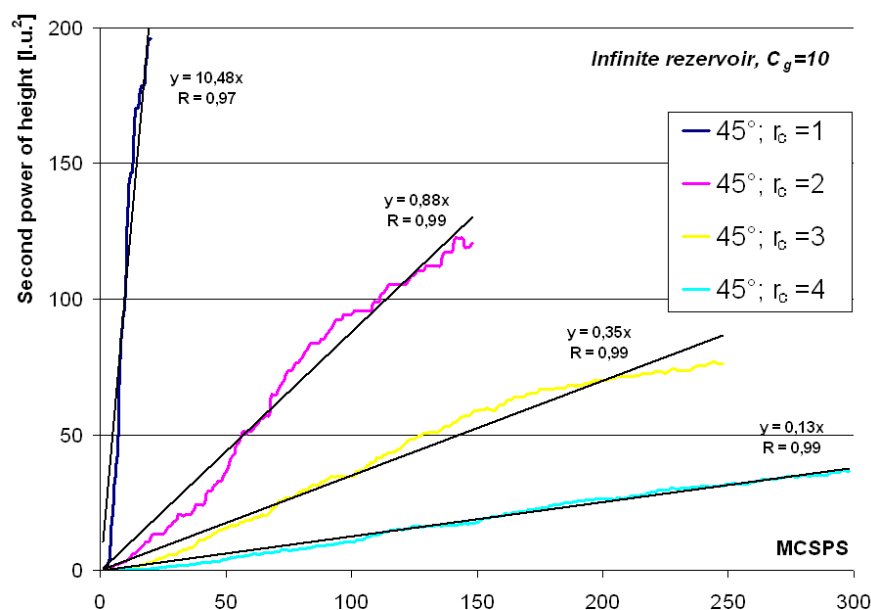


Fig.3.31: Second power of height of liquid column inside a cylindrical capillary versus MCSPS at the beginning period of liquid wicking simulation.

The conclusions of the liquid wicking into cylindrical capillary simulations are mainly these:

- 1) Influence of capillary radius to liquid wicking dynamics into cylindrical capillary is obvious as it is visible in Fig.3.30 and Fig.3.31. These simulation processes follows exactly Lucas-Washburn equation for all used capillary radiuses. The simulation fully describes the dynamics of the liquid wicking into cylindrical capillary.
- 2) Influence of contact angle on dynamics of liquid wicking into cylindrical capillary is obvious, for example from Fig.3.32. The set of simulations shows that the model does not respect real Newton dynamics, but only Monte Carlo dynamics. The acceleration does not appear in the total mass in this kind of simulation. It is not mistake, because the proper balance is achieved at the end of the simulation. The results only show the example, where the simulation system does not follow the real dynamics of the liquid wicking process.
- 3) There was found no difference between using finite or infinite liquid reservoir. See Fig.3.33
- 4) The simulation systems without gravitation had different behavior then systems with gravitation. The system, where $C_g = 0$, slows down, but never reach the energy equilibrium. Graphs are introduced in Fig. 3.34. According these results, all conclusions written here are valid only for simulation processes with gravitation ($C_g = 10$).
- 5) Generally, the dynamics of liquid wicking into cylindrical capillary is obviously registered these simulation processes. Certainly, the simulation results show that at the beginning of simulation the liquid penetrates into the cylindrical capillary as it is theoretically described in chapter 2.2.1 for this type of liquid penetration into cylindrical capillary. According equation (2.9) from the chapter 2.2.1, there is known dynamics is characterized by linear dependence of second power of height of liquid cells inside the cylindrical capillary on time (MCSPS in the presented simulations). The examples of these dependences from the beginning of simulation processes are introduced in Fig. 3.31., where also very high regression coefficients R are presented for each example.

The simulation study showed that there is possible to take this type of simulation (automodels with Method Monte Carlo and Kawasaki dynamics for long distances) in consideration as an appropriate tool for liquid wicking into cylindrical capillary dynamics studies. This is probably due to the fact that the dynamics is driven mainly by capillary forces.

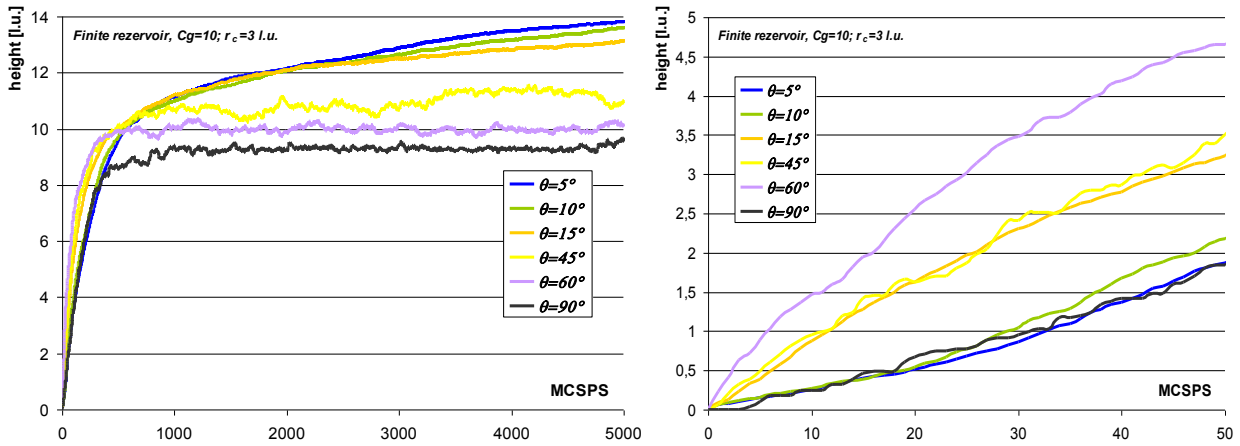


Fig.3.32: Height of liquid inside cylindrical capillary versus MCSPS with change of contact angle.

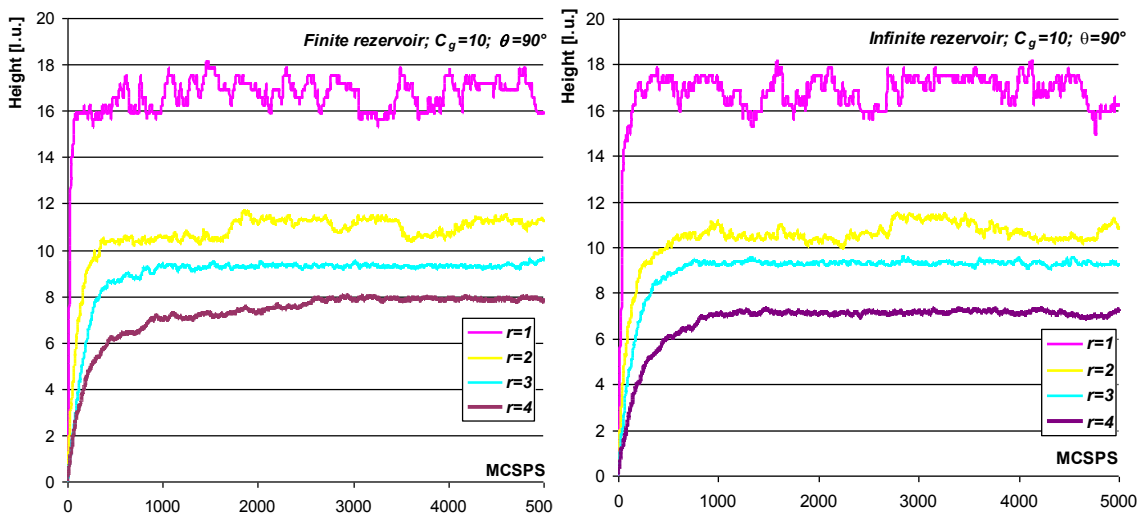


Fig.3.33: Graphs presenting a difference between results from simulation with finite liquid reservoir (left side) and infinite liquid reservoir (right side). Other simulation parameters were: contact angle 90°; gravitation C_g=10; MCSPS 5000, change of capillary radius r_c from 1 l.u. to 4 l.u.

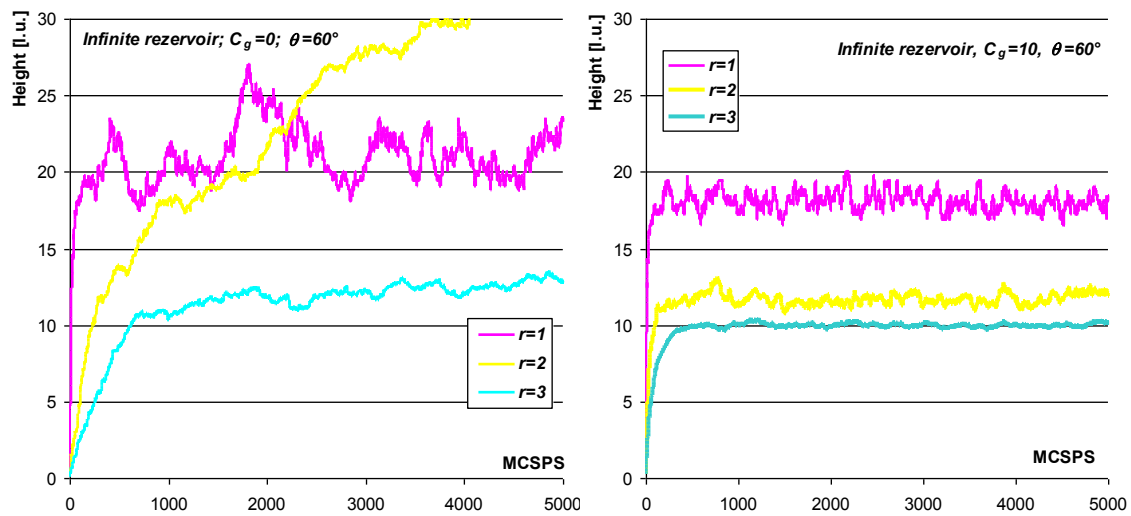


Fig.3.34: Difference between results from simulations with C_g=10 (left side) and simulations without gravitation C_g=0 (right side).

Drop penetration into a radial capillary

The second simulation in the chapter devoted to the dynamics study is the one of the spherical drop's penetration into radial capillary. Dynamic characteristics of drop's penetration into radial capillary, represented by penetration rate, were derived by Marmur, as it was described in the chapter 2.2.2. The rate of drop's penetration into a radial capillary can be calculated only from geometrical parameters of liquid body and contact angle of a liquid. All these parameters can be found or set up in the simulation processes. This simulation can be also relatively simply evaluated with regards to liquid penetration dynamics.

Ising models (automodels) are based only on the interaction energies and on surface tension, it's called hamiltonian system. For these systems was not expected that hey would work with the pressures, they are characterized only by interaction energies as it is written above.

The chapter 2.2.2 shows that the Laplace pressure is the most important parameter for a starting of the drop's penetration into a radial capillary. Thus the first part of these simulations devoted to the drop's penetration into radial capillary, is dedicated to answering a question.

The simulation box had $90 \times 90 \times 70$ l.u.. Contact angle was $\theta=60^\circ$. MCSPS was 2000 for all simulations. Statistical temperature corresponds with normal laboratory conditions $\tau=30$. There were used simulation with gravitation thus $C_g=10$ and without gravitation $C_g=0$. The initial set up of the simulation is introduced in Fig.3.35. Midpoint of the liquid sphere having the diameter $rk=20$ was placed in height $h=20$ l.u. above the higher plate of radial capillary. The upper plate of radial capillary had a hole in diameter 1 l.u.² and the distance between plates is 4 l.u.

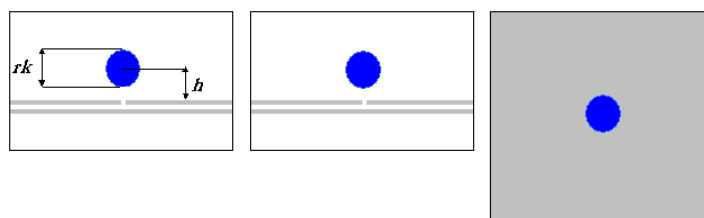


Fig.3.35: Initial set up of the drop's penetration into radial capillary simulation.

Returning back to the condition described in chapter 2.2.2 for the spontaneous penetration into radial capillary. The condition of spontaneous penetration also says that it no external force, which would force the liquid to penetrate capillaries and make a liquid body with a radius r_p , will be available, then there will be no spontaneous penetration of liquids into capillaries. Such an external force can be of course the force of gravity. Thus there were used simulation with gravitation thus $C_g=10$ and without gravitation $C_g=0$. If the simulations using the simulation model did not include or register the Laplace pressure is evident that all simulation behavior and results should be along similar. However, if the simulation includes the Laplace pressure completely, assuming that the droplet should not penetration into radial capillary during the simulation without gravity ($C_g=0$), since no outside force creating the initial radius of liquid inside the radial capillary exists there. The following graph (Fig.3.36) delivers final results of set of ten simulations for each setting.

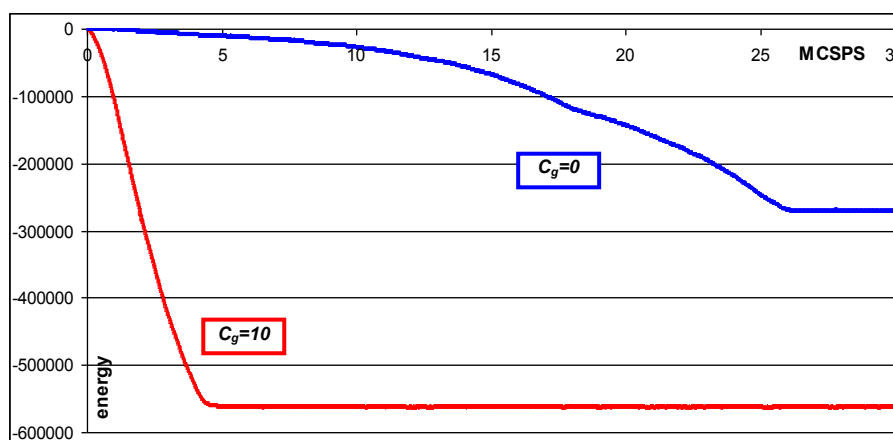


Fig.3.36: Averages of the system total energy versus MCSPS compare a behavior of the simulation systems with and without gravitation.

There is clear from Fig.3.36, these two simulations (with and without gravitation) differ a lot. The simulation working with gravity energy shows immediate penetration into the radial capillary. The effect of gravitation as the external force is evident. But absolutely different output of the simulation with no gravitation is visible from the same graph. The drop did a large number of steps to spread out and regrouped on the upper plate surface before its penetration into the capillary. But finally all drops went into the radial capillary opposite to real situations and theoretical explanations. According these two very different simulation runnings, there is obvious that the simulations approximate the condition of spontaneous penetration of liquids into radial capillary. If the simulation does not include gravitation energy, then the drop had not such tendency to penetrate into the radial capillary and subsequently to establish equilibrium, compared to the second set of simulations including gravitation.

As the second set of simulations there was used the same simulation program but there was included other part dealing with recording of liquid cells number inside radial capillary (in the space between upper and lower plate) per MCSPS. Thus the penetration rate of liquid into the radial capillary could be study. These changes were studied in simulation: i) change of the size of drop – change of drop diameter; ii) change of the distance between plates of the radial capillary; iii) change of contact angle and iv) change of simulation space size. The parameters of the simulations are introduced in Table 3.2. The arrangement within the simulation system is the same as described above, only a liquid spherical drop was placed just above the top plate radial capillaries. In all simulations gravitation was used ($C_g=10$). Final results are shown in graphs presenting dependence of liquid volume inside the radial capillary versus MCSPS.

Table 3.2: The detail table of simulation parameters

Simulation	Size of simulation box[l.u. ³]	rk [l.u.]	d [l.u.]	θ [°]
1	120x120x70	10	4	60
2	120x120x70	10	3	60
3	120x120x70	10	5	60
4	100x100x60	10	4	60
5	160x160x90	10	4	60
6	120x120x70	8	4	60
7	120x120x70	6	4	60
8	120x120x70	10	4	90
9	120x120x70	10	4	0

Simulations provides following results:

i) Influence of the drop diameter in the initial configuration

There is obvious from results introduced in Fig.3.37 and appendix V that the larger radius of the liquid sphere rk , the greater rate of the liquids penetration into the radial capillary. But this fact does not correspond to expectation from theoretical background. That would be the higher rk the smaller the rate of penetration. May be the failure can be explained by unsuitable usage of Kawasaki kinetics for long distances. But also it can be just the weakness of the simulation models (automodels with Method Monte Carlo).

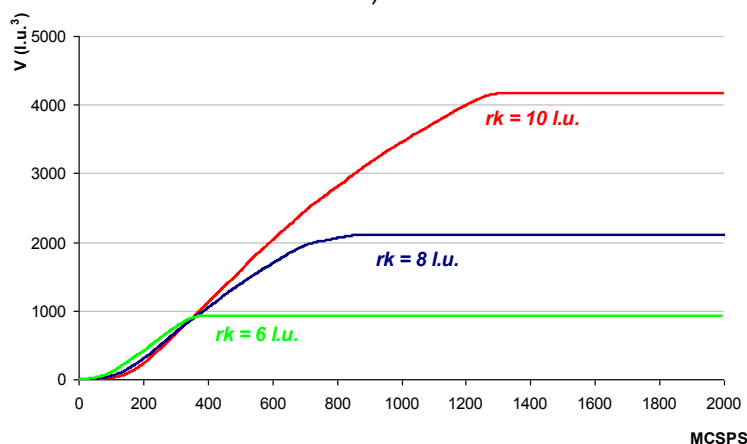


Fig.3.37: Influence of the initial drop size (sphere diameter) to liquid volume inside the radial capillary versus MCSPS.

ii) Change of distance between plates of the radial capillary

Graphs in Fig.3.38 and appendix V show no big difference among each other, but there is possible to find that the bigger distance between plates of the radial capillary the smaller rate of liquid penetration into the radial capillary. The result again relate to Laplace pressure knowledge, which is higher if the curvature radius is smaller. The curvature radius is of course smaller if the distance between radial capillary plates is smaller (if the liquid body radius of curvature inside the radial capillary perpendicular to a plate of the capillary).

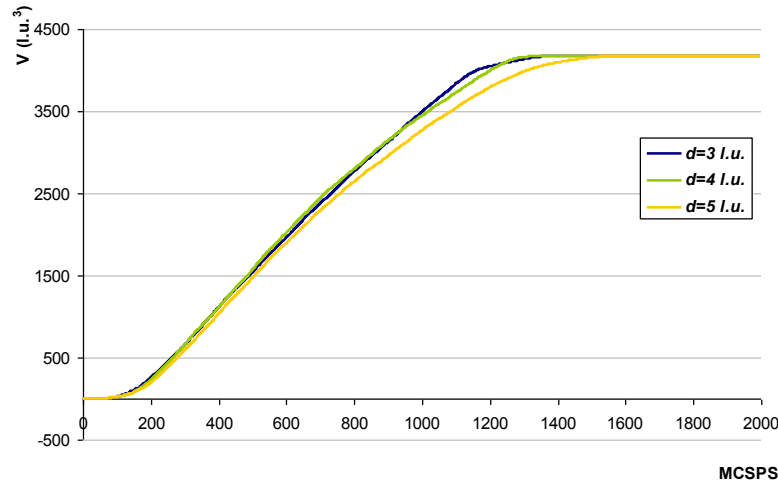


Fig.3.38: Influence of the distance between plates of the radial capillary to liquid volume inside radial capillary versus MCSPS.

iii) Change of the simulation box size

It was noted from simulation results that the larger simulation box means the higher speed of penetration into the radial capillary. This phenomenon is due to usage of the time steps – MCSPS. The largest box has the most of cells. If we divide the number of spin exchange attempts by the total number of cells for the calculating MCSPS, it follows a logical explanation, that the shortest "time" (MCSPS) will be needed to droplet penetrating in the largest simulation box. In addition, if there are compared the sizes of the simulation boxes described in Table 3.2. as 1, 4 and 5 and result graphs in Fig.3.39 and appendix V, one can say that speed is proportional to the size of the simulation box.

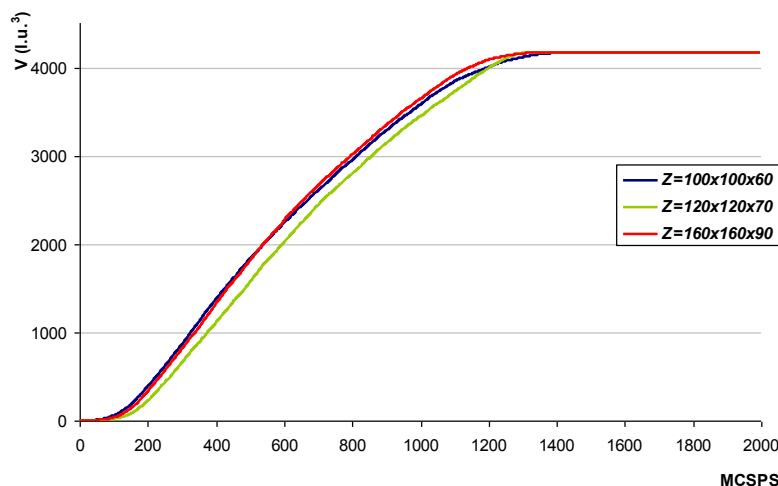


Fig.3.39: Influence of the simulation box size to liquid volume inside radial capillary versus MCSPS.

iv) Change of contact angle

Results for three different contact angles are again quite similar (see Fig.3.40 and appendix V). However, it is possible to recognize that the larger contact angle, the penetration rate is lower.

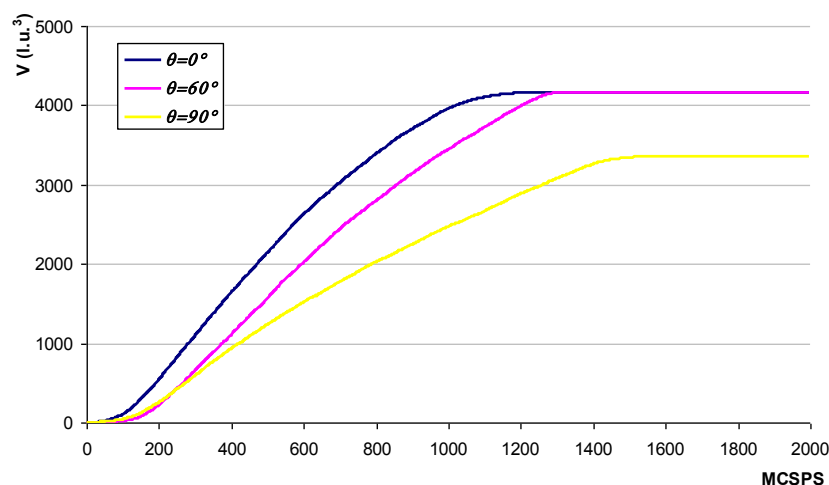


Fig.3.40: Influence of the contact angle change to liquid volume inside radial capillary versus MCSPS.

Further graphs were obtained from the simulations data recalculating simulations according to equation (2.22) in subsection 2.2.2. Thus the influences of τ_p (dimensionless time) on MCSPS were obtain there. These graphical results are given in Appendix VI, also for four series of simulations. Trends in areas of simulation, where there was no penetration at the beginning or the end (so you can talk about the penetration of liquids similar to the infinite reservoir of liquid penetration into the radial capillary), agrees with the results mentioned above. The agreement is in the meaning that the higher rate of penetration in the dependencies listed in Appendix V, the higher the conversion rate (i.e. the regression lines interspersed linearly growing region) between τ_p and MCSPS.

3.4. Recapitulation of Simulation Results

The part devoted to computer simulation showed:

- a) how to find critical temperature in the simulation model, what is very important for comparison between statistical and thermodynamical temperature;
- b) how work with different surface energies – contact angles in these simulations;
- c) how input fibrous materials into these simulation and visualized liquid body inside them;
- d) how hydrophobic fibrous materials behave, if liquid body is installed inside.

Beside these equilibrium observed computer simulation, also dynamic process were studied. Liquid wicking into cylindrical capillary and droplet penetration into radial capillary was simulated at different conditions. The most of presented influences agrees with theoretical prediction. Although some limits, where simulation did not agree with predictions, were shown and discussed there too.

Many authors, for example in [12, 27, 28], wrote that the computer simulation (Ising model with Kawasaki kinetics) can be used to study the dynamics of systems, although the method is based on the principle of equilibrium thermodynamics. But there exist only a few articles, which really bring a proof, that the Ising model with Kawasaki kinetics is available to simulate also dynamic processes. Among these publications belongs [27] from Manna, Herrmann and Landau and [28] from Lukas et al. The first work is devoted to the study of the height of the center of mass of the drop on a wall as a function of time (Monte Carlo exchanges). The second work [28] introduced the simulation model for correct Rayleigh instability prediction finding, which has dynamic nature.

Thus the main benefit of the simulation part of the thesis is showing of other proofs, that the Ising model with Kawasaki kinetics can simulate also dynamic processes as liquid penetration into fibrous or porous materials is.

3.5. References

- [1] Lukas, D., Kostakova, E., Sakar, A.: Computer simulation of moisture transport in fibrous materials, *Thermal and moisture transport in fibrous materials*, edited by N. Pan and P. Gibson, Woodhead Publishing Limited, Cambridge, pp. 469-541. ISBN-13: 978-1-84569-057-1.
- [2] Ising, E.: Beitrag zur theorie des Ferromagnetismus, *Z. fur Phys*, Vol.31, pg.253-58, 1925
- [3] Lenz, W.: Baitrag zur Verstandnis der magnetischen Erscheinung in festen Korpern, *Z. fur Phys*, Vol 21, pg 613-15, 1920
- [4] Soukupová, V.: Computer simulation of wetting and wicking phenomena; Technicka univerzita v Liberci, 2005, ISBN 80-7083-996-1
- [5] Lukas, D., Glazirina, E., Pan, N.: Computer simulation of liquid wetting dynamics in fibre structures using the Ising model, *Journal of the Textile Institute*, Vol. 88, pg.149-161,1997
- [6] Lukas, D., Soukupova, V.: Recent studies of fibrous material wetting dynamics, Index 99 Congress, Geneva, Swititzerland, 1999
- [7] Lukas, D., Pan, N.: Wetting of a fibre bundle in fibrous structures, *Polymer composites*, Vol.24, pg.314-322,2003
- [8] Lukas,D., Chaloupek, J.: Wetting between parallel fibres; column-unduloid and column disintegration trsitions, *Journal of Enginering in Medicine*, Vol. 217, pg. 273-277, 2003
- [9] Lukas, D., Pan, N., Soukupova, V., Parikh, D., V.: Computer simulation of 3Dliquid transport in fibrous materials, *Simulation*, Vol. 80, pg 547-557, 2004
- [1] Paget, R., D.: Nonparametric Markov Random Field Models for natural Images, Ph.D. thesis, The University of Queensland, 1999
- [2] Besag, J.: Spatial Interaction and the Statistical Analysis of Lattice Systems, *Journal of the Royal Statistical Society, series B*, Vol. 36, 1974
- [12] Binder, K, Hermann, D., W.: Monte Carlo Simulation in Statistical Physics, Springer, 1997, ISSN 0171-1873
- [13] Kittel, Ch.: Thermal Physics, John Wiley and Sons, Inc., New York (1969)
- [14] Nezbeda, I., Kolafa, J., Kotrla, M.: Úvod do počítačových simulací: Metody Monte Carlo a molekulární dynamiky, Nakladatelství Karolinum, Praha, 2003, ISBN: 80-246-0649-6
- [15] Charvát, R., Kostakova, E., Lukas, D.: Computer simulation and modeling of Liquid droplets deposition on nanofibers, 7th international conference – TexSci 2010, Liberec, Czech Republic, pg.103-108 ISBN:978-80-7372-635-5
- [16] Kostakova, E.: Výpočet síly potřebné k uvolnění jedné molekuly z objemu kapaliny, písemná práce ke zkoušce „přírodovědný základ“ v doktorském studiu, Technical University of Liberec, Faculty of Textile Engineering, Liberec 2004
- [17] Rowlinson, J., S., Widom, B.: Molecular Theory of Capillarity, Clarendon Press, Oxford (1982) ISBN 0-19-855612-8
- [18] Ščukin, E., D., Percov, A., V., Amelinová, E., A.: Koloidní chemie, Academi, Praha (1990)
- [19] Košťáková, E., Chaloupek, J., Lukáš, D.: Mysteries in fibre mass wetting. In: Incontinence: The engineering challenge, UCL, London (2005) Registered number:206882
- [20] Lukáš D. Chaloupek J., Košťáková E., Pan N.: Morphological transitions of capillary rise in a bundle of two and three solid parallel cylinders, *Physica A*, 371 (2006) 226-248.
- [21] Košťáková, E.: Liquid Penetration through the Ledger Point (The Simulation Using the Ising Model – The Monte Carlo Method), conference XXII. Reinforced Plastics, Balatonfüred 2002
- [22] Košťáková, E.: Computer Simulation of Drop's Penetration into the Fibrous Materials, 2nd International Textile, Clothing & Design Conference – Magic World of Textiles, Dubrovnik – Croatia, 2004, ISBN 953-7105-05-9
- [23] Marmur, A., *Journal of Colloid and Interface Science*, Vol.122, Issue 1, pg.209, 1988
- [24] Princen H., M. (1970) 'Capillary phenomena in assemblies of parallel cylinders', III. Liquid columns between horizontal parallel cylinders, *Journal of Colloid and Interface Science*, Vol. 30, pp.171-184.[25] Brochard, F. (1988) *J. Chem. Phys.*, Vol. 84, pp.4664-4672.
- [26] Bacri, J., C., Peryznski, R., Salin, D.: Magnetic wetting transition, In: *Lecture notes in physics*, Vol. 354, Edited by J. De Conick and F. Dunlop, Springer, pp.1-11, 1988
- [27] Manna, S., S., Herrmann, H., J., Landau, D.,P.: A Stochastic Method to Determine the Shape of a Drop on a Wall, *Journal of Statistical Physics*, Vol. 66, No.3/4, 1992
- [28] Lukas, D., Pan, N., Sarkar, A., Weng, M., Chaloupek, J., Kostakova, E., Ocheretna, L., Mikes, P., Pociute, M., Amler, E.: Auto-model based computer simulation of Plateau-Rayleigh instability of mixtures of immiscible liquids, *Physica A*, Vol.389, pg.2146-2176, 2010

4. Fiber Reinforced Composites

4.1. Fiber Reinforced Composite Materials

Composite is generally a material that consists of two or more components. However, technical terminology has a little more particular description. There are several definitions for composite materials in technical literature. An easy definition is, for example:

“A composite material can be defined as a combination of two or more materials that results in better properties than when the individual components are used alone [1].”

Final properties of composite materials exhibit so called synergic effect. It means a state where at least one property of the composite system is greater than the sum of the properties of all constituents. It is not stated what kind of effect, property or character of materials it should be and this is why almost every material can be considered to be a composite material. Videlicet, almost every material is compounded from more than one basic material when all kind of structures are taken into consideration (macrostructure, microstructure, nanostructure or molecular structure). And almost everywhere, there is at least one property, effect or character that is better than its sum of individual components. Consequently, composites can be found almost everywhere and they have been known since prehistoric ages, for example the well known natural materials such as muscles, wood or man-made materials like concrete.

In the technical field composites are usually created using a discontinuous, harder and stronger constituent denoted as the *reinforcement* and a continuous constituent denoted as the *matrix*. The properties of the resultant composite material are heavily influenced by the properties and distribution of components and their mutual relations, i.e. the interactions between them. The geometry of the reinforcement should also be considered. The best description of geometry contains the specification of shape, volume fraction, orientation and distribution of the reinforcement particles. If fibers as a special group of materials are used as reinforcement, then the resultant material is called a *fiber reinforced composite material*. The high-strength fibers (for example Kevlar, glass and carbon fibers) result in composites with high strength, stiffness and toughness. Presently, these materials are very popular mainly due to their low surface density, very good resistance against corrosion, high dimensional stability, etc. If diameters of fibers are greater than several micrometers and these fibers are used as reinforcement, the resultant composites are referred to as classical fiber reinforced composite materials in this thesis. This classification is not generally used but it is necessary to create it since these classical fiber reinforced composite materials have to be separated from nanofiber reinforced composite materials.

Quite a number of excellent monographs devoted to composite materials in general and also to classical fiber reinforced composite materials were issued mainly in the last few years. There is also an older but excellent book written by Czech author Bareš [2] pertaining to the complex problems of composite materials. Another older essential book written by Agarwal & Broutman [3] focuses only on classical fiber reinforced composite materials, especially on their final properties. As it was mentioned above, a huge amount of books is available on composite materials currently. Examples of monographs on classical fiber reinforced composites are [4 -9]. If one would like to prepare an untraditional composite material, there is necessary to understand the manufacturing of fiber reinforced composites. Possibility the best way to achieve success is to find a good book, as for example a book from Campbell [1], and to study the manufacturing processes of a real producer of classical composite materials. This procedure had been followed by the author of this thesis and the result was a document about the current manufacturing technologies of composite materials consisting of fiber reinforcement and polymer matrix [10].

4.2. Review on Nanofiber Composites

Prefix “nano” means ten on the minus ninth power, or one billionth. The definition of nanocomposite material encompasses a large variety of systems made of distinctly dissimilar components, where one or more components have nanometer scale sizes. In nanocomposites generally nanoparticles (clay, metal, carbon nanotubes, etc.) act as fillers or reinforcement in a matrix.

In this chapter, a utilization of nanofiber materials as a component of composite materials is introduced. The part is devoted to the best-known nanofibers (carbon nanofibers, carbon nanotubes and polymer electrospun nanofibers) and their combinations in composites. These fibers – not visible to the naked eye – cannot be produced by classical textile manufacturing methods. Nanofiber materials have generally a plenty of interesting properties that influence the characteristics of other materials, if these fibrous nanomaterials are added as their component.

Nowadays, electrospinning methods and their nanofibrous products have been studied all over the world. The technology uses electrostatic forces for self-organization of polymer solution/melt into a nanofibrous layer. An excellent literature review on so called needle electrospinning was written by Huang et al in [29]. Presently, the most electrospinning techniques used for the production of nanofibrous materials is based on capillary electrospinning. On the other hand, electrospinning from free surface of liquids was named as a needleless electrospinning by Yarin [67]. However, the needleless modification of continuous production of nanofibers was patented by Jirsák et al [61] beforehand, Fig.4.1. This modified technology is called Nanospider™, in which a polymer solution is supplied into the electric field using a surface of a rotating charged cylindrical electrode. Thus no syringes, capillaries, nozzles or needles are needed. The main advantages of the technology are: (i) continuous mass production, (ii) high production capacity (up to $1 \text{ g min}^{-1} \text{ m}^{-1}$ of one spinning electrode) and (iii) ease of upkeep.

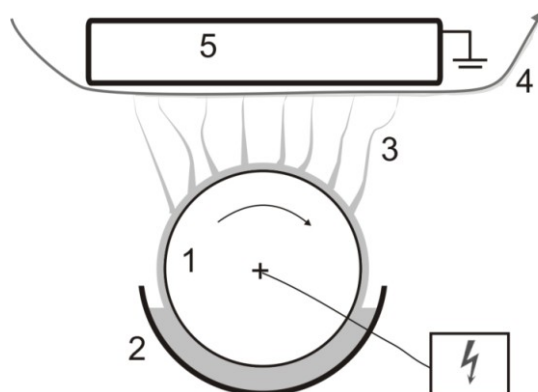


Fig.4.1. Modified electrospinning method – basic principle: 1 - metal roller (positive charge); 2 – reservoir of polymer solution; 3 – direction of fiber formation; 4 – nonwoven substrate (support material for creating nanofibers); 5 – grounded collector.

Carbon nanotubes are stunning materials closely related to fullerenes, discovered in 1985, and its inventors were awarded with a Nobel Prize eleven years later. It proves that the expectations of carbon nanotube utilization are high. On the other hand, only a few related applications of both fullerenes and carbon nanotubes have presently reached the market [11]. There is an enormous number of publications (for example in [12-21]), which deal with its structural parameters, physical and chemical properties, utilization etc. Generally, carbon nanotubes are divided into two groups according to their structure: a) Single-wall nanotubes (SWNTs) and b) Multi-wall nanotubes (MWNTs). Carbon nanotubes are hollow carbon fibers. Carbon nanotubes, in macroscopic scale, look like very fine black powder. Structurally carbon nanotubes are perfect graphene sheets rolled (twisted) into cylindrical shape. A scheme of a part of a single-wall nanotube can be seen in Fig.4.2. Then two caps that usually have a shape of a hemi/fullerene with the appropriate diameter can terminate the tube. If the carbon nanotube is built up only from one wall cylinder, the nanotube is called a single-wall carbon nanotube. Reversely, carbon nanotubes containing two or more of these cylinders from graphene sheets are denoted as multi-wall carbon nanotubes. The easiest MWNT to imagine is the concentric type, in which SWNTs with regularly increasing diameters are located coaxially. However, there are several other MWNT morphologies. According to Bushman [11] hetero-nanotubes are carbon nanotubes the carbon atoms of which, some or all of them, are substituted with another element while the overall honeycomb lattice-based graphene structure is maintained. Hybrid carbon nanotubes are

defined in the same publication [11] as carbon nanotubes, SWNTs or MWNTs, the inner cavity of which has been filled, partially or entirely, with foreign atoms, molecules, compounds, or crystals.

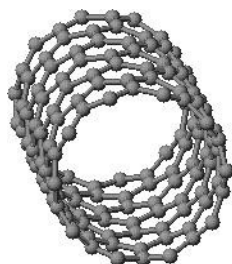


Fig.4.2: Scheme of part of single wall nanotube without caps (half fullerenes).

4.2.1. Composite Nanofibers

Composite nanofibers are the first composite materials mentioned in this chapter. These materials originate from the connection of carbon nanotubes and electrospun nanofibers. Hence this chapter is devoted to carbon nanotubes within electrospun nanofibers. Generally carbon nanotubes are admixed into polymer solution destined for electrospinning. The results are composite nanofibers of special properties. The idea of dispersing carbon nanotubes in a nanofiber matrix to produce nanofiber composites has real perspectives mainly in the mechanical and electrical area. Here is a summary from several exemplary publications dedicated to this type of composite nanofiber.

Electrospinning of polyacrylonitrile nanofibers reinforced with single-wall nanotubes (SWNTs) is a part of Lam's thesis [22]. Composite nanofibers with various SWNTs contents, up to 10wt% within the diameter range of 40-300 nm were successfully electrospun. The main aim of Lam's work was to prepare carbon nanofibers from electrospun composite (polyacrylonitrile plus SWNTs) precursor. The results revealed a promising way for the production of high performance carbon nanofibers reinforced with carbon nanotubes. The same topic is described in a publication by Ko et al. [23]. Composite fibers in this case were subjected to carbonization and also to graphitization.

Polyacrylonitrile electrospun nanofibers were used as a basic material by Ge et al. [24]. He described composite nanofiber materials made from surface-oxidized multiwalled carbon nanotubes (MWNTs) and polyacrylonitrile, successfully developed using the electrospinning method. Concentrations of carbon nanotubes in electrospun polyacrylonitrile nanofibers were really high, up to 20 wt%. The resultant composite nanofiber materials had enhanced electrical conductivity, mechanical properties, thermal stability and dimensional stability. Of course, thermal deformation temperature increased if MWNT concentration was higher.

The electrospinning of synthetic spider silk combined with SWNTs is a subject of another publication [25] and patent [26] from Ko et al.. The initial test results showed excellent growth in the mechanical properties of composite nanofibers in comparison with pure electrospun synthetic spider silk materials. For example when the SWNT content was only 1 wt% in an electrospun material, the growth of modulus was tenfold, growth of tensile strength fivefold and growth of elongation to fracture threefold.

Testing of nanocomposite nanofibers is very complicated. It is not adequate or sometimes also possible to use classical testing methods for the mechanical testing of these materials. Thus presently methods that can clarify the mechanical properties of composite nanofibers are being developed. Two of these publications describing the behavior of composite nanofibers consisting of electrospun nanofibers reinforced with carbon nanotubes are reviewed below.

Mechanical deformations of electrospun polycarbonate nanofibers containing MWNTs have been studied by Kim et al. [27]. Special tensile tests were carried out in a way that tensile loading was applied in a transmission electron microscope. The tensile stress, parallel to the fiber axis, is generated by a thermally induced electron beam. The elongation of fibers and their diameter reduction is measured during the process. The MWNTs were uniformly embedded into fibers, highly aligned parallel to each other along the fiber axis. Electrospun nanofibers showed ultra-high nanoporous morphology. The deformation of nanopores was measured too. According to the authors of the article, result materials had extreme strength and toughness, but unfortunately there is no exact numeral data of the mechanical properties.

The so called rupture behavior, respectively mechanical behavior of electrospun polyacrylonitrile nanofibers, reinforced with both SWNTs and MWNTs (content as high as 10 wt%) was studied by Ye et al. [28]. A high-resolution transmission electron microscope was also used in these observations. The studies revealed a very interesting two-stage rupture behavior in case of the

composite nanofiber material under tension. The behavior included crazing of the polymer matrix (polyacrylonitrile nanofibers) and the pullout of carbon nanotubes. The images from transmission electron microscopy showed a surprising result, i.e. regularly arranged crazing along both types of composite fibers (both SWNTs plus polyacrylonitrile and MWNTs plus polyacrylonitrile).

The first publication dealing with the production of composite electrospun nanofibers by needleless electrospinning, depicted in Fig.4.1, was published in 2009 [66]. A needleless electrospinning method was used to prepare polyvinyl alcohol nanofibers with single walled and multi walled carbon nanotubes. The needleless process of electrospinning from the free surface of a polymeric solution requires perfect solutions of polymers and additives (carbon nanotubes in that case). The solutions were prepared by sonication and using surface modified carbon nanotubes. The presence of carbon nanotubes inside the electrospun nanofibrous materials was proved by means of Raman spectroscopy. This process example can be modified for other polymer solutions to produce nanocomposite fibrous structures by electrospinning in mass scale.

4.2.2. Composites Reinforced by Nanofibers

There are generally known advantages of using traditional polymer fibers as reinforcement material of composites. Nanofibers will also eventually find important application areas in composite materials production. Nanofibers can have even better mechanical properties than microfibers of the same material; since fibers are elongated in an electrostatic field and as a result there are fewer defects per unit length of nanofibers [29]. The enlargement of surface area means greater possibility to stop the progress of defect. The enlargement of fiber surface also leads to the formation of more functional groups at the surface and consequently to an increase in the amount of transitions between the matrix and reinforcement.

In the following part is divided according to the type of nanofiber material.

Composites reinforced with carbon nanofibers and nanotubes

Carbon nanotubes, both SWNT and MWNT, or carbon nanofibers are used as a reinforcement in several polymeric matrixes including both thermosetting (epoxy, polyamide, phenol etc.) and thermoplastic ones (polypropylene, polystyrene, polymethylmethacrylate, polyamide etc.). Carbon nanofibers and nanotubes are known for their structural heterogeneity and for this reason several publications describing composite materials reinforced with carbon nanotubes and carbon nanofibers can be found in the literature. Nanotubes have a lot of very interesting properties such as the following ones assumed by Chronakis [30]: high aspect ratio, small size, high strength and stiffness, low density, high conductivity, high flexibility, ability to withstand cross sectional and twisting distortions, ability to withstand compression without fracture. Hence carbon nanotubes are perfect candidates for the production of nanocomposites. Most articles devoted to composite materials reinforced with nanofibers are focused on carbon nanofiber or nanotubes as reinforcement.

Several examples of carbon nanofiber used as reinforcement in composite materials are briefly described here:

Different types of carbon nanofibers + polypropylene

The best nanofibers concerning the adhesion between fibers and matrix were found to be carbon nanofibers produced by a technology called "long gas phase feedstock". These composite materials showed an improvement in tensile strength and elasticity modulus. The oxidation of carbon nanofiber surface improves the adhesion of nanofibers to the polypropylene matrix and consequently the tensile strength of these composites increases. Optimal parameters of the treatment were found, because for instance long time of surface oxidation can vice versa worsen properties of these nanofibers and thus properties of result composites [31, 32].

Carbon nanofibers + polystyrene matrix

A particular project for the usage of these composites is described in the publication, i.e. the substitution of classical vehicle bumpers. These bumpers are presently mass-produced from polymer matrix composites reinforced with glass fibers. This material can be substituted with carbon nanofiber reinforced polymer matrix. These goods are produced by injection molding technology, and the end materials have better mechanical and manufacturing properties (for example a special method was applied that made paint application easier on the products due to using electrostatic forces) at identical fiber content [33, 34].

Carbon nanofibers + polypropylene and polycarbonate matrix

Recently, the financially most accessible carbon nanofibers produced by the so called CCVC technology were used as the reinforcement. These fibers were connected with the matrix during an

extrusion process. The presence of a small amount of carbon nanofibers increased the conductivity of the final composite material (for instance 10 wt% of carbon nanofibers in the polypropylene matrix decreased the resistance of the matrix from more than $10^{13}\Omega\text{cm}$ to $10^5\Omega\text{cm}$) and improved the mechanical properties of the composite (in case of composites with 15wt% carbon nanofiber and polypropylene matrix Young's modulus increased by 90%) [35].

The price of carbon nanotubes (mainly the price of SWNTs) is noticeably higher than that of carbon nanofibers recently. Nevertheless there are several publications on carbon nanotubes as a perspective reinforcement of composites devoted to special applications:

SWNTs plus polyimide matrix; A potential application of composites made up of SWNTs and polyimide matrix is in future cosmos ships. The aim was to find a particular conductivity level – 10^{-8} S/cm – without worsening other important properties and especially without the loss of transparency. The acceptable conductivity level was achieved at an SWNT content smaller than one tenth of weight percent and no distinct loss of transparency occurred [36].

MWNTs plus phenol resin; Composites set up using the interconnection between MWNTs with diameters smaller than 50 nm and length larger than $10\ \mu\text{m}$ produced by CCVD method and phenol resin showed an improvement in Young's modulus and tensile strength [37].

MWNTs plus epoxy resin; Double-wall carbon nanotubes (DWNTs) were used to reinforce epoxy resin. Again a very small nanotube amount (0.1 wt%) in the composite was already sufficient to achieve a significant improvement in strength, Young's modulus and unequivocal enhancement of fraction toughness in comparison with the non-reinforced matrix [38].

MWNTs plus polystyrene matrix [39]

SWNTs and MWNTs plus silicone matrix; The reinforcement in silicone elastomers caused a significant increase in the initial modulus as well as strength and toughness of composites. However, it is necessary to note that the relative values of improvement in composite properties under loading declined with higher nanotube content, since result composites with higher content of carbon nanotubes became more fragile [40, 41].

Other interesting applications of carbon nanotubes as a part of composite materials can be found in the following publications [42-45]. Nanocomposites with carbon nanotubes have open fields of development and research due to their already known excellent electrical and mechanical properties. However, only a fraction of weight percent is used as a reinforcement of composites mainly because their price is high. But as it is written in publication [46], it is possible to achieve more than 50wt% carbon nanotube content in a polymer matrix through blending nanotubes with polyelectrolyte. These materials have unique mechanical properties that can be improved further by additional chemical crosslinking of nanotubes and the polymer phase and also by the parallel alignment of nanotubes in a definite direction. This allows uniform dispersion of nanotubes in a polymer matrix and enhanced carbon nanotube adhesion to the polymer matrix.

It is commonly known that most efforts to produce excellent nanotube reinforced composites have failed due to the poor dispersion of the nanotubes. But in the work of Dalton et al. [47] an efficient methodology to "tightly wrap" specifically engineered conjugated polymers onto the surface of carbon nanotubes is presented. Of course, besides polymer matrixes there are papers that describe carbon nanotube and nanofiber behavior in metal [35] and ceramic matrixes [46].

Carbon nanotubes can be also used as supplementary reinforcement in composites. It means the addition of nanotubes into the matrix of composite materials primarily reinforced with classical fibers. The method was described for example in the article of Iwahori et al. [48]. The matrix modified by means of carbon nanotubes helps the final composites improve the elastic modulus and resistance to propagation of damage or cracks, and thus compressive and interlaminar strength also increased.

Composites reinforced with electrospun nanofibers

The next topic is the usage of polymer nanofibers as reinforcement. It was already mentioned above that most publications on fiber nanocomposites deal with carbon nanofibers or nanotubes as reinforcement. It is necessary to note that carbon nanofibers can be produced from electrospun polymer nanofiber precursor [29, 49-52], and most research work in this area is based on polyacrylonitrile electrospun nanofibers as a precursor [53-56]. Unfortunately, these carbon nanofiber materials derived from electrospun precursors have dissimilar properties and worse mechanical characteristics; hence they are not appropriate for the mechanical reinforcement of composites.

Only a few papers deal with the manufacturing of composite materials reinforced by polymer nanofibers produced by electrospinning, and the most important publications written by research groups dealing with a possibility to use electrospun nanofiber materials as composite reinforcement

are reviewed below. It is necessary to refer to the first review devoted to this type of composites written by Huang et al. [29].

Kim & Reneker [57, 58] studied the reinforcing effect of polybenzimidazol (PBI) nanofibers produced by electrospinning in epoxy resin and rubber matrix in 1999. Several electrospun nanofiber sheets were impregnated with epoxy resin and then were put into a vacuum oven with elevated temperature for curing. The second type of composites was prepared by mixing the rubber matrix with chopped nanofiber webs (sheets were cut into $0,5\text{ cm}$ squares) and compression molding the mixture. The result nanofiber content in the composites was $3\text{-}15\text{ wt}\%$. The bending Young's modulus and fracture toughness partially increased and fracture energy grew significantly with the increasing fiber content in those composites. The Young's modulus of composites with rubber matrix increased ten times and the tear strength increased two times compared to the unfilled rubber material.

Bergshoef & Vancso [59] produced a composite material reinforced with nanofibers PAD-4.6 obtained from electrospinning with epoxy resin as a matrix in 1999. The production process involves subsequent washing of electrospun nanofiber webs with ethanol, drying at room condition, impregnation with the diluted resin and normal resin and curing at room temperature. The appreciable improvement in mechanical properties of reinforced materials compared to a film of pure matrix was registered in case of both events in spite of the very low weight fraction of fibers in composite ($3,9\text{ wt}\%$ - elemental analysis, $4,6\text{ wt}\%$ - thermal analysis). In the latter research the transparency of composites reinforced by nanofibers was used.

Besides the improvement of stiffness and strength, researchers also tried to modify other mechanical properties of composites by using electrospun nanofibers. The particularity of nanofiber material is its very high surface area to volume ratio. This property of nanofiber materials may be advantageous if the aim is to increase the resistance against delamination of composite laminates. This information came from a US patent [60], the authors of which, Dzenis & Reneker, used polymer electrospun nanofiber (polybenzimidazol, diameter $300\text{-}500\text{ nm}$) layers between laminates (made up of classical fibers used as the composite reinforcement material, for example prepreps of carbon fibers and epoxy resin) of a composite. The obtained results showed improvement in delamination resistance. In other terms we can say that the interlaminar toughness of such type of hybrid composites was improved. The improvement was achieved without a substantial reduction of in-plane properties and growth of weight and/or thickness of result composites.

Electrospun nanofiber reinforced polymer composites have been developed mainly for outstanding physical (e.g. optical and/or electrical) and chemical properties while sustaining their appropriate mechanical performance. One of the outstanding properties is the transparency of these composites reinforced by electrospun nanofiber layers as shown by Fig.4.7.

4.3. Composites Reinforced by Electrospun Nanofibrous Layers

Totally new possibilities were opened for composites with electrospun nanofibers due to the development of a special modification of the electrospinning technology by Jirsak et al. [61]. Nanofiber nonwoven layers made by this modified electrospinning technology fulfill the basic requirements of application in composites. The main advantage is a continuous production of nanofiber layers with unlimited width (the only limiting factor is the width of the cylinder which is covered by a thin layer of electrospun liquid and is used as one electrode). The fibers are far longer than the critical length of fibers that are being used in composites. Such a system is composed of straight endless fibers that can be partially oriented using additional devices; and the chemical structure of fibers can also be modified easily. It is well known that the yield strength of materials increases as the characteristic length of material elements (grains or fiber diameter) is made smaller, to achieve easier dislocation or crash movement. Moreover, the previously mentioned strengthening effect could provide us with extremely thin and hence flexible plates. All those extraordinary properties of nanofiber-reinforced composite materials induce us to follow this streamline of research.

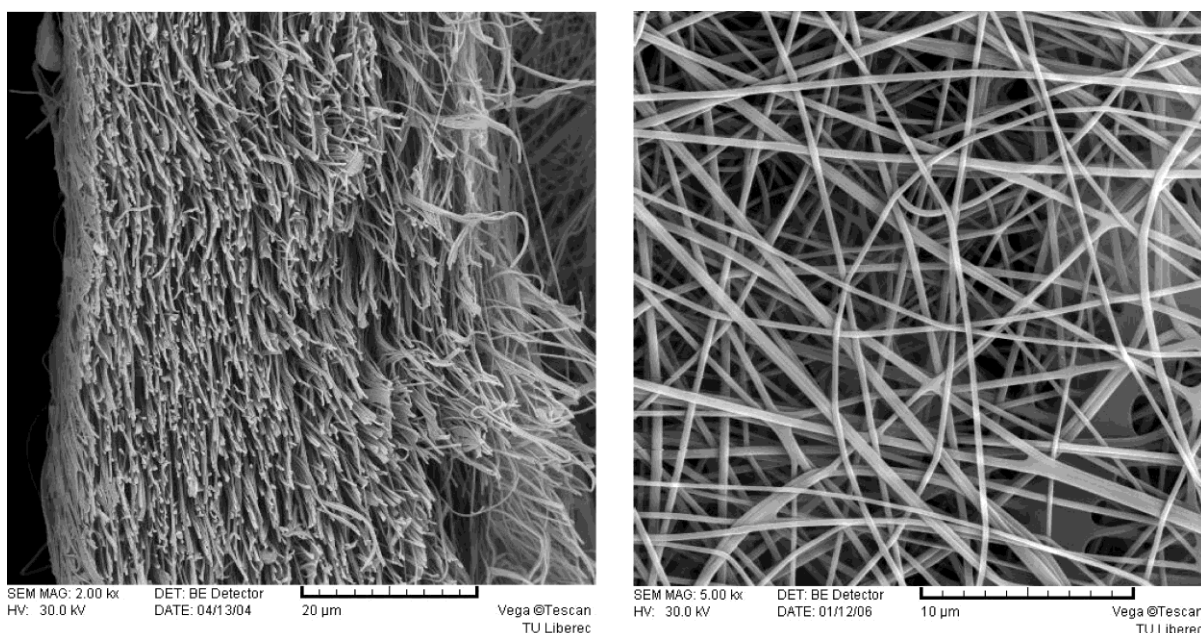


Fig.4.3: Polyvinyl alcohol nanofibers produced by modified electrospinning method at the Technical University of Liberec; a cross-section and a front view.

Special materials require special technologies. It is not easy to fully impregnate electrospun nanofiber layers especially with highly viscous liquid matrixes. Therefore new approaches are needed. The following chapter is devoted to one of them where the impregnation of electrospun nanofiber layers was enhanced by ultrasound. A part of the study was published in [62]. The benefit of ultrasound usage for nonwoven materials impregnation is described in subsection 2.3.3.

Firstly, a set of experiments relating to the production of composite materials reinforced with only nanofibrous materials is introduced. As it is explained below, such a system does not bring any special properties and application. Thus later a particular application test using two different fibrous reinforcements where only one is nanofibrous is detailed.

The following electrospun nanofibrous materials were used:

PVA I - polyvinyl alcohol nanofibers; polyvinylalcohol (molecular weight M_w approximately 60 000 g/mol; polymerization degree approximately 1100) in 16 wt% - Sloviol R from Novácké chemické závody, Slovakia; cross-linking agent polyacrylic acid was added (in weight ratio 67/33); 12 wt% water solution was used for the modified electrospinning process; cross-linking at temperature 150°C for 5 minutes; fibers were oriented randomly; surface density of the produced material was 3 gm⁻², average diameter of fibers 236 ± 79 nm; thickness 42 ± 15 µm measured using a scanning electron images; tensile strength of nanofiber web 5.7 MPa (without considering the volume fraction of fibers in the nanofiber material) and 81.4 MPa (considering the volume fraction of fibers, 7%, calculated from the ratio between nanofiber material density and PVA density); see Fig.4.3.

PVA II – Basic polymer polyvinylalcohol (molecular weight M_w approximately 60 000 g/mol; polymerization degree approximately 1100) in 16 wt% - Sloviol R from Novácké chemické závody, Slovakia; Polyvinyl alcohol nanofibers produced by Nanospider technology from 12 wt% water solution and crosslinked by means of glyoxal and phosphoric acid after production at initiating temperature 140°C for 10 minutes, surface density - 4 g/m², average diameter of fibers - 245±98 nm, thickness 50±13 μm tensile strength – 5.8 MPa (without calculation of nanofiber material volume fraction).

PA 6.12 - Polyamid 6.12; electrospinning proceeds after the addition of a mixture of formic acid and acetic acid, surface density 2 gm⁻², average of fibers 279±117 nm, thickness 17±7 μm measured from scanning electron images, tensile strength of nanofiber web 9.9 MPa (without considering the volume fraction of fibers in the nanofiber material) and 82.8 MPa (considering the nanofiber material volume fraction of fibers, 12%, calculated from the ratio between nanofiber material density and PA6.12 density). The origin polyamid 6.12 was obtained from Sigma-Aldrich.

PAN - Polyacrylonitrile electrospun nanofiber web produced by Nanospider technology from dimethylformamide solution, surface density - 4 g/m², average diameter of fibers - 175 ± 62 nm, tensile strength 12.4 MPa (without calculation of nanofiber material volume fraction of fibers). The origin polyacrylonitrile was obtained from Sigma-Aldrich and its average molecular weight M_w was 150 000.

The following materials were used as the matrix:

Epoxy - epoxy resin EPOXY 3711/1200 (high viscosity 60 Pas, surface tension 35.52 mNm⁻¹, density 1.09 gcm⁻³) with hardener P11 (both from SINDAT Plzeň Ltd., Czech Republic) in ratio 100:7.

Epodur – special epoxy resin for fiber reinforced composite materials CHS-Epodur 619-0600 (Spolchemie Inc., low viscosity 0.92 mPas, surface tension 38.14 mNm⁻¹, density 1.16 gcm⁻³, tensile strength 70 ± 5 MPa).

Lamit – polyester resin for fiber reinforced composite materials Lamit 109 (Kittfort, Ltd., low viscosity - 0.68 mPas, surface tension 36.02 mNm⁻¹, density 1.08 gcm⁻³).

Sokrat – acrylate binder Sokrat S942 (Arnaud Česká, Ltd., viscosity 0.32 mPas, surface tension 28.06 mNm⁻¹, density 1.04 gcm⁻³).

Viapal – polyester resin for glass fiber reinforced composite materials VIAPAL VUP 4627 BEMT/56 provided by Novia Kft. Hungary, viscosity is 670 mPas, surface tension is 33.4 mN/m.

All parameters were obtained from producers or were measured under normal conditions (temperature - 21°C and humidity 60%RH).

The tensile strength of cured resins (Epoxy, Epodur and Lamit) and acrylic binder Sokrat, important for the evaluation of the below mentioned experiments. Producers declared the following values: Epoxy 21.5 MPa; Epodur 70 MPa, which are of course ideal or maximal. This is why measurements of cured samples of these resins were carried out. Tensile strength of Sokrat and Lamit is not known from the producer. Samples were produced using a silicon mold and the specimen shape was prepared according to ČSN 64 0604. The results were significantly lower: Epoxy 4.9±3.1 MPa; Epodur 6.4±2.0 MPa. However, very high standard deviations show that there are several issues to discuss, mainly the non-standard process of mixing resin and hardener in very small amounts and non-standard conditions in laboratories. But the same conditions were used also during the production of composite materials described below and this is why it is necessary to take these results into consideration. Tensile strength of Sokrat was measured to be 8.3±0.4 MPa and tensile strength of Lamit was 5±1.3 MPa.

Before the study on the production of composite materials, the wetting characteristics of the most used nanofibrous material PVA I in “contact” with three different liquid matrixes are described briefly. The first experiment was done by means of microtensionmeter Krüss K121 (specimen size was 20x40 mm). The average values from 20 measurements for each liquid are introduced in Fig.4.4, where standard deviation is not noted because for all samples it was very small, about 3%. It is visible that the epoxy resins (Epodur and Epoxy) show the predictable behavior, thus viscosity has the most significant influence on the wicking of liquids into fibrous materials, and in this case also into a nanofibrous electrospun material. However, not only viscosity has impact on the process. Surface tension, structure of fibrous material in the tested, structure of the edge of the sample that is in contact with the liquid and so on play an important role in the wicking process. This is why polyester resin Lamit has worse results than epoxy resin Epodur, even if Lamit has a little lower viscosity than Epodur.

The second method used for the better description of the wetting characteristics of the resins used was the drop test described in chapter 2.3.1. Five measurements for each liquid – resin and an example of each tested resin is visible at Fig.4.5. The tests were only additional, that is why there is only a short note about their evaluation. The results clearly relate to the above introduced results of the wicking testing. It is obvious that the drop of epoxy resin Epoxy “stand” on the nanofibrous material

even after 60 seconds. The high viscosity does not allow the resin to penetrate into the nanofibrous material. Hence, if no external force will be used to help resin to penetrate inside the reinforcing material, resin will cure before the impregnation of the nanofiber reinforcement.

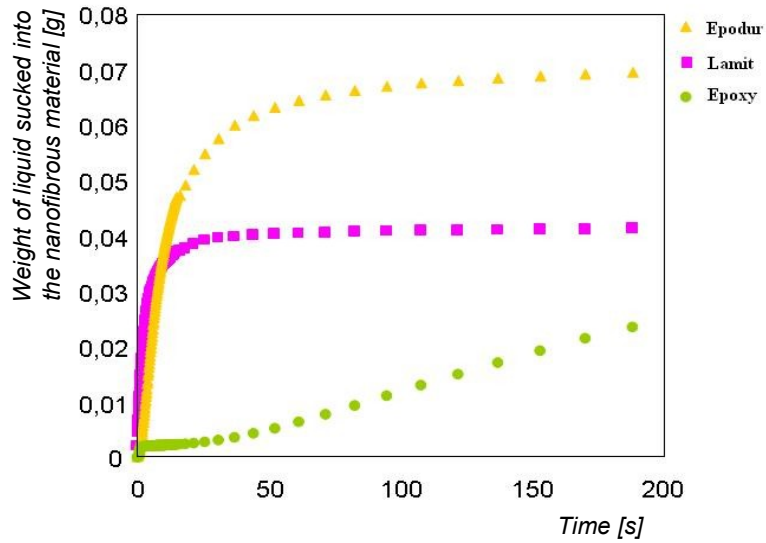


Fig.4.4: Weight (average values) of the liquid sucked into PVA I nanofibrous material as a function of time.

<i>EPODUR</i>	<i>Time [s]</i>	<i>LAMIT</i>	<i>Time [s]</i>	<i>EPOXY</i>	<i>Time [s]</i>
	0		0		0
	8		8		8
	14		14		14
	22		22		22
	30		30		30
	40		40		60
	50		50		90
	60		60		180

Fig.4.5: Graphical input of one drop test for each tested resin with PVA I electrospun nanofibrous material.

Hereafter real experiments devoted to production of composite materials with electrospun nanofibrous reinforcement are described. The following study can be divided into several parts according to the materials used and the production of samples: a) composite material produced by Hand Lay-up method without ultrasound impregnation enhancement; b) composite material produced by Hand Lay-up method with ultrasound impregnation enhancement; c) composite material produced by Hand Lay-up method with ultrasound impregnation enhancement and nanofiber plasma treatment; d) composite material produced by Hand Lay-up method with ultrasound impregnation with change of nanofibers polymer material; e) composite materials produced by Hand Lay-up method with ultrasound impregnation with different types of matrixes. It is necessary to note that samples were tensile tested according to standard ČSN EN ISO 527-3.

The Hand Lay-up fabrication method, described in [10], was used for producing all samples. The initial experiment dealt with production of composite material reinforced by electrospun nanofibers. PVA I nanofibers and epoxy resin EPOXY were used. It is well known that these constituents are not suitable for the production of composite materials due to their mechanical properties. However, polyvinyl alcohol electrospun material is easy to produce at normal conditions without toxic solvents. Polyvinyl alcohol is soluble in pure water, but it is necessary to stabilize it against water after electrospinning. And as a matrix, epoxy resin with extremely high viscosity was used. Thus these constituents are easily producible and available for consequential studying of nanofibers impregnation enhanced by ultrasound. There were two limiting factors in this procedure: the content of reinforcing nanofibers in such a composite was extremely low – estimation is about 2.3% of total volume; and the air that was being trapped in the resin during the manufacturing process as later it was not possible to remove it from the composite. Facing those challenges it was decided to focus our research on the improvement of the manufacturing process in order to increase nanofibers content in composites, which do not contain any bubbles.

To obtain better impregnation of nanofiber materials and to remove the air bubbles that were trapped inside the wetted material we decided to use ultrasound. The decision was based on the knowledge that the application of ultrasound enhances the sorption of highly viscous impregnants [63]. Ultrasonic treatment significantly decreased viscosity and surface tension of the resin; also the presence of ultrasonic cavitation effect improved the penetration of the resin into the fibrous system [64]. Therefore, the usage of ultrasound in the impregnation process brings improvement in resin adsorption and in removal of air from the impregnated material [65]. The short literature review related to this issue can be found in subsection 2.2.5.

The parameters of the system used in the described experiments were as follows: frequency of 30 kHz and power of 60 W. Ultrasound device *Calemard & Cie* was used. The set up of our experiments for impregnation of nanofiber nonwovens is shown in Fig.4.6. PVA I electrospun nanofibrous material and epoxy resin EPOXY were used again.

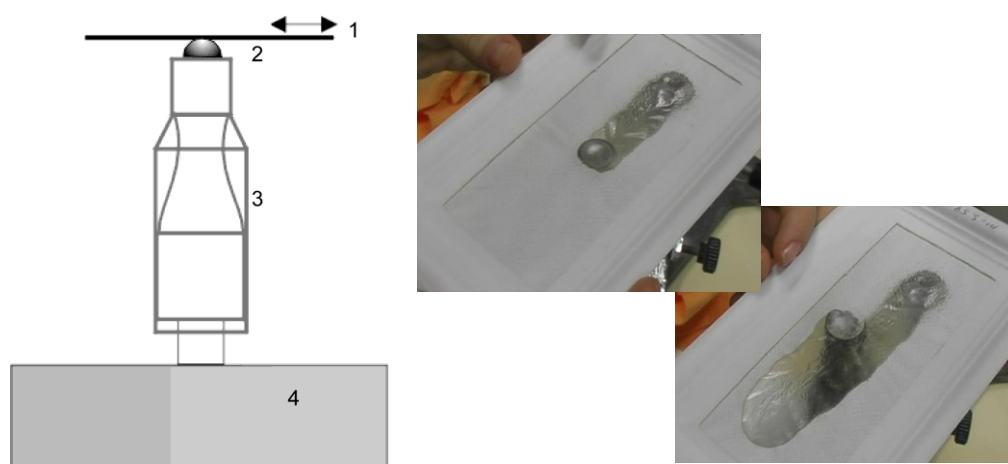


Fig.4.6: Set up of the experiment for impregnation of nanofibrous layers (1 – nanofiber nonwoven material, 2 - drop of liquid matrix, 3 - ultrasonic transducer, 4 - ultrasonic generator) and two photos of the real production of composites.



Fig.4.7: Transparent electrospun nanofiber reinforced composite material in front of a flower for illustration.

Redundant resin or binder was drained using a woven fabric after the nanofiber layer was impregnated. Then ultrasonic treatment was used again to obtain better uniformity of resin distribution and to remove air bubbles from the inner structure of the impregnated nanofiber samples. The curing of resin and binder was performed under normal conditions, at ambient temperature. Just an exsiccator was used for the reduction of humidity during curing.

The whole structure was completely transparent (see Fig.4.7). The system has a plastic foil-like behavior. The fiber content in this composite material was about 15 wt% and about 9 vol%. Mechanical characteristics were also measured. Standard ČSN EN ISO 527-3 was used during the preparation of specimens from all materials. However, as it was mentioned above, it is obvious that the tensile strength of this composite material is very low ($11,7 \pm 2.5$ MPa), almost the same as the sum of the nanofiber layer (PVAI – 5,7 MPa) and epoxy resin (Epoxy – 4,9 MPa) tensile strength. A delamination is visible in the pictures made with a scanning electron microscope (see Fig.4.8).

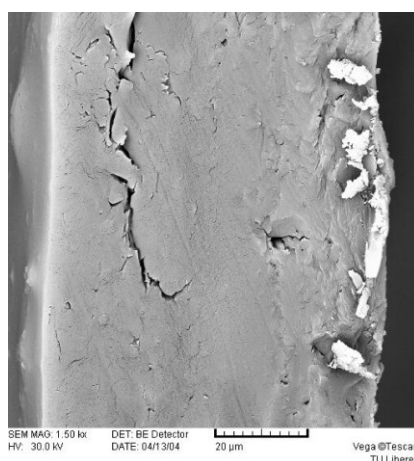


Fig.4.8: SEM image of composite (PVA electrospun nanofibers and epoxy resin) cross-section.

The conclusion that this type of epoxy resin and PVA nanofibers has very bad adhesion can be drawn. It can also be said that there is no adhesion or synergic effect. The surface modification of PVA nanofibers is not easy, because the surface cannot be treated in a “wet” way because the fibers swell in water and nonreversible change of specific structure surface properties takes place. Hence, the surfaces of nanofibers were modified using oxygen plasma. The optimum parameters of plasma treatment were found for PVA I nanofiber material: power 50W, time of treatment 1 minute, pressure 12Pa, distance between the sample and electrode 20 mm, gas flow 50 sccm. These tests were carried out at the Department of Materials, Faculty of Mechanical Engineering, Technical University of Liberec. If an inappropriate, non-optimal power of plasma treatment is used, nanofibers can fail, see Fig.4.9.

The plasma treated nanofibrous materials were impregnated by means of ultrasound by a special epoxy resin for fiber reinforced composites production, named Epodur. Specimens with nanofibers without plasma treatment were also prepared for the better comparison of the treatment effect. Tensile strength of these composites was two times higher (58.6 ± 6.9 MPa compared to composites with not plasma treated reinforcement 32.3 ± 4.0 MPa).

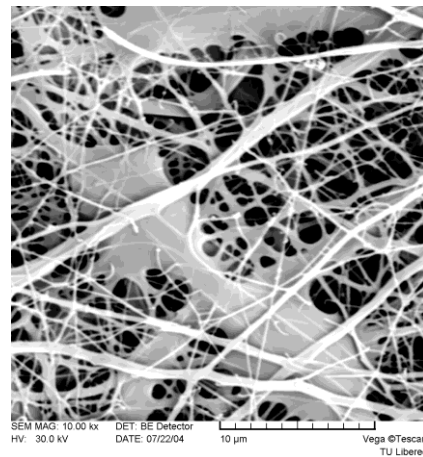


Fig.4.9: PVA nanofiber failure due to inappropriate power of plasma treatment (100 W).

However, it was not the aim of the work to produce composite materials with excellent mechanical behavior. The main success is the full impregnation of electrospun nanofiber layer by means of ultrasound. Usage of ultrasound for the impregnation of nanofiber materials is an “elegant” method to accomplish higher fiber content and better uniformity of liquid matrix allocation in the nanofiber web.

The usage of other basic polymers for production of electrospun nanofiber layers was a theme of subsequent experiments with the aim of achieving better composite mechanical properties. PA 6.12 nanofibers were used as reinforcement. The manufacturing of composites was the same as in case of composites with polyvinyl alcohol nanofibers detailed above. Also the same epoxy resin was used. The results of mechanical characteristics are much better than in case of the previous experiment ($18,4 \pm 1,1$ MPa). The better cohesion in this composite is visible also in Fig.4.10 in comparison with Fig.4.8. The elasticity of polyamide based electrospun nanofibers is much better than PVA, but the strength was lower for the materials tested by us. So manipulations with these materials and preparing composites have been really complicated and experimenter must be very sensitive. Result materials have been relatively good as it was supposed. Tensile test results showed 24% growth of composite strength versus a sum of nanofiber material (PA6.12 – 9,9 MPa) and pure cured resin (Epoxy-4,9 MPa) tensile strengths in average.

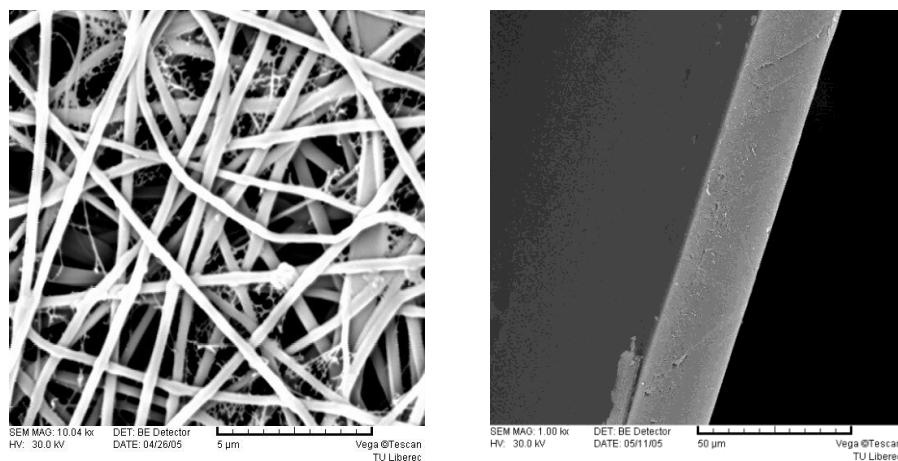


Fig.4.10: SEM image of PA 6.12 electrospun nanofibers and composite containing PA 6.12 nanofibers in epoxy resin Epodur - cross-section.

The usage of other matrix types, e.g. high viscosity epoxy resin Epoxy and Epodur is described in the following chapter. Liquid matrixes have been used for impregnation of polyvinyl alcohol electrospun nanofiber PVA II layers: polyester resin Lamit and as a low viscosity choice – water solution of acrylate binder Sokrat. These different structures can be seen in Fig.4.11.

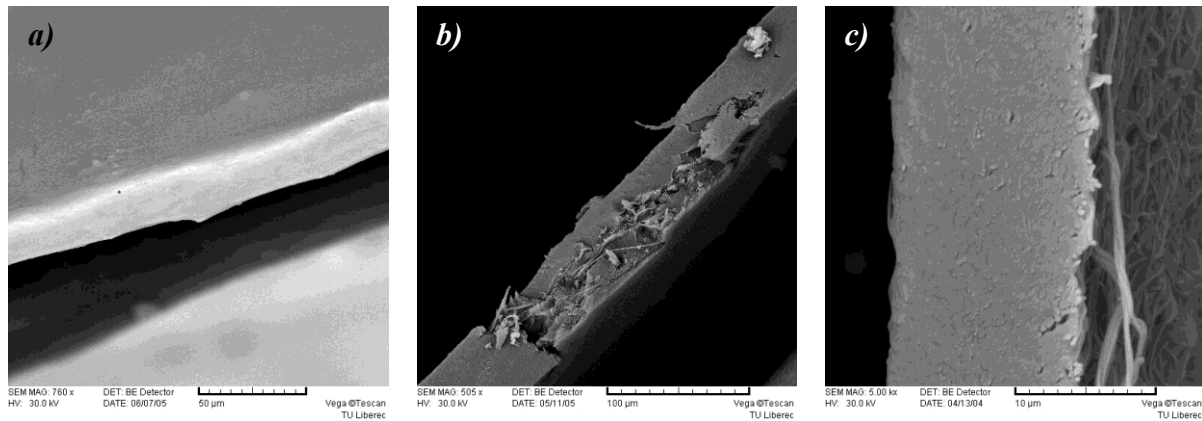


Fig.4.11: Cross sections of composite materials composed of a) polyvinyl alcohol electrospun nanofiber webs and polyester resin Lamit; b) polyvinyl alcohol electrospun nanofibers and epoxy resin Epodur; c) polyvinyl alcohol electrospun nanofibers and acrylic binder Sokrat.

Regarding the composite production process there is a very important value to express the final content of fibers inside a produced composite material. Of course, the higher content of fibers in a composite is better as is generally known from the theory of composite materials.

Thus, here all tested materials are summarized in terms of fiber content (see Tables.4.1 and Fig.4.12): (i) epoxy resin Epoxy and PVA I - the average fiber content was 15% by weight and 9% by volume; (ii) epoxy resin Epodur and PVA I - the average fiber content was 6.5% by weight and 4.8% by volume, (iii) polyester resin Lamit and PVA II - the fiber content was 26% by weight and 24% by volume; (iv) acrylate binder and polyvinyl alcohol nanofibers had the best fiber contents, about 34% by weight and 31% by volume; (v) epoxy resin Epoxy and PA6.12 – the average fiber content was 4.9% by weight and 3.1% by volume.

Tensile strength of PVA II and polyester resin Lamit composite (23.8 MPa) was about 120% better than the pure sum of tensile strengths of the nanofiber layer (PVA II – 5.8 MPa) and the specimen made from polyester resin (Lamit – 5 MPa). In case of acrylate binder and polyvinyl alcohol nanofibers the tensile strength of the composites (32.0 MPa) was about 127% better than the pure sum of the tensile strengths of the nanofiber (PVA II – 5.8 MPa) and the specimen made from the acrylic binder (Sokrat – 8.3 MPa). All final composites were transparent and had foil-like behavior.

Table.4.1: Overview of produced composites and their fiber content.

No.	Producing method	Nanofibers	Matrix	Fiber content [vol%]	Fiber content [wt%]
1	Hand lay-up	PVA	EPOXY 371/1200	2.3	-
2	Hand lay-up + US*	PVA	CHS-Epodur	4.8	6.5
3	Hand lay-up + US*	PVA	EPOXY 371/1200	9	15
4	Hand lay-up + US*	PVA	Lamit	24	26
5	Hand lay-up + US*	PVA	Sokrat	31	34

*Hand lay-up method with impregnation of nanofibrous layer by means of ultrasound.

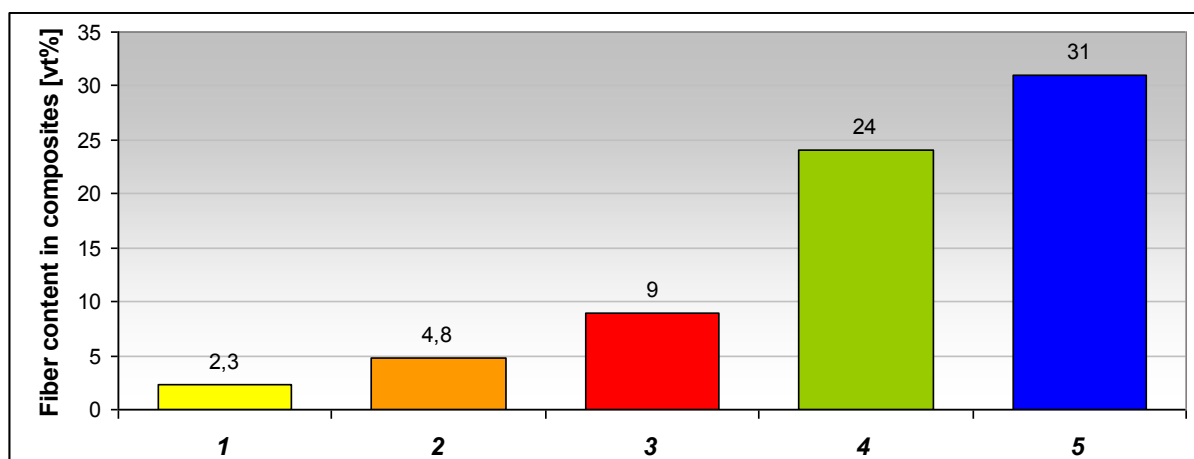


Fig.4.12: Fiber content in produced composite materials correspondent to table.4.1.

Ultrasound is not needed for low viscosity liquid matrixes. But ultrasound application for spraying the liquids can be used and different porous composites with electrospun nanofiber layers can be produced as it can be seen in Fig.4.13.

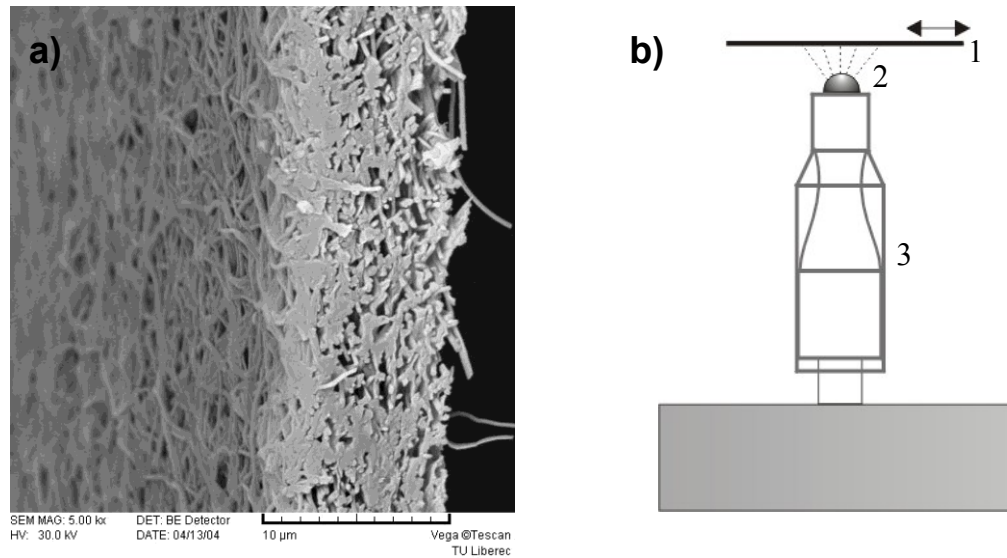


Fig.4.13: (a) Cross sections of porous composites composed of polyvinyl alcohol electrospun nanofibers and acrylic binder Sokrat. (b) Set up of the experiment for impregnation of nanofibrous layers (1 – nanofiber nonwoven material, 2 - drop of liquid matrix, 3 - ultrasonic transducer, 4 - ultrasonic generator) is on the left side. Spraying the matrix is necessary for production of porous composite materials.

The conclusion of the above mentioned details is that the method of impregnation by means of ultrasound is really good for the full impregnation of electrospun nanofiber webs especially by high viscosity liquid matrixes. However, the result mechanical properties are pure, due to the very low mechanical properties of nanofiber layers. Therefore these materials are not suitable for the production of common composites, they cannot substitute known and used fiber reinforced composite materials or foils. Very special applications of these composite materials “reinforced” with electrospun nanofiber webs have to be found where they would be useful and their low manipulating strength would not cause problems, as they will perform other functions. It is sure that a new set of tests will be necessary for this particular new application, because other matrixes and polymers for nanofiber production will be necessary. Their potential usage as filters is described in [29], but it describes mainly presumptions or dreams maybe.

The real success application of electrospun nanofiber materials in constructive composites is based on US patent 6265333 of Dzenis and Reneker [60]. The subject of the patent is a fiber reinforcement of composite material comprising a resin matrix and primary reinforcement fibers and further comprising secondary - smaller diameter (for example electrospun) reinforcement fibers at one or more ply interfaces or portion thereof.

This composite structure provides improvement in interlaminar toughness, strength, and delamination resistance without substantial reduction of in-plane properties and without substantial increase in weight. The experiments were repeated with a simplified method in the cooperation of Technical University of Liberec and (Czech Republic) and Budapest University of Technology and Economics (Hungary). The obtained results are promising.

The so called three-point test was chosen as the test method. The set of samples for three-point test consisted of: (i) primary reinforcement presented by glass nonwoven fabric made from fibers with a diameter of $12\ \mu\text{m}$; the linear density of roving was $30\ \text{tex}$, the surface mass was $300\ \text{g/m}^2$, provided by company *Ahlstrom*; (ii) secondary reinforcement with fibers of small diameter –PVA II, PAN; and resin matrix – polyester resin Viopal. Each specimen for the three-point test was composed of four different layers of primary reinforcement and each specimen (except the so called blind samples) contained three layers of electrospun layers. Glass primary reinforcements were impregnated by means of hand lay-up method.

Half of the nanofiber interlayers were impregnated separately with the help of an ultrasound device, in the same way as described in the above mentioned experiments (frequency 30 kHz, power 60 W) and then they were placed between glass fibrous material layers. The impregnation of the second half was not aided by ultrasound. Afterwards the hardened samples were submitted to a separation test. The apparent interlaminar shear strength was determined by the short-beam method for fiber reinforced plastic composites according to international standard ISO 14130:1997(E). The thickness of the prepared samples were (the thickness of specimens, b was 2 ± 0.5 mm, width of specimens, a was 10 mm, overall length was 20 mm and distance (L) between the bottom two specimen supports in the test machine was 10 mm. The test system is schematically sketched in Fig.4.14.

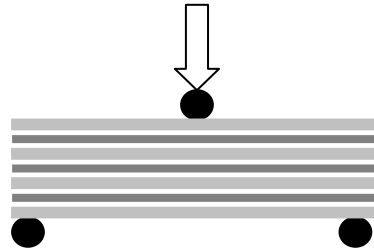
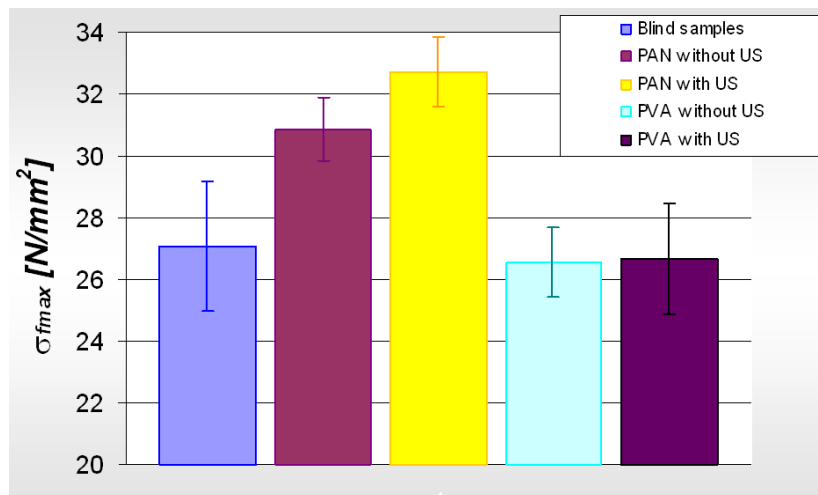


Fig.4.14: Three point bending specimen (four layers of primary reinforcement and three layers of nanofibrous materials) and test system in principle with denoted direction of loading.

The three-point bending flexural test provides values for flexural stress σ_f , response of the material. σ_{max} [N/mm²] is the flexural stress calculated according to the following equation:

$$\sigma_{f_{max}} = \frac{3F_{max}L}{2ab^2}, \text{ where } F_{max} \text{ is the reached force [N]; } L \text{ is support span length [mm]; } a \text{ is specimen width [mm] and } b \text{ is specimen thickness [mm].}$$

The main advantage of a three point flexural test is the ease of specimen preparation and testing. However, this method has also some disadvantages: the results of the testing method are sensitive to specimen and loading geometry and strain rate.



Samples	Average σ_{max} [N/mm ²]	Standard deviation [N/mm ²]	Average σ_{LSS} [N/mm ²]	Total fiber content [wt%]	Total fiber content [vol%]
Blind samples	27,06	2,10	2,71	37,5	26,9
PAN without US	30,87	1,03	3,09	32,3	24,7
PAN with US	32,73	1,13	3,27	33,8	26,7
PVA without US	26,57	2,24	2,66	28,0	21,9
PVA with US	26,67	1,81	2,67	29,3	23,9

Fig.4.15: Final results from three-point tests of composites reinforced with both glass mats and nanofibrous layers in comparison with composites reinforced only with glass mats. Table presents also values of interlaminar shear strength of the composite materials and total fiber content in final composites.

The three-point test showed (see Fig.4.15) – in accordance with the previously mentioned experiments with only nanofibrous layer as reinforcement – that polyvinyl alcohol nanofibers are not suitable reinforcement for both epoxy and polyester resins. The polyvinyl alcohol nanofibrous layer behaves rather as a separator than as reinforcement. However, good results were achieved from testing composites with polyacrylonitrile nanofibers as secondary reinforcement. The previous figure shows 14% growth in the flexural stress of composites reinforced with secondary PAN reinforcement (*PAN without US*) compared to blind samples reinforced only with primary reinforcement (*Blind samples*). A more obvious result is the increase of flexural stress when using polyacrylonitrile electrospun layers previously impregnated with resin by means of ultrasound (growth is 21% in comparison with blind samples). The success was continued by another testing of a more suitable electrospun nanofiber material from polyacrylonitrile as an interlayer in composites used for the production of aircraft propellers, where serious delamination problems in some parts of the vane can appear during utilization.

It is also necessary to have some knowledge on nanofiber orientation in the electrospun nanofiber web; and also on the alignment, direction and orientation of these fibers to be able to design and predict the properties of result composites. Based on the literature review it was found that several research teams have studied the possibilities of electrospun nanofiber alignment but none of them did the complete examination or used their methods on a larger amount of nanofibers. The five techniques listed below are examples of the overall possible techniques to align electrospun nanofibers [29]: a cylinder collector at high rotation speed, an auxiliary electrode/electrical field, a thin wheel with a sharp edge collector, a frame collector and a multiple electrostatic field technique.

The effect of electrospun fiber orientation in composites has not been properly studied yet in experiments. The problem is not easy to solve because to produce a continuous uniform electrospun nanofiber web with nanofibers oriented in the preferred way is technologically very complicated. This is why the question is still unsolved.

At the end of the chapter it is necessary to review why research in the electrospun nanofiber reinforced composite field is not easy regarding the experimental part. It is necessary to realize that characteristics known for classic fibers can be interpreted in a completely different way in case of nanofibers. When a diameter of fibers is hundred times smaller, then their surface is hundred times larger. The surface area of cross section of fibers is ten thousand times smaller and thus tensile manipulating strength is smaller. Transverse strength of these fibers depends on the cube of fiber diameter and flexural rigidity is determined by the biquadrate of fiber diameter. Brittleness of fibers, expressed by the ratio of diameter of circle in which the fiber can be folded in without rupture to fiber diameter, has a linear character. These phenomena complicate manipulation with nanofiber layers during their subsequent treatment and during composite manufacturing, too.

4.4. Conclusions

Chapter 4 is devoted to the production of composite materials reinforced with electrospun nanofibers in the so-called wet way, where liquid matrix impregnates the nanofibrous reinforcement. The method is the easiest composite producing method, but the nontraditional reinforcement brings new facts to the process.

The very important conclusion is that it is necessary to help the highly viscous matrix to impregnate the electrospun nanofibrous reinforcement. One possibility which was described in this thesis and has really good results is the application of ultrasound enhancement. The usage of ultrasound helps impregnation and also the removal of air bubbles from all the volume of the forming composite material.

Another important but predictable fact is that the lower matrix viscosity is, the higher fiber content in the final composite material can be reached (see Table.4.1 and Fig.4.15). Nevertheless, the fiber content depends strongly on the skillfulness of the producer and the production process, on the number of layers in the final composite material, the wetting ability of fibrous materials by the resin and related surface properties or efficient surface modification of the fibrous material with respect to the properties of liquid matrix, also fiber form is very important with respect to the final composite material fiber content* (uniaxial orientation, two-directional orientation – for example woven fabrics, random orientation of fibers in plane – nonwoven materials, three-dimensional textile materials) etc.

* An example can be prepared from glass fiber reinforced composite materials to illustrate the effect of fiber orientation on fiber content, where uniaxial fiber orientation means approximately 70 wt% fiber content, woven fabric means approximately 50 wt% and random oriented fibrous materials about 20 wt% [2].

4.5. References

- [1] Campbell, F., C.: Manufacturing Processes for Advanced Composites; Elsevier Advanced Technology, Great Britain, 2004, ISBN 1-8561-7415-8
- [2] Bareš, R. : Kompozitní materiály (Composite materials), SNTL, Prague 1988
- [3] Agarwal, B., D., Broutman, L., J.: Vláknové kompozity (Fiber reinforced composites), SNTL, Prague, 1987
- [4] Chawla, K.,K.: Composite Materials: Science and Engineering, Springer, Second Edition, 2001, ISBN 0387984097
- [5] Stokes, R., J., Evans, D.,F.: Fundamentals of Interfacial Engineering, Wiley-VCH, USA, 1997, ISBN 0-471-18647-3
- [6] Chung, D.: Carbon Fiber Composites, Butterworth-Heinemann, 1994, ISBN 0750691697
- [7] Mallick, P.: Fiber-Reinforced Composites: Materials, Manufacturing and Design, Second Edition, Marcel Dekker,1993, ISBN 0824790316
- [8] Miravete, A.: 3-D textile reinforcements in composite materials, Woodhead Publishing Ltd., 1999, ISBN 1855733765
- [9] Long, A., C.: Design and manufacture of textile composites, Woodhead Publishing Ltd., 2005, ISBN 1855737442
- [10] Košťáková, E.: Přehled technologií výroby kompozitních materiálů s vláknennou výztuží a plastovou maticí (Survey of manufacturing technologies of composites consisting from fiber reinforcement and polymer matrix), work to Ph.D. exam, 2004, Liberec
- [11] Bhushan, B.: Springer Handbook of Nanotechnology, Springer (2004), ISBN 3-540-01218-4
- [12] Hillert, M., Lange, N.: The structure of graphite filaments, Zeitschr. Kristall., Vol. 111, pg. 24-34 (1958)
- [13] Hughes, T., V., Chambers, C., R.: US patent 405,480 (1889)
- [14] Maruyama, B., Alam, A.: Carbon nanotubes and nanofibers in composite materials, SAMPE J. Vol. 38, pg. 59-70 (2002)
- [15] Schutzenberger, P., Schutzenberger, L.: Sur quelques faits relativa a l'histoire du carbone, C.R. Academy of Science Paris, Vol .111, pg. 774-778 (1890)
- [16] Pélabon, D., Pélabon, H. : Sur une variété de carbone filamenteux, C. R. Academy of Science Paris, Vol. 137, pg. 706-708 (1903)
- [17] Iijima, S. : Nature 354, pg. 56 (1991)
- [18] Iijima, S., Ichihashi, T. : Single-shell carbon nanotubes of 1nm diameter, Nature, Vol. 363, pg. 603-605 (1993)
- [19] Bethune, D., S., Kiang, C., H., de Vries, M., S., Gorman, and co.: Cobalt-catalysed growth of carbon nanotubes with single-atomic-layer walls, Nature, Vol. 363, pg. 605-607 (1993)
- [20] Ledoux, M., J., Vieira, R., Pham-Huu, C., Keller, N.: New catalytic phenomena on nanostructured (fiber and tubes) catalysts, Journal of Catalysis, 216 (2003), pg.333-342
- [21] Robertson, S., D.: Nature Vol. 221, pg. 1044 (1969)
- [22] Lam, Hoa Le: Electrospinning of single wall carbon nanotube reinforced aligned fibrils and yarns, a thesis, Drexel University, 2004,
- [23] Ko, F., et al.: Electrospinning of continuous carbon nanotube-filled nanofiber yarns, Advance Materials, Vol. 15(14), pg. 1161-5 (2003)
- [24] Ge, J., J., et al.: Assembly of well-aligned multiwalled carbon nanotubes in confined polyacrylonitrile environments: electrospun composite nanofiber sheets, J. Am. Chem. Soc., Vol. 126 (4), pg. 15754-61 (2004)
- [25] Ko, F., K., et al.: Carbon Nanotube Reinforced Spider Silk – A model for the Next Generation of Super Strong and Tough Fibers, In: Proceedings of the 19th American society for composites annual technical conference, USA (2004)
- [26] Ko, F., K., et al.> Electrospun carbon nanotube reinforced silk fibers, World patent, WO2005045122 (2005)
- [27] Kim, G., M., Michler, G., H., Pötschke, P.: Deformation processes of ultrahigh porous multiwalled carbon nanotubes/polycarbonate composite fibers prepared by electrospinning, Polymer, Vol. 46, Issue 18, 2005, pg.7346-7351,
- [28] Ye, H., Lam, H., Titchenal, N., Gogotsi, Y., Ko., F.: Reinforcement of rupture behavior of carbon nanotubes-polymer nanofibers, Applied physics letters, Vol. 85, No. 10, 2004pg. 1775-1777
- [29] Huang, Z.-M., Zhang, Y.-Z., Kotaki, M., Ramakrishna, S.: A review on polymer nanofibers by electrospinning and their applications in nanocomposites, Composites Sciences and Technology, 63 (2003), 2223-2253
- [30] Chronakis, I.: Novel nanocomposites and nanoceramics based on polymer nanofibers using electrospinning process – A review, Journal of Materials Processing Technology, Vol.167, 2005, pg 283-293
- [31] Finegan, I., C., Tibbetts, G., G., Glasgow, D., G.: Surface treatments for improving the mechanical properties of carbon nanofiber/thermoplastic composites, Journal of Material Science, Vol. 38 (16), pg.3485-90 (2003)
- [32] Finegan, I., C., Tibbetts, G., G., Gibson, R., F.: Modeling and characterization of damping in carbon nanofiber/polypropylene composites, Composite Science and Technology, Vol. 63(11), PG. 1629-35 (2003)
- [33] Koelling, K., et al.: Characterization of Nanoparticle/Polymer Melt Composites, AIP Conference Proceedings, Vol. 712, Issue 1, pg. 316-320 (2004)
- [34] DeMora, M., et al.: Applications of Carbon nanofiber and Nanotube Polymer Composites, Available online at World Wide Web 8.2.2005: http://www.er6.eng.ohio-state.edu/~CE_REGNER/Proposal.htm
- [35] Hammel, E., et al.: Carbon nanofiber for composite applications, Carbon, Vol. 42, pg.1153-1158 (2004)

- [36] Park, C., et al.: Polymer – Single Wall Carbon Nanotube Composites For Potential Spacecraft Application, Available online at 8.2.2005: <http://techreports.larc.nasa.gov/ltrs/PDF/2002/cr/ica-se-2002-36.pdf>
- [37] Tai, H., N., Weh, M., K., Liu, J., H.: Enhancement of the mechanical properties of carbon nanotube/phenolic composites using a carbon nanotube network as the reinforcement, *Carbon*, Vol. 42 (12-13), pg. 2774-7 (2004)
- [38] Gojny, F., H., et al.: Carbon nanotube-reinforce epoxy –composites.: enhanced stiffness and fracture toughness at low nanotube content, *Composite Science and Technology*, Vol. 64 (15), pg. 2363-71 (2004)
- [39] Thostenson, E., T., Chou, T., W. : Aligned multi-walled carbon nanotube-reinforce composites : processing and mechanical characterization, *Journal of Physics D*, Vol, 35(16), Pg. 77-80 (2002)
- [40] Frogley, M., D., Ravich, D., Wagner, H., D.: Mechanical properties of carbon nanoparticle-reinforced elastomers, *Composite Science and Technology*, Vol.63 (11), pg.1647-54 (2003)
- [41] Nasa Technological Briefs, 2004, Pg.46NASA TSP MSC 23301 “Elastomer Filled with Single-Wall Carbon nanotubes”
- [42] R.H. Baughman, A.A. Zakhidov, W.A. deHeer, ‘Carbon nanotubes the route toward application’, *Science* 2002, Vol. 297. Issue 787. pg. 92.
- [43] K.H. Lau, D. Hui, ‘The revolutionary creation of new advanced materials – carbon nanotube composites’, *Composites Part B*, Vol. 33(4). Issue 263. pg. 46 (2002)
- [44] B. Maruyama, K. Alam, ‘Carbon nanotubes and nanofibers in composite materials’, *SAMPE J*, Vol. 38(3). Issue 59. pg.70 (2002)
- [45] E.T. Thostenson, Z.F. Ren, T.W. Chou, ‘Advances in the science and technology of carbon nanotubes and their composites: a review’, *Composites Science and Technology*, Vol. 61(13). Issue 1899. pg. 912 (2001)
- [46] Borchardt, J., K.: Nanotechnology providing new composites, *Reinforced Plastics*, pg. 36-39, November 2003
- [47] Dalton, A. B., C. Stephan, et al.: Selective interaction of a semiconjugated organic polymer with single-wall nanotubes, *Journal of Physical Chemistry B*, Vol. 104, Issue 43, pg. 10012-10016, (2000)
- [48] Iwahori, A., Ishiwata, S., Ishikawa, T.: Mechanical properties of CFRP using CNF (carbon Nano-Fiber) dispersed resin. In: Proceedings of the 14th international conference on composite materials (ICCM-14), San Diego (2003)
- [49] Available online at <http://webpages.sdsmt.edu/~hfong/1.1.html>
- [50] Chand, S.: Review: Carbon fibers for composites, *Journal of Material Science* 2000, Vol.36, Issue 1303, Pg.13
- [51] Dzenis, Y., A., Wen, A., K.: Continuous carbon nanofibers for nanofiber composites, *Material Research Society Symposium Proceedings* 2002, Vol.702, Issue 173, Pg.8
- [52] X.Y. Wang, S. Serrano, J., J. Santiago-Aviles, ‘Conductivity measurement of electrospun PAN-based carbon nanofibers’, *Journal of Material Science Letters*, Vol. 21 (13), Issue 1055, pg. 7 (2002)
- [53] Zussman, E. et al.: Mechanical and structural characterization of electrospun PAN-derived carbon nanofibers, *Carbon*, Vol. 43, pg.2175-2185 (2005)
- [54] Fennessey, S., F., Farris, R., J.: Fabrication of aligned and molecularly oriented electrospun polyacrylonitrile nanofibers and the mechanical behavior of their twisted yarns, *Polymer*, Vol. 45, pg 4217-4225 (2004)
- [55] Gu, S., Y., Ren, J., Wu, Q., L.: Preparation and structures of electrospun PAN nanofibers as a precursor of carbon nanofibers, *Synthetic Metals*, Vol. 155, pg. 157-161 (2005)
- [56] Wang, Y., Serrano, S., Santiago-Avilés, J., J.: Raman characterization of carbon nanofibers prepared using electrospinning, *Synthetic Metals*, Vol. 138, pg. 423-427 (2003)
- [57] Kim, J-S., Reneker, D., H.: Mechanical properties of composites using ultrafine electrospun fibres, *Polymer composites* 1999, Vol.20(1), Issue 124, Pg.31
- [58] Kim, J-S.: Improved mechanical properties of composites using ultrafine electrospun fibers, PhD.Dissertation, The Graduate Faculty of The University of Akron 1997
- [59] Bergshoeff, M., M., Vancso, G., J.: Transparent nanocomposites with ultrathin electrospun Nylon-4,6 fiber reinforcement, *Advanced Materials* 1999, Vol.11(16), Issue1362, Pg.5
- [60] Dzenis, Y., A., Reneker, D., H.: Delamination resistant composites prepared by small diameter fiber reinforcement at ply interfaces, US Patent No.626533, 2001
- [61] Jirsák, O.; Sanetrník, F.; Lukáš, D.; Kotek, V.; Martinová, L.; Chaloupek, J.; CZ Patent, 294274 (B6), A Method of nanofibers production from polymer solution using electrostatic spinning and a device for carrying out the method WO 2005024101 (2005).
- [62] Kostakova, E., Polachova, J., Krsek, J.: Electrospun Nanofiber Nonwoven Web as a Reinforcement for Composite Materials, *Strutex 04 Proceedings*, Liberec – Czech Republic, 2004, ISBN 80-7083-891-4
- [63] Shoh, A.: *IEEE Trans. Sonics and Ultrasonics* 1975, Vol.22 (2), Pg.60
- [64] Huang, Y., D., Liu, L., Qiu, H., Shao, L.: Influence of ultrasonic treatment on the characteristics of epoxy resin and the interfacial property of its carbon fiber composites, *Composites science and technology* 2002, Vol.62, Pg.2153
- [65] Stor-Pellinen, J., Haeggstrom, E., Luukkala, M.: Measurement of the effect of high-power ultrasound on wetting of paper, *Ultrasonics* 2000, Vol.38, Pg.953
- [66] Kostakova, E., Meszaros, L., Gregor, J.: Composite nanofibers produced by modified electrospinning method; *Material Letters*, Vol.63, pg.2419-2422 (2009)
- [67] Yarin, AL, Zussman, E. *Polymer* 2004;45:2977-80

5. General Conclusions

The presented work goes from the basic theoretical descriptions of liquid behavior in contact with solid capillary, through their experimental verifying with textile material as solid porous systems, through introduction of computer simulations studying equilibrium states and wetting process dynamics, to the particular example of the previous knowledge usage for the special composite material production.

The review on wetting, in section 2.2, brings not only generally known models but also nontraditional solutions of Lucas-Washburn equation and except the cylindrical capillary model also model of the radial capillary. In addition, it is also devoted to the specific drops penetration into porous materials and ultrasound enhancement of liquid penetration. Wetting experiments, in section 2.3, are based on the experimental procedure with new, more accurate principle – the method of pixel calculation. These experiments dealing mainly with drops penetration into nonwoven materials show except expected also several interesting new results:

i) Both theoretical (the solutions of Lucas-Washburn equation, see the subsection 2.2.1 and in Appendix I) and experimental analysis (see the subsection 2.3.3 – Volume fraction effects) of the dynamics of drops penetrating into fibrous structures observation leads to allometric relations (exponential relations) $V=kt^\alpha$, where V is penetrated volume; k is constant; t is time and α is a scaling exponent. Experimentally was found dynamics of drop penetration into nonwovens depends significantly on nonwovens volume fraction. The two different dynamic regimes are graphically shown there and can be described by the exponent α . The drops penetration into bulky nonwovens follows regime where $\alpha=1$. Thus the penetration follows the third solution of Lucas-Washburn equation for downward liquid flow. On the other hand, the drops penetration into nonwovens with higher volume fraction of fibers follows regime with $\alpha=1/2$. Thus the penetration agrees mainly with the first solution of Lucas-Washburn equation for horizontal capillary flow. The question for additional research is whether there is any other regime with a different exponent α and where is the boundary volume fraction between these two penetration dynamic regimes.

ii) The third suction regime is described here. The radial capillary model introduced only two suction regimes. Although according drops observation during their penetration into nonwovens, there exists clearly the third regime in initial phase of penetration. The regime characteristics are described in subsection 2.3.4.

iii) Usage of ultrasound as an enhancement of liquid penetration is efficient only for high viscous liquids as epoxy resin described in the subsection 2.3.3. The drop penetration dynamics with usage of ultrasound follow also the third solution of Lucas-Washburn equation. The drops penetration follows regime with $\alpha=1$; apparently the liquid flow is guided over the needle, which transmits ultrasound, and the vibration minimizes the viscosity effect.

The second part, devoted to computer simulation of wetting phenomena based on Auto models and Monte Carlo method, brings these very interesting results:

i) The exact thermodynamical temperature determination, according to statistical temperature input to this type of simulation, is shown in subsection 3.3.1 and exactly agree with Schukin theory. This is very important for all these simulation results explanation and their comparison with real wetting processes. Such experimental (using computer simulation as it was described here) agreement with Schukin theoretical predictions was not published yet, as the author knows.

ii) The computer simulations describe easy possibility how to show and study liquid body inside the fibrous material after a drop penetration in the subsection 3.3.1, what is not possible in real experiments.

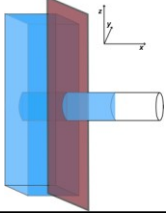
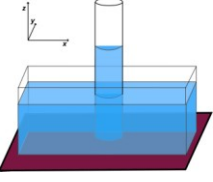
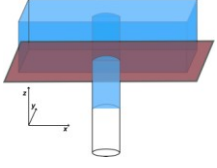
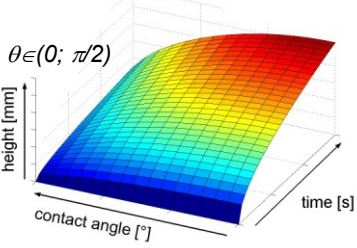
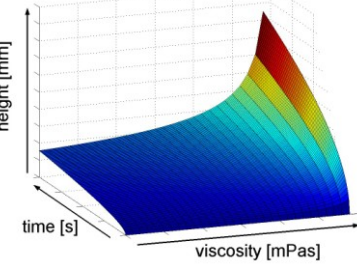
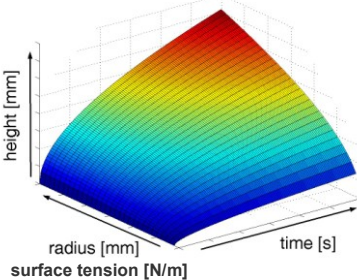
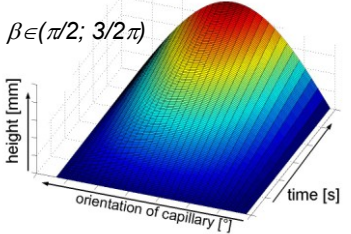
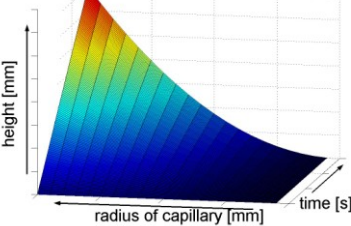
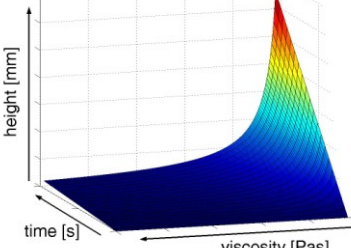
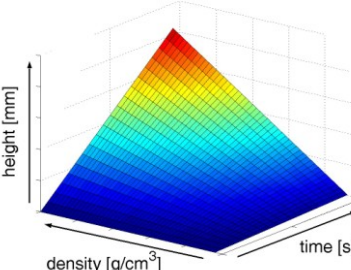
iii) Special situations, when liquid with contact angle 180° , are studied by the computer simulations in the subsection 3.3.1 too. The situations are not easy to use in real wetting experiments. The computer simulation shows there is possibility when such liquid cannot escape from fibrous material.

iv) Dynamics of capillary wetting processes is described for the first time in the subsection 3.3.2. Real proofs that the computer simulation (both liquid wicking into cylindrical capillary and drop penetration into the radial capillary) is able to simulate some wetting process of porous material are presented here. Unfortunately now there cannot be done any clearly explanation why in some cases it works and in other the simulation does not work according theoretical presumptions. There is necessary to continue in this study deeply.

The last part, introduced real application of knowledge from the first and the second parts. Novel (new, untraditional) composite material, combination classical fiber reinforcement and electrospun nanofibers, manufacturing and testing is written here, to complement previous two parts of the work.

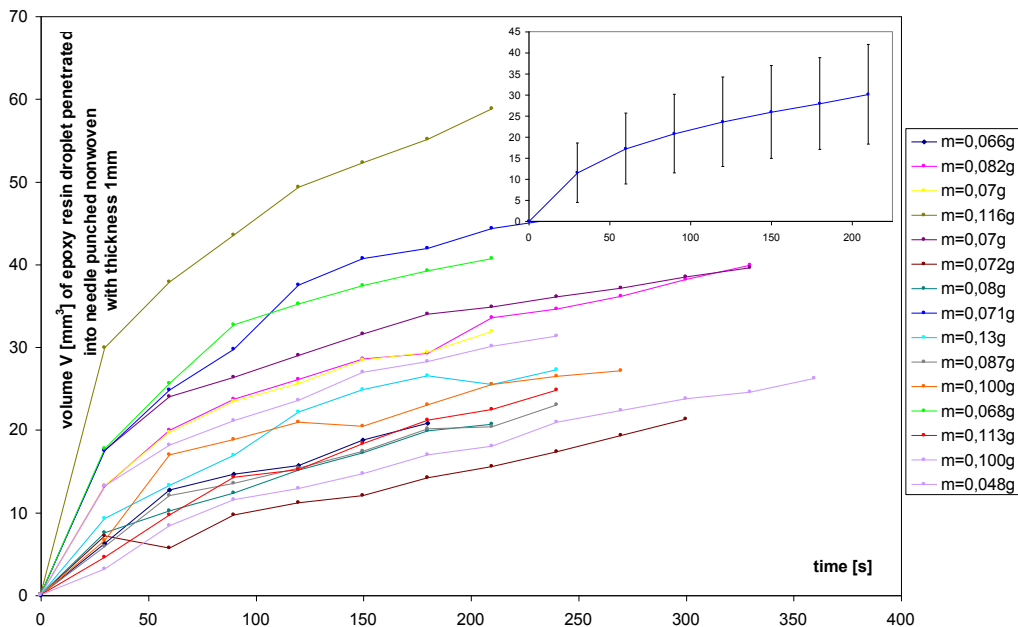
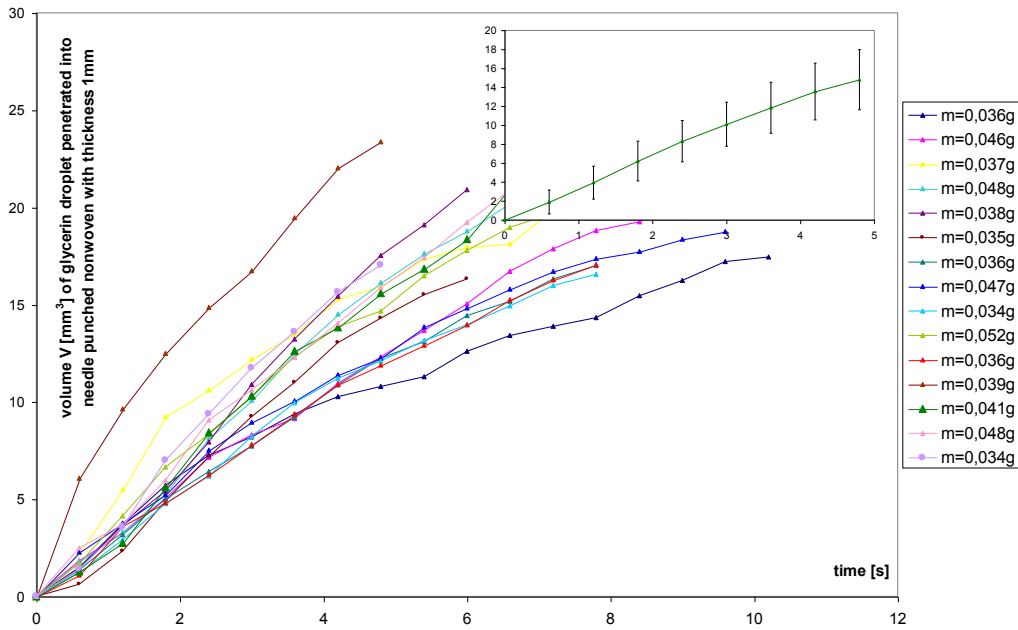
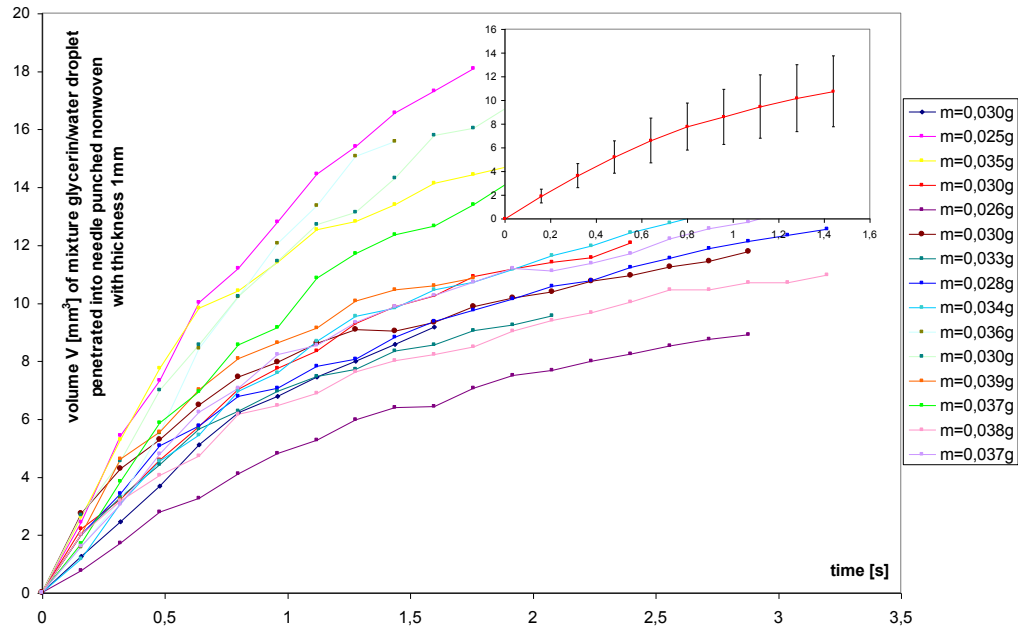
Appendixes

APPENDIX I: Summary of all three solutions of Lucas-Washburn equation of a liquid penetration into a cylindrical capillary for three limiting orientation of a capillary.

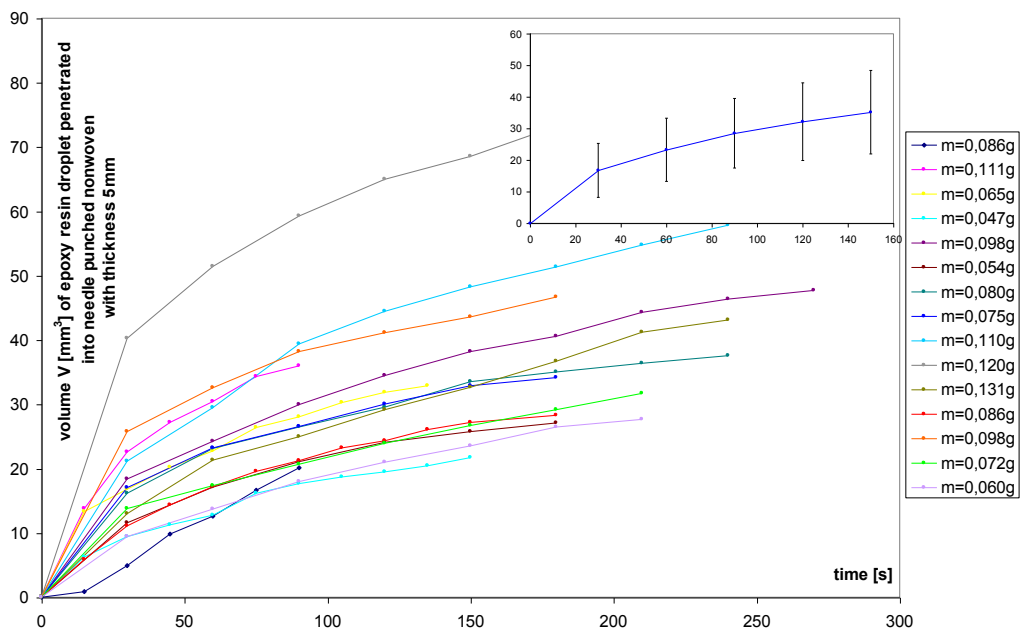
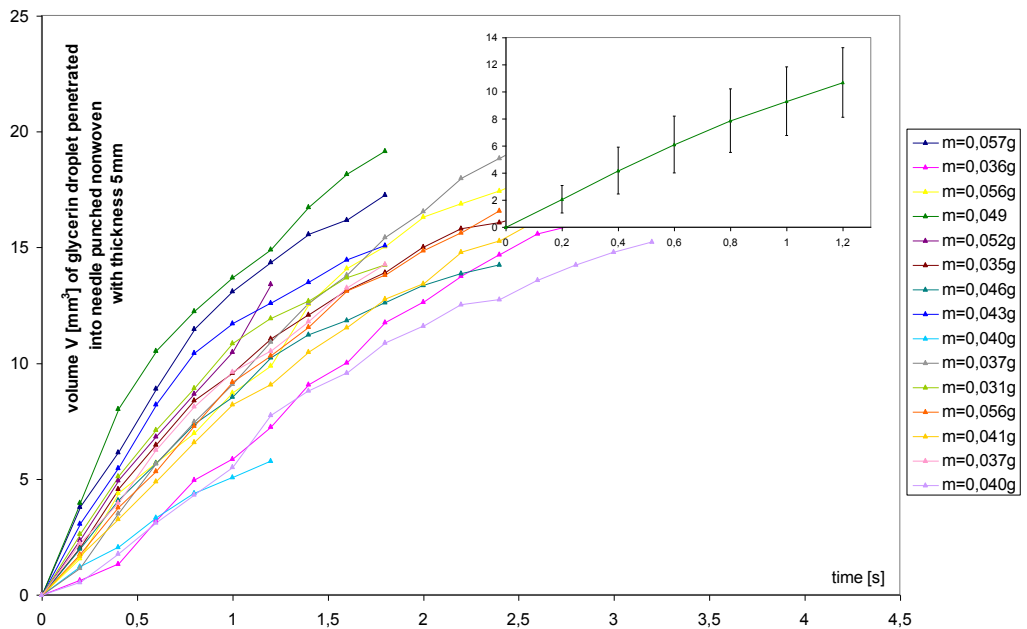
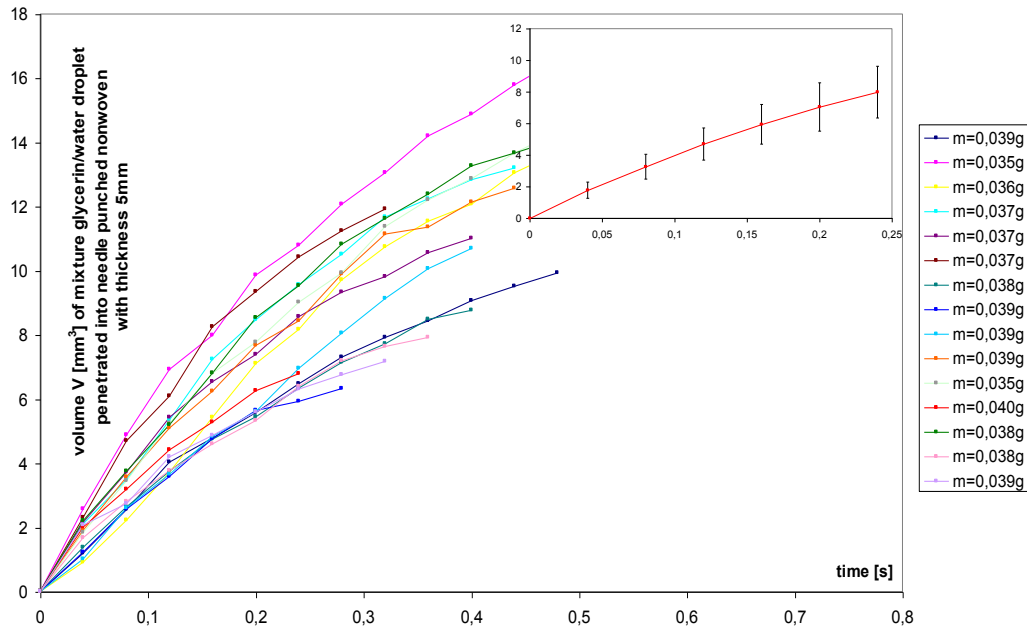
Orientation of a capillary		
		
<p>Lucas-Washburn's theoretical assumptions of a liquid penetration into cylindrical capillary <i>h...height, r...radius of capillary, γ...surface tension, μ...viscosity, θ...contact angle, g...gravitational coefficient, ρ...density, β...angle of capillary's orientation, t...time</i></p>		
$h = \sqrt{\frac{r\gamma \cos \theta}{2\mu} t}$    <p>The process does not depend on gravitation and density of liquid.</p>	$t = -\frac{4h\mu}{r\gamma \cos \theta} - \frac{16\gamma \cos \theta \mu}{r^3 (\rho g \cos \beta)^2} \ln \left(1 - \frac{\rho g \cos \beta}{2\gamma \cos \theta} h \right)$ <p>A solution of function above for $h(t)$ can be realized by means of a series expansion.</p> $h = \sqrt{\frac{r\gamma \cos \theta}{2\mu} t}$ <p><i>If the second equation term on the right side of Lucas-Washburn equation so-called gravitational term can be neglected behavior of the studying system is exactly alike a liquid penetration into cylindrical capillary oriented horizontally. Then the process does not depend on gravitation and density of liquid.</i></p>	$h = -\frac{r^2 \rho g \cos \beta}{8\mu} t$     <p>The process does not depend on surface tension and contact angle.</p>

APPENDIX II: Graphs (for individual droplets represented by weight m) relating to influence of three liquid's viscosities to drop's penetration into three materials

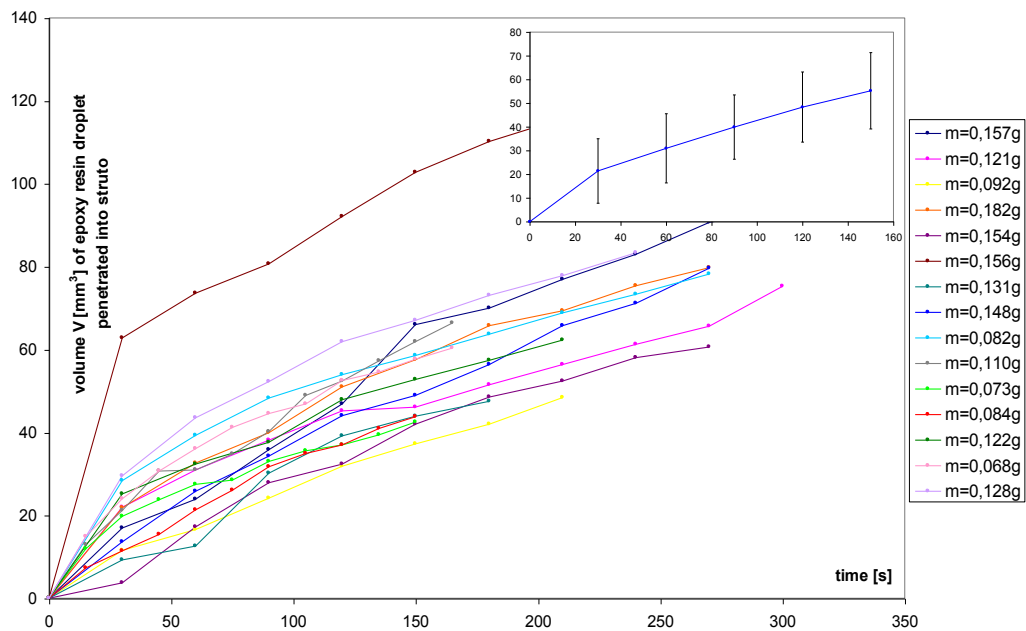
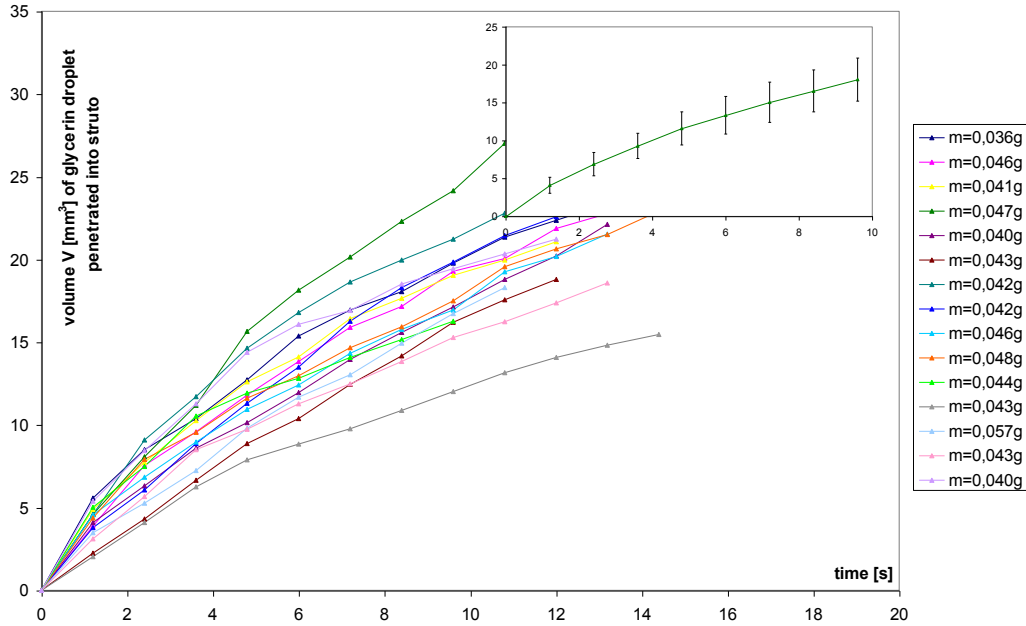
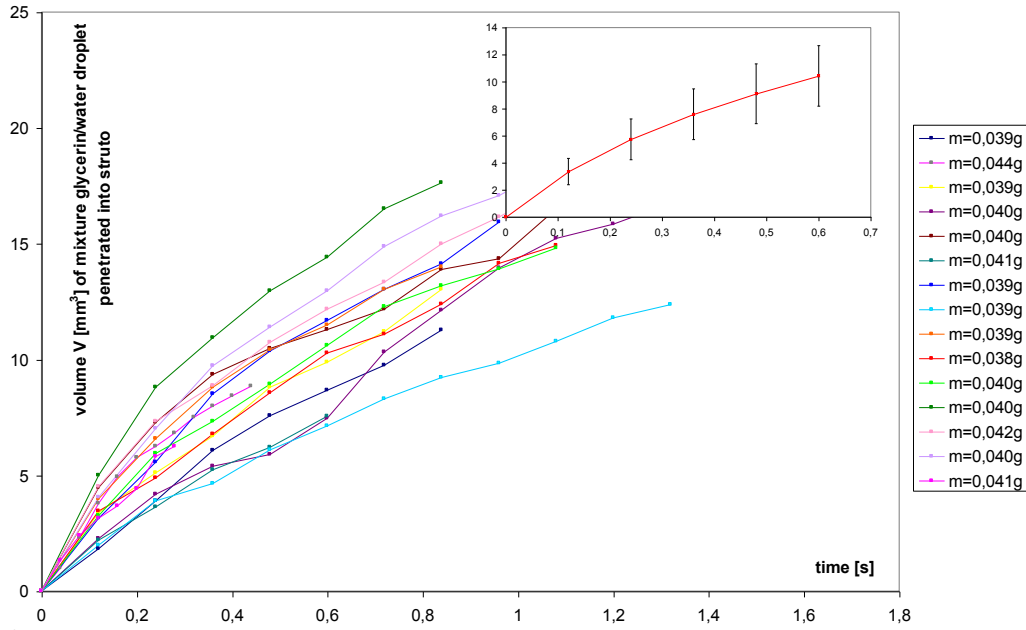
1) NEEDLE PUNCHED NONWOVEN (1 mm)



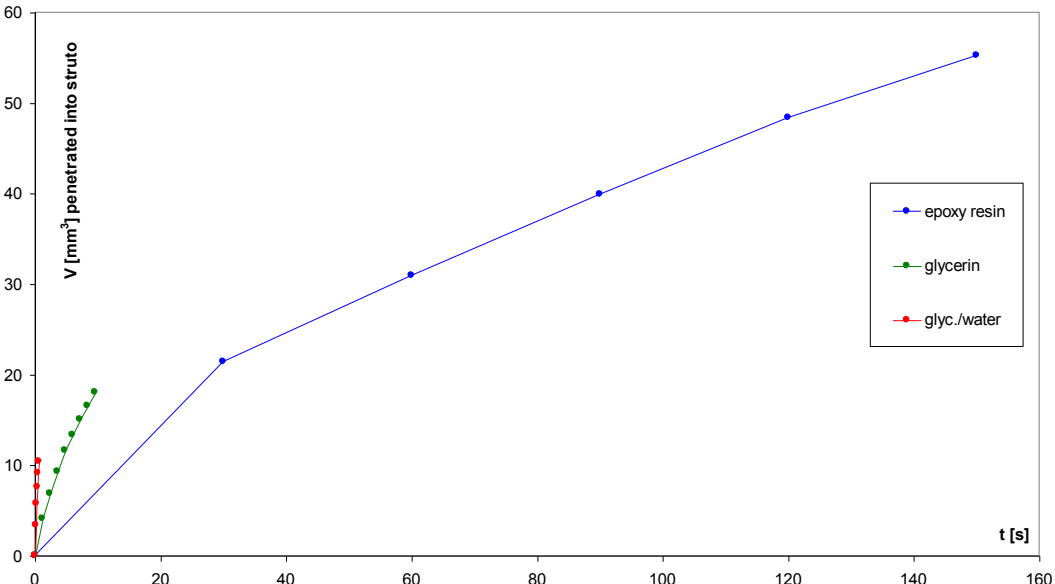
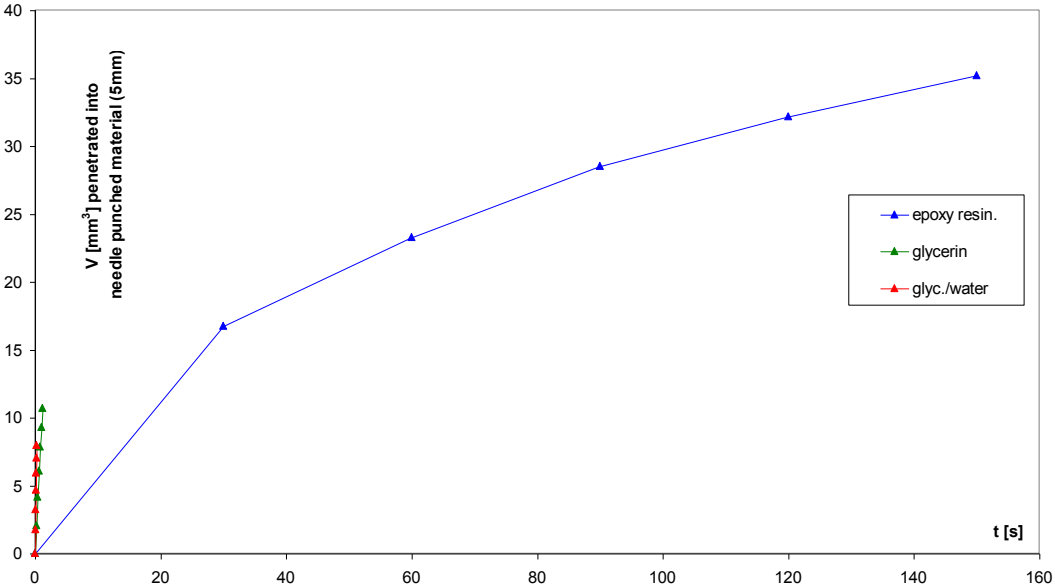
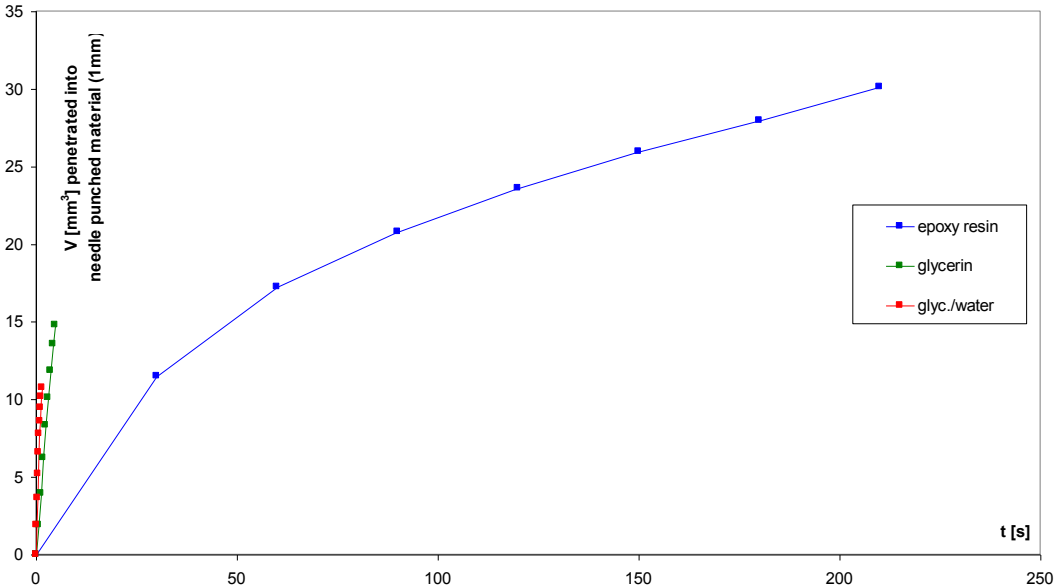
2) NEEDLE PUNCHED NONWOVEN (5 mm)



3) STRUTO



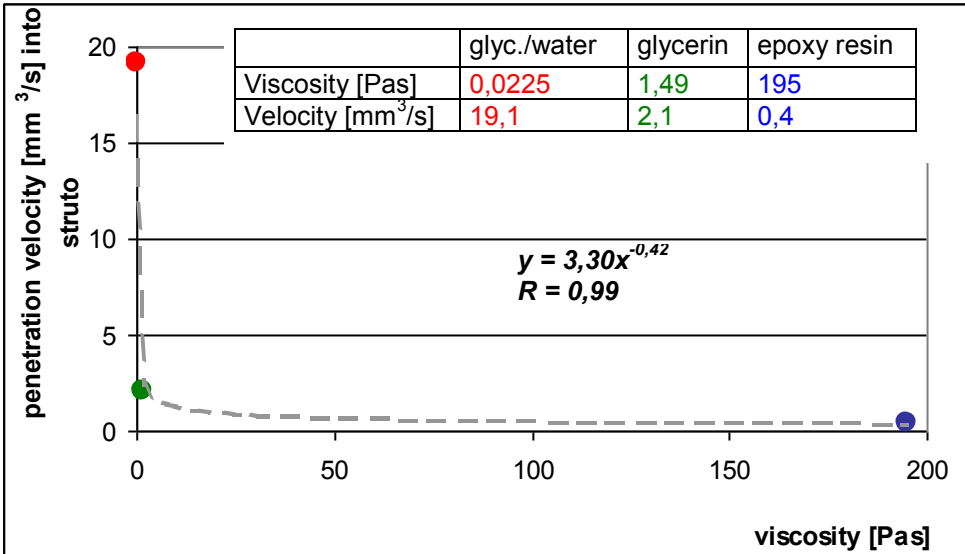
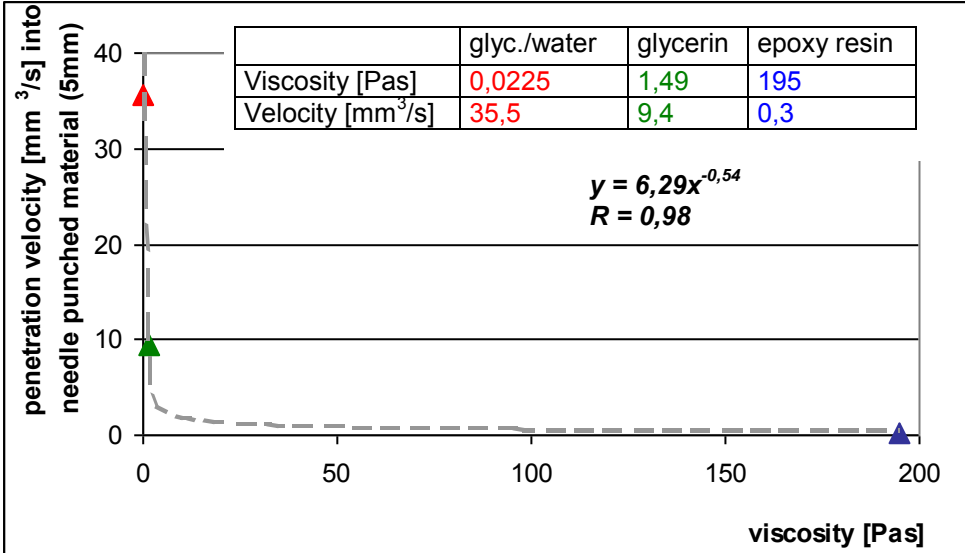
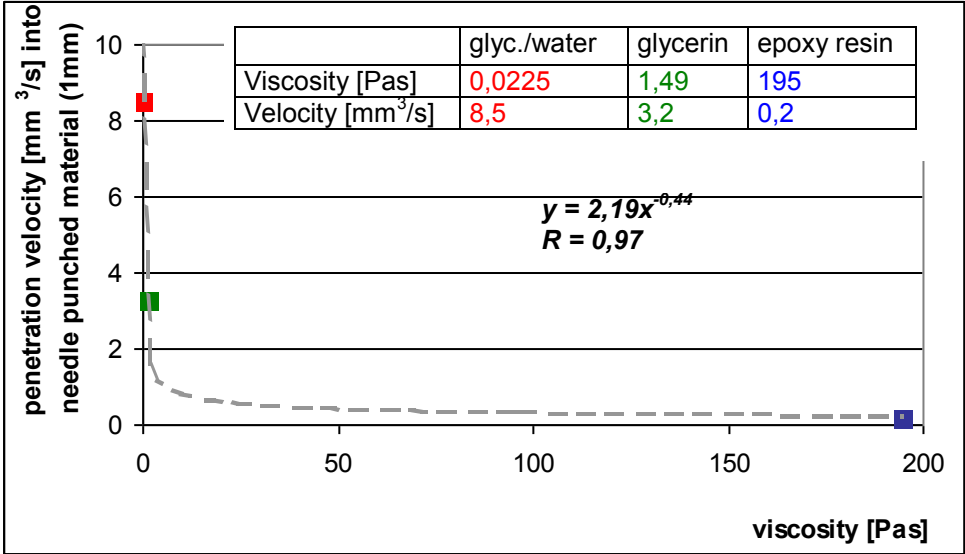
APPENDIX III: Complete graphs and table relating to influence of viscosity to drop's penetration into three types of nonwovens and a table presenting data approximation using linear and polynomial functions.



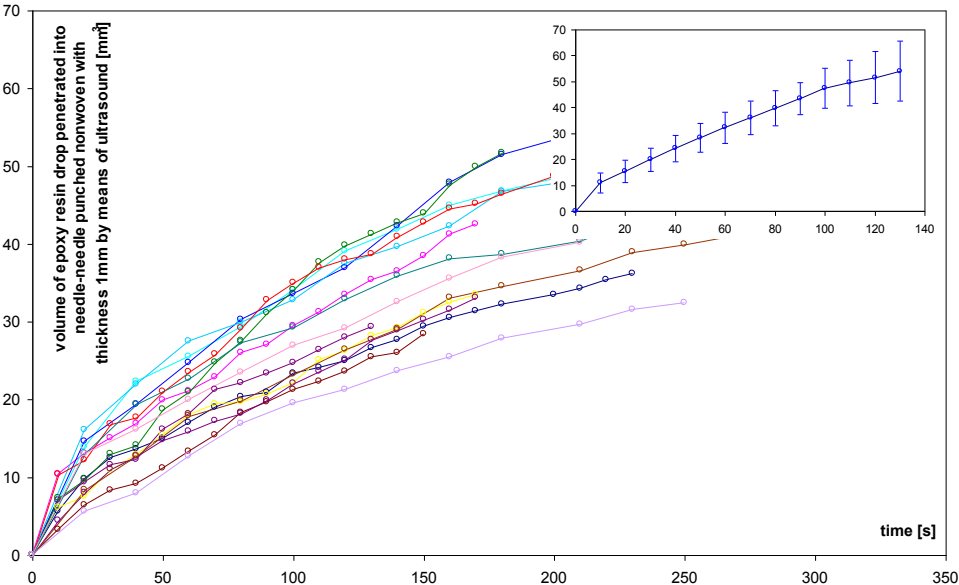
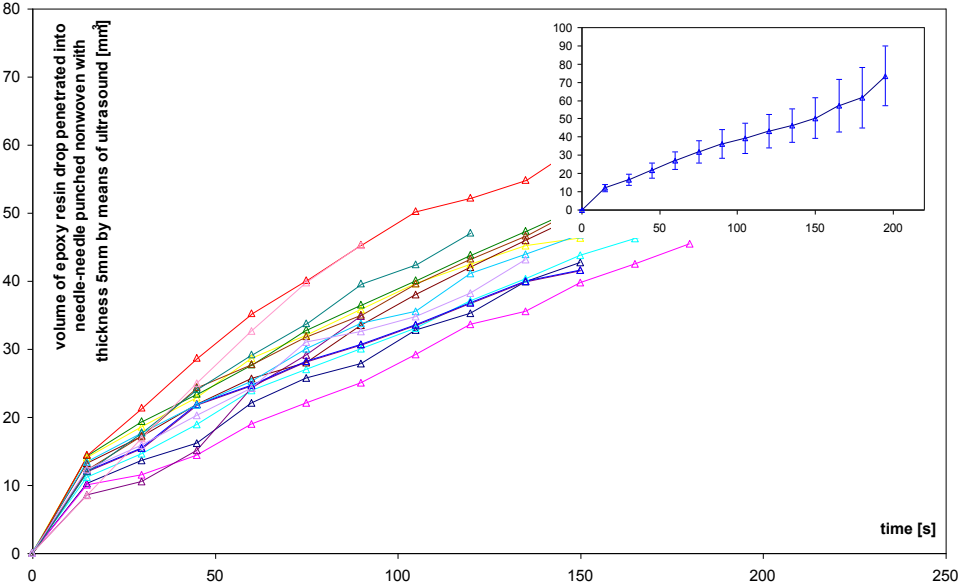
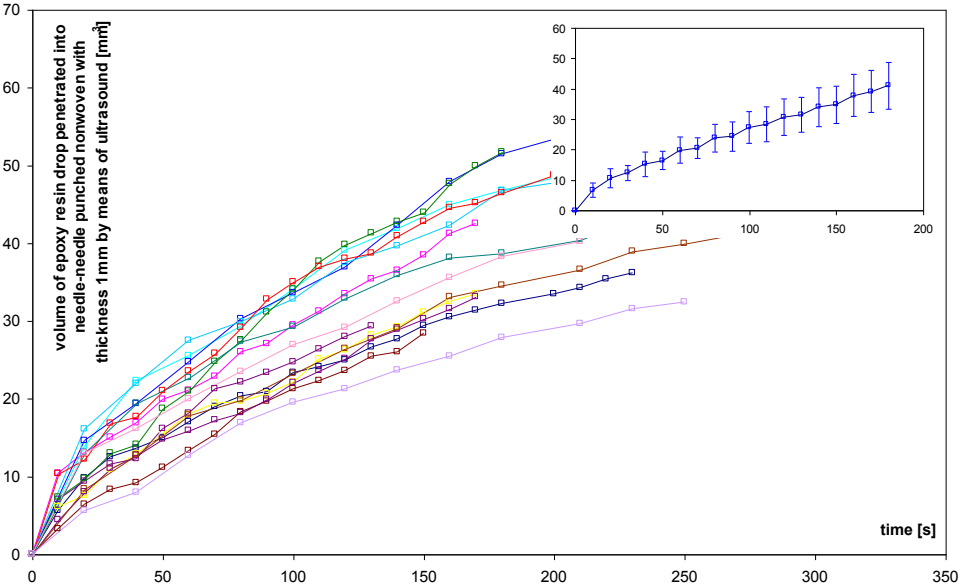
V (t)		<i>Type of regression</i>	<i>Function</i>	<i>Regression coefficient - R</i>
Needle-punched nonwoven <i>t=1mm</i>	Epoxy resin	linear	$y=0,1694x$	0,8696
		polynomial	$y= - 0,0008x^2 +0,3039x$	0,9848
	Glycerin	linear	$y=3,2395x$	0,9973
		polynomial	$y= - 0,1143x^2 +3,6752x$	0,9994
	Glycerin/water	linear	$y=8,4682x$	0,9677
		polynomial	$y= -3,4927x^2 +12,439x$	0,9998
Needle-punched nonwoven <i>t=5mm</i>	Epoxy resin	linear	$y=0,2749x$	0,8920
		polynomial	$y= - 0,0018x^2 +0,4941x$	0,9889
	Glycerin	linear	$y=9,3792x$	0,9951
		polynomial	$y= - 1,9743x^2 +11,293x$	0,9998
	Glycerin/water	linear	$y=35,514x$	0,9914
		polynomial	$y= - 49,093x^2 +45,03x$	0,9999
Struto	Epoxy resin	linear	$y=0,4077x$	0,9561
		polynomial	$y= - 0,0018x^2 +0,6237x$	0,9836
	Glycerin	linear	$y=2,0818x$	0,9695
		polynomial	$y= - 0,1213x^2 +3,0064x$	0,9983
	Glycerin/water	linear	$y=19,1260x$	0,9724
		polynomial	$y= - 17,996x^2 +27,96x$	0,9990

V²(t)		<i>Type of regression</i>	<i>Function</i>	<i>Regression coefficient - R</i>
Needle-punched nonwoven <i>t=1mm</i>	Epoxy resin	linear	$y=4,4453x$	0,9977
		polynomial	$y=-0,0036x^2 +5,0559x$	0,9996
	Glycerin	linear	$y=39,356x$	0,9549
		polynomial	$y=7,937x^2 +9,1023x$	0,9981
	Glycerin/water	linear	$y=77,379x$	0,9875
		polynomial	$y=20,211x^2 +54,402x$	0,9955
Needle-punched nonwoven <i>t=5mm</i>	Epoxy resin	linear	$y=8,5698x$	0,9976
		polynomial	$y=-0,012x^2 +9,8232x$	0,9998
	Glycerin	linear	$y=83,213x$	0,9635
		polynomial	$y=59,251x^2 +25,786x$	0,9985
	Glycerin/water	linear	$y=236,88x$	0,9699
		polynomial	$y=747,58x^2 +91,967x$	0,9984
Struto	Epoxy resin	linear	$y=19,256x$	0,9925
		polynomial	$y=0,0453x^2 +13,697x$	0,9998
	Glycerin	linear	$y=31,402x$	0,9861
		polynomial	$y=1,5596x^2 +19,513x$	0,9987
	Glycerin/water	linear	$y=170,65x$	0,9885
		polynomial	$y=121,75x^2 +110,88x$	0,9987

Graphs showing relations between velocity of drop penetration and viscosity of used liquids for three different used nonwoven materials. Numbers of velocity were taken from linear regression of graphs mentioned above in this appendix.

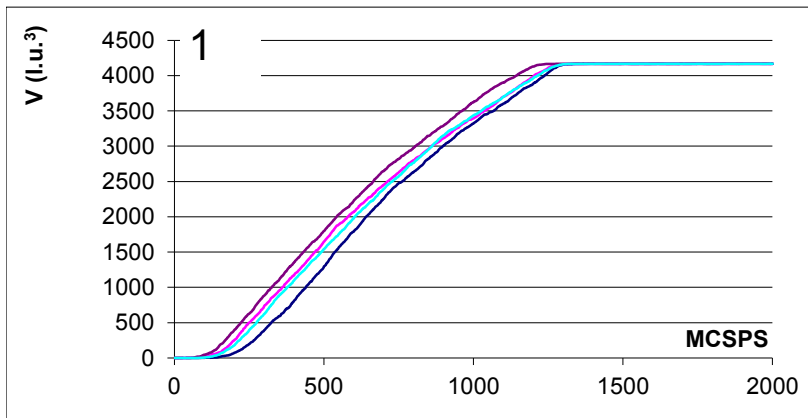


APPENDIX IV: Graphs (for individual droplets) relating to dynamics of penetration enhanced by ultrasound of epoxy resin into three types of nonwoven materials



APPENDIX V: Results from drop penetration into radial capillary simulations.

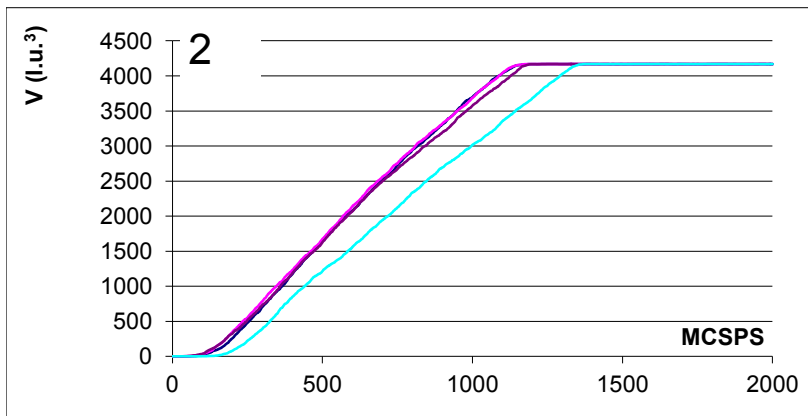
Change of distance between plates of the radial capillary



d=4 l.u.

average regression line*	R
y=3,73x-289	0,995

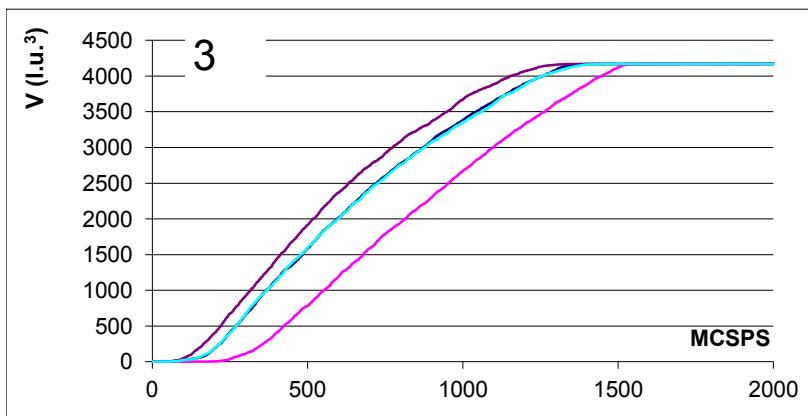
* for data from interval MCSPS (300-1200)



d=3 l.u.

average regression line*	R
y=3,97x-453	0,999

* for data from interval MCSPS (300 -1200)

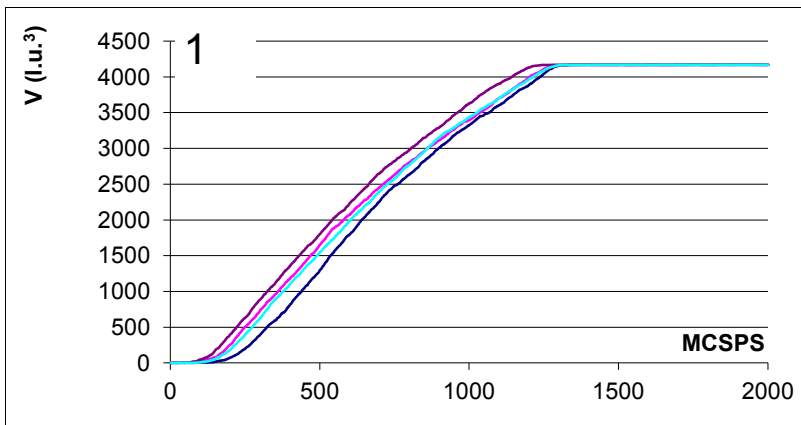


d=5 l.u.

average regression line*	R
y=3,43x-230	0,994

* for data from interval MCSPS (300 - 1200)

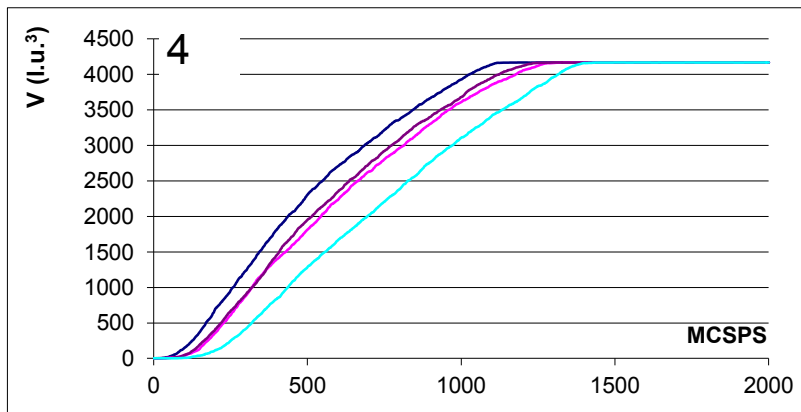
Change of the simulation box size



Z = 120x120x70

average regresion line*	R
$y=3,73x-289$	0,995

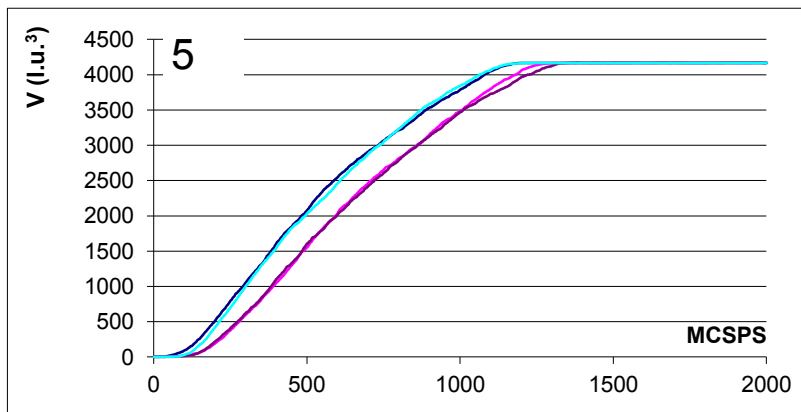
* for data from interval MCSPS (300-1200)



Z = 100x100x60

average regresion line*	R
$y=3,51x+50$	0,995

* for data from interval MCSPS (300-1200)

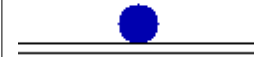
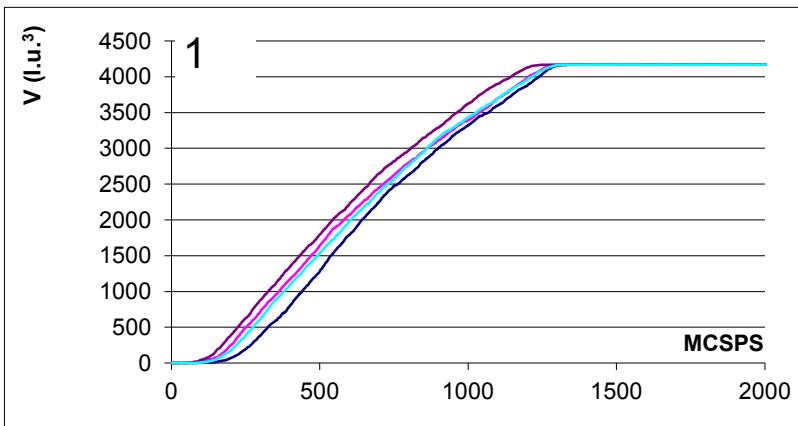


Z = 160x160x90

average regresion line*	R
$y=3,68x-41$	0,992

*for data from interval MCSPS (300-1200)

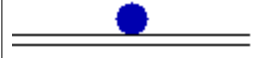
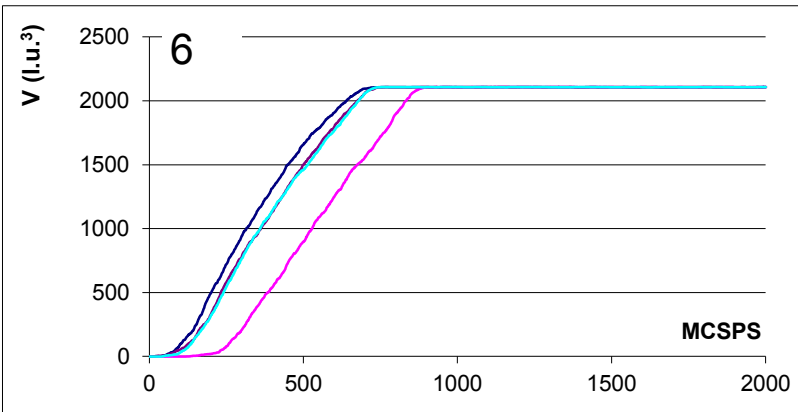
Change of the drop (liquid sphere) diameter in the initial configuration



rk=10 l.u.

average regression line*	R
$y=3,73x-289$	0,995

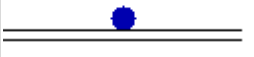
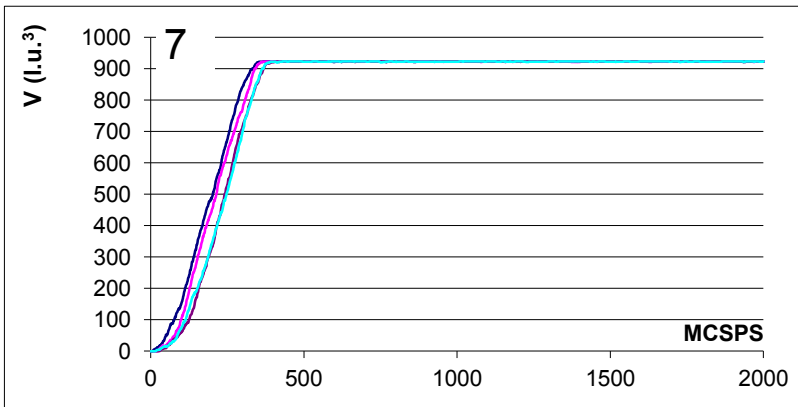
* for data from interval MCSPS (300-1200)



rk=8 l.u.

average regression line*	R
$y=3,50x-382$	0,999

* for data from interval MCSPS (200 - 600)

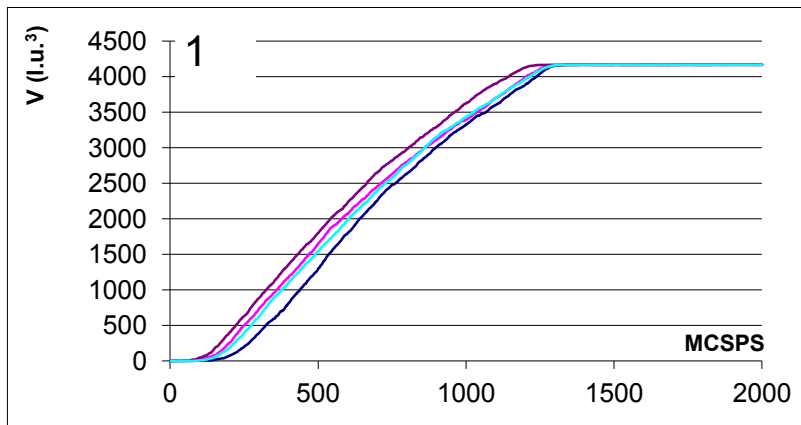


rk=6 l.u.

average regression line*	R
$y=3,30x-255$	0,999

*for data from interval MCSPS (100-300)

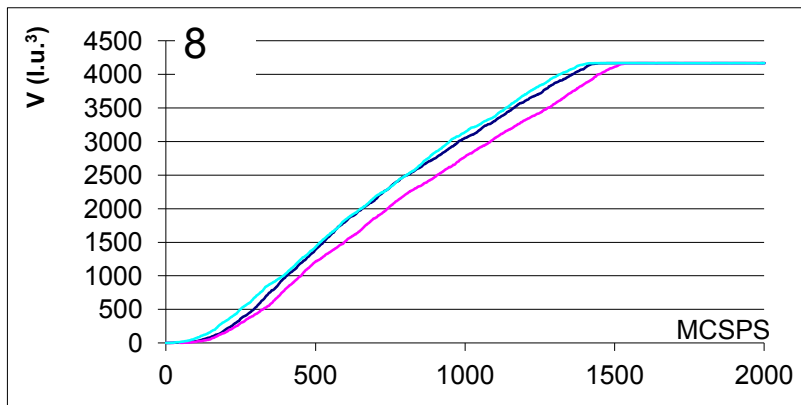
Change of contact angle



$\theta=60^\circ$

average regression line*	R
$y=3,73x-289$	0,995

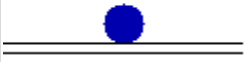
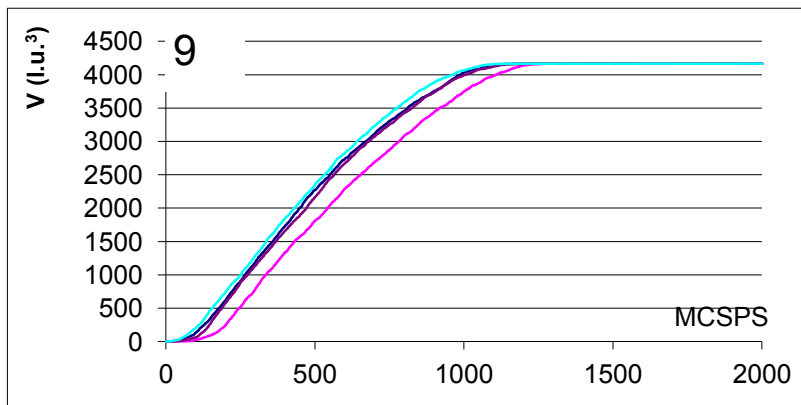
* for data from interval MCSPS (300 - 1200)



$\theta=90^\circ$

average regression line*	R
$y=2,82x-234$	0,997

*for data from interval MCSPS (100-700)



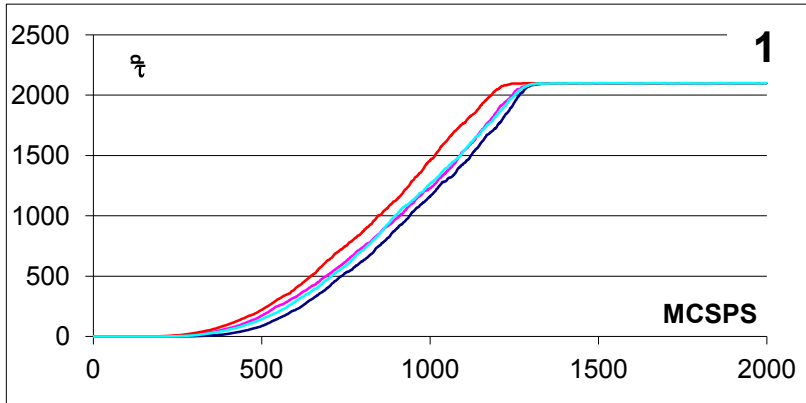
$\theta=0^\circ$

average regression line*	R
$y=5,09x-434$	0,999

*for data from interval MCSPS (100-700)

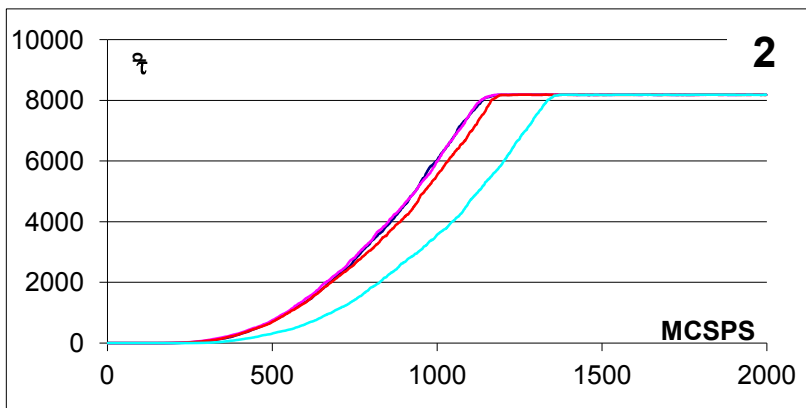
APPENDIX VI: Results from drop penetration into radial capillary simulations.
Influence of the dimensionless time τ_p on MCSPS.

Change of distance between plates of the radial capillary



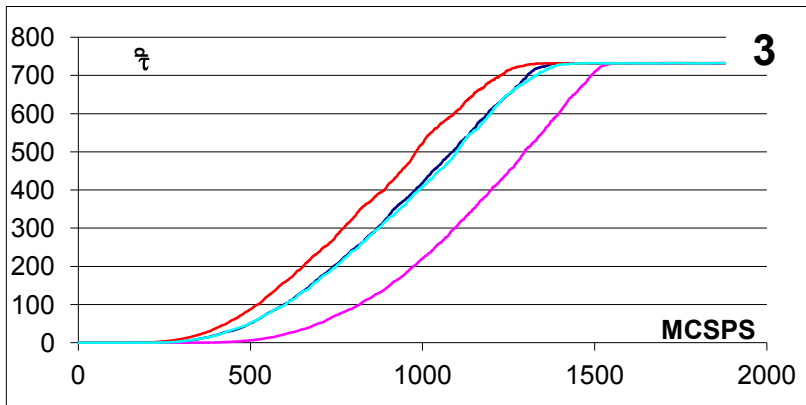
d=4

average regresion line*	R
y=2,850x-1560	0,9971
* for data from interval MCSPS (800-1300)	



d=3

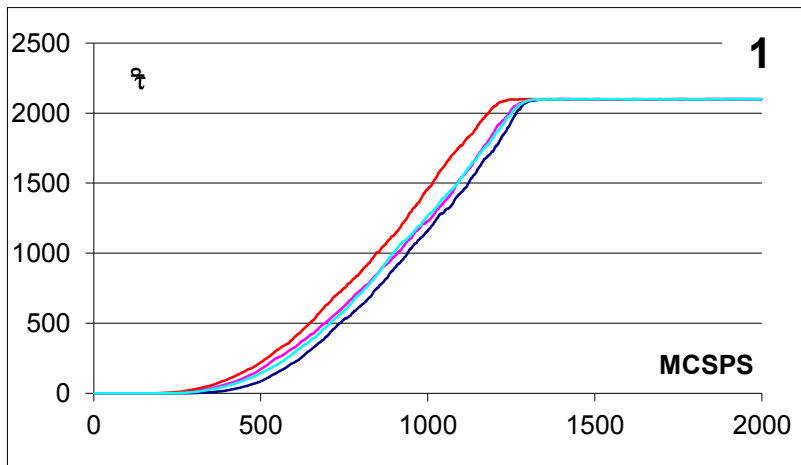
average regresion line*	R
y=11,805x-6514	0,9971
* for data from interval MCSPS (700-1100)	



d=5

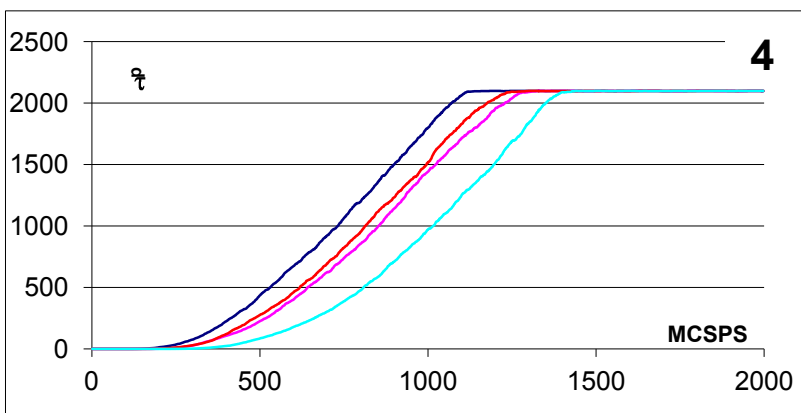
average regresion line*	R
y=0,821x-428	0,9973
* for data from interval MCSPS (700-1100)	

Change of the simulation box size



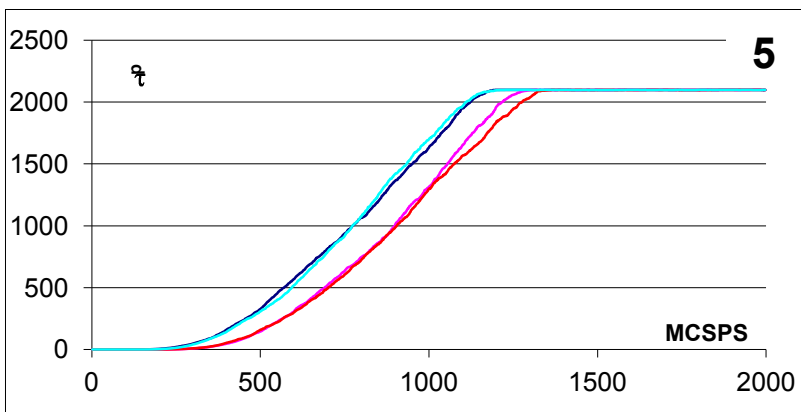
Z = 120x120x70

average regresion line*	R
y=2,850x-1560	0,9971
* for data from interval MCSPS (800-1300)	



Z=100x100x60

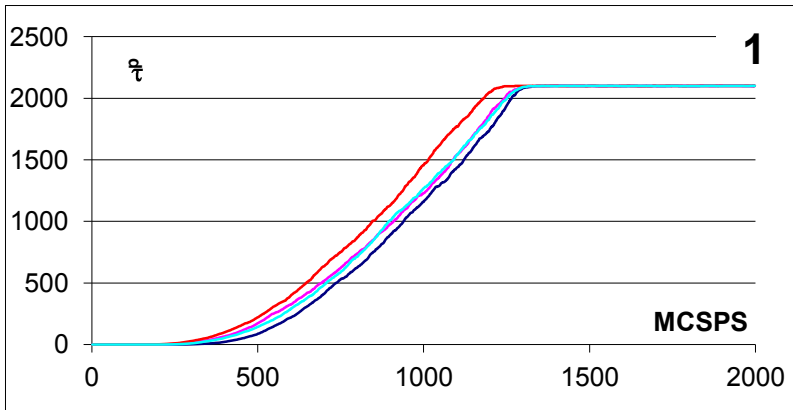
average regresion line*	R
y=2,755x-1312	0,9989
* for data from interval MCSPS (700-1100)	



Z=160x160x90

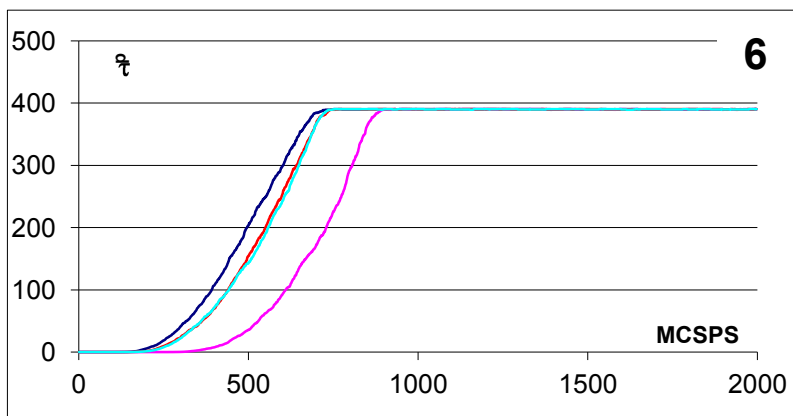
average regresion line*	R
y=2,881x-1384	0,9985
* for data from interval MCSPS (700-1100)	

Change of the drop (liquid sphere) diameter in the initial configuration



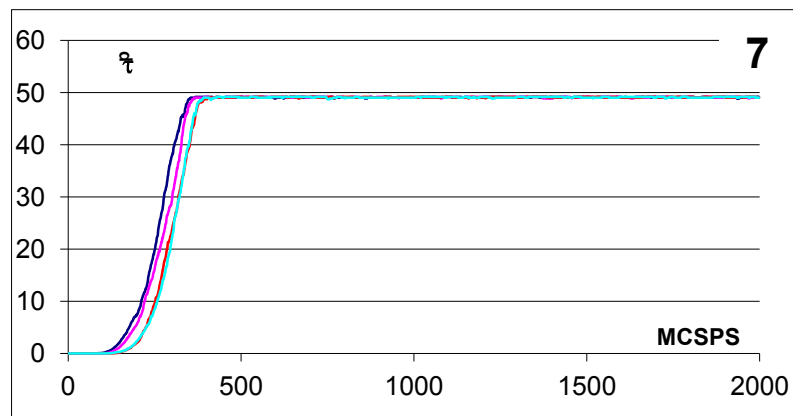
$rk=10$

average regression line*	R
$y=2,850x-1560$	0,9971
* for data from interval MCSPS (800-1300)	



$rk=8$

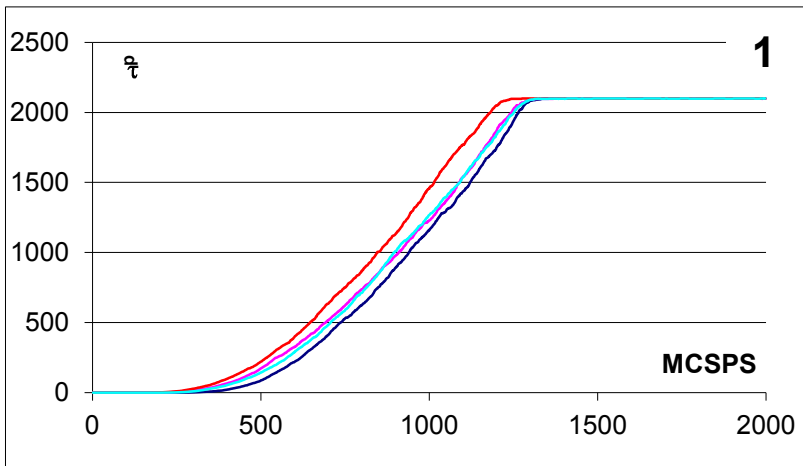
average regression line*	R
$y=0,770x-238$	0,9829
* for data from interval MCSPS (300-700)	



$rk=6$

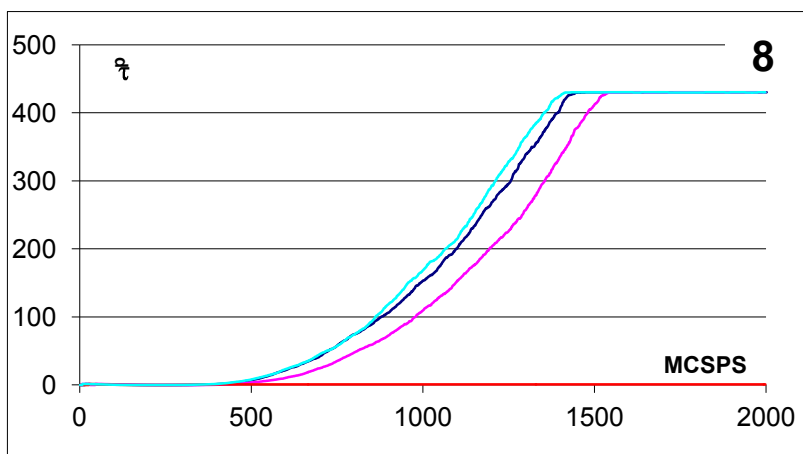
average regression line*	R
$y=0,238x-45$	0,9886
* for data from interval MCSPS (200-300)	

Change of contact angle



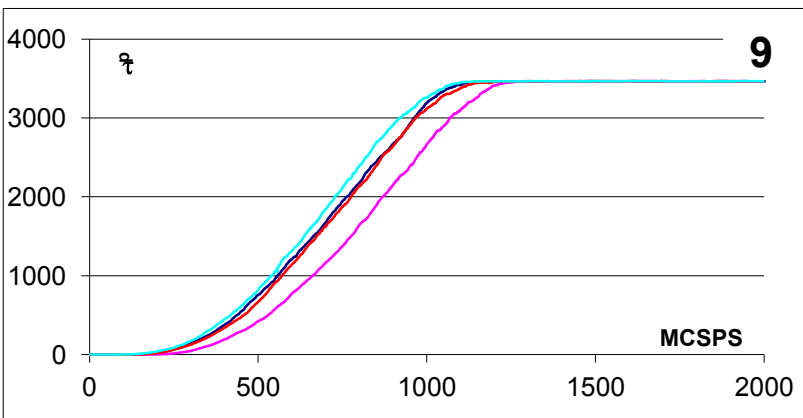
$\theta=60^\circ$

average regression line*	R
$y=2,850x-1560$	0,9971
* for data from interval MCSPS (800-1300)	



$\theta=90^\circ$

average regression line*	R
$y=0,585x-443$	0,9953
* for data from interval MCSPS (900-1400)	



$\theta=0^\circ$

average regression line*	R
$y=4,73x-1690$	0,9978
* for data from interval MCSPS (400-1000)	

APPENDIX VII: And example of computer simulation program written in program language C++ in software Borland C++ corresponding with subsection 3.3.1 (Liquid-gas interface at various temperatures)

```

/* monitoring the density profile in the surface layer between the liquid and gas for kT=200 */

#include<graphics.h>
#include<stdlib.h>
#include<stdio.h>
#include<conio.h>
#include<math.h>
#include<float.h>
#include<time.h>

#define SMERX 100
#define SMERY 100
#define SMERZ 30

//global variables
int a[SMERX][SMERY][SMERZ];
int cas,krok,pockr=100,pocspin,kont,kont1,n,hustota;
int x,y,z,i,j,l,xk,yk,zk,xv,yv,zv,apomoc,apomoc1,rez1=50,rez2=50,rez3=10,x1,x2,y1,z1,yp,zp,
int indikator;
int _rtl_close(int handle);
float Cgg=-40.,Cll=-30.,Cgl=-1.,Cgf=21.,Cfl=-2.,kT=200.,deltaH,Z,fi=.87266,theta,pi=3.1415,vzdal,energie=0.;
/* interaction energies Cgg - gas-gas,Cll- liquid-liquid,Cgl- gas-liquid*/
float J[4][4]={{Cgg,Cgl,0.,Cgf},{Cgl,Cll,0.,Cfl},{0.,0.,0.,0.},{Cgf,Cfl,0.,0.}};
float G=0.;
int sig=10;
char str[25];
float
enkap1,envz1,engpr,enpred,enkap2,envz2,engpo,enpo,evrstvy,eevrstvy,ebunky1,ebunky,ekontaktu,MCS=0.,MCS
=0.;
int main(void)
/*****/
//regularly repeating part – opening libraries
{ FILE *vystup1,*vystup0,*vystup3,*vystup2;
/*request auto detection*/
int gdriver = DETECT, gmode, errorcode;
int y, ymax;
/*initialize graphics and local variables*/
initgraph(&gdriver, &gmode, "c:\\TC\\BGI");
/*read result of initialization*/
errorcode =graphresult();
/*an error occured*/
if (errorcode != grOk)
{ printf("Graphics error: %s/n",grapherrormsg(errorcode));
printf("Press any key to halt:");
getch();
exit(1); }
setfillstyle(1,0);
/*****/
//SYSTEM
//original values of a file a[][],gas=0,liquid=1, fiber=3
for(x=0;x<SMERX;x++)
{for(y=0;y<SMERY;y++)
{for(z=0;z<SMERZ;z++)
{a[x][y][z]=0;}}}

randomize();

```

```

//INPUT OF LIQUID
for(x=0;x<SMERX;x++)
    {for(y=0;y<SMERY;y++)
        {for(z=0;z<15;z++)
            {a[x][y][z]=1;}}}

//GRAPHIC OUTPUT (x,y)
for(x=0;x<SMERX;x++)
    {for(y=0;y<SMERY;y++)
        {putpixel(x,4*SMERZ-z,a[x][y][rez1]);}
    }
//GRAPHIC OUTPUT (x,z)
for(x=0;x<SMERX;x++)
    {for(z=0;z<SMERZ;z++)
        {putpixel(x,2*SMERZ-z+20,a[x][rez2][z]);}
    }
//GRAPHIC OUTPUT (y,z)
for(y=0;y<SMERY;y++)
    {for(z=0;z<SMERZ;z++)
        {putpixel(y,3*SMERZ-z+40,a[rez3][y][z]);} }
/*****/
//OUTPUT 1
if((vystup1=fopen("C:\\energie.cpp","w"))==NULL)
    {printf("output file error\n");getch();return 1; }

// CYCLE START
cas=0;krok=0;pocspin=SMERX*SMERY*SMERZ;
nav1:

//SELECTION OF RANDOM VALUE x,y,z
x=random(SMERX-2)+1;
y=random(SMERY-2)+1;
z=random(SMERZ-2)+1;

// SEARCHING OF LIQUID NODE
if(a[x][y][z]==1)
    {for(i=x-1;i<x+2;i++)
        {for(j=y-1;j<y+2;j++)
            {for(l=z-1;l<z+2;l++)
                {//INTERFACE WITH GAS
                    if(a[i][j][l]==0){xk=x;yk=y;zk=z;goto nav11;} }}//z,j,i
                goto nav1;//INTERNAL LIQUID NODE
            }
        }
    }
    }//if
    else {goto nav1;}

nav11:
// SELECTION OF RANDOM VALUE x,y,z
x=random(SMERX-2)+1;
y=random(SMERY-2)+1;
z=random(SMERZ-2)+1;

//SEARCHING OF NODE WITH GAS AT THE INTERFACE WITH LIQUID
if(a[x][y][z]==0)
    {for(i=x-1;i<x+2;i++)
        {for(j=y-1;j<y+2;j++)
            {for(l=z-1;l<z+2;l++)
                {//INTERFACE WITH LIQUID
                    if (a[i][j][l]==1){xv=x;yv=y;zv=z;goto nav111;} }}//l,j,i
                goto nav11;
            }
        }
    }
    }//if
    else {goto nav11;}

```

```

//{if (a[x][y][z]==1){xv=x;yv=y;zv=z;goto nav111;}
// }/if kont2
//{goto nav11;}
nav111:
//if(a[xk][yk][zk]==a[xv][yv][zv]){goto nav1;}
MCS++;if(MCS==pocspin)
    {MCS=0.;MCSPS++;fprintf(vystup1,"%8.f %8.f\n",
    MCSPS,energie);
    krok=0;cas=0;}

//CALCULATION OF TWO NODES BEFORE EXCHANGE
//BONDS ENERGY
enkap1=0.;envz1=0.;enpred=0.;
for(i=-1;j<=1;i++)
    {for(j=-1;j<=1;j++)
        {for(l=-1;l<=1;l++)
            {enkap1=enkap1+J[a[xk][yk][zk]][a[xk+i][yk+j][zk+l]]-J[a[xk][yk][zk]][a[xk][yk][zk]];
            envz1 =envz1+ J[a[xv][yv][zv]][a[xv+i][yv+j][zv+l]]-J[a[xv][yv][zv]][a[xv][yv][zv]]; } }/l,j,i
//GRAVITATIONAL ENERGY
engpr=G*zk;
//TOTAL ENERGY
enpred=engpr+enkap1+envz1;

//NODES EXCHANGE
apomoc=a[xk][yk][zk];a[xk][yk][zk]=a[xv][yv][zv];a[xv][yv][zv]=apomoc;

// CALCULATION OF TWO NODES AFTER EXCHANGE
//BONDS ENERGY
enkap2=0.;envz2=0.;enpo=0.;
for(i=-1;j<=1;i++)
    {for(j=-1;j<=1;j++)
        {for(l=-1;l<=1;l++)
            {enkap2=enkap2+J[a[xv][yv][zv]][a[xv+i][yv+j][zv+l]]-J[a[xv][yv][zv]][a[xv][yv][zv]];
            envz2 =envz2+J[a[xk][yk][zk]][a[xk+i][yk+j][zk+l]]-J[a[xk][yk][zk]][a[xk][yk][zk]]; } }/l,j,i
//GRAVITATIONAL ENERGY
engpo=G*zv;
//TOTAL ENERGY
enpo=engpo+enkap2+envz2;

//COMPARISON OF TWO TOTAL ENERGIES (BEFORE AND AFTER THE EXCHANGE)
deltaH=enpo-enpred;
//Boltzman rule
if(deltaH>0.){ Z=random(10000)/10000.;W=exp(-(deltaH)/(kT));
    if(Z>W)
        {apomoc1=a[xk][yk][zk];a[xk][yk][zk]=a[xv][yv][zv];a[xv][yv][zv]=apomoc1;
        goto nav1;} //end if Z
    } //end if deltaH
if(zk==rez1){putpixel(xk,4*SMERZ-yk+60,a[xk][yk][rez1]);}
if(zv==rez1){putpixel(xv,4*SMERZ-yv+60,a[xv][yv][rez1]);}
if(yk==rez2){putpixel(xk,2*SMERZ-zk+20,a[xk][rez2][zk]);}
if(yv==rez2){putpixel(xv,2*SMERZ-zv+20,a[xv][rez2][zv]);}
if(xk==rez3){putpixel(yk,3*SMERZ-zk+40,a[rez3][yk][zk]);}
if(xv==rez3){putpixel(yv,3*SMERZ-zv+40,a[rez3][yv][zv]);}
//OUTPUTS TO SCREEN DURING SIMULATION RUN
    krok++;
// if (krok>0){goto konec;}
    setfillstyle(1,0);
    bar(getmaxx()-70,getmaxy()-30,getmaxx(),getmaxy()-10);
    outtextxy(getmaxx()-100,getmaxy()-20,"k=");
    outtextxy(getmaxx()-70,getmaxy()-20,gcvt(krok,sig,str));
    if(MCSPS>(pockr)){goto konec;}
energie=energie+(enpo-enpred);

```

```

cas++;
/*****
//STATEMENTS ON THE SCREEN
setfillstyle(1,0);
bar(getmaxx()-220,getmaxy()-30,getmaxx()-150,getmaxy()-10);
outtextxy(getmaxx()-250,getmaxy()-20,"cas=");
outtextxy(getmaxx()-200,getmaxy()-20,gcvt(MCSPS,sig,str));
if(MCSPS>(pockr)){goto konec;}
goto nav1;
konec:
z=0;
        if((vystup0=fopen("c:\\hustota.cpp","w"))==NULL)
        {printf("output file error0\n");getch();return 1; }
nava:
hustota=0;
z++;
for(x=0;x<SMERX;x++)
    {for(y=0;y<SMERY;y++)
      { if (a[x][y][z]==1){hustota++;}}{fprintf(vystup0,"%8d %8d\n",z,hustota);}
      if(z>(SMERZ)){goto navb;}}
goto nava;
navb:
        if((vystup3=fopen("c:\\vrstva.cpp","w"))==NULL)
        {printf("output file error0\n");getch();return 1; }
z=1;
navb1:
z++;
evrstvy=0;
for(x=5;x<SMERX-5;x++)
    {for(y=5;y<SMERY-5;y++)
      {for(i=-1;i<=1;i++)
        {for(j=-1;j<=1;j++)
          {for(l=-1;l<=1;l++)

{ekontaktu=J[a[x][y][z]][a[x+i][y+j][z+1]];
  ebunky=ebunky+ekontaktu; } }/l,j,i
  ebunky1=ebunky-J[a[x][y][z]][a[x][y][z]];
  ebunky=0;
  evrstvy=evrstvy+ebunky1;}}/x,y BOUNDARY CONDITIONS (MINUS 5 CELLS)
eevrstvy=evrstvy/100;
{fprintf(vystup3,"%8d %8.f\n",z,eevrstvy);}
if(z>(SMERZ-3)){goto koneckonec;}
goto navb1; //z

koneckonec:
// OUTPUT 2,Open file, testing for success
        if ((vystup2=fopen("c:\\droplet.dat", "w"))==NULL)
        {
                printf("output file error2\n");
                exit(0);
        }
        for(x=0;x<SMERX;x++)
        {for(y=0;y<SMERY;y++)
        {for(z=0;z<SMERZ;z++)
        {fprintf(vystup2,"%8d %8d %8d %8d\n",x,y,z,a[x][y][z]); } }/y,x,z
fclose(vystup1);fclose(vystup0);fclose(vystup3);fclose(vystup2);
fclose (vystup1);fclose (vystup0);fclose(vystup3);
fclose(vystup1); fclose(vystup0);
fclose(vystup1);
getch ();
closegraph();
return 0;
}

```